Adhesion to the Bone Marrow Niche
-
Podosome-like structures in Hematopoietic Stem Cells

Von der Naturwissenschaftlichen Fakultät der
Gottfried Wilhelm Leibniz Universität Hannover

zur Erlangung des Grades
Doktorin der Naturwissenschaften (Dr. rer. nat.)

genehmigte Dissertation
von
Miriam Frommer, M. Sc.

2024

Abstract

Maintenance and homeostasis of the hematopoietic system is enabled by hematopoietic stem and progenitor cells (HSPC). These multipotent cells ensure the replenishment of all hematopoietic cells by giving rise to progeny with the ability to differentiate into respective cells while also self-renewing themselves. A crucial factor to regulate this essential feature of HSPC is their interaction with a specific microenvironment – the hematopoietic stem cell niche in the bone marrow (BM). The interaction of HSPC with their niche provides the signals necessary for the cells to maintain their stemness and to sustain the HSPC population. In order to provide these signals constantly, adhesion of the stem cells to the extracellular matrix (ECM) of the BM niche is of the utmost importance. Yet, the way in which HSPC anchor to their specific microenvironment is not well understood. In the here presented work, the adhesion structures established by HSPC upon contact with fibronectin are investigated in regard to their appearance, maturity state and composition of cell adhesion molecules (CAM).

By investigating the spatial distribution of native and mature adhesion structure markers alongside the actin cytoskeleton in adherent HSPC using super resolution microscopy it was found, that HSPC adhere in a dynamic manner and display varying morphologies that can contain protrusions and/or structures resembling podosomes. Further investigation of these podosome-like structures (PLS) revealed that these structures are defined by an F-actin spot strongly co-localizing with phosphorylated PYK2 (pPYK2). Assessment of the spatial distribution of pPYK2, alongside the classic podosome proteins vinculin and paxillin, showed a distribution of these molecules towards the periphery of the F-actin spot. This distribution pattern became more pronounced - resembling classic podosomes more - in cells with round morphology and increased number of PLS. Additionally, examining the differentiation state of HSPC with different morphologies, it was found that the round, PLS containing cells were less differentiated compared to cells with deviating observed morphologies.

Together, these findings indicate a highly dynamic adhesion behavior of HSPC, involving PLS. Given the importance of proper stem cell retention in the BM niche environment, for full function of the hematopoietic system, understanding the adhesion processes involved is an essential step in gaining insight into hematopoiesis in health and disease.

Kurzzusammenfassung

Die Instandhaltung des hämatopoetischen Systems wird durch hämatopoetische Stamm- und Progenitorzellen (HSPZ) ermöglicht. Diese multipotenten Zellen sorgen für die Bildung aller hämatopoetischen Zellen, indem sie Nachkommen hervorbringen, die in die entsprechenden Zellen differenzieren. Gleichzeitig können sich HSPZ selbst erneuern. Ein entscheidender Faktor, um diese essenzielle Eigenschaft zu regulieren, ist die Interaktion der HSPZ mit einer spezifischen Mikroumgebung - der hämatopoetischen Stammzellnische im Knochenmark. Die Adhäsion der Stammzellen an die extrazelluläre Matrix (EZM) der Nische ist für die Zelle von größter Bedeutung, um die Signale zu erhalten, die den Erhalt der Stammzelleigenschaften gewährleisten. Die Art und Weise, wie HSPZ in ihrer Nische adhärieren ist nicht gut verstanden. In der hier vorgestellten Arbeit werden die von HSPZ gebildeten Adhäsionsstrukturen bei Interaktion der Zellen mit Fibronektin im Hinblick auf ihre Architektur, ihren Reifegrad und die Molekülzusammensetzung untersucht.

Durch die Untersuchung von nativen und reifen Adhäsionsstrukturmarkern nebst dem Aktinzytoskelett wurde in adhärenten HSPZ mit Hilfe von hochauflösender Mikroskopie festgestellt, dass HSPZ dynamisch adhärieren und unterschiedliche Morphologien aufweisen, die Zellausläufer und/oder podosomen-artige Strukturen (PAS) enthalten können. Weiterführende Untersuchung dieser PAS ergab, dass die Strukturen durch einen F-Actin-Punkt definiert sind, der stark mit phosphoryliertem (p)-PYK2 kolokalisiert ist. Die Untersuchung der räumlichen Verteilung von pPYK2 zusammen mit den klassischen Podosomen-Proteinen Vinculin und Paxillin zeigte eine Verteilung dieser Moleküle in Richtung der Peripherie des F-Actin-Punktes. Dieses Verteilungsmuster war bei Zellen mit runder Morphologie und höherer Anzahl an PAS ausgeprägter und ähnelte mehr den klassischen Podosomen. Darüber hinaus wurde bei der Untersuchung des Differenzierungsstatus von HSPZ mit unterschiedlichen Morphologien festgestellt, dass diese Zellen auch weniger differenziert waren als die Zellen mit anderen Morphologien, die beobachtet wurden.

Zusammen deuten diese Ergebnisse auf ein hochdynamisches Adhäsionsverhalten von HSPZ hin, an dem PAS beteiligt sind. Angesichts der Bedeutung von erfolgreicher Retention der Stammzellen im Knochenmark ist das Verständnis der beteiligten Adhäsionsprozesse ein wesentlicher Schritt um einen besseren Einblick in die Blutbildung in Gesundheit und Krankheit zu gewinnen.

Schlagworte: Hämatopoetische Stammzellen, Knochenmark Nische, Adhäsion, Podosomen, Hämatopoese

Table of Contents

List of Abbreviations

%	percent
(v/v)	volume per volume
(w/v)	weight per volume
°C	degree celcius
µg	microgram
µL	microliter
µm	micrometer
µM	micromolar
µm²	square micrometer
µs	Microseconds
2D	two-dimensional
3D	three-dimensional
AM	adhesion media
APS	ammonium persulfate
AR	aspect ratio
Arp3	actin-related protein 3
ASAP3	Arf-GAP with SH3 domain, ANK repeat and PH domain-containing protein 3
a.u.	Arbitrary units
BCA	bicinchoninic acid
BM	bone marrow
BSA	bovine serum albumin
CAAM	Cell adhesion associated molecules
CAM	cell adhesion molecules
CAR cells	CXCL12-abundant reticular cells
CD	cluster of differentiation
CLP	common lymphoid progenitors
C-M-H-Test	Cochran-Mantel-Heanszel-Test
c-MLP	cloned myeloproliferative leukemia protein
CMP	common myeloid progenitors
CTCF	Corrected total cell fluorescence
CTTN	cortactin
CXCR4	CXC-chemokine receptor 4
DAPI	4′,6-Diamidin-2-phenylindol
ddH$_2$O	double deionised water
DNA	desoxyribonucleic acid
DPBS	Dulbecco's Phosphate Buffered Saline
EC	endothelial cells
ECM	extracellular matrix
EDA	extracellular domain A
EDB	extracellular domain B
EDTA	ethylenediaminetetraacteic acid
EtOH	ethanol
EV	extracellular vesicles
FA	focal adhesions
FACS	fluorescence activated cell sorting/scanning
F-actin	filamentous actin

FAK	focal adhesion kinase
FBS	fetal bovine serum
FERM-domain	4.1-Protein (Four-point-one), Ezrin, Radixin, Moesin - domain
Flt3L	Fms-like tyrosine 3 ligand
FN	fibronectin
FWHM	full width at half maximum
GAG	glycosaminoglycans
GAP	GTPase-activating protein
GAPDH	glyceraldehyde 3-phosphate dehydrogenase
G-CSF	granulocyte colony-stimulating factor
GMP	granulocyte/macrophage progenitors
h	hour
HA	hyaluronic acid
HPLC	high performance liquid chromatography
HRP	horse raddish peroxidase
HS1	hematopoietic lineage cell-specific protein 1
HSC	hematopoietic stem cells
HSPC	hematopoietic stem and progenitor cells
IF	immunofluorescence
JAK/STAT	janus kinase/signal transducer and activator of transcription protein
kDa	kilo dalton
LT-HSC	long-term hematopoietic stem cells
M	molar
mA	milliampere
MACS	magnetic activated cell sorting
MeOH	methanol
MEP	megakaryocyte/erythrocyte progenitors
mg	milligram
min	minute
mL	milliliter
mM	millimolar
MMP-9	matrix-metalloprotease 9
MPP	multipotent progenitor
ms	milliseconds
MSC	mesenchymal stem/stromal cells
MT1-MMP	membrane type-1 matrix metalloproteinase
nm	nanometer
OB	osteoblasts
Opn	osteopontin
PBMC	peripheral blood mononuclear cells
PBS	Phosphate Buffered Saline
PFA	paraformaldehyde
PIC	protease inhibitor cocktail
PIP2	phosphatidylinositol-4,5-biphosphat
PLS	podosome-like structure
PMA	phorbol 12-myristate 13-acetate
PMSF	phenylmethanesulfonyl fluoride
PYK2	proline-rich tyrosine kinase 2
pPYK2	phosphorylated PYK2
R^2	coefficient of determination

RGD	arginine-glycine-aspartatic acid
ROI	region of interest
rpm	rounds per minute
RPMI	Roswell Park Memorial Institute
RT	room temperature
SCF	stem cell factor
SD	standard deviation
SDS	sodium dodecyl sulfate
sec	second
SNO cells	spindle-shaped N-cadherin$^+$ CD45$^-$ osteoblastic cells
SR-cLSM	Super Resolution confocal Laser Scanning Microscopy
ST-HSC	short-term hematopoietic stem cells
TBS	Tris-Buffered Saline
TBS-T	Tris-Buffered Saline with Tween® 20
TEMED	N,N,N´,N´-tetramethyl-ethylenediamine
TKS5	SH3 and PX domain-containing protein 2A
TPO	thrombopoietin
tPYK2	total PYK2
UCB	umbilical cord blood
V	volt
VR	variable region
WASP	Wiskott-Aldrich syndrome protein
x g	relative centrifugal force

List of Figures

List of Tables

1. Introduction

1.1. Hematopoietic stem cells and their niche

Throughout life the organism is met with the challenge of cell loss, be it aging-, injury- or sickness-related. Replenishment of the cell pool is dependent on adult stem cells, which possess the ability to self-renew as well as to give rise to progeny that can differentiate to meet tissue-specific functions. These multipotent stem cells only give rise to multiple cells within one germ layer. The capacity of stem cells do differentiate, however, can vary beyond this, especially in embryonic development. Thus they are further classified as totipotent, if they are able to give rise to cell lineages of the entire organism including extraembryonic tissue and pluripotent, if they give rise to various cell types from all embryonic germ layers (endoderm, ectoderm and mesoderm), (Tabansky and Stern, 2016). Hematopoietic stem cells (HSC) belong to the multipotent category, as they are responsible for replenishing the cells of the hematopoietic system, producing around 10^{12} cells in adult human bone marrow (BM) daily (Doulatov et al., 2012). However, HSC can also be found in fetal liver, in umbilical cord blood (UCB) of newborns, and in peripheral blood. The number of HSC in peripheral blood can be increased by stimulation with granulocyte colony-stimulating factor (G-CSF), which induces mobilization of the cells from BM to peripheral blood. This is utilized during the harvesting of HSC for transplantation (Giebel, 2007). Transplantation of HSC can be used in the treatment of leukemic diseases, wherein the malignant hematopoietic cells are eradicated and exchanged for HSC from a compatible, healthy donor. The HSC then engraft into the BM and repopulate the entire hematopoietic system, potentially curing the leukemic disease (Bishop, 2009). Ever since the first successful HSC transplantation in the 1960s, the source of HSC for transplantation has shifted from BM-aspirates to UCB and mobilized HSC from peripheral blood (Bishop, 2009; Mathé et al., 1965). Especially the collection of UCB is an elegant approach for HSC harvesting, as it is a non-invasive procedure during childbirth. The transplantation of stem cells collected from UCB has been shown to carry a lower risk of graft-versus-host disease than transplants from BM or peripheral blood, even with less strict donor-recipient matching (MacMillan et al., 2009; Rocha et al., 2000; Wagner et al., 1996). The reason for this is found in the tolerogenic nature of UCB derived cell

populations (Kim and Broxmeyer, 2011). While this fact should translate into a higher accommodation of patients in need, the low number of CD34^{+} hematopoietic stem and progenitor cells (HSPC) in one UCB unit poses a significant limitation to successful HSC transplantation (Page et al., 2011; Wagner et al., 2002). The clinical significance of HSC highlights the overall importance of hematopoiesis in health and disease.

1.1.1. Hematopoiesis

The capability of HSC to keep their population size constant, while also producing daughter cells that are able to further differentiate, is organized via asymmetric cell division, which is influenced by cell polarity, extrinsic signals and intrinsic molecule distribution (Giebel, 2007). As a result, a small amount of HSC can maintain the entire blood production throughout life in a process called hematopoiesis. HSC need to keep their stem cell properties, called stemness, which is only the case for a few cells that stay in a quiescent state (Rieger and Schroeder, 2012). In this state the cells are mainly present in a dormant condition in the cell cycle G0-phase and are labelled long term (LT)-HSC (Chen et al., 2022; Osawa et al., 1996; Rieger and Schroeder, 2012). LT-HSC are the starting point of hematopoiesis and are very similar to their successors – the short term (ST)-HSC. These two populations are distinguished only by their ability to repopulate the BM of lethally irradiated mice, which is only weeks to months for ST-HSC but can be longer than 6 months for LT-HSC (Bartelmez, 2016). The two HSC populations are still marked by self-renewal capacity, while their progeny, the multipotent progenitor (MPP), already displays a finite capability of this property (Majeti et al., 2007; Reya et al., 2001; Rieger and Schroeder, 2012). MPP differentiate into two types of lineage committed cells: common myeloid progenitors (CMP) or common lymphoid progenitors (CLP) (Akashi et al., 2000; Kondo et al., 1997). CLP further differentiate into B-, T- and natural killer cells (Inlay et al., 2009; Zhang et al., 2018). The differentiation of CMP marks two distinct progenitor groups – the megakaryocyte/erythrocyte progenitors (MEP) and the granulocyte/macrophage progenitors (GMP) that finally form the cell types indicated in the progenitors name (Akashi et al., 2000; Zhang et al., 2018). Lastly, dendritic cells are listed to be differentiated from both, myeloid and lymphoid precursors (McLellan and Kämpgen, 2000; Puhr et al., 2015). In these classical descriptions of hematopoiesis, it is

described as a step like process, with distinct groups superseding each other. While this is helpful to explain the progression of hematopoiesis, it is not a representation of what actually happens *in vivo.* The differentiation of HSC towards distinct cell types of the blood is rather a continuous process (Velten et al., 2017). On a molecular basis the transition of HSC towards differentiated cell types is marked by the regulation of cell-division related genes and lineage-specific genes (Macaulay et al., 2016; Zhang et al., 2018). Yet, when researching hematopoiesis and HSC, the method of separating HSC from other cells, depends not on gene expression, but on the resulting surface marker production.

Discrimination of cells within the differentiation process is performed by immunophenotyping of so called cluster of differentiation (CD) molecules. To gather human HSC from the sources mentioned above (with the exception of fetal liver) the cells are usually isolated by utilizing the phenotypic presence of CD34. CD34 is a transmembrane phosphoglycoprotein that is characterized by its extracellular interaction with L-selectin and CrkL (Baumheter et al., 1993; Civin et al., 1984; Felschow et al., 2001). That CD34 is a suitable marker for the proliferative HSPC-population, was proven by the ability of $CD34^+$-cells to reconstitute the hematopoietic system (Huss, 2000; Servida et al., 1996; Sidney et al., 2014). Thus, this marker is used to isolate a cell population that ensures proper and quick engraftment of cells after transplantation (Berardi et al., 1995; Berenson et al., 1991). In the work presented here, isolation of $CD34^+$-cells was performed to gather enriched populations of HSPC for analysis. Since CD34 is produced late into the HSC progeny during hematopoiesis and not exclusively on cells of hematopoietic origin, the distinction of LT-/ST-HSC to their progeny is made possible by including other markers of differentiation (Sidney et al., 2014). The following segment highlights some markers, that were of special interest within the here presented work. The lack of CD38, together with the low production of CD90 and the absence of a panel of mature hematopoietic lineage markers (lin^-) are indicative of early LT-/ST-HSC (Huss, 2000; Sidney et al., 2014). CD38 starts emerging as HSPC start to lose their stem cell properties. Around this point in time, other markers can give indication of lineage commitment. CLP cells start producing CD45RA before gaining CD38, thus this cell population is also labelled $CD34^+CD38^-CD45RA^+$. *Vice versa*, if a cell is committed to the myeloid lineage it starts producing the markers CD33 and CD38, but not CD45RA. Thus, CMP and their progeny are immunophenotyped by $CD34^+CD38^+CD33^+CD45RA^-$ marker presence. Cells that produce both, CD38 and

3

CD45RA are accounted to the GMP fraction (see. Figure 1.1) (Laszlo et al., 2014; Rieger and Schroeder, 2012; Sumide et al., 2018).

The process of hematopoiesis is tightly regulated to keep the equilibrium between differentiation and self-renewal according to the acute need of the organism. Regulation does not only occur from within the cell, but is indeed majorly facilitated by extracellular input (Moore and Lemischka, 2006).
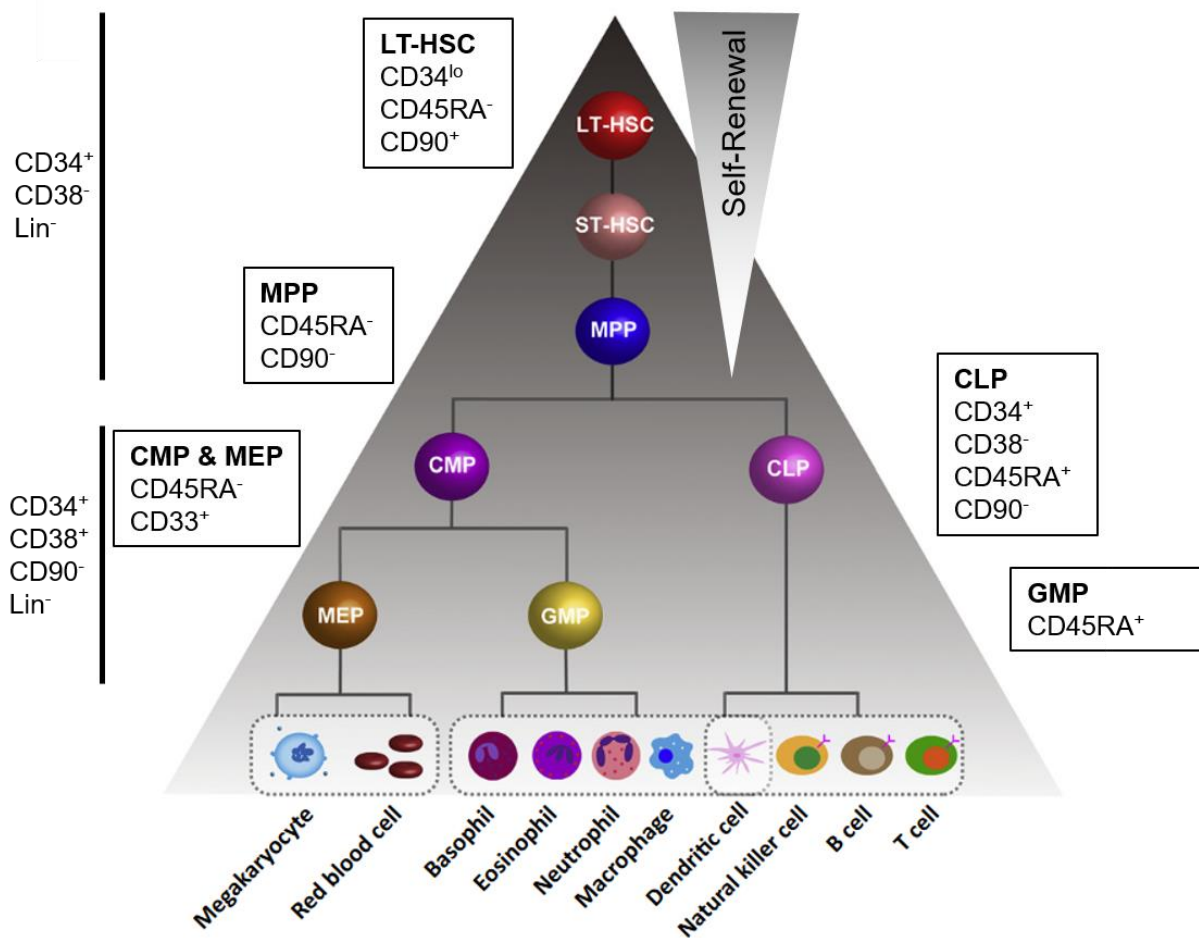
Figure 1.1 Schematic representation of hematopoiesis. *HSC maintain the hematopoietic system by differentiation into myeloid and lymphoid cells via a variety of progenitor cells. These are marked by characteristic production of CD molecules. The markers listed here are mostly selected by relevancy to this work and based on Rieger and Schroeder (2012). Gradual loss of self-renewal potential and gradual differentiation are indicated by gradient triangles. LT-HSC: Long-term hematopoietic stem cell; ST-HSC: Short-term hematopoietic stem cell; MPP: Multipotent progenitor; CMP: Common myeloid progenitor; CLP: Common lymphoid progenitor; MEP: Megakaryocyte/Erythrocyte progenitor; GMP: Granulocyte/Macrophage progenitor. Imaged altered from Zhang et al. (2018) with kind permission of Elsevier.*

1.1.2. The hematopoietic stem cell niche

For decades until now the hypothesis of the stem cell niche, postulated by Schofield in 1978, has been widely accepted and proven. Stem cell niches provide a specific microenvironmental context to stem cells to ensure stem cell function (Scadden, 2006). To achieve this feature, different factors come together: first, as was already described initially by Schofield, "the stem cell is seen in association with other cells which determine its behavior" (Schofield, 1978). The cellular composition of the stem cell niche builds the basis for stem cells to interact with their environment and receiving the signals for proper function. This goes beyond just cell-cell interaction, as HSC also receive signals from two other sources: the extracellular matrix (ECM) provided by niche cells and soluble components like cytokines and growth factors that can supplied by niche cells or more distant cells as a reaction to injury or sickness. Stem cells interact and receive signals from all these factors alone and in concert with each other (Hines et al., 2008; Levesque and Winkler, 2016). The HSC niche is found in the BM of trabecular bones (Boulais and Frenette, 2015; Pinho and Frenette, 2019). Here, HSC have been found close to the endosteum (labelled "endosteal niche") or in close proximity to BM sinusoids/arterioles ("perivascular niche") (Calvi et al., 2003; Kiel et al., 2005; Kunisaki et al., 2013; Zhang et al., 2003). Even though these two niches seem to be distinct microenvironments, containing specific HSC, it is not clear if the two niches also fulfill distinct functions or if they act together as a continuum (Ding and Morrison, 2013; Morrison and Scadden, 2014). Apart from the aforementioned factors (cells, ECM and soluble factors) that play crucial roles in the BM niche, other factors were also shown to have an impact on HSC fate. Factors of biophysical nature, for example, have a large impact on HSC fate. These factors contain the three-dimensional (3D) interface of the environment, the presented stiffness of niche cells and ECM to the HSC and the shear flow of circulating blood or other mechanical stimuli the HSC might be subjected to (Adams and Scadden, 2006). The importance of the bone marrow niche to HSC is highlighted by the fact, that HSC cannot be expanded *ex vivo* without losing their unique stem cell properties by rapidly inducing differentiation. As a result, decades of research have been aimed at defining culture conditions that enable the maintenance of self-renewing HSC *in vitro* (Walasek et al., 2012). Attempts span from incorporation of niche components, like niche cells and soluble factors in conventional cultures to recreation of the niche using 3D systems,

bioreactors or highly complex BM-on-a-chip approaches (reviewed by Chatterjee et al., 2021). Until now, none of these approaches has proved superior, especially given the context that different models need to fulfill different task. These tasks go beyond *ex vivo* expansion of HSC, as artificial niches also pose promising platforms for fundamental studies of the healthy and diseased BM niche or drug testing (Chramiec and Vunjak-Novakovic, 2019; Lee-Thedieck et al., 2022).

The following section will highlight important components of the BM niche, from cells and cytokines to ECM. A schematic representation of the niche and the interactions described below can be found in Figure 1.2.

1.1.2.1.   Cells of the BM niche

The endosteum of the BM, where HSC are found, is lined primarily with osteoblasts (OB). *In vitro,* OB are able to maintain primitive HSC for up to two weeks (Taichman et al., 1996). Still, major expansion of native HSC was not yet proven successful under these conditions (Hines et al., 2008). HSC interact with a specific subset of OB, labelled spindle-shaped N-cadherin$^+$ CD45$^-$ osteoblastic (SNO) cells. Increase in SNO cells correlated with rising number of HSC and LT-HSC that were found in contact with these cells, in *in vivo* studies in mice. This supports the notion, that the endosteal niche keeps HSC in a dormant state with high self-renewal potential (Kulkarni and Kale, 2020). Furthermore, the adherens junctions established between SNO cells and HSC via N-cadherin seems to be crucial for HSC to maintain stemness (Zhang et al., 2003). During adult hematopoiesis, the Notch-receptor and its downstream signaling pathway also contribute to the regulation of HSC fate. HSC interact with the Notch-ligand jagged-1 on mesenchymal stem/stromal cells (MSC), OB and endothelial cells (EC) (Butler et al., 2010; Calvi et al., 2003; Poulos et al., 2013; Varnum-Finney et al., 1998). This interaction functions as a regulating element in adult hematopoiesis (Lampreia et al., 2017). OB are usually found in a tight homeostasis with osteoclasts. This is the same in BM, where osteoclasts influence HSC to mobilize via G-CSF (Miyamoto, 2013).

In the vascular niche, HSC interact with EC that make up the inner lining of the blood vessels. However, MSC, macrophages and CXCL12-abundant reticular (CAR) cells are also found in this microenvironment and interact with the CXC-chemokine receptor

4 (CXCR4) on HSC, either by presenting or releasing CXCL12 (Chatterjee et al., 2021; Nagasawa, 2014). The CXCL12-CXCR4 signaling axis is one of the most important contributors to proper HSPC homing but has also be found to play a role in B-cell development (Nagasawa, 2006; Sugiyama et al., 2006; Zou et al., 1998). Again, this shows that the regulation of HSPC function is a tightly regulated process, keeping balance between differentiation and self-renewal.

1.1.2.2.   Soluble components of the BM niche

Soluble factors further regulate stem cell fate. They either originate from within the niche or arrive from outside the BM to signal the current state of the organism (e.g. sickness, injury etc.). Soluble factors include cytokines, chemokines and growth factors. Some of these secreted mediators (G-CSF and CXCL12) have already been highlighted in 1.1.2.1. Endothelial and stromal cells in the BM niche (or adipocytes as an emergency response) supply the stem cell factor (SCF) that binds to the receptor c-Kit on HSC (Ding et al., 2012; Zhou et al., 2017; Zsebo et al., 1990). c-Kit activation via SCF regulates HSC population *in vivo*, and *in vitro* studies suggest that this is achieved by the SCF concentration-dependent modulation of HSC expansion (Audet et al., 2002; Kent et al., 2008). OB provide the niche with soluble thrombopoietin (TPO), which also promotes self-renewal and expansion of HSC. Upon interaction of TPO with the cloned myeloproliferative leukemia protein (c-Mpl) receptor, cell function is regulated via the janus kinase/signal transducer and activator of transcription protein (JAK/STAT) pathway (reviewed by Hitchcock and Kaushansky, 2014). Stromal cells within the murine BM niche produce the Fms-like tyrosine 3 ligand (Flt3L) (Hannum et al., 1994). In both human and murine HSC, this cytokine binds to its receptor Flt3 that plays a crucial role in maintenance of HSC homeostasis in humans, so much so that its genetic modification is commonly associated with acute myeloid leukemia (Carow et al., 1996; Kikushige et al., 2008). SCF, TPO and Flt3L are commonly used in the *ex vivo* expansion of HSPC, due to their well established HSC supporting properties (Bhatia et al., 1997; Conneally et al., 1997). Other soluble factors that play a prominent role in the regulation of hematopoiesis are interleukin 3 and 6, the transforming growth factor beta and the insulin-like growth factor 1 (Lee et al., 2020)

1.1.2.3. ECM of the BM niche

In addition to providing soluble components, cells of the BM niche also supply the extracellular environment with matrix proteins. The interplay of these two niche components provided by cells has a large impact to HSC. The "soluble" factors are frequently presented in association with ECM proteins. This has a striking effect: commonly, if soluble growth factors bind a receptor, they are submitted to receptor-mediated endocytosis, however, if signal transmitters are immobilized to the ECM, the signal persists in the extracellular space. Thus, the composition of the niche microenvironment impacts cell fate in a variety of ways (Hines et al., 2008). The proteins of the BM ECM can be divided into three major classes: structural proteins, glycoproteins and glycosaminoglycans (GAG) (Chatterjee et al., 2021).

Many of the structural proteins present in the HSC niche are part of the collagen family. These molecules are characterized by triple helical structures assembled from homo- and heterotrimeric polypeptides (Van Der Rest and Garrone, 1991). The collagens shown to play a role in BM are type I-VI, IX-X, XIV and XVIII collagens (Hines et al., 2008; Lee-Thedieck et al., 2022). Collagens mainly present adhesive substrates to cells of hematopoietic lineage, and some studies suggest, that the presence of certain collagen types determine the type of hematopoietic cell that retains in a specific space (Klein, 1995; Koenigsmann et al., 1992).

GAGs consist of repeating disaccharide units that are mostly found as parts of proteoglycans with a respective protein core (Rodgers et al., 2008). Most of the GAGs present in the BM are sulfated proteoglycans, that bind CXCL12 and thus modulate HSC anchorage and migration via the CXCL12/CXCR4 axis (Netelenbos et al., 2003). An exemption of this is the GAG hyaluronic acid (HA) that is not sulfated or bound to a core protein. It plays a prominent role in the BM niche, as it can activate cell-signaling pathways respective to its molecular weight. By doing so it functions as an intricate balance keeper in development, homeostasis and disease in the hematopoietic context (Hines et al., 2008; Tammi et al., 2002).

Many glycoproteins play a role in the BM microenvironment. Laminins are heterotrimeric proteins assembled of different α-, β-, and γ-chains respectively, which are a crucial component of the basement membrane in almost all animal tissue (Colognato and Yurchenco, 2000). In BM, laminins 421, 521 and 522 are prevalent

and influence cycling and homing of HSPC (Gu et al., 2003; Susek et al., 2018). A family of laminin related proteins are the netrins. They modulate adhesion, migration, proliferation and differentiation in general and regulate stemness in HSC specifically (Cirulli and Yebra, 2007; Renders et al., 2021). Tenascin-C is a prominent member of the tenascin family in the BM and has an important role in regulating normal HSC development (Klein et al., 1993; Lee-Thedieck et al., 2022). Other glycoproteins in the hematopoietic niche are thrombospondins that offer anchorage sites to hematopoietic cells of erythroid, megakaryocytic and myeloid lineages. The interaction with thrombospondin seems to diminish as these cells start to mature, making thrombospondins a modulator for this process (Lee-Thedieck et al., 2022; Long and Dixit, 1990; Long et al., 1992). Osteopontin (Opn) is an acidic glycoprotein that makes up around 2 % of the non-collagenous protein in the endosteal region (Haylock and Nilsson, 2006). Opn acts restrictive on HSC proliferation and thus regulates stem cell quiescence (Nilsson et al., 2005). An ubiquitously present glycoprotein of the ECM is fibronectin (FN). Due to the importance of FN to the here presented work, it will be highlighted separately and in more detail.
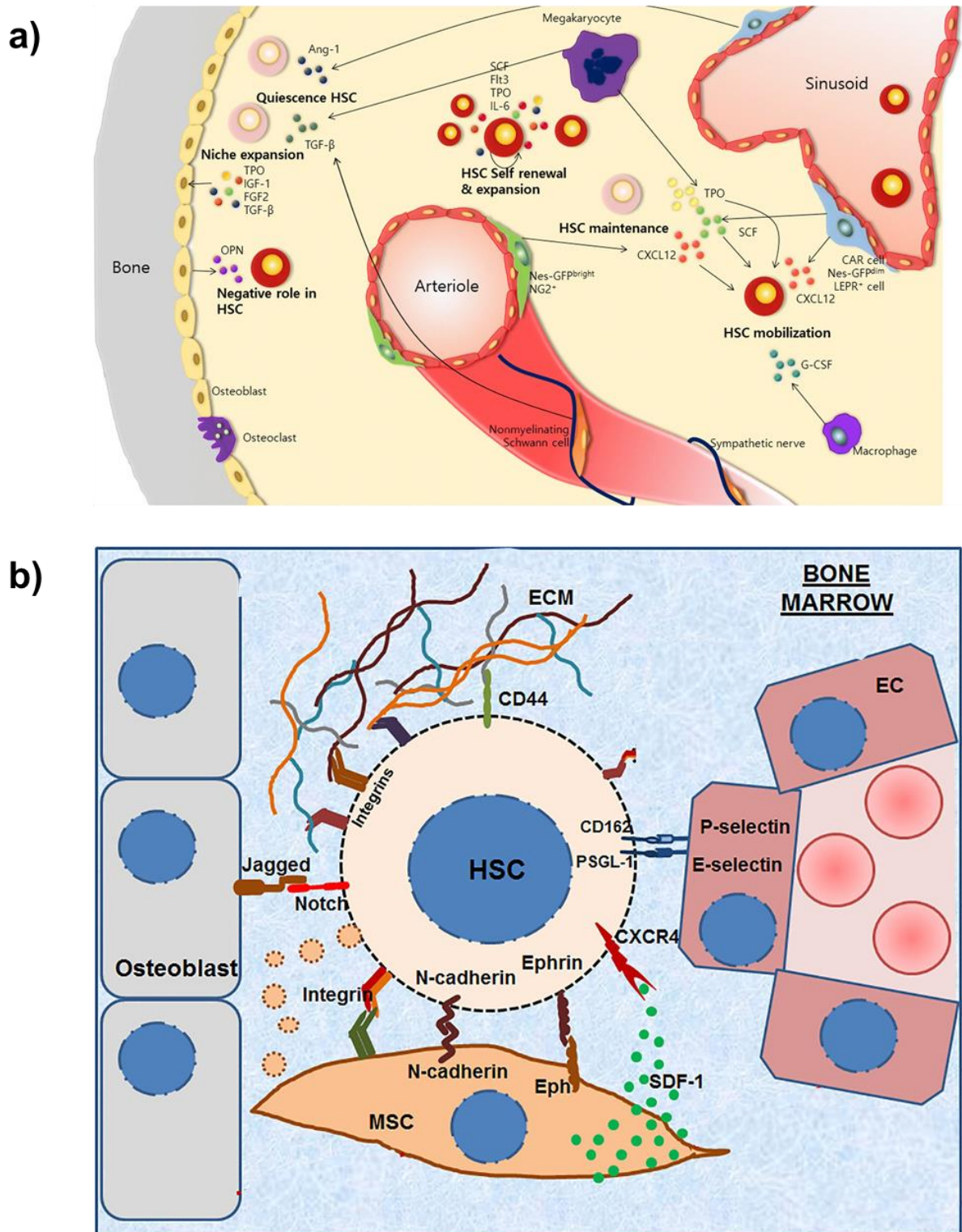
Figure 1.2 Schematic representation of the BM niche and the interactions therein. a) *shows cells of the distinct BM niches (endosteal and vascular from left to right) and the cells that are present in these compartments. Additionally, the factors secreted by these cells (predominantly soluble) and their effects on HSC are shown. Image based on Lee et al. (2020) with kind permission of Springer Nature.* **b)** *displays the interaction of the HSC with its niche, the receptors that play a role therein and their ligands. Image altered from Kulkarni and Kale (2020) under Creative Commons Attribution License (CC BY 4.0 DEED).*

<u>Fibronectin</u>

FN is a glycoprotein that is produced as a dimer of two almost identical molecules each of around 250 kDa. These are covalently linked near the C-termini by a pair of disulfide bonds. FN can be produced as a soluble molecule in the blood plasma, but in context of the ECM, it is labelled tissue FN and is an important structural element. Tissue FN plays a prominent role in adhesion, migration, differentiation and proliferation for a variety of cell types (Hynes, 1990). Its soluble variant, called plasma FN, plays a relevant role in wound healing. Each FN molecule is composed of three types of repeating subunits, called FN-repeats type I, type II and type III. FN-repeat types are defined by the number of amino-acid residues and the presence of disulfide bonds (Pankov and Yamada, 2002). Most subunits of FN are similar between FN-molecules, however three regions between the chains might differ: the extracellular domain A (EDA), the extracellular domain B (EDB) and the so-called variable region (VR). These can undergo alternative splicing. In the isoform labelled plasma FN neither EDA nor EDB are present, however in all other cases the inclusion of EDA conditions the exclusion of EDB, resulting in a "yes or no" type of splicing. These alternate splicing variants of FN result in alternate presentation of binding motifs by FN (Leiss et al., 2008; Pankov and Yamada, 2002; Wirth et al., 2020). Dozens of integrin receptors (see below 1.2.1) can recognize and bind to FN. The best understood recognition sequence of FN for this is the Arg-Gly-Asp sequence. The recognition of this simple tripeptide sequence depends on the flanking residues within the FN dimer, on its spatial presentation and the individual features of the integrin binding pockets. Other cell-recognition patterns in FN are the Leu-Asp-Val or the Arg-Glu-Asp-Val sequences in the VR. Additionally, proteolytic cleavage of FN can influence the interaction with cells, as it alters the presentation of binding sequences that were masked prior to cleavage (Hynes, 1990). Apart from cell-interaction FN displays functional activity by binding ECM molecules like collagen, heparin, fibrin or other proteoglycans, thus forming larger ECM complexes (Pankov and Yamada, 2002). Around 4-9 % of FN are glycosylated and while the physiological function is not fully understood, it is likely that carbohydrates stabilize and modulate substrate-affinity (Pankov and Yamada, 2002). An overview of FN structure and its interaction sides can be found in Figure 1.3.

In the BM niche, FN is abundantly present as it is produced by many cell types in this space. As described above, a variety of FN isoforms can be produced, different binding sites might be available and thus FN can modulate many cell-functions, depending on the cell receptor interacting with the ECM molecule. These include modulation of proliferation, inhibition of apoptosis, support of migration and regulation of differentiation (Wirth et al., 2020). However, since FN is ubiquitously present in the BM niche, its impact on hematopoiesis is often evaluated via the role of the receptors that interact with the molecule. FN helps in engraftment and homing of HSC via integrin β1 interaction (Potocnik et al., 2000; Sagar et al., 2006). This is supported by the isoform of CD44 in HSPC, called HCELL, that also bind to FN and has a role in HSPC homing (Cao et al., 2016; Sackstein et al., 2008). Proliferation is indirectly suppressed in HSC via αvβ3 integrin interaction with FN (Umemoto et al., 2012; von Au et al., 2013). The toll-like receptor 4 is produced by HSC, which binds to EDA-fibronectin, enhances proliferation and differentiation in myeloid favor upon pathogen interaction (Liu et al., 2015). Most important to the work presented here, FN supports HSC attachment to the BM niche. The integrins facilitating this function of FN are α4β1, α5β1 and αvβ3. The role of α4β1 is proven by the migration of HSC out of the niche when α4 is impaired (Scott et al., 2003). The binding of LT-HSC in mice to FN via α5β1 was observed by van der Loo et al. (1998). αvβ3 has been shown to maintain LT-HSC in culture and is known to bind to EDB-FN, which is secreted by OB (Sens et al., 2017; Umemoto et al., 2012). A direct interaction with αvβ3 of HSPC and EDB-FN of OB has yet to be shown. The role of FN in HSPC attachment is so prevalent, that it is often used to study the adhesion behavior of these cells (Cancelas, 2011).
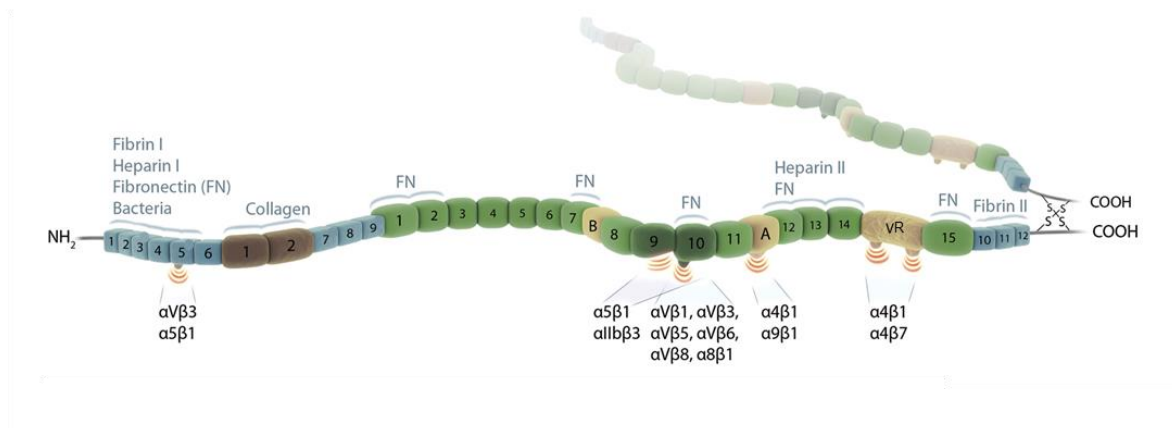
Figure 1.3 Structure of fibronectin *FN-repeats are labelled by color: type I, blue; type II brown; type III green. Alternate splicing regions extracellular domain A (EDA), extracellular domain B (EDB) and variable region are labelled by A, B and VR respectively. Binding sites of integrins and other ECM molecules are indicated in the respective FN-repeat. Image altered from Leiss et al. (2008) with kind permission of Elsevier.*

1.2. Adhesion in general and in HSC in particular

Within the BM niche, HSC encounter a variety of signals that influence their fate and hematopoiesis overall (as described so far in 1.1). The process of forming persistent attachment with other cells or the ECM in the niche, is called cell adhesion (Christen et al., 2016). In the context of hematopoiesis, adhesion is a crucial determinant regulating continuous signal reception of a stem cell, prohibiting unregulated migration from the niche and thus is an important factor in HSC behavior.

1.2.1. The role of integrins in adhesion

Integrins are important adhesion receptors, as alluded to in 1.1.2. Integrins are heterodimeric transmembrane proteins, consisting of an α- and β-subunit that are non-covalently bound. In humans, 18 isoforms of α-subunits and 8 isoforms of β-subunits are reported, which pair differently to result in a total of 24 integrin-receptors that can facilitate cell-matrix interaction (Takada et al., 2007). Each subunit of an integrin spans the cell-membrane separately and shows short intracellular domains, with exception of the β4-subunit, where the extracellular domain is quite large in comparison to other integrin subunits (de Pereda et al., 1999; Springer and Wang, 2004). While the

13

cytoplasmic domains of integrins bind intracellular activators of the receptors, like talin, the ectodomains bind specific ligands to the integrin heterodimer variant (Ye et al., 2010) The integrin ectodomains undergo conformational changes from an inactive "bent"-state to an active "extended" conformation (see Figure 1.4). The stability of the active state, and thus also the ligand binding, is dependent on the presence of divalent cations like Mg^{2+}, Ca^{2+} or Mn^{2+} (Arnaout et al., 2005; Shattil, 2005). Conformational changes between integrin states occur fast, are reversible and are not only induced by ligand binding but also regulated by intracellular binding of molecules, like talin, to the heterodimer (Anthis and Campbell, 2011; Ye et al., 2010). This "*outside-in*" versus "*inside-out*" activation of integrins makes them a bidirectional platform of not only signaling events but also force-transmission. Ligand-bound integrins generate force against the ECM indirectly by linking via talin or vinculin to the actomyosin retrograde flow established within the cell upon integrin activation. This process is named the "molecular clutch", a system that is quickly adjustable to the ECM rigidity (Mitchison and Kirschner, 1988). With higher substrate stiffness the mechanical force leads to unfolding events in talin, revealing more interaction sites for vinculin and actin which in turn increase force transmission (Anthis and Campbell, 2011; Ye et al., 2010; Zhu et al., 2008). On substrates with low rigidity, the forces are not strong enough to unfold talin and induce the molecular clutch reinforcement. Therefore, integrins "feel" their surrounding not only by the ligands available but also by the biophysical context they are presented in. As even more molecules are involved in the molecular clutch and at integrin-engaging adhesion sites in general, it comes to no surprise that the mechanotransduction at these sites influences biochemical processes as well. Signaling events at integrin interaction sides, of both mechanic and biochemical nature, have impact on cell morphology, migration, differentiation or proliferation, making integrins one of the most important adhesion receptor types (Sun et al., 2016).
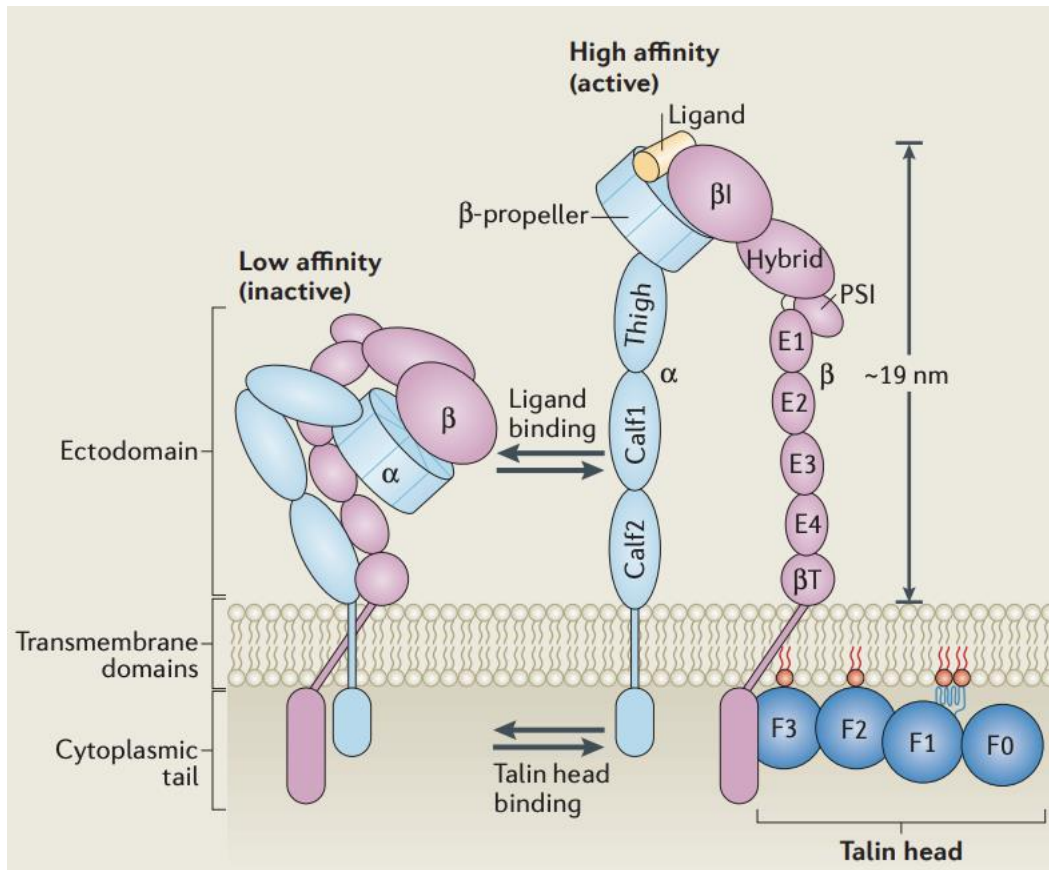
Figure 1.4 Schematic representation of integrin structure, states and activation *Shown is the structure of integrins with α- and β-subunits (blue and pink respectively). Each integrin subunit consists of an ectodomain, a transmembrane domain and a cytoplasmic tail. Upon ligand binding (outside-in) and/or talin binding (inside-out) the integrin switches from an inactive (bend, left side) state to a high-affinity (extended, right side) state. Image based on Calderwood et al., 2013 with kind permission of Springer Nature.*

HSPC seem to be a good example demonstrating the role of integrins as bidirectional mechanotransduction sites. They are known to produce β1, β2, β3 and β7 integrins. The best studied among these are the integrins coupling β1, these being α1, α2, α4, α5 and α6 (Levesque and Winkler, 2016). β1 integrins have a crucial role in HSPC homing and migration, as is indicated by the involvement of α4β1, α5β1 (and αLβ2) integrins in the migration towards CXCL12 in the homing process (Peled et al., 2000). *Vice versa*, it was shown, that under G-CSF induced HSPC migration out of the niche, integrin production by HSC was significantly reduced (Wagers et al., 2002). The interactions of HSC with FN via integrin α4β1 and periostin via αvβ3 have an impact on quiescence and cell proliferation (Khurana et al., 2016; Oostendorp and Dörmer, 1997). Additionally, while the specific interactions of these integrins on HSC are not known, α6β1 and αII2β3 are used as markers of a specific subset of LT-HSC (Gekas and Graf, 2013; Notta et al., 2011). Furthermore, matrix stiffness has been proven to

be a regulator in HSC homeostasis (Holst et al., 2010; Lee-Thedieck et al., 2012). This elucidates the role of integrin-facilitated adhesion for HSC fate.

1.2.2. Focal Adhesions

The mechanotransduction mechanisms described so far are classically displayed by focal adhesions (FA). These adhesion structures are usually formed by fibroblastic cells as dense F-actin plaques of 2-6 μm width. FA are multimolecular interaction sites, lasting up to hours upon establishment, and are usually found in the leading edge of the cell (Eleniste and Bruzzaniti, 2012a). Initially upon integrin-ECM interaction, the receptors start to interact with other ligand-bound and unligated integrins, forming so called intergrin-clusters (Cai and Sheetz, 2009; Lin and Asaro, 2022; Vicente-Manzanares et al., 2009). These cluster-sites are found in filopodia that protrude beyond the leading edge radially. Along the filopodia-contact sites, nascent adhesions are formed linking the integrins via talin to the actin cytoskeleton (Partridge and Marcantonio, 2006). An important event in FA maturation after this initial process is the tyrosine kinase dependent phosphorylation of multiple substrates, but most importantly paxillin (Albiges-Rizo et al., 2009; Thomas et al., 1999). The focal adhesion kinase (FAK), or its relative, the proline-rich tyrosine kinase 2 (PYK2), found predominantly in cells of the nervous and hematopoietic system, mediates these phosphorylations (Eleniste and Bruzzaniti, 2012a). Phospho-paxillin provides a binding platform for vinculin, which is activated upon interaction with talin, a process mediating adhesion strengthening (Case et al., 2015). In nascent FA the actin nucleator complex Arp2/3 is present interacting with FAK in the cell periphery, but it is absent from mature complexes (see Figure 1.5; Serrels et al., 2007). The Arp2/3 complex might be one of the early acting players coupling integrin activation to F-actin polymerization (DeMali et al., 2002a). FA share many molecules with other adhesion structures discussed below (see 1.2.3), yet they differ drastically in formation, dynamically and architecture-wise. One of the few FA exclusive molecules is the Arf GTPase-activating protein (GAP) with SH3 domain, ankyrin repeat and PH domain 3 (ASAP3). GAPs control structural changes in the cytoskeleton, and ASAP3 specifically is important in the control of cell movement (Albiges-Rizo et al., 2009; Ha et al., 2008).
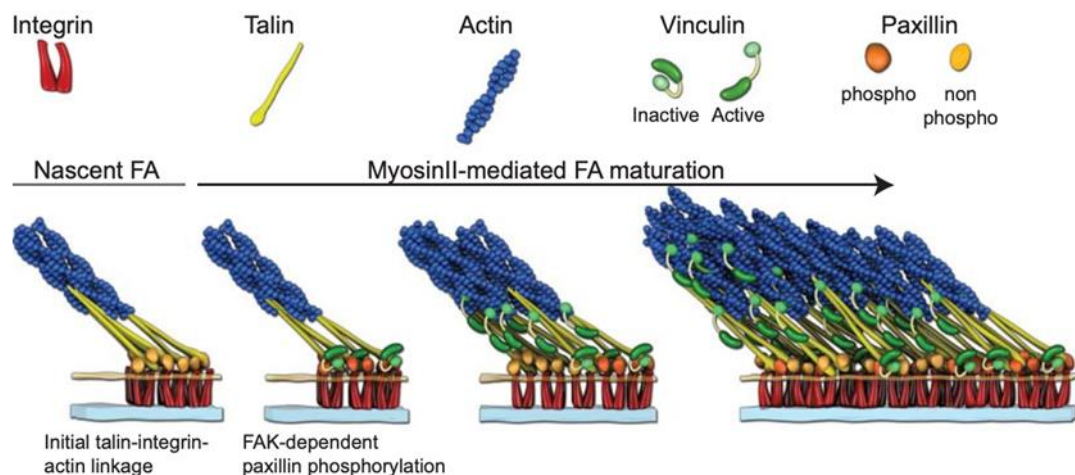
Figure 1.5 Schematic representation of focal adhesion structure and maturation. From left to right: Upon integrin interaction with the matrix, talin binds F-actin and paxillin. FAK facilitated phosphorylation of paxillin, which enables binding of vinculin. Integrin clustering, the F-actin retrograde flow facilitated by myosin-II and force transmission via vinculin are factors promoting FA maturation. Image based on Case et al., 2015 with kind permission of Springer Nature.

1.2.3. Invadosomes

Many of the molecules involved in the establishment and function of FA are also present in a different sub-set of adhesion structures – the invadosomes. This term refers to structures with matrix-degrading properties called podosomes or invadopodia. Structures are usually labelled podosomes if they are established by somatic cells, while invadopodia are established by cancer cells. Both structures show distinct features and organizational traits. However, the overall structure of invadosomes is very similar, with a punctate F-actin core surrounded by an adhesive ring, containing molecules such as vinculin and paxillin, and associated with matrix degrading proteases (Cambi and Chavrier, 2021). The entire structure is around 0.5-2 µm in diameter. While podosomes display a half-life of just minutes, invadopodia can persist up to several hours (Eleniste and Bruzzaniti, 2012a). If integrins interact with the ECM at sites of invadosome formation, areas accumulating with phosphatidylinositol-4,5-biphosphat (PIP2) at the plasma membrane are formed. PIP2 downstream signaling leads to engagement of the non-receptor tyrosine kinase Src, which constitutes a critical step in invadosome formation. Src leads to a major reorganization of the actin cytoskeleton and phosphorylates important molecules involved in the protrusive structures, such as cortactin, Wiskott-Aldrich syndrome protein (WASP) and FAK. The

activation of cortactin and WASP is necessary to allow continuous actin nucleation via the Arp2/3 complex that is enriched at the core of the invadosome. The interaction of these components establishes a dense branched actin network, which, upon structure maturation, is elongated into a column and finally into a network of radial F-actin filaments to connect neighboring invadosomes (see Figure 1.6 a); Albiges-Rizo et al., 2009). Between the initial steps of building the nascent structure and the establishment of the adhesive ring, the key proteinase membrane type-1 matrix metalloproteinase (MT1-MMP) is recruited to facilitate matrix degradation (Hoshino et al., 2013).

Despite the overall similarity in structure and assembly, podosomes and invadopodia show important differences. In the initial steps of integrin engagement and maturation of podosomes, Pyk2 autophosphorylation is a prominent event in the formation of these structures, while its role in invadopodia is subordinate to FAK (Eleniste and Bruzzaniti, 2012a). Additionally, the matrix-metalloprotease MMP-9 is predominantly recruited, activated and secreted at sites of podosome formation. More importantly, while MMP-9 is not crucial for podosome formation, its recruitment and activation is important for the degrading activity at these adhesion structures, making the protease an indicator of podosome activity (Delaissé et al., 2000; Xiao et al., 2010). MMP-9 is not involved in invadopodia formation and function, as matrix degradation by these structures is primarily performed by MT1-MMP1. Cortactin is accumulated prior to F-actin nucleation and MT1-MMP1 recruitment and thus an early indicator of invadopodia formation (Artym et al., 2006; Ayala et al., 2008). The formation of invadopodia is promoted by the tyrosine kinase substrate with five SH3 domains (Tsk5), a scaffolding protein tightly associated with malignant matrix degradation, a driving factor of invasion (Eleniste and Bruzzaniti, 2012a; Stylli et al., 2009). While podosomes and invadopodia appear as very similar structures, they can assemble and transform into larger structures that show distinct features. Depending on the cell type they are produced in, podosomes can form large, interconnected assemblies, that act as mechanosensing platforms in dendritic cells, form sealing zone belts in osteoclasts or smaller so called rosettes in endothelial cells (see Figure 1.6 b); Cambi and Chavrier, 2021; van den Dries et al., 2019). Invadopodia display transformation into larger, elongated protrusive structures, depending on how the underlying matrix presents to the cell. Matrix properties influencing invadopodia shape are first and foremost thickness, with thin matrix layers inducing the elongated invadopodia shape, that seems to follow the presented matrix fibers (see Figure 1.6 c); Cambi and Chavrier,

2021; Juin et al., 2012). Overall invadosomes are a versatile type of adhesion sites, displaying protrusive and mechanosensing properties.
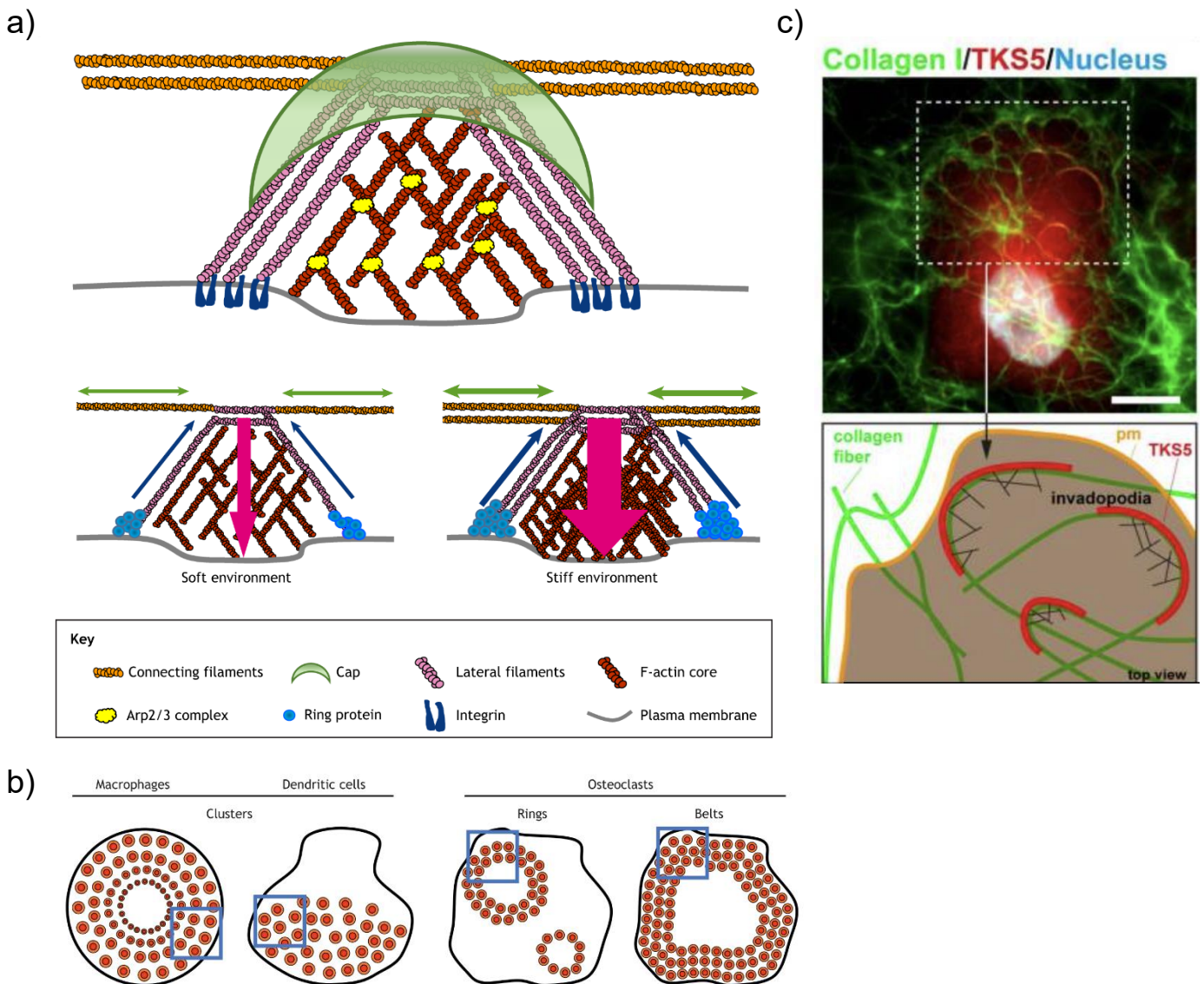
Figure 1.6 Invadosome structures a) *Schematic representation of invadosomes with a branched F-actin core and an adhesive ring. Interconnection between invadosomes is indicated next to forces extruded by invadosomes. **b)** Representation of larger podosome formation. Images a) & b) based on van den Dries et al., 2019 with kind permission of the Journal of Cell Science. **c)** Fluorescent image and schematic representation of transformed invadopodia on collagen I matrix. Pm: plasma membrane. Image based on Cambi and Chavrier, 2021 under Creative Commons Attribution License (CC BY 4.0 DEED).*

1.2.4. Adhesion in HSC

Attachment of HSPC is important in context of the hematopoiesis regulated by the BM niche (see 1.1). This is further supported by the number of CAM that were shown to have an impact on HSPC maintenance. A variety of adhesion receptors are known to influence HSPC behavior including integrins, HCELL, selectin ligands and Eph receptors (mentioned in 1.1 and reviewed by Levesque and Winkler, 2016). Integrin signaling in HSPC is mediated by PYK2 that is produced in high levels, contrary to FAK (Dikic et al., 1998). PYK2 activation in HSPC leads to quiescence and downstream recruitment of paxillin (Dylla et al., 2004; Wang et al., 2000). Another intracellular player in HSPC adhesion is vinculin. While silencing of this actin-linker in mice did not affect homing of HSPC, it did prohibit proper repopulation of transplanted stem cells in the BM niche (Ohmori et al., 2010). While these classic molecules of adhesion have an influence on HSPC, they have not been shown to establish the fully matured structures of FA, podosomes or invadopodia in these cells. Rademakers et al. (2018) showed that HSPC form podosome-like structures, containing vinculin and hematopoietic lineage cell-specific protein 1 (HS1) upon stimulation with phorbol 12-myristate 13-acetate (PMA). These structures are speculated to be involved in transcellular migration processes of the HSPC across the BM endothelium in the homing process. Whether HSPC form these kinds of structures without stimulation or what kind of adhesion structures are established for cell retention in the niche is subject of further research.

1.3. Aim

The retention of HSPC to their niche in the BM is of upmost importance to the maintenance of their stem cell properties. Secure anchorage of a cell to its environment is achieved by cell adhesion and a variety of cell adhesion molecules have been observed to play a role in HSPC regulation.

The aim of the here presented work was to identify and analyze cell-matrix adhesion structures established by HSPC. For this purpose, an approach based on super resolution confocal laser scanning microscopy (SR-cLSM) was chosen. HSPC isolated from UCB were brought to adhesion on FN. Then, marker proteins of FA, podosomes

and invadopodia were labelled and the spatial distribution of the adhesion marker were assessed.

Understanding the mechanisms and molecules involved in HSPC adhesion opens up possibilities to target these processes *in vitro* to support the expansion and preservation of these valuable cells *ex vivo.* The maintenance of HSPC in long-term culture has been the objective of ongoing research, utilizing cytokine and growth factor supplements in culture or providing artificial platforms of specific biomaterials and topography to mimic the BM niche conditions. If prolonged culture of HSPC would be possible, these cells would be readily available for, first and foremost, clinical purposes and medical treatment, but also for further research on the cells themselves and the leukemic diseases they can succumb to. The work presented in this thesis aims to support this important research field by providing an understanding of a fundamental part of HSPC-matrix interaction.

2. Materials

2.1. Cell lines

Table 2.1 Used cell lines

Cell Line	Supplier
KG-1a	Leibniz-Institut - Deutsche Sammlung von Mikroorganismen und Zellkulturen GmbH, Braunschweig, Germany
THP-1	kindly provided by Prof. Jörg Overhage (formerly associated with Institute of functional interfaces, Karlsruhe Institute of Technology (KIT), currently: Carleton University, Canada)

2.2. Chemicals

Table 2.2 Used chemicals

Chemical	Supplier
Ammonium persulfate (APS)	Merck KGaA, Darmstadt, Germany
Ammoniume chloride (NH$_4$Cl)	Merck KGaA, Darmstadt, Germany
Bromphenole blue	Merck KGaA, Darmstadt, Germany
Dabco® 33-LV	Merck KGaA, Darmstadt, Germany
Ethanol 99,8 %, denatured (EtOH)	AppliChem GmbH, Darmstadt, Germany
Ethylenediaminetetraacteic acid disodium salt dihydrate (Di-sodium-EDTA)	Merck KGaA, Darmstadt, Germany
Glycerol, anhydrous	Merck KGaA, Darmstadt, Germany
Glycine for molecular biology	AppliChem GmbH, Darmstadt, Germany
Manganese(II) chloride monohydrate (MnCl$_2$ · H$_2$O)	Carl Roth GmbH + Co. KG, Karlsruhe, Germany
Methanol (MeOH), for HPLC, gradient grade, ≥99,9 %	Merck KGaA, Darmstadt, Germany
Mowiol® 4-88	Merck KGaA, Darmstadt, Germany
N,N,N´,N´-tetramethyl-ethylenediamine (TEMED)	Merck KGaA, Darmstadt, Germany
Paraformaldehyde (PFA)	Merck KGaA, Darmstadt, Germany
Phenylmethanesulfonyl fluoride (PMSF)	Merck KGaA, Darmstadt, Germany
Sodium dodecyl sulfate (SDS)	Merck KGaA, Darmstadt, Germany
Sodium hydrogen carbonate (NaHCO$_3$)	Merck KGaA, Darmstadt, Germany
Sodium hydroxide (NaOH)	Merck KGaA, Darmstadt, Germany
Sodium orthovanadate (Na$_3$VO$_4$)	Merck KGaA, Darmstadt, Germany
Tris (hydroxymethyl)aminomethane	Merck KGaA, Darmstadt, Germany
Triton^{TM} X-100	Merck KGaA, Darmstadt, Germany
Tween® 20	Merck KGaA, Darmstadt, Germany

2.3. Media, buffers and solutions

Table 2.3 Ready-to-use media und supplements

Name	Supllier
Cytokine Mix E	PromoCell GmbH, Heidelberg, Germany
Fetal Bovine Serum (FBS), sterile filtered, Cell culture tested	Merck KGaA, Darmstadt, Germany
Freezing Medium Cryo-SFM	PromoCell GmbH, Heidelberg, Germany
Hematopoietic Progenitor Expansion Medium XF; kit containing Expansion Media DXF and HPC supplement P	PromoCell GmbH, Heidelberg, Germany
Pancoll separation medium; Pancoll human, Density: 1.077 g/mL	PAN-Biotech GmbH, Aidenbach, Germany
Penicillin-Streptomycin, solution stabilized, suitable for cell culture	Merck KGaA, Darmstadt, Germany

Table 2.4 Prepared cell culture media

Media	Contents	Concentration
Adhesion Media (AM)	RPMI 1640	
	$MnCl_2$	25 µM
Culture Media 1	RPMI 1640	90 % (v/v)
	FBS	10 % (v/v)
Culture Media 2	RPMI 1640	80 % (v/v)
	FBS	20 % (v/v)
Freezing Media	Cryo-SFM	
HPC Expansion Media	HPC Expansion Media DXF	90 % (v/v)
	HPC supplement P	10 % (v/v)
HSPC Culture Media	HPC Expansion Media	98 % (v/v)
	Cytokine Mix E	1 % (v/v)
	Penicillin	100 units
	Streptomycin	100 µg/mL
Thawing Media	HPC Expansion Media	98 % (v/v)
	Penicillin	100 units
	Streptomycin	100 µg/mL

Table 2.5 Ready-to-use buffers and solutions

Name	Supplier
Dulbecco's Phosphate Buffered Saline (DPBS), with $CaCl_2$ and $MgCl_2$	Merck KGaA, Darmstadt, Germany
Dulbecco's Phosphate Buffered Saline (DPBS), without $CaCl_2$ and $MgCl_2$	Merck KGaA, Darmstadt, Germany
Ethylenediaminetetraacetic acid (EDTA) 1 % in PBS, w/o Ca, Mg, sterile filtered	PAN-Biotech GmbH, Aidenbach, Germany
FACSClean™	Becton, Dickinson and Company
FACSFlow™	Becton, Dickinson and Company

Name	Supplier
Pierce^{TM} RIPA Buffer	Thermo Fisher Scientific Inc., Waltham, MA USA
Roswell Park Memorial Institute (RPMI) 1640 Media	Merck KGaA, Darmstadt, Germany
ROTI®Free Stripping Buffer 2.0	Carl Roth GmbH + Co. KG, Karlsruhe, Germany
ROTIPHORESE®Gel 30 (37.5:1)	Carl Roth GmbH + Co. KG, Karlsruhe, Germany
Trypan Blue solution, 0,4 %, sterile filtered	Merck KGaA, Darmstadt, Germany

Table 2.6 Prepared buffer and solutions

Buffer/Solution	Contents	Concentration
0.1 % Bovine Serum Albumin (BSA)	PBS (with $CaCl_2$ and $MgCl_2$) BSA → filtered (0,2 µm pore size)	 0.1 % (w/v)
0.1 % Triton X-100	ddH_2O Triton X-100	 0.1 % (v/v)
1 % Bovine Serum Albumin (BSA)	PBS (with $CaCl_2$ and $MgCl_2$) BSA → filtered (0,2 µm pore size)	 1 % (w/v)
10x Running Buffer	Tris Glycine SDS →in ddH_2O	250 mM 1,92 mM 1 % (w/v)
10x Tris-Buffered Saline (TBS)	Tris NaCl →in ddH_2O →pH 7,6	200 mM 1,5 M
4 % Paraformaldehyde (PFA)	Paraformaldehyde NaOH PBS ddH_2O → to pH 7,4 with 1 M NaOH	4 % (w/v) 2 mM 1 X
Blocking Solution	BSA → in 1x TBS → filtered (0,2 µm pore size)	5 % (w/v)
Erylysis Buffer Stock (10x)	ddH_2O NH_4Cl $NaHCO_3$ Di-Sodium-EDTA → to pH 7,4	 1,5 M 100 mM 1 mM w. 1 M NaOH
FACS Buffer	Rinsing Solution BSA	 0,5 % BSA (v/v)

Buffer/Solution	Contents	Concentration
Lysis Buffer	PMSF	1 mM
	Na_3VO_4	1 mM
	10x PIC in ddH_2O	1x
	→in RIPA Buffer	
Mowiol	Glycerol	24 % (w/v)
	Mowiol 4-88	9,6 % (w/v)
	TRIS-Cl (pH 8,4)	0,1 M
	DABCO 33-LV	2,5 % (w/v)
	ddH_2O	
Rinsing Solution	PBS	
	1 % EDTA/PBS	2 mM
SDS-Loading Dye	0,5 M Tris-HCl	190 mM
	Gylcerol	40 % (v/v)
	SDS	9 % (w/v)
	Bromphenole Blue	0,09 % (w/v)
	→in ddH_2O	
TBS-T	Tween® 20	0,05 % (v/v)
	→in 1x TBS	
Transfer Buffer	Running Buffer	1x
	Methanol	10 % (v/v)
	→in ddH_2O	

2.4. Biological molecules, proteins and antibodies

Table 2.7 Biological molecules and proteins

Name	Supplier
Bovine Serum Albumin (BSA), lyophilized powder, ≥96 %	Merck KGaA, Darmstadt, Germany
Fibronectin (FN) human plasma	Merck KGaA, Darmstadt, Germany
ROTI®Mark TRICOLOR proteinmarker	Carl Roth GmbH + Co. KG, Karlsruhe, Germany
SIGMA*FAST*™ Protease Inhibitor Cocktail Tablets (PIC), EDTA-Free	Merck KGaA, Darmstadt, Germany

Table 2.8 Antibodies used for Flow Cytometry

Antigen	Isotype	Conjugate	Clone	Dilution	Supplier ID (RRID)	Supplier
Human-CD33	Mouse IgG1κ	PE	WM53	1:20	303403 (AB_314347)	BioLegend, Inc.
Human-CD34	Mouse IgG2aκ	FITC	AC136	1:50	130-113-740	Miltenyi Biotec B.V. & Co. KG
Human-CD38	recombinant human IgG1	APC	REA671	1:50	130-124-044	Miltenyi Biotec B.V. & Co. KG
Human-CD45RA	recombinant human IgG1	PE	REA1047	1:50	130-117-852	Miltenyi Biotec B.V. & Co. KG

Table 2.9 Isotype control antibodies used for Flow Cytometry

Isotype	Conjugate	Clone	Dilution	Supplier ID (RRID)	Supplier
human IgG1	APC	REA293	1:50	130-113-434	Miltenyi Biotec B.V. & Co. KG
human IgG1	PE	REA293	1:50	130-113-438	Miltenyi Biotec B.V. & Co. KG
Mouse IgG1, κ	PE	MOPC-21	1:20	400111 (AB_2847829)	BioLegend, Inc.
mouse IgG2a	FITC	S43.10	1:50	130-113-833	Miltenyi Biotec B.V. & Co. KG

Table 2.10 Primary antibodies for immunofluorescent staining

Antigen	Host	Concentration	clone	Incubation time and temperature	Supplier ID (RRID)	Supplier
Human CD38	rabbit	300 µg/mL	Polyclonal	Over Night, 4 °C	PA5-82791 (AB_2789947)	Invitrogen by Thermo Fisher Scientific Inc
human CD45RA	mouse	0,5 µg/mL	HI100	Over Night, 4 °C	304102 (AB_314406)	BioLegend, Inc.
Human Paxillin	mouse	2,5 µg/mL	349/Paxillin	Over Night, 4 °C	610051 (AB_397464)	Becton, Dickinson and Company
Human Phospho-Pyk2 (Tyr402)	rabbit	800 ng/mL	polyclonal	Over Night, 4 °C	44-618G (AB_2533697)	Invitrogen by Thermo Fisher Scientific Inc
Human Vinculin	mouse	4 mg/mL	VLN01	1 h, RT	MA5-11690 (AB_10976821)	Invitrogen by Thermo Fisher Scientific Inc
human-CD33	mouse	5 µg/mL	WM53	Over Night, 4 °C	ab30371	Abcam plc

Table 2.11 Secondary antibodies and dyes for immunofluorescent staining

Molecule	Conjugate	Concentration/Dilution	Supplier ID (RRID)	Supplier
DAPI		1 µg/mL	62248	Thermo Fisher Scientific Inc
Phalloidin	Alexa Fluor™ 488	1:1000	ab176753	Abcam plc
Antigen	**Host**			
mouse IgG (H+L)	Alexa Fluor™ 647	goat 2 µg/mL	A21236 (AB_2535805)	Invitrogen by Thermo Fisher Scientific Inc
rabbit IgG (H+L)	Alexa Fluor™ 568	goat 2 µg/mL	A11036 (AB_10563566)	Invitrogen by Thermo Fisher Scientific Inc

Table 2.12 Antibodies used in protein-immunoblotting

Antigen	Host	Clone	Dilution	Supplier ID (RRID)	Supplier
Human phospho-Pyk2 (Tyr402)	rabbit	polyclonal	1:1000	44-618G (AB_2533697)	Invitrogen by Thermo Fisher Scientific Inc
Human PYK2	rabbit	polyclonal	1:1000	PA5-115810 (AB_2900444)	Invitrogen by Thermo Fisher Scientific Inc
Human GAPDH	rabbit	polyclonal	1:10.000	Ab9485	Abcam plc
		Conjugate			
Rabbit IgG	Goat	Horseradish peroxidase (HRP)	1:10.000	#7074	Cell Signalling Technology, Inc.

2.5. Kits

Table 2.13 Used kits

Name	Supplier
CD34 MicroBead Kit	Milteny Biotec, Miltenyi Biotec B.V. & Co. KG; Bergisch Gladbach, Germany
Pierce™ BCA Protein Assay Kit	Thermo Fisher Scientific Inc., Waltham, MA USA
WesternSure® PREMIUM Chemiluminescent Substrate	LI-COR Biotechnology – GmbH, Bad Homburg, Germany

2.6. Equipment

Table 2.14 Used equipment

Equipment	Supplier
Analytik Jena US UVP ChemStudio	Analytik Jena GmbH & Co KG, Jena, Germany
Corning® CoolCell® container	Corning Incorporated, Corning, NY, USA
Electrophor Unit Mini Vert. SE260 Com	VWR International GmbH, Radnor, PA USA
Eppendorf 5702 G Centrifuge	Eppendorf SE, Hamburg, Germany
Eppendorf Multipette M4 dispenser pipette	Eppendorf SE, Hamburg, Germany
Eppendorf®Research® plus piston pipette	Eppendorf SE, Hamburg, Germany
FACSVerse Flow Cytometer	Becton Dickinson Rowa Germany GmbH, Kelberg, Germany
Shaker with Orbital Motion	Thermo Fisher Scientific Inc., Waltham, MA USA
Heracell Vios 160i CO_2 incubator	Thermo Fisher Scientific Inc., Waltham, MA USA
Herasafe 2030i 1.5 Biological Safety Cabinets	Thermo Fisher Scientific Inc., Waltham, MA USA
Infinite® M200 Pro Plate Reader	Tecan Group AG, Männedorf, Switzerland
Laboklav 160 MV autoclave	SHP Steriltechnik AG, Detzel Schloß, Germany
Locator 4 Plus liquid nitrogen storage tank	Thermo Fisher Scientific Inc., Waltham, MA USA
Luna Reusable Counting Slide	Logos Biosystems by Aligned Genetics, Inc., Anyang, South Korea
Luna-II Automated Cell Counter	Logos Biosystems by Aligned Genetics, Inc., Anyang, South Korea
MACS® MultiStand	Milteny Biotec, Miltenyi Biotec B.V. & Co. KG; Bergisch Gladbach, Germany
MACSmixTM Tube Rotator	Milteny Biotec, Miltenyi Biotec B.V. & Co. KG; Bergisch Gladbach, Germany
Microfuge 20R centrifuge	Beckman Coulter GmbH, Brea, CA USA
MiniMACSTM Seperator	Milteny Biotec, Miltenyi Biotec B.V. & Co. KG; Bergisch Gladbach, Germany
Multi-Dancer Shaker L045-N	Kisker Biotech GmbH & Co. KG, Steinfurt, Germany
Neubauer counting chamber	Paul Marienfeld GmbH & Co.KG, Lauda Königshofen, Germany
PerfectBlue Power Supply Universal	VWR International GmbH, Radnor, PA USA
PIPETBOY acu 2	INTEGRA Biosciences GmbH, Biebertal, Germany
Primovert Inverse Light Microscrope	Carl Zeiss AG, Oberkochen, Germany
PURELAB® flex 2 ultrapure water unit	VWS Ltd, ELGA LabWater, High Wycombe, UK
Tank-Blotting. TE 22 Mini Tank Transfer Unit	Hoefer Inc., Holliston, MA USA
Thermoshaker	CellMedia GmbH & Co. KG, Zeitz, Germany
Tilt/roller mixer RS-TR 05	Phoenix Instrument GmbH, Garbsen, Germany
VWB2 18 waterbath	VWR International GmbH, Radnor, PA USA
Zeiss LSM 980 Airyscan system	Carl Zeiss AG, Oberkochen, Germany
RS-VA 10 Vortex Mixer	Phoenix Instrument GmbH, Garbsen, Germany

2.7. Consumables

Table 2.15 Consumable materials

Material	Supplier
8-well cell culture chamber, on glass slide, removable frame	SARSTEDT AG & Co. KG, Nümbrecht, Germany
Amersham™ Hybond™ blotting paper	Merck KGaA, Darmstadt, Germany
Amersham™ Protan® 0,2 µm NC Nitrocellulose Blotting Membrane	Merck KGaA, Darmstadt, Germany
Bio-One LeucoSEP™ Tubes	Greiner Bio-One GmbH, Frickenhausen, Germany
Cell scrapers, sterile, blade width 20 mm	Carl Roth GmbH + Co. KG, Karlsruhe, Germany
Cryovials; Cryo.S, 2 mL, PP, Round bottom	Greiner Bio-One GmbH, Frickenhausen, Germany
High Precision Microscope Cover Glasses, thickness 1,5H, 24 x 50 mm	Carl Roth GmbH + Co. KG, Karlsruhe, Germany
Injekt® Luer Lock Solo single use syringes, 2 mL, 5 mL, 10 mL, 20 mL	B. Braun SE, Melsungen, Germany
Microplate, 96 well, PS, F-Bottom, Clear	Greiner Bio-One GmbH, Frickenhausen, Germany
MS Columns plus tubes	Milteny Biotec, Miltenyi Biotec B.V. & Co. KG; Bergisch Gladbach, Germany
Multiwell plate for suspension culture, Sterile, 6 well, 12 well, 24 well	Greiner Bio-One GmbH, Frickenhausen, Germany
Pasteur pipettes without cotton plug, 2 ml, 230 mm	Carl Roth GmbH + Co. KG, Karlsruhe, Germany
Pipette tip, transparent, 20 µL, 100 µL, 1000 µL	SARSTEDT AG & Co. KG, Nümbrecht, Germany
Pipette, Sterile, 5 mL, 10 mL, 25 mL, 50 mL	Greiner Bio-One GmbH, Frickenhausen, Germany
Reaction vials; Fisherbrand™ Microcentrifuge Tubes with Locking Snap Cap; 0,5 mL, 1,5 mL, 2 mL	Thermo Fisher Scientific Inc., Waltham, MA USA
Suspension culture flask, Cellstar®, Sterile, 50 mL (T25), 250 mL (T75)	Greiner Bio-One GmbH, Frickenhausen, Germany
Syringe filter, Filtropur S, PES, pore size: 0.2 µm, for sterile filtration	SARSTEDT AG & Co. KG, Nümbrecht, Germany
Tube, Conical bottom, Cellstar®, Sterile, 15 mL, 50 mL	Greiner Bio-One GmbH, Frickenhausen, Germany
VWR® NITRILE LIGHT, Nitrile Gloves	VWR International GmbH, Radnor, PA USA
VWR®, Bottle-Top Vacuum Filtration System, PES, 150 mL, 250 mL, 500 mL, 1000 mL	VWR International GmbH, Radnor, PA USA

2.8. Software

Table 2.16 Used software

Program	Supplier
Microsoft Excel 2016	Microsoft Corporation, Redmond, WA USA
FiloQuant - Plugin for ImageJ	Guillaume Jacquemet, Turku Centre for Biotechnology, University of Turku and Åbo Akademi University, Turku, Finland
Poji – Macro for ImageJ	Robert Herzog, Institute for Medical Microbiology, Virology and Hygiene, University Medical Center Eppendorf, Hamburg, Germany
Origin 2022 9.9.0.220	OriginLab Corporation
FlowJo v.10.9.0	Becton Dickinson Rowa Germany GmbH, Kelberg, Germany
ZEN 3.3 (ZEN system) and ZEN 3.0 (blue edition)	**Carl Zeiss Microscopy GmbH**
ImageJ 1,54f and (Fiji Is Just) ImageJ 2.14	Wayne Rasband, National Institutes of Health, Maryland,USA

3. Methods

Double deionized water (ddH$_2$O) used within this work was prepared using an ultrapure water unit (PURELAB flex 2). All liquid volumina under 1000 µL were pipetted using respective piston pipettes. Volumina up to 100 mL were pipetted using serological pipettes and a pipettor.

3.1. Cell culture

Primary cells and cell lines utilized within this work were, if not explicitly stated otherwise, kept at 37 °C, 5 % CO$_2$ in a saturated aqueous vapor atmosphere using an incubator. All media and solutions were brought to 37 °C using a waterbath prior to usage, except where otherwise noted. To avoid contamination of the biological material, the cells were handled under sterile conditions at all times in ethanol cleaned sterile benches while wearing gloves. If consumables or solutions were not already supplied sterile, they were sterilized using an autoclave. Table 2.4 contains all culture media used within this work.

3.1.1. Cell counting

In order to determine viable cell number and density when necessary, cells were stained using trypan blue. For this, cells were resuspended thoroughly in medium and submitted to trypan blue in a ratio 1:2.

Subsequently the mix was submitted to a Luna reusable counting slide, which was inserted into the Luna-II automated cell counter. Primary cells were submitted to a Neubauer counting chamber. Both counting methods are based on the same principle; the Luna counting device is automated while counting has to be performed manually with the Neubauer chamber.

Bringing the stained single cell suspension between the coverslip and the counting chamber ensures a defined volume in a defined area of the chambers, in case of using a Neubauer counting chamber 1x10^{-4} mL per grand square. Submitting the chambers into a light microscope enables counting of the living cells, that, under trypan blue staining, will appear in bright contrast to the background and not dark blue, as it is the

case for dead cells since the cell membrane of these cells is ruptured. For manual counting Equation 3.1 was used to determine cell concentration. Using the Luna-II automated cell counter cell concentration was determined automatically.

$$\text{Cell number}/_{\text{mL}} = \frac{\sum \text{Cell Number in grand squares}}{\text{Number of grand squares}} \cdot \text{Dilution factor} \cdot \frac{10^4}{\text{mL}}$$ **Equation 3.1**

3.1.2. Cell lines

3.1.2.1. KG-1a

KG-1a is a cell line generated as a subclone of the cell line KG-1. These cells were immortalized from BM of a 59-year-old male patient with acute myeloid leukemia at relapse. While KG-1 was established as a prototypical myelocytic cell line, the subclone, KG-1a, that was used within the work presented here, is less mature and displays a similar surface marker profile as hematopoietic stem cells (Drexler et al., 2005). KG-1a were used as a positive control for the presence of CD45RA.

KG-1a were initially maintained in Culture Media 2 before transferring them to Culture Media 1 (see Table 2.4) after a week of culturing. Cells were split Monday, Wednesday and Friday of every week to a density of 5×10^5 cells/mL and 3×10^5 cells/mL respectively. For this, cells were resuspended thoroughly to acquire a single cell suspension and 10 µL were submitted to cell counting as described in 3.1.1. The volume containing the desired amount of cells, as referenced above, was then added to fresh medium to a final volume of 5 mL and kept in a T25 suspension cell culture flask.

3.1.2.2. THP-1

THP-1 is a monocytic cell line that was established from peripheral blood cells of a 1-year-old male acute myeloid leukemia patient at relapse. The cell line is usually used as a reference or model of monocytic cells or for further differentiation (Drexler et al., 2005). Within this work, THP-1 was used as a positive control for the presence of CD38 and CD33.

THP-1 were maintained in Culture Media 1 (see Table 2.4) at a density of $1x10^6$ cells/mL. Every Monday and Wednesday of each week the cells were subcultured to the aforementioned density. To do so the cells were resuspended thoroughly to acquire a single cell suspension and 10 µL were submitted to cell counting as described in 3.1.1. The volume containing the desired amount of cells, as referenced above, was then added to fresh medium to a final volume of 5 mL and kept in a T25 suspension cell culture flask. Every Friday a whole media change was performed. To do so, the volume containing the desired amount of cells was centrifuged using program 5 (see Table 3.1). Supernatant was discarded and the cells were resuspended in fresh media. The cell suspension was then transferred to a new cell culture flask.

3.1.3. Primary cells

The primary cells used in this work are CD34-positive cells isolated from UCB. UCB was received from the gynecological hospital of Hannover Medical School (*Frauenklinik, Medizinische Hochschule Hannover,* MHH), after parents signed informed consent on cord blood donation. The central ethics commission of Leibniz University Hannover (EV LUH 06/2019) approved this study. The UCB was collected into a 50 mL tube containing 1 mL heparin as soon as possible after birth, and left on a shaking device until further processing. Cells from UCB were isolated within 24-48 h after donation. All samples and isolated cells were carried with an internal identification number to reference birth date of donor and donation date. CD34-positive cells from UCB will be referred to as HSPC throughout this work.

3.1.3.1. Isolation of HSPC from UCB

The UCB was diluted with cold rinsing solution (see Table 2.6) in a ratio 1:2. 15 mL Pancoll separation medium (see Table 2.3) was added to a respective number of Bio-One LeucoSEP™ Tubes and centrifuged to the bottom of the tubes below the diaphragm with centrifugation program 1 (see Table 3.1). The tubes were filled with 35 mL diluted blood and centrifuged with centrifugation program 2 (see Table 3.1) to separate the erythrocytes/granulocytes, peripheral blood mononuclear cells (PBMC)

and plasma using density gradient centrifugation. After taking up and discarding some of the plasma above the "white ring"-phase containing the PBMCs (see Figure 3.1), the remaining volume above the diaphragm was transferred to a new tube by simply pouring. Each "white ring"-phase was transferred to a new vial, diluted with rinsing solution to a volume of 50 mL and centrifuged with program 3 (see Table 3.1). The supernatant was carefully removed and the pellets were resuspended and combined in 12 mL rinsing solution before again centrifuged with program 4 (see Table 3.1). Supernatant was discarded and pellet was resuspended in 1 x erylysis buffer (see Table 2.6; stock diluted 1:10 with sterile ddH$_2$O). The cells were incubated in erylysis buffer for 5 min at room temperature while gently moving the tube back and forth by hand. The cells were centrifuged with program 5 (see Table 3.1). If the pellet still looked red, indicating that erythrocytes were still present, another erylysis step was performed. The pellet was resuspended in 10 mL rinsing solution and centrifuged with program 5. The cells were then resuspended in 1 mL rinsing solution and counted as described in 3.1.1 in a dilution with rinsing solution 1:40. Cells were centrifuged one more time (program 5) and resuspended in 300 µL FACS Buffer/1x10^8 cells (see Table 2.6). 100 µL FcR Blocking reagent and 100 µL CD34 Micro Beads were added per 300 µL cell suspension. Cells were incubated with Micro Beads in a MACSmix^{TM} tube rotator for 30 min at 4 °C while rotating at 20 rpm. After incubation 10 mL cold FACS Buffer was added and the cells were centrifuged with program 5 and resuspended in 500 µl/1x10^8 cells FACS Buffer. During centrifugation the MACS$^®$ MultiStand and MiniMACS^{TM} Seperator were set up and the MS Columns plus tubes were equilibrated with 750 µL FACS Buffer. During all following steps, all liquid was left to completely pass through the column before moving on. The cell suspension was transferred onto the column. The vial was rinsed 3 times with 500 µl FACS buffer, that were also transferred to the column. The column was then removed from the magnet and the content was eluted in 1 mL FACS Buffer with the plunger. This process was repeated with a second column. The yield of CD34+ cells was determined, counting the cells as described in 3.1.1 in an 1:10 dilution with FACS Buffer.
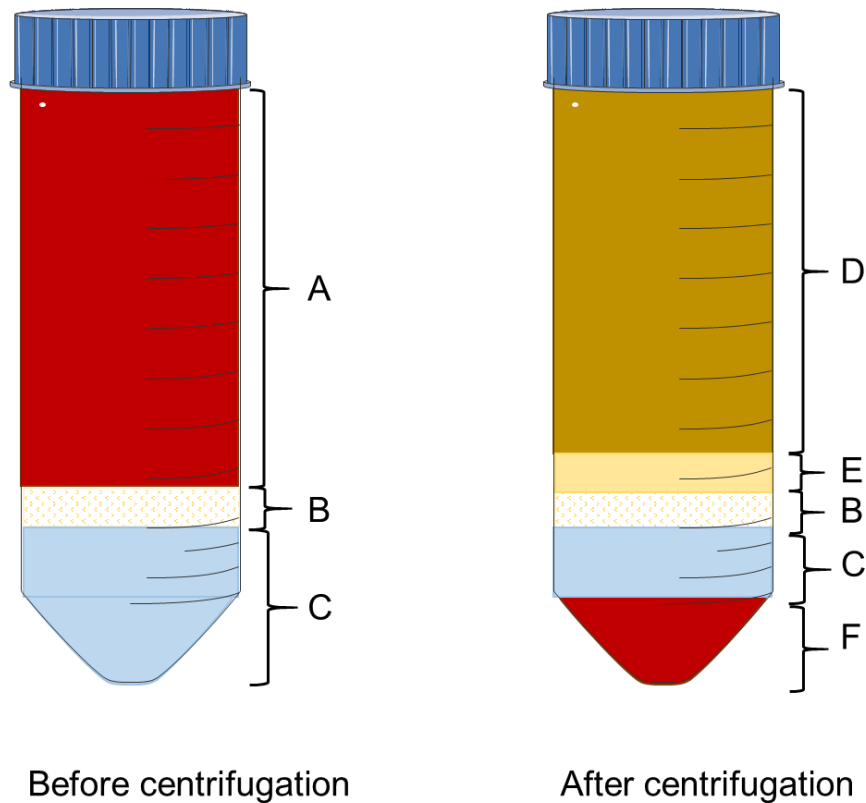
Figure 3.1 Schematic representation of separation of mononuclear cells from human UCB by density gradient centrifugation. *Left: Before centrifugation human umbilical cord blood (A) is separated by the LeucoSEP^TM diaphragm (B) from Pancoll separation media (C). Right: After centrifugation the following phases are present: plasma (D), enriched cell fraction containing lymphocytes and peripheral blood mononuclear cells (PBMCs)/"White ring"-phase (E), LeucoSEP^TM diaphragm (B), Pancoll separation media (C), erythrocyte and granulocyte pellet (F).*

Table 3.1 Centrifugation parameters of Eppendorf 5702 G Centrifuge

Program	Speed [xg]	Time	Acceleration	Deceleration
1	1000	30 sec	9	9
2	800	15 min	9	0
3	300	15 min	9	9
4	300	10 min	9	9
5	300	5 min	9	9

3.1.3.2. Culturing of HSPC

Freshly isolated HSPC were transferred to HSPC Culture Media (see Table 2.4) and kept at a density of 1×10^5 cells/mL in a suspension *well* plate or suspension cell culture flask fitting to cell suspension volume. Cells were frozen the day after isolation, if the percentage of CD34-positive cells was determined to be above 95 % (see 3.1.4).

3.1.3.3. Freezing of HSPC

After overnight expansion in HSPC Culture Media (see Table 2.4) cells were centrifuged using centrifugation program 5 (see Table 3.1). Supernatant was discarded and cells were resuspended in Freezing Media (see Table 2.4) at a density up to 1×10^6 cells/mL and stored in a cryo vial. The cryo vial was put into a Corning® CoolCell® container and gradually brought to -80 °C for 48 h before transferring the vial to liquid nitrogen for long term storage.

3.1.3.4. Thawing of HSPC

The frozen cells were taken from liquid nitrogen and as quickly as possible thawed in a 37 °C waterbath. The cell suspension was then added to 9 mL Thawing Media (see Table 2.4) and centrifuged using program 5 (see Table 3.1). The supernatant was discarded and cells were resuspended in HSPC Culture Media (see Table 2.4) to a density of 1×10^5 cells/mL and submitted to a suspension *well* plate or suspension cell culture flask according to cell suspension volume. Cells were further processed after overnight expansion.

3.1.4. Analysis of surface markers on HSPC

To confirm the successful isolation of CD34-positive cells as described in 3.1.3.1 and to further characterize the isolated cells in terms of other presented progenitor markers, namely CD38; CD33 and CD45RA; primary cells were analyzed using Flow Cytometry.

3.1.4.1. Flow Cytometry

Using this technique cells are labelled with fluorophore-conjugated antibodies. The sample is then brought to an optimal flow to pass through a laser beam one cell at a time. By doing so, not only are information about the presence of respective antigens through fluorescence signal gathered, but also on size and granularity of the cells by gathering the information on forward and sideward scattered light of the laser. This enables the distinction of different cell populations that might still be present in the primary sample. To account for unspecific antibody binding, a sample containing an

isotype antibody coupled to the same fluorochrome is prepared. Alongside the primary cells, cell lines that were positive for the analyzed surface markers were evaluated to be used as positive controls for the immunofluorescence staining (see 3.2.1). The cells of these positive cell lines (see 3.1.2.1, 3.1.2.2) were administered unstained and stained with single marker antibodies. These were used to compensate fluorescent signal overlap, if present. This made it possible to stain the primary cells for multiple markers at once, saving these valuable cells for downstream application.

Each sample was prepared containing $2x10^4$ cells. Cells were centrifuged with program 5 (see Table 3.1) and resuspended in 100 µL FACS Buffer (see Table 2.6). Respective antibodies were added according to Table 2.8 and Table 2.9. Cells were then incubated at 4 °C for 10 min. 1 mL cold FACS buffer was added to the cells, before again centrifuging with program 5. The cells were then resuspended in 300 µl FACS buffer before measuring.

Calculation of fluorescence overlap and determination of population size according to labelled markers was performed using the program FlowJo. Positive signals were defined as signals >99 % of all data point of isotype-controls, effectively limiting false negative signals to 1 %. Hierarchic assignment of population limits is depicted in the Appendix Figure A.1.

3.1.5. Adhesion of HSPC to fibronectin

In order to observe adhesion structures in HSPC, primary cells were brought to adhesion on FN alongside cell lines, that were positive for investigated surface markers indicating differentiation status (see. 3.1.2.1, 3.1.2.2).

8-*well* chamber slides were coated with FN. For this, FN stock (0,5 mg/mL in sterile ddH$_2$O) was brought to a concentration of 20 µg/mL with PBS (with CaCl$_2$ and MgCl$_2$). 500 µL FN solution were then added to the chamber slide *wells* as needed and incubated at 37 °C for 1 h. The *wells* were washed with PBS one time. The cells were counted (see 3.1.1) and $5x10^4$ cells/*well* were centrifuged with program 5 (see Table 3.1) and resuspended in 500 µL AM (see Table 2.4) per *well.* The cells were let to adhere for 1 h at 37 °C, 5 % CO$_2$ before washing one time with AM to remove non-attached cells. Cells were then submitted to IF-staining procedure (see 3.2.1).

3.2. Analysis of cell adhesion structures in HSPC

In order to investigate adhesions structures in HSPC, adherent cells were visualized using Super Resolution Confocal Microscopy. In case of certain proteins of interest, their production was validated using Immunoblotting.

3.2.1. Immunofluorescence staining (IF)

To evaluate which molecules are involved at adhesions sides in HSPC and how they are organized spatially, cells were submitted to immunofluorescence staining. Cells that adhered to FN were stained for proteins of interest, as described under 4.2 and listed in Table 4.3. HSPC were also stained for F-Actin using fluorescently labelled phalloidin and for the nucleus, to validate cell integrity, using DAPI. FN-adherent cells, obtained as described under 3.1.5, were fixed by applying 4 % PFA solution (see Table 2.6) for 15 min at room temperature (RT). Cells were subsequentially washed three times for 2 min with PBS (with $CaCl_2$ and $MgCl_{2)}$. If needed the cells were left in PBS at the last washing step and stored at 4 °C for up to 48 h. The cells were then permeabilized using 0.1 % Triton X-100 (see Table 2.6) for 5 min at RT. Again, the cells were washed three times for 2 min with PBS and then blocked with 1 % BSA (see Table 2.6). Three washing steps for 2 min with PBS followed before the primary antibody was added to 0,1 % BSA and incubated with the cells as indicated in Table 2.10. Once more, cells were washed with PBS 3x for 5 min before adding the secondary antibodies in 0,1 % BSA as described in Table 2.11. Lastly, stained cells were washed 3x for 5 min with PBS and one time with ddH_2O, to remove salt residues. The *well*-chamber frame was then removed from the sample slide and the cells were mounted with a high precision coverslip on Mowiol (see Table 2.6).

3.2.1.1. Confocal Laser Scanning Microscopy

Immunoflurescently labelled cells were visualized using Confocal Laser Scanning Microscopy (cLSM) with Airyscan detection. For this, a Zeiss LSM 980 Airyscan system was utilized. Acquisition settings are listed in Table 3.2.

Table 3.2 Acquisition settings for cLSM *Listed are the settings chosen for imaging on the Zeiss Axio Observer 7, LSM 980 Airyscan system. All listed equipment was provided within this system.*

Parameter	Setting			
Image Size (Pixels)	2220 x 2220			
Scaling (per Pixels)	0,035 µm x 0,035 µm			
Bit Depth	8 Bit / 16 Bit			
Objective	Plan-Apochromat 63x/1,40 Oil DIC M27			
Immersion oil	Immersol^{TM} 518 F (refractive index n_e=1,518 (23 °C))			
Channel-Name/Fluophore	DAPI	Alexa Fluor 488	Alexa Fluor 568	Alexa Fluor 647
Excitation Wavelength [nm]	353	493	577	653
Emission Wavelength [nm]	465	517	603	668
Pinhole	6,04 AU/ 324 µm	5,00 AU/ 247 µm	5,00 AU/ 283 µm	5,00 AU/ 324 µm
Laser Wavelength	405 nm	488 nm	561 nm	639 nm
Laser Power	Adjusted until maximum pixel saturation could be observed		5,00 %	
Detection Wavelength	300-720	420-480, 495-555	422-477, 573-627	573-620, 655-720
Detector Type	GaAsP-PMT			
Detector Gain	Adjusted until maximum pixel saturation could be observed			
Scan Zoom	1,7			
Pixel Time	1,82 µs			
Scan Direction	Unidirectional			
Effective NA	1,4			

3.2.2. Detection of cell adhesion associated molecules by immunohistochemical blot

Since the CAAM phosphorylated PYK2 (pPYK2), that was a mayor focus point of this work, is not universally produced in all cell types (see 1.2.2), its production was further verified using an immunohistological method. For this HSPC were brought to adhesion and subsequentially lysed. Protein concentration was determined using BCA-Assay before the protein of interest was detected via protein-immunoblotting.

3.2.2.1. Sample preparation and lysis of HSPC

Primary cells were submitted to BSA and FN coated *wells*. BSA was prepared in PBS (with $CaCl_2$ and $MgCl_2$) to a concentration of 1 % (w/v) and sterile filtered. FN was

brought to a concentration of 20 µg/ml using PBS (with $CaCl_2$ and $MgCl_2$). 3 mL of both solutions were submitted to a *well* of a 6-*well* plate respectively and left for 1 h at 37 °C and 5 % CO_2. The *wells* were then washed with PBS and left in RT until needed.

In order to apply sufficient cell numbers to result in enough total protein upon lysis, primary cells of multiple cord blood donors were frozen and stored after isolation (see 3.1.3.3) to be combined for further processing. After thawing and overnight expansion of the primary cells (see 3.1.3.4), cell number and viability was accessed as described under 3.1.1. If no heavy cell loss occurred during the freeze-thawing process, the cells were combined and submitted to FACS-analysis to access for CD34-positive cells (see 3.1.4.1). If the population of CD34^{+}-cells exceeded 95 %, a volume containing $4x10^6$ cells was centrifuged using program 5 (see Table 3.1). The cells were resuspended in 6 ml AM (see Table 2.4) and submitted to the coated *wells* to result in $2x10^6$ cells per *well*. The cells were then left to adhere for 1 h at 37 °C and 5 % CO_2. The non-adherent cells were removed and collected by transferring the supernatant to a new vial and washing the *well* once with AM, also to be added to the respective vial. Non-Adherent cells were then centrifuged using program 5 (see Table 3.1) and the supernatant was discarded. 100 µL of lysis buffer (see Table 2.6) were added to pellets of non-adherent cells and adherent cells in the *wells.* To ensure lysis of all cells, material was accumulated in buffer with the help of a cell scraper and the lysis of cells was supported by aspirating the lysate with a 1000 µL piston pipette. The lysates were then transferred to a 1,5 ml reaction vial on ice. The cell-lysates were left in 4 °C for 30 min while rotating at 20 rpm to ensure even homogenization. Subsequentially the lysates were centrifuged for 5 min at maximum speed using a Microfuge 20R. The supernatant was transferred to a new 1,5 ml reaction vial and stored at -20 °C.

3.2.2.2. *Determination of protein concentration using BCA-Assay*

To ensure that equal amount of protein was submitted to the detection process, protein concentration was determined using the BCA Assay. This assay utilizes the Biuret-reaction, in which bivalent copper-ions form a complex compound with the peptide bond of proteins, reducing them to monovalent ions in the process. The latter form violet compounds with bicinchoninic acid (BCA), which can be photometrically quantified by measuring extinction at 562 nm (Smith et al., 1985).

The assay was performed using the microplate procedure as described in the user manual of the Pierce^{TM} BCA Protein Assay Kit (see Table 2.13). Cell lysates were diluted 1:10 in previous used lysis buffer (see Table 2.6). Additionally a standard row was prepared, using the included protein-standard and diluted using lysis buffer as instructed in the user guide. The standard row enabled a quantification of protein concentrations ranging from 25-2000 µg/mL. 25 µL of diluted sample and each standard was admitted to a 96-*well* plate in triplicates. The BCA working solution was prepared by adding reagents A and B together in a 50:1 ratio. 200 µL of the working solution was added to each sample on the plate. The reaction mixture was left at 37 °C for 30 min. The photometric measurement was then performed by accessing the extinction at 562 nm.

Protein concentration was calculated by extrapolation of the standard row. For this defined protein concentration of the standard samples were plotted against the measured extinction of the respective sample. A linear regression line was plotted and its line equation was drafted from the program. The equation was adjusted to calculate protein concentration according to measured extinction of the samples as shown in Equation 3.2. Herein $c_{Protein}$ is the protein concentration, E is the measured extinction. n_{reg} is the value where the regression line crosses the y-axis. m_{reg} represents the slope of the regression line.

$$c_{Protein} = \frac{E - n_{reg}}{m_{reg}} \cdot \text{Dilution Factor}$$

Equation 3.2

3.2.2.3. *Protein separation using SDS-gelelectrophoresis*

To enable the detection of pPYK2, the total protein lysate was submitted to SDS-gelelectrophoresis to separate the proteins according to molecular weight. By loading sodiumdodecylsulfate (SDS) onto the protein lysate while submitting heat, secondary- and tertiary protein structures are cleaved, so that intrinsic charges of the protein are effectively masked by SDS. This results in a constant mass-to-charge-ratio and ensures that the speed at which proteins pass through the gel upon applying voltage is solely determined by mass (Kurreck et al., 2022).

A 10 % Bis-Tris-polyacrylamide-gel was used for protein segregation (see Table 3.3). According to the protein concentration accessed in 3.2.2.2, 5 µg of protein were

supplied with SDS-loading dye (5x, see Table 2.6) to result in a 1x concentration. Samples were incubated at 95 °C for 5 min. The electrophoresis chamber was flooded with 1x running buffer (see Table 2.6) before submitting the prepared samples alongside the ROTI®Mark TRICOLOR proteinmarker to determine molecular mass of proteins. A current of 20 mA per gel in electrophoresis chamber was applied and electrophoresis was allowed to run for roughly 90 min until the dye front reached the lower end of the gel.

Table 3.3 Contents of 10 % Bis-Tris-Polyacrylamide Gel

Reagent	Volume Collection Gel (3 mL)	Volume Separating Gel (20 mL)
ddH$_2$O	2,1 mL	7,9 mL
Rotiphorese® Gel30 (37,5:1)	0,5 mL	6,7 mL
Tris (1,0 M, pH 6,8)	0,38 mL	
Tris (1,5 M, pH 8,8)		5 mL
10 % SDS	30 µL	200 µL
APS, 10 %	30 µL	200 µL
TEMED	3 µL	20 µL
Bromphenole Blue	30 µL	

3.2.2.4. Immunohistochemical blot detection of protein

Phosphorylated PYK2 in the segregated protein lysate was detected via immunoblotting. Using this method, proteins are being transferred onto a carrier membrane by applying an electrical field. Afterwards detection of proteins of interest is possible via immunohistochemical staining.

Following the gelelectrophoresis, proteins were transferred onto a nitrocellulose membrane using Tank-Blotting. For this, the Tank Transfer Unit was assembled on ice. Fitted filterpapers and membrane were prepared together with the SDS-gel as shown in Figure 3.2 in transfer buffer (see Table 2.6). The cassette containing the "blotting-sandwich" was quickly transferred into the blotting-tank that was already filled with transfer buffer, while applying pressure to ensure that no air-bubbles formed. If needed, the Tank-Blot was further filled with transfer buffer until the cassette was fully submerged. A constant voltage of 100 V was applied with a power supply and blotting was performed for 1 h.
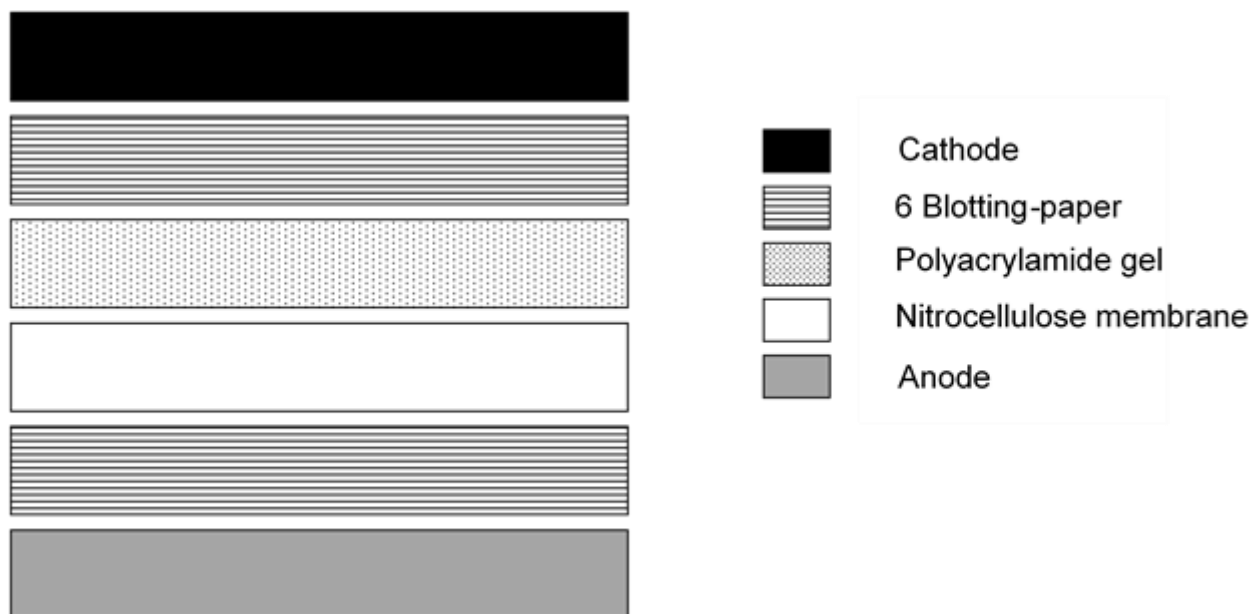
Figure 3.2 Schematic representation of immunoblot assembly *In the cassette submerged in transfer buffer the blotting-"sandwich" is assembled as follows: 6 blotting paper, polyacrylamide gel containing separated protein sample, nitrocellulose membrane, 6 blotting paper. Air bubbles are removed from between the sheets. Cassette is then transferred to the blotting device so that polyacrylamide gel is oriented towards the cathode, while the nitrocellulose membrane is oriented towards anode.*

After blotting the membrane was immediately transferred to blocking solution (see Table 2.6) and incubated at RT for 1 h. Afterwards antibodies were directly added to the blocking solution as described in (see Table 2.12) and incubated at 4 °C over night while shaking at 50 rpm orbital rotation. The membrane was then washed 3 x 5 min with TBS-T (see Table 2.6) while shaking. Secondary HRP-linked antibody (see Table 2.12) was then added to the membrane as indicated in blocking buffer and incubated for 30 min at RT, while shaking in the dark. Afterwards the membrane was washed 3x 10 min with TBS-T, again left to shake in the dark. The membrane was then transferred into the chemiluminescence detection imager and freshly prepared chemiluminescent substrate was admitted. Chemiluminescent signal was then detected using the "Chemiluminescent Blot"-mode of the imaging device, with exposure times gradually increasing from 500 ms up to 1 h. If necessary, another protein detection was performed on the same membrane. For this, the membrane was submitted to stripping buffer (see Table 2.5) and left for 1 h at RT while shaking. Afterwards the procedure was repeated from primary antibody incubation onward.

3.3. Data processing of microscopy images

To differentiate morphologies of adherent HSPC, images were submitted to an image processing system. For this, the open source image processing program *ImageJ* was utilized (Schneider et al., 2012). After data was obtained with *ImageJ* it was processed using Microsoft Excel 2016.

Single cell images of F-Actin staining were submitted to phenotyping. Using the *ImageJ* batch processing option the images were converted to 8-bit format and scaled according to the acquisition settings (usually 1 pixel ≙ 0,035 µm; s. Table 3.2).

3.3.1. Accessing shape descriptor values

Using the *Threshold Color* interface, brightness of each image was set to a value of 10. This resulted in an even signal brightness around the cell border. In case the cell was not being lined correctly, gaps were closed using the pen tool. The same tool was used if two cells were too close to be separated properly by this process. The even cell border lining that resulted from this adjustment enabled the automated cell area selection using the *Wand* tool. Once the cell area was determined in this way, it was admitted as a *region of interest* (ROI) to the *ROI manager*. Here the region was measured. Each measurement gave data on area size and aspect ratio (AR), amongst other data sets that were not further utilized. AR is a value that is determined by an elliptical fit around the ROI. The ratio between the minor and major axis of this ellipse equates the AR.

3.3.2. Accessing filopodia descriptor values

For determining the filopodia descriptor values the free ImageJ Plugin *FiloQuant* was used (Jacquemet et al., 2017). Summarized shortly, this plugin enables automated detection and quantification of filopodia and other protrusions from the cell edge. For this, the code detects the cell edge that, in this context, can be understood as a baseline from which protrusions extend. Afterwards filopodia are detected in the entire cell area, in a process based on the ImageJ *skeletonize* function. This results in all line- or finger-like protrusions exceeding the cell edge being detected as filopodia as

depicted in Figure 3.3. The detection parameters of the *FiloQuant* plugin are listed in Table 3.4.

The cell edge | The image used to detect filopodia | The result image. Detected filopodia are in purple.
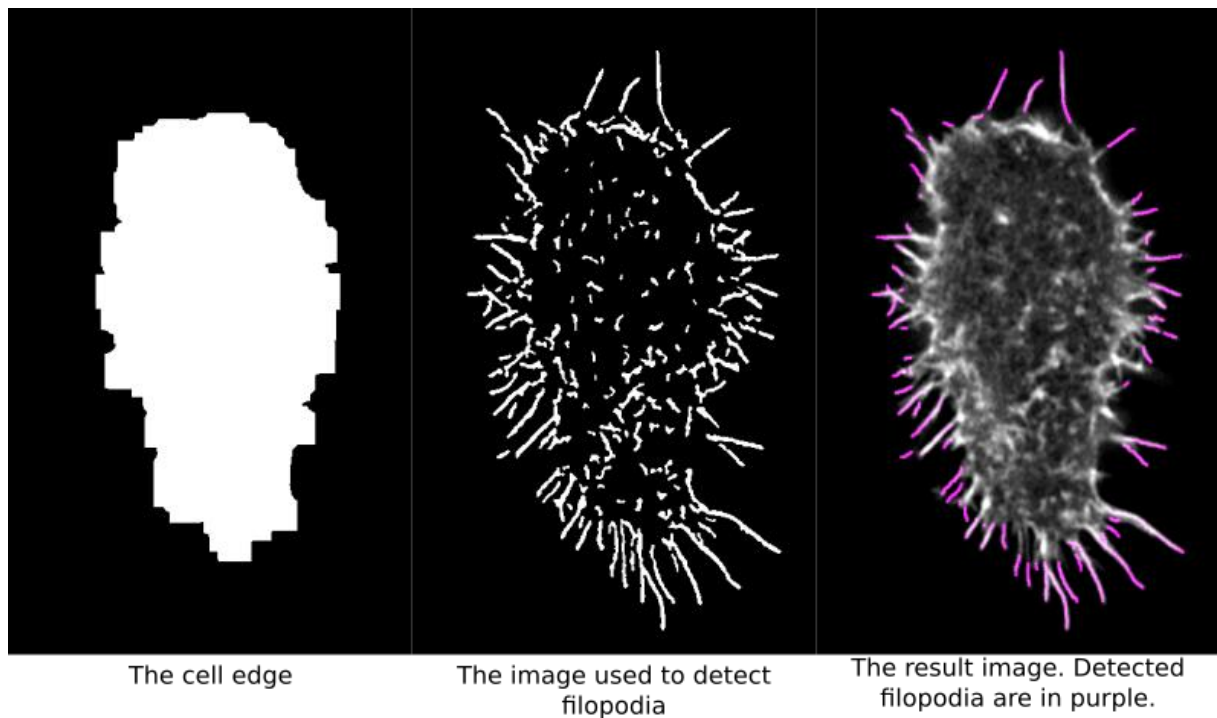
Figure 3.3 ***Depiction of filopodia detection by FiloQuant on an exemplary HSPC****. The cell edge is detected according to edge detection parameters of the FiloQuant plugin (left), Filopodia detection according to the plugin parameters is performed using the ImageJ skeletonize function (middle), Filopodia/other protrusions analyzed by the plugin are all detetcted filopopodia exceeding the cell edge (right). Image based on Jacquemet et al., 2017, depicted is a cell imaged within the here presented work.*

Table 3.4 FiloQuant parameters for filopodia detection in HSPC phenotyping process *Numbers indicate the set values, ✓ indicated a checked box, x indicated that a box was not checked. For parameter explanation see Jacquemet et al., 2017.*

Process Step	Parameter	Setting
	Threshold for cell edge	6
	Number of iterations for Open	15
Edge Detection	Number of Cycle for Erode Dilate	0
	Fill holes on edges?	✓
	Fill holes?	✓
	Threshold for filopodia	25
	Filopodia minimum size	10
	Use convolve to improve filopodia detection?	✓
Filopodia Detection	Use local contrast enhancement to improve filopodia detection?	x
	Maximal distance from edges	0

3.3.3. Accessing podosome descriptor values

Lastly, cells were checked for the podosome descriptor values. The *ImageJ* macro code published under the name *Poji* was used (Herzog et al., 2020). *Poji* defines and analyzes punctate structures above a set threshold in fluorescent images. In context of the here presented phenotyping process *Poji* was used to access podosome number on cells. For this, cell area was marked in each image and macro parameters were set as listed in Table 3.5. Figure 3.4 shows an example of podosomes detected in a podosome phenotype cell, using this process.
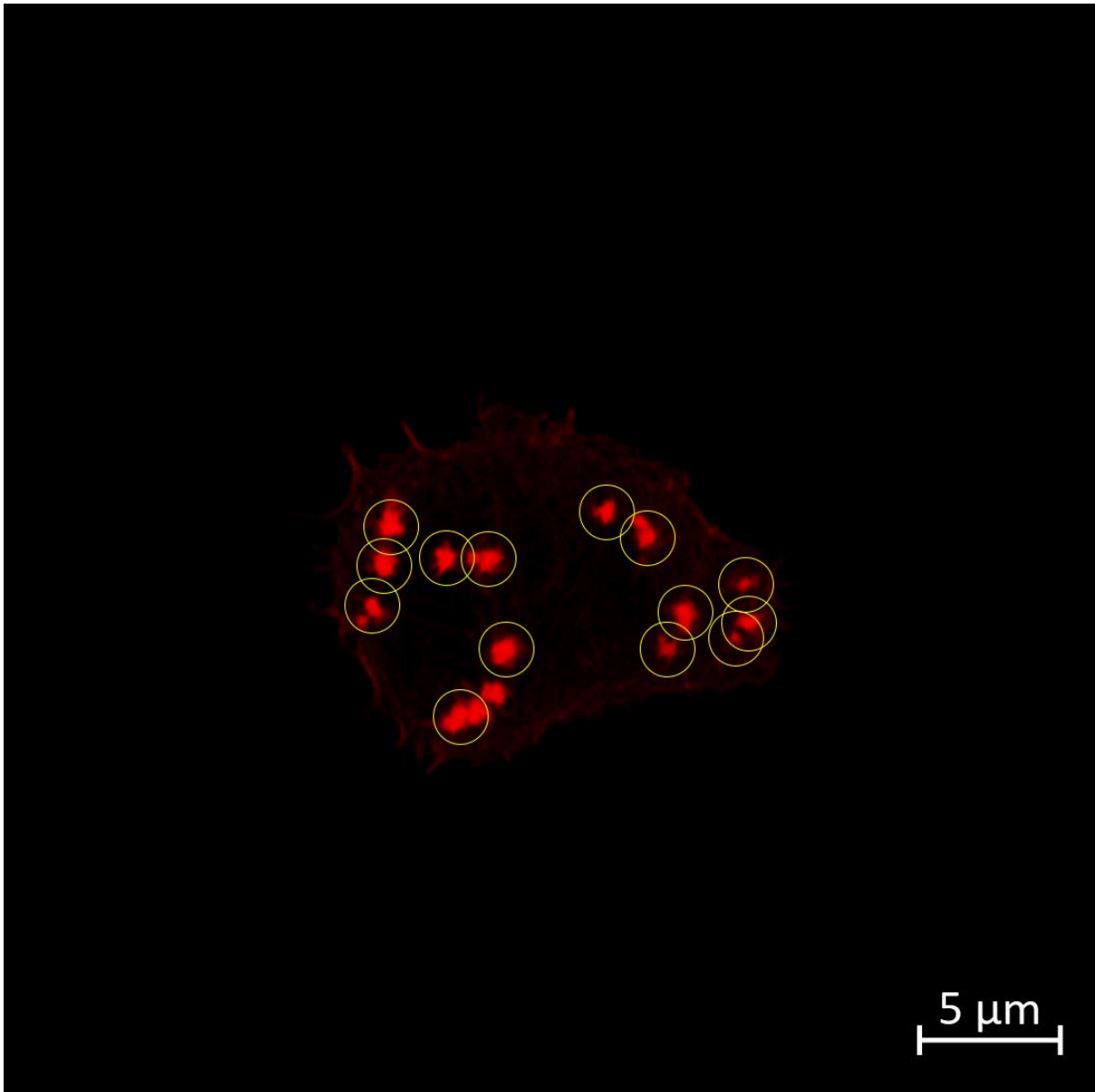
Figure 3.4 Exemplatory podosome detection in HSPC using Poji macro. *Image of F-actin (red) immunofluorescence staining in exemplary HSPC. Podosomes detected by the macro are marked in yellow circles*

Table 3.5 Poji parameter for podosome detection on HSPC phenotyping process Numbers indicated the set values, ✓ indicated a checked box, x indicated that a box was not checked. For parameter explanation see Herzog et al., 2020.

Process Step	Parameter	Setting
General analysis options	Normalize fluorescence intensity in cell area?	x
	Additionally select podosome clusters?	x
	Identical cell and cluster areas for all images?	x
	Identical detection conditions for all images?	x
	Calculate average profiles?	x
	Also calculate individual profiles? (very slow!)	x
	Save data from analysis	Essential
Podosome Detection	Prominence	30
	Smoothing Steps	3
	Circle size (intensity)	55
	Square Size (Profile)	55

With the total podosome number, the podosome density was calculated by using Equation 3.3.

$$\text{Podosome Density}=\frac{\text{Total podosome number p. cell}}{\text{Cell Area}}$$

Equation 3.3

3.3.4. Acquiring podosome profiles

To evaluate the spatial distribution on adhesion molecules in podosomes assembled by HSPC podosome profiles were acquired using *Poji*. In this case the same plugin settings were used as described in Table 3.5, but the checkboxes for "Calculate average profiles?" and/or "Also calculate individual profiles? (very slow!)" were checked. By doing so, the plugin acquires fluorescence intensities profiles along the diameter of the circle marking the podosomes (see Figure 3.4). The profile line is then

rotated 360 times with a 1 degree offset and the plugin delivers an average radial intensity profile per cell/podosome depending on what is desired. These profiles are normalized to maximum bit-range (0-255 for 8 bit) for F-actin.

To quantify differences between podosome profiles, the profiles for each analyzed molecule were submitted to Guassian Fitting using Origin 2022. Only fits with $R^2 >95$ % were accepted for analysis. The full width at half maximum (FWHM) of the profile was acquired with this procedure.

3.3.5. Determining corrected total cell fluorescence

The progenitor markers labelled in IF (namely CD38, CD33, CD45RA; see 3.2.1) are produced according to the state of the cell within the hematopoiesis process (see 1.1.1). To determine at which level the markers are present in each imaged cell, the corrected total cell fluorescence (CTCF) of the respective staini

ngs was acquired. Each cell was outlined with the *ImageJ* Freehand ROI tool. Additionally three ROIs of background noise were assigned. The ROIs were measured acquiring data on Area, Integrated density and Mean grey value. Equation 3.4 and Equation 3.5 show how *ImageJ* obtains these values according to the User manual (Ferreira and Rasband).

$$\text{Mean grey value} = \frac{\sum \text{gray values of all pixels}}{\text{number of pixels}} \qquad \textit{Equation 3.4}$$

$$\text{Integrated density} = \text{Area} \times \text{Mean grey value} \qquad \textit{Equation 3.5}$$

The mean grey value of all background ROIs was calculated. This value was submitted to Equation 3.6 to calculate CTCF according to the Keith R. Porter Imaging Facility, University of Maryland.

$CTCF$ = Integrated density - (Area of selected cell × Mean Fluorescence of Background readings)

Equation 3.6

3.4. Statistical analysis

FWHM acquired from podosome profiles (see 3.3.4) where submitted to statistical analysis using Origin 2022. The data underwent an *One-Way* ANOVA analysis with Tukey post-hoc test.

Statistical testing of association between differentiation marker classes and morphology descriptors was kindly performed by Dr. rer. hort. Frank Schaarschmidt, PD, of the Institute of Cell biology & Biophysics, Department of Biostatistics, Leibniz University Hannover. This entailed the analysis of data sets by Cochran-Mantel-Haenszel-Test (C-M-H-Test) (see Digital Appendix). The method can be used to find associations within stratified or matched data between binary variables. These statistics are often used in observational studies, as is the case for this work. C-M-H-Test cannot give information about the specific groups between which significant associations are present.

4. Results

To assess the adhesion structures of HSPC, primary CD34$^+$ cells from UCB are brought to adhesion on FN for 1 h and IF-labelled for F-actin and cell adhesion associated molecules (CAAM). A phenotyping process is established based on F-actin labelling to account for diverse morphologies of adherent HSPC, which results in an overview of the phenotype distribution within primary adherent HSPC. IF-labelling of CAAM gives further information on the kind of adhesion structures established by HSPC and their respective maturity state. As a consequence, podosome-like structures (PLS) emerge as structures of interest, which are further analyzed in the aforementioned donors. This is accomplished by IF-labelling of proteins of interest and generation of radial intensity profiles of the structures to assess spatial distribution of the involved molecules. Lastly, by IF-labelling the cells of the three independent UCB donors for markers of differentiation, the differentiation status is brought into relation to the observed cell morphology, to assess whether the establishment of certain structures correlates with differentiation of HSPC. All results are gathered from a minimum of three independent UCB donors, some of which were used for multiple analyses, enabling the cross-reference of the respective data (internal label #117, #143 and #153).

4.1. Assessing the adhesion behavior of HSPC

The adhesion behavior of HSPC is observed to be quite dynamic. Time series show, that within a time span of 10 min, a HSPC can migrate over a distance twice its own size. In a time span of 60 min the cells move over 100 µm (see Figure 4.1, white arrow). Additionally, not all cells display this kind of migration, as some cells stay in the same place over the same time span (see Figure 4.1, black arrow). The time series show a dynamic adhesion behavior that can vary between cells.
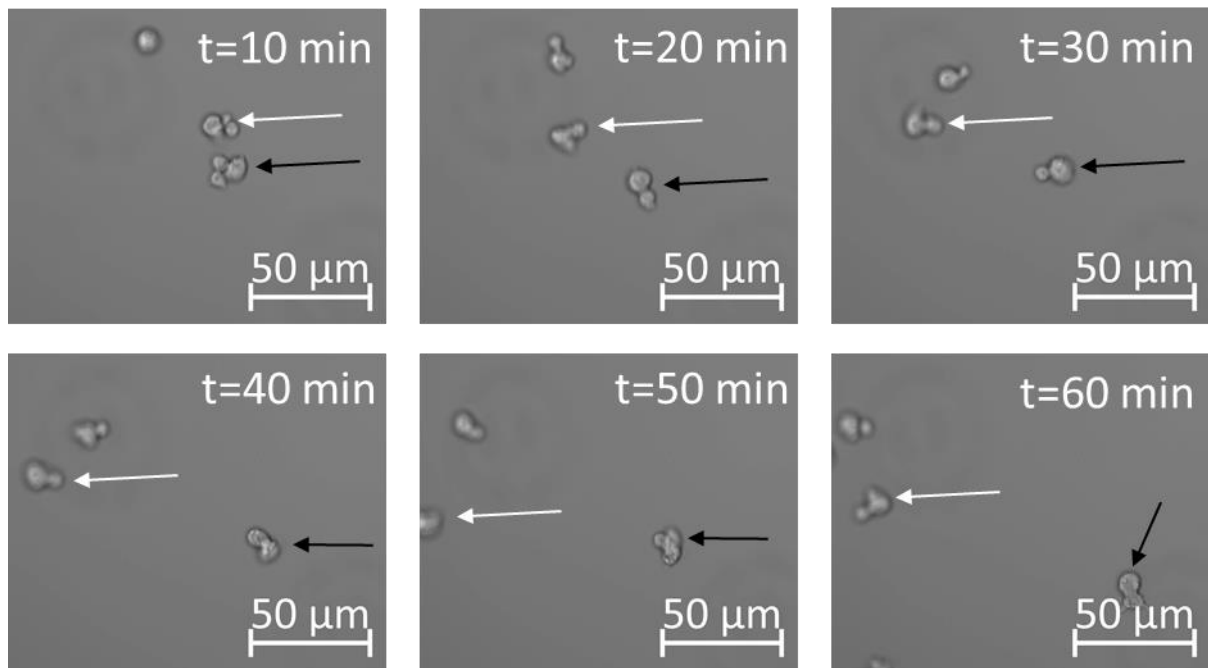
Figure 4.1 Time series of HSPC reveal dynamic adhesion behavior of HSPC. *A cell spanning more than 100 µm of distance in the assessed time span is labelled by white arrow. A cell staying in the same area in the same time is labelled by black arrow. Depicted are phase contrast images of HSPC on a FN-coated surface. An image of living cells was acquired at every minute for 1 h. Depicted are the images after 10, 20, 30, 40, 50, 60 min respectively. Representative images for 1 h time series of N=3 independent cord blood donors. Full video of time series can be found in Digital Appendix.*

4.1.1. Phenotypes of adherent HSPC

In agreement with the dynamic adhesion behavior observed in live cell imaging, adherent HSPC display a variety of different shapes or structures, when observed via cLSM (see Figure 4.2). For readers convenience and clarity, both cell shape and established F-actin structures are referred to as cell morphology. Labelling of F-actin reveals cells to either have round or polarized morphology. Some cells of large cell area also show long F-actin fibers along the cell periphery, resembling F-actin archs. In some adherent HSPC, the actin cytoskeleton displays filopodia beyond the cell edge or strongly pronounced F-actin puncta that could be PLS. The observed morphologies are, accordingly, defined by cell shape (round, polarized or arch) and the presence of filopodia and/or PLS (labelled podosome morphology).

The imaged cells are submitted to an image processing system to assign phenotypes to each observed cell, by assigning descriptors according to the displayed morphology. Methodological specifics of this process can be found in 3.3. By doing so, cells could be grouped together to assess whether adhesion structures in these phenotypes differ

in organizational states. A schematic overview of the phenotyping process is displayed in Figure 4.3.
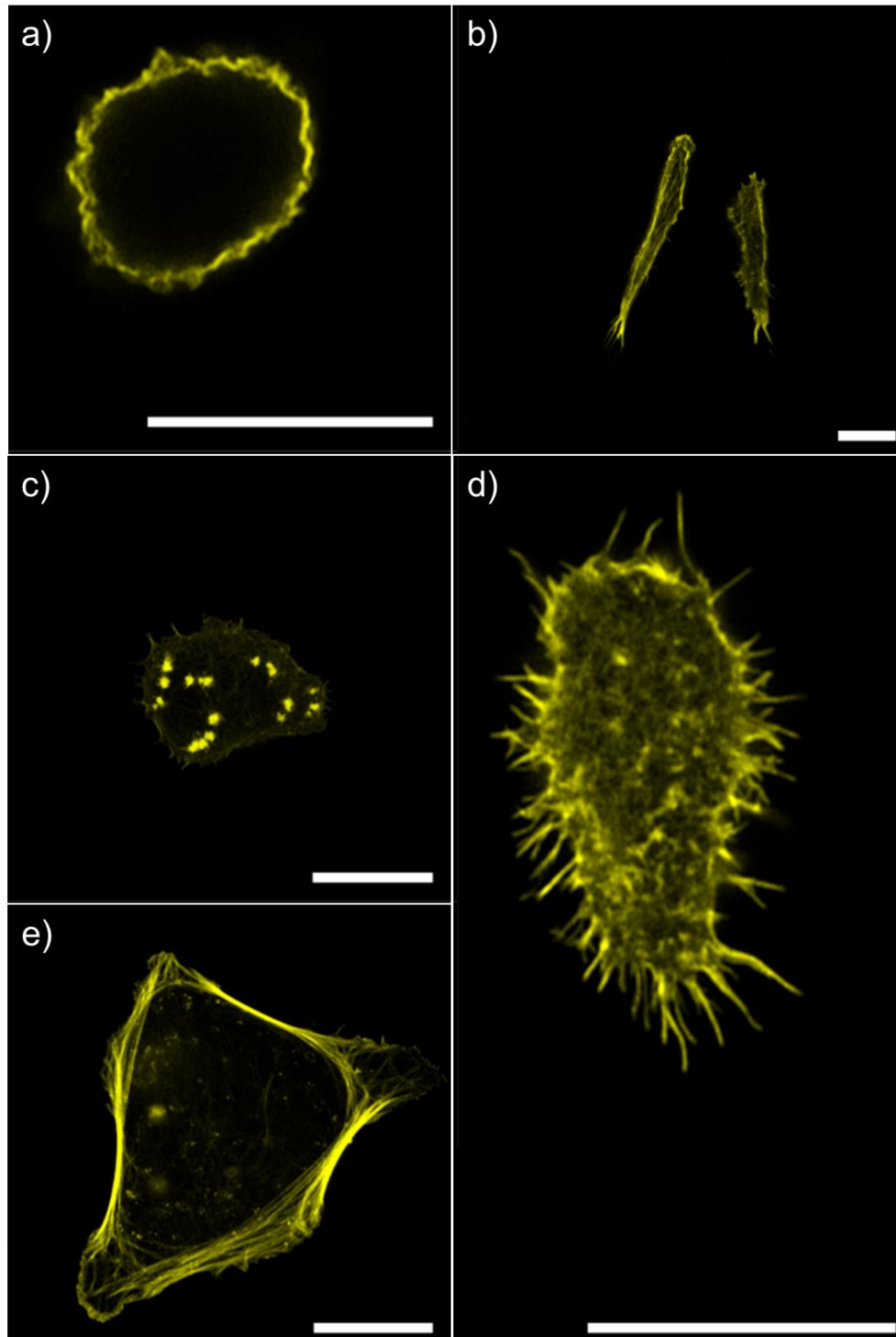
Figure 4.2 Different morphologies of adherent HSPC *Observation of FN-adherent HSPC reveals a variety of morphologies. Depicted are F-actin labelled cells strongly representing the morphologies observed in n=363 images acquired of cells from N=11 cord blood donors:* ***a)*** *round morphology;* ***b)*** *polarized morphology;* ***c)*** *podosome morphology;* ***d)*** *filopodia morphology;* ***e)*** *arch morphology. Scale bar = 10 µm.*

Figure 4.3 Schematic outline of the phenotyping process for adherent HSPC *FN-adherent HSPC display different shapes and/or structures defined as morphologies. Each cell is assigned descriptors representing its morphology in shape and established F-actin structures. According to the combination of the assigned descriptors, a phenotype for each cell is defined.*

4.1.1.1. Assigning the shape descriptor

In the first step of the phenotyping process, cells are assigned one of three shape descriptors: round, polarized or arch. These descriptors are defined to be mutually exclusive to one another.

54

For shape descriptor assignment, first cells with the arch morphology are determined. Since this morphology correlates to a phenotype with a striking difference in size to the rest of observed cells, the area size is the determining factor of this morphology. The area size limit for assigning the arch morphology is determined by using values of cells clearly displaying the arch morphology and contrasting them to all other cells, finding the median area size between the two groups. Thus, the cutoff limit for assigning the arch descriptor is defined as a cell area larger than 346 µm^2, as listed in Table 4.1.

Every cell that the arch descriptor is not assigned to is appointed the polarized or round descriptor according to its AR. An AR larger than 2 is considered to be indicative of a polarized morphology, since this correlates to the major axis of the fitted ellipse being twice as long as the minor axis. Conversely the AR of a perfect circle would be 1, thus round cells are defined as having an AR between 1 and 2. Deciding values of AR for round and polarized shape descriptors are listed in Table 4.1.

4.1.1.2.   Assigning the filopodia descriptor

In order to assign the filopodia descriptor to cells the values of filopodia number and mean filopodia length are assessed from the results of the *FiloQuant* detection (see 3.3.2). Similar to the way that limits are set for the assignment of the arch descriptor (s. 4.1.1.1) cells that very strongly display the filopodia morphology are selected and compared to the rest of the cells. Mean filopodia number and mean filopodia length are looked at in these two groups and median between the respective values are used as the cut off value. Cells with few long protrusions or many very short protrusions are not considered to display the filopodia phenotype. In order to exclude these cells, both, total filopodia number and mean filopodia length, need to exceed the cutoff value in order for the filopodia descriptor to be assigned. This translates to the filopodia descriptor being accredited if a cell displays more than 17 filopodia with a mean filopodia length over 0.401 µm, as listed in Table 4.1

4.1.1.3. Assigning the podosome descriptor

For assignment of the podosome descriptor, the number of PLS in each cell is utilized together with PLS density. Again, mean of both values, accessed via the *Poji* plugin (see 3.3.3), are compared between cells clearly displaying the podosome morphology and all other cells. Cut off values are defined as the median of the respective data, resulting in cutoff values of 15 PLS in a cell and $0.084 \frac{PLS}{\mu m^2}$. To account for small cells, that are limited in the number of PLS that could be formed, just one of the values of PLS number or PLS density needed to exceed the limiting value for the podosome descriptor to be appointed (see Table 4.1).

Table 4.1 Limitation values for descriptor assignment according to morphology in adherent HSPC

Morphology descriptor	Limitation value
Arch	Cell Area ≥ 346 µm^2
Polarized	AR ≥ 2
Round	AR < 2
Filopodia	Total filopodia number ≥ 17 **and** Mean filopodia length ≥ 0,401 µm
Podosome	Total podosome number ≥ 15 **and/or** podosome density ≥ 0,084 $\frac{PLS}{\mu m^2}$

4.1.1.4. Final assignment of phenotype

After individual assignment for shape, filopodia and podosome descriptors for each cell, a final phenotype was appointed. In certain cases, phenotypes were defined to represent a mixture of two morphologies. This served the purpose of displaying the dynamic attachment process of HSPC as detailed as possible. The following prequisites were defined for the phenotyping process:

- Arch, podosome and filopodia morphologies are considered equal
- Round morphology descriptors are dropped in the phenotype in favor of arch, podosome and filopodia morphology
- A polarized morphology is dropped in the phenotype if two or more of the following three morphologies are assigned: arch, podosome and filopodia

This resulted in the phenotype assignment matrix that is depicted in Table 4.2.

Table 4.2 Phenotype assignment matrix

Phenotype	Arch	Polarized	Round	Filopodia	Podosome
Round			✓		
Podosome			✓		✓
Filopodia			✓	✓	
Polarized		✓			
Polarized-Filopodia Mix		✓		✓	
Polarized-Podosome Mix		✓			✓
Podosome-Filopodia Mix			✓	✓	✓
Arch	✓				
Arch-Podosome Mix	✓				✓
Arch-Podosome-Filopodia Mix	✓			✓	✓

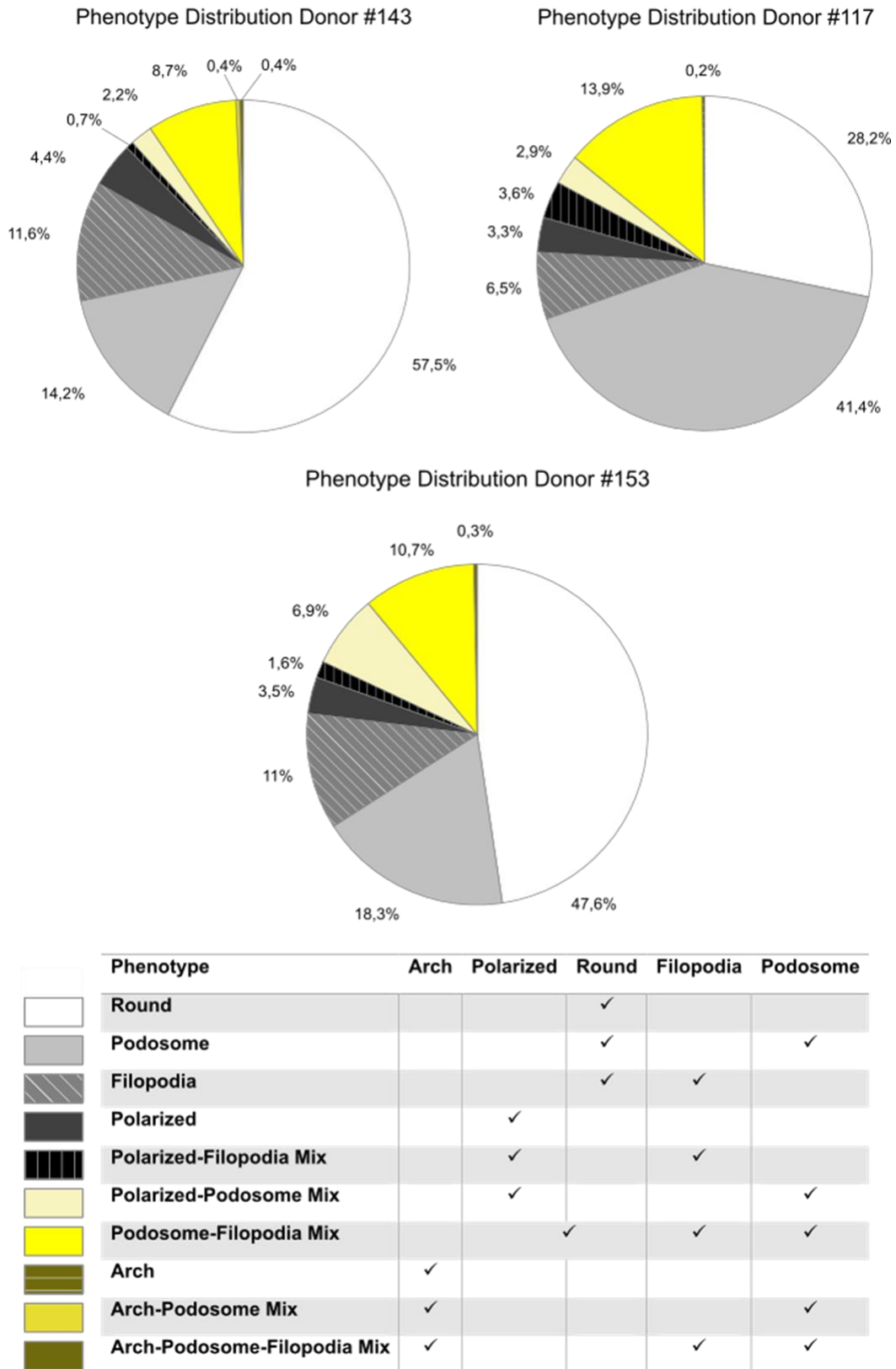### 4.1.1.5. Distribution of presented phenotypes in adherent HSPC

After assigning phenotypes to every imaged cell, it is assessed how often certain phenotypes are present in adherent HSPC. An overview of this is depicted in Figure 4.4.

Looking at shape descriptors the majority of cells display the round morphology (round, filopodia and podosome phenotypes), ranging from 76.1-83.3 % of total cells. *Vice versa*, only 7.3-12 % of cells show a polarized shape. The arch cells are a rare type in adherent HSPC, making up less than 1 % in every donor analyzed. Regarding the presence of adhesion structures, PLS are present in more cells than filopodia ranging from 14.9-45 % of total cells for the former compared to 9.4-17.9 % for the latter. In 8.7-13.9 % of cells both adhesion structures are present. It is to be noted that for the filopodia-podosome mix phenotype both, round and polarized morphologies are present, so this data was not considered when comparing these two morphologies earlier. For the groups that can clearly be differentiated into round and polarized morphology, PLS are more often present in round cells than in polarized cells (mean of 31.6 % of round cells versus 20 % of polarized cells), while the ratio of cells with filopodia morphology is higher in polarized cells (mean of 39 % of polarized cells versus 12.2 % of round cells).

When comparing overall phenotypes of adherent cells, round phenotype cells and cells with the podosome phenotype are the two largest groups within adherent HSPC in all donors. However, in donor #143 and #153 round phenotype cells make up the biggest population while in donor #117 the podosome phenotype is the largest, making up

41 % of total cells. These populations are followed up in size by cells with filopodia phenotype and filopodia-podosome phenotype. Again, in donor #117 the cells to which the filopodia-podosome phenotype was assigned (containing podosome morphology) are a larger population than cells just displaying the filopodia phenotype, while this is reversed for the other two donors. The populations of cells with polarized morphology make up the second smallest group fraction across all analyzed donors, only bigger than the arch morphology group. The distributions within these polarized morphology groups vary between all cord blood samples. Cells of donor #143 contain more cells of polarized phenotype than polarized-filopodia (2.2 %) and polarized-podosome (0.7 %) phenotypes. Donor #117 strongly displays cells with podosome morphology. Here the polarized-podosome phenotype makes up 3.6 % of cells, followed up with cells of polarized (3.3 %) and polarized-filopodia phenotypes (2.9 %). Lastly, HSPC of cord blood donor #153 display mostly polarized-filopodia phenotype cells (6.9 %), before showing polarized (3.5 %) and polarized-podosome phenotype groups (1.6 %). To summarize shortly, for all analyzed donors, most adherent HSPC show a round morphology. Additionally, the adhesive structure predominantly present is that of PLS.

Phenotype Distribution Donor #143

Phenotype Distribution Donor #117

Phenotype Distribution Donor #153

Phenotype	Arch	Polarized	Round	Filopodia	Podosome
Round			✓		
Podosome			✓		✓
Filopodia			✓	✓	
Polarized		✓			
Polarized-Filopodia Mix		✓		✓	
Polarized-Podosome Mix		✓			✓
Podosome-Filopodia Mix			✓	✓	✓
Arch	✓				
Arch-Podosome Mix	✓				✓
Arch-Podosome-Filopodia Mix	✓			✓	✓

Figure 4.4 Phenotype distribution in adherent HSPCs isolated from three independent cord blood donors. *Depicted are pie chart diagrams of the phenotype distribution per donor alongside the phenotyping matrix. CD34+ cells were isolated from three independent cord blood donors labelled by internal identification number (#143, #117, #153 respectively) and left to adhere for 1 h on fibronectin before being submitted to immunofluorescence staining. The images acquired by cLSM imaging were then submitted to a phenotyping process.*

4.2. Cell adhesion associated molecules in HSPC

To evaluate which adhesion structures are assembled by HSPC upon matrix-contact, a variety of CAAM were immunofluorescently labelled after cell adhesion (see 3.2.1). CAAM were selected to indicate the different adhesion structures FA, invadopodia and podosomes in native and mature states respectively (see 1.2). This resulted in the adhesion structure marker matrix depicted in Table 4.3.

Table 4.3 Matrix of markers indicative of native and mature adhesion structures

	Focal Adhesion	Podosomes	Invadopodia
Native	Actin-related protein 3 (**Arp3**)	Phosphorylated protein tyrosine kinase 2 beta (**pPYK2**)	Cortactin (**CTTN**)
Mature	Arf-GAP with SH3 domain, ANK repeat and PH domain-containing protein 3 (**ASAP3**)	Matrix metallopeptidase 9 (**MMP-9**)	SH3 and PX domain-containing protein 2A (**TKS5**)

As adhesion structures are to be expected at the ventral cell side, the images depicted in the following sections display this region on the cell, if not explicitly stated otherwise. To account for unspecific secondary antibody binding, controls with omitted primary antibody were carried for each experiment. These controls for all fluorescence images depicted in this section (4.2) are shown in the Appendix (Figure A.3).

### 4.2.1. Mature and native focal adhesion markers in HSPC

The overall display of FA markers Arp3 and ASAP3 in adherent HSPC are shown in Figure 4.5, alongside a merged channel images and F-actin images (subimages a) and b)). The native FA marker Arp3 presented only very faintly in most of the adherent

HSPC that were visualized for this marker. In the majority of cells small (~0,3 µm diameter[1]) Arp3 signals above background intensity (at maximum ~70, Figure 4.6 a)) could be observed, meaning raw fluorescence intensity reached ~160 for these signals in the cell center and ~80 for signals found closer to cell periphery (see Figure 4.5 d) and Figure 4.6 b), arrowheads). These Arp3 signals are evenly distributed throughout the ventral cell side. Rarely some strong Arp3 signals around a fluorescence intensity value of 1400 can be observed in the ventral cell side as well (see Figure 4.5 d) and Figure 4.6 c), arrows). Neither regular, nor strong Arp3 signals colocalize to any specific F-Actin structures or spots. Analyzing the spatial distribution of Arp3 in z-direction shows that most of Arp3 in HSPC is located at the dorsal cell side (Figure 4.7). Here, the raw fluorescence intensity values of Arp3 are almost five times higher than the values in ventral cell regions.

The mature FA marker ASAP3 is ubiquitously present at high levels throughout the HSPC ventral cell side (see Figure 4.5 c)). In cells with the arch morphology, ASAP3 forms ring like structures (see Figure 4.8 arrowheads). Rarely these are lined by F-Actin (indicated by arrows in Figure 4.8).

---

[1] Rounded mean of n=10 representative signals presented in Figure 4.5, accessed using the ZEN measuring tool
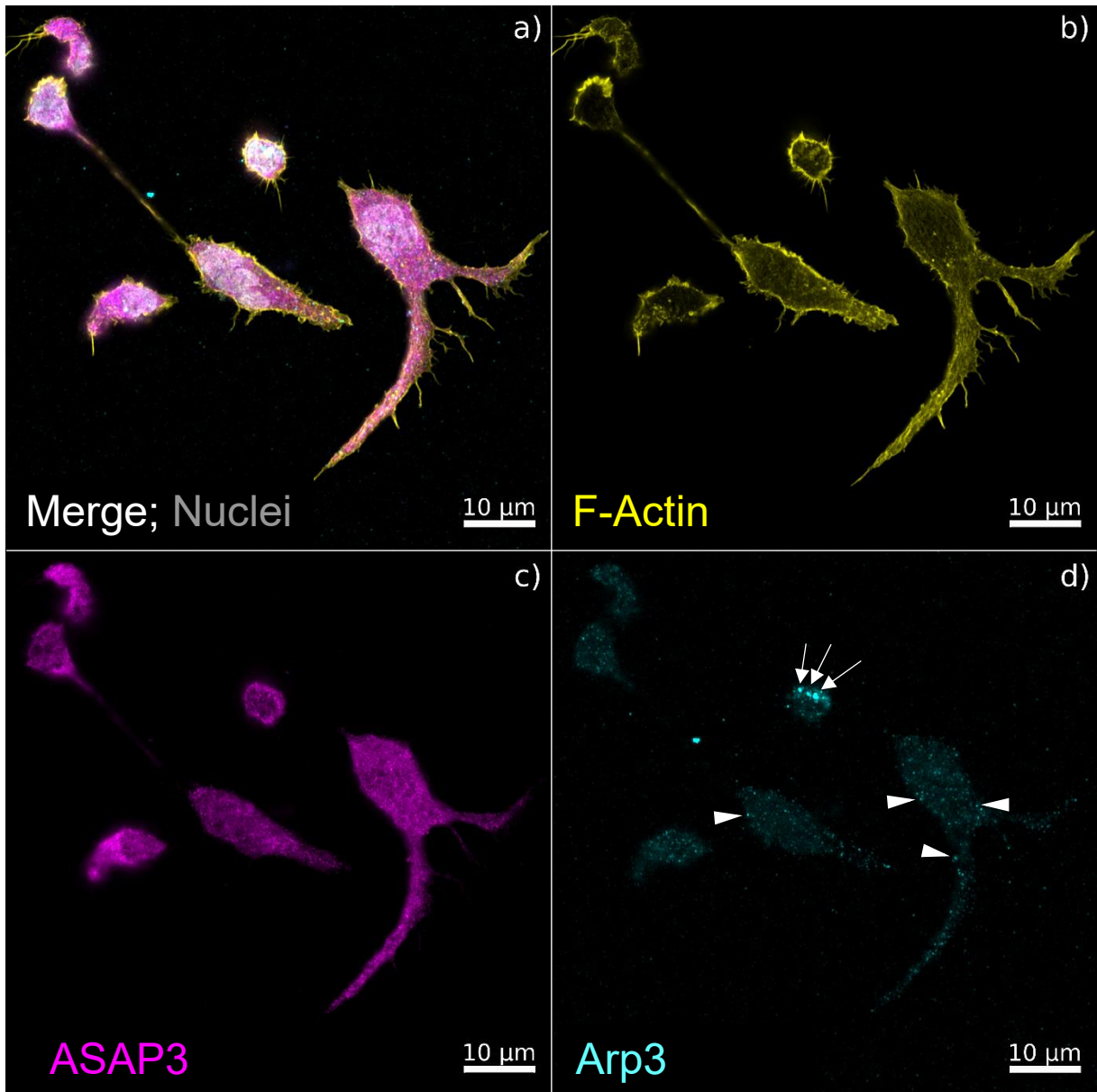
Figure 4.5 Focal Adhesion markers at the ventral cell side of adherent HSPC *Arrowheads indicate small signals above background fluorescence, arrows indicate especially bright signals. Depicted is the IF labelling of **a)** all assessed marker, including the nuclei/DNA (grey) – merged image; **b)** F-actin (yellow); **c)** ASAP3 (magenta); **d)** Arp3 (turquoise), of a representative image for n=35 images of cells acquired from N=3 cord blood donors.*
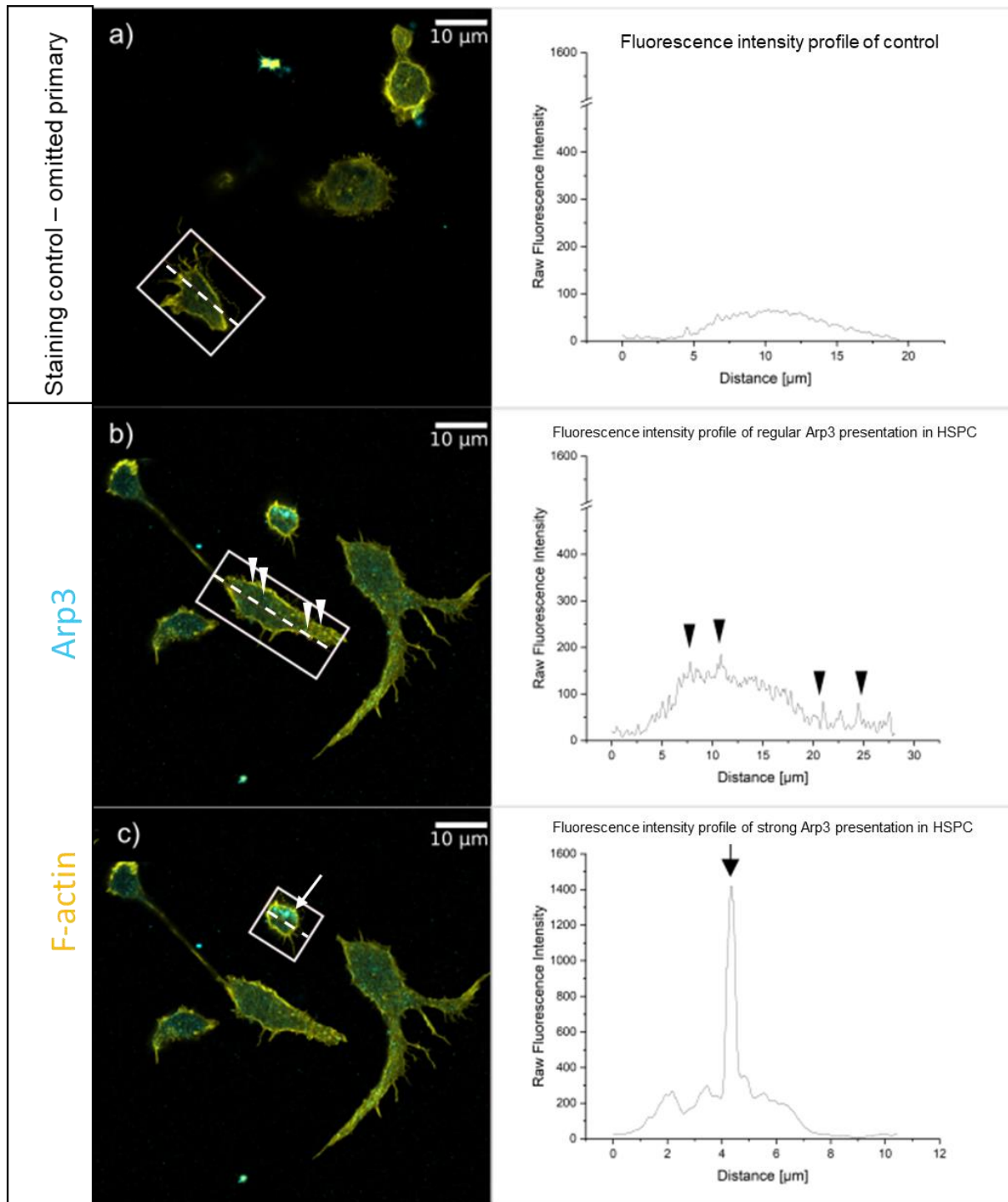
Figure 4.6 Fluorescence intensity profiles of Arp3 at the ventral cell side of adherent HSPC
*Depicted are fluorescence intensity profiles along the dotted lines in corresponding image areas of **a)** Immunofluorescence staining control (omitted primary antibody) – background signal; **b)** regular Arp3 presentation - arrowheads indicate small signals above background fluorescence; **c)** strong Arp3 presentation - arrows indicate especially bright signal. F-Actin is labelled in yellow, Arp3 is shown in turquoise. Fluorescence intensity profiles are representative of for n=35 images of cells acquired from N=3 cord blood donors.*
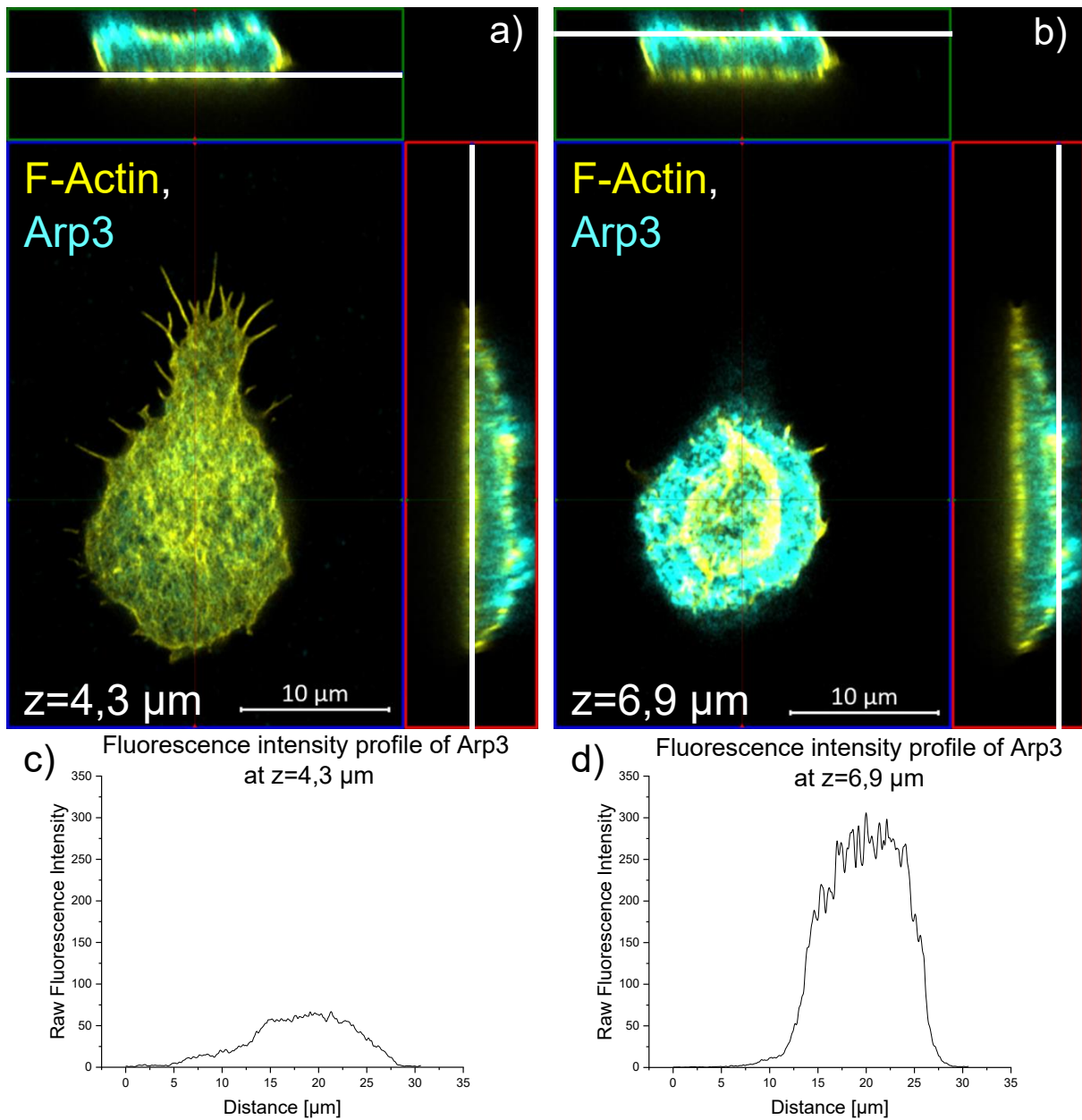
Figure 4.7 Spatial distribution in z-direction of Arp3 in adherent HSPC *Depicted are the orthogonal views of a representative HSPC of n=20 images of cells acquired from N=2 cord blood donors showing the spatial distribution of F-Actin (yellow) and Arp3 (turquoise) in x-y direction (blue frame), y-z direction (red frame) and x-z direction (green frame) in* **a)** *z=4,3 µm and* **b)** *z=6,9 µm. Orthogonal views are accompanied by raw fluorescence intensity profiles of Arp3 at* **c)** *z=4,3 µm and* **d)** *z=6,9 µm, respectively. Total distance in z=8.7 µm. White line indicates respective z-position in the orthogonal view.*
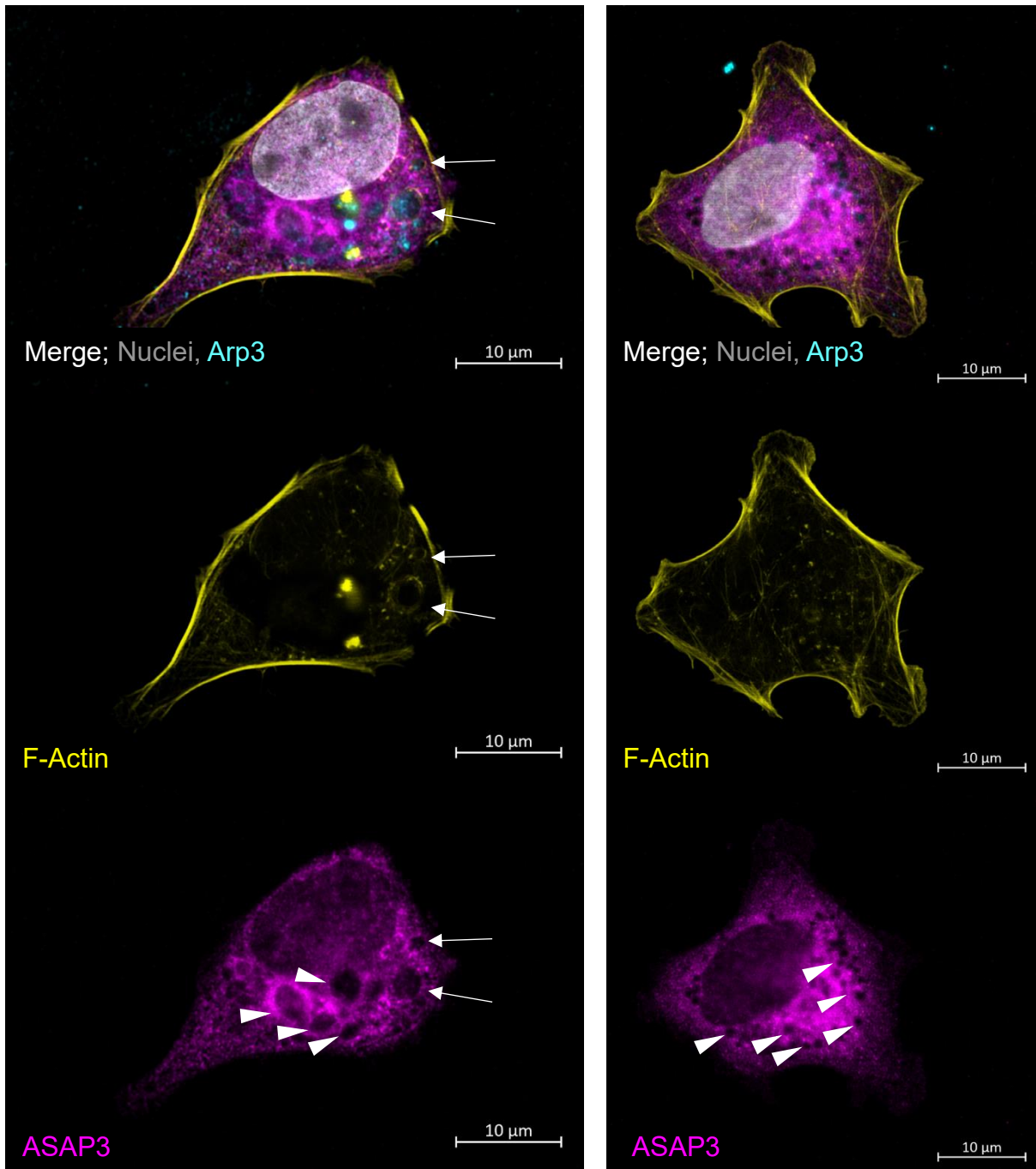
Figure 4.8 ASAP3 in HSPC with arch morphology. *Arrowheads indicate ring-like structures of ASAP3, arrows show ring-like structures of ASAP3 lined by F-Actin. Depicted are merge and single channel images of two representative HSPC ventral cell sides in each column respectively (n=4 images of cells labelled for ASAP3 displaying arch morphology from one cord blood donor). F-Actin labelled in yellow. ASAP3 in magenta, Nuclei/DNA in grey, Arp3 labelled in turquoise.*

### 4.2.2. Mature and native invadopodia marker in HSPC

At the ventral cell side of HSPC, the native invadopodia marker cortactin is observed at high levels throughout the entire cell area. However, no distinct structures are noticeable regarding this marker (see Figure 4.9d), Figure 4.10d), Figure 4.11a)). The mature invadopodia marker TKS5, on the contrary, shows a variety of noticeable formations, depending on cell morphology. In polarized cells, TKS5 forms long fiber-like structures that stretch across the cell body. These structures are not colocalized to F-actin fibers, as these appear closer to the cell periphery and the nucleus (see Figure 4.9 a)-c)).
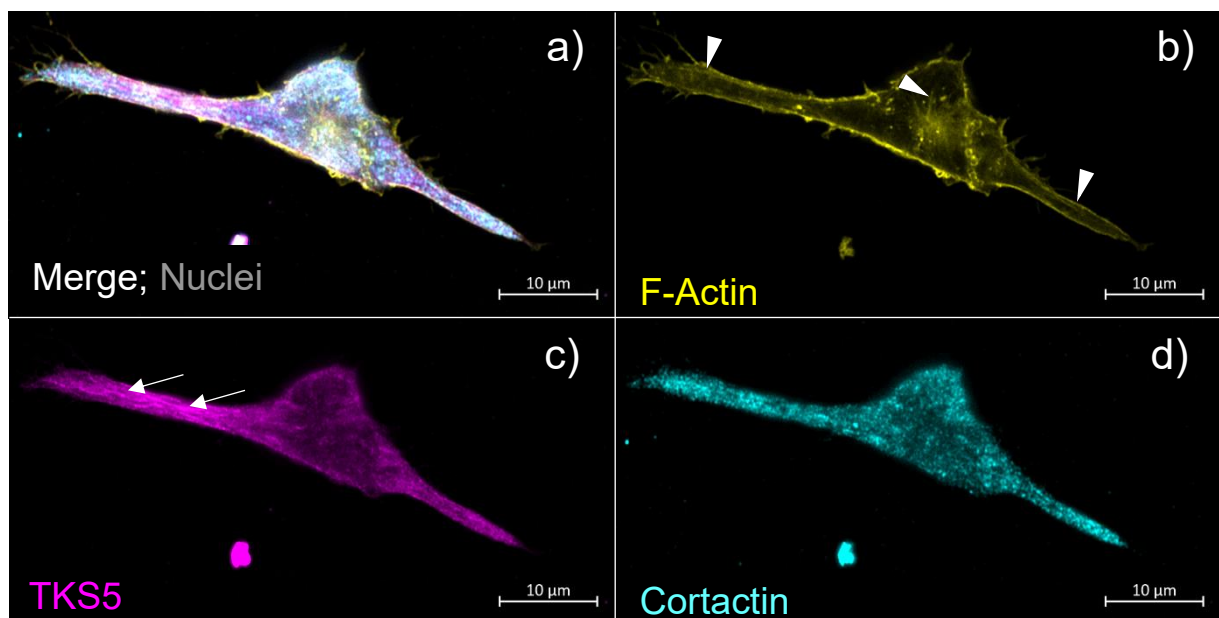
Figure 4.9 Invadopodia marker at the ventral cell side of polarized, adherent HSPC *In FN-adherent HSPC of polarized morphology, TKS5 shows elongated fiber-like structures, while cortactin is evenly distributed. None of the markers colocalize to F-actin fibers. Depicted are images of **a)** the merged channel images, including the nuclei/DNA (grey); **b)** F-actin (yellow); arrowheads indicate F-actin fibers **c)** TKS5 (magenta); arrows indicate long TKS5 fibers **d)** cortactin (turquoise) of a representative cell (n=35 cell with polarized morphology labelled for TKS5 and cortactin from N=5 independent cord blood donors)*

In cells where strong F-actin puncta are observed, TKS5 does not colocalize with these spots (see Figure 4.10). However, even in cells with a smaller area, small, fiber-like structures are observed in the cell body (e.g. Figure 4.10 c), arrowheads, cell area=134 μm^2; compared to the cell depicted in Figure 4.9, cell area=259 μm^2). Additionally, in Figure 4.10 (arrows) it is visible, that small F-actin protrusions extending

beyond the cell edge are colocalized with TKS5, which is representative for multiple cells labelled for this marker.
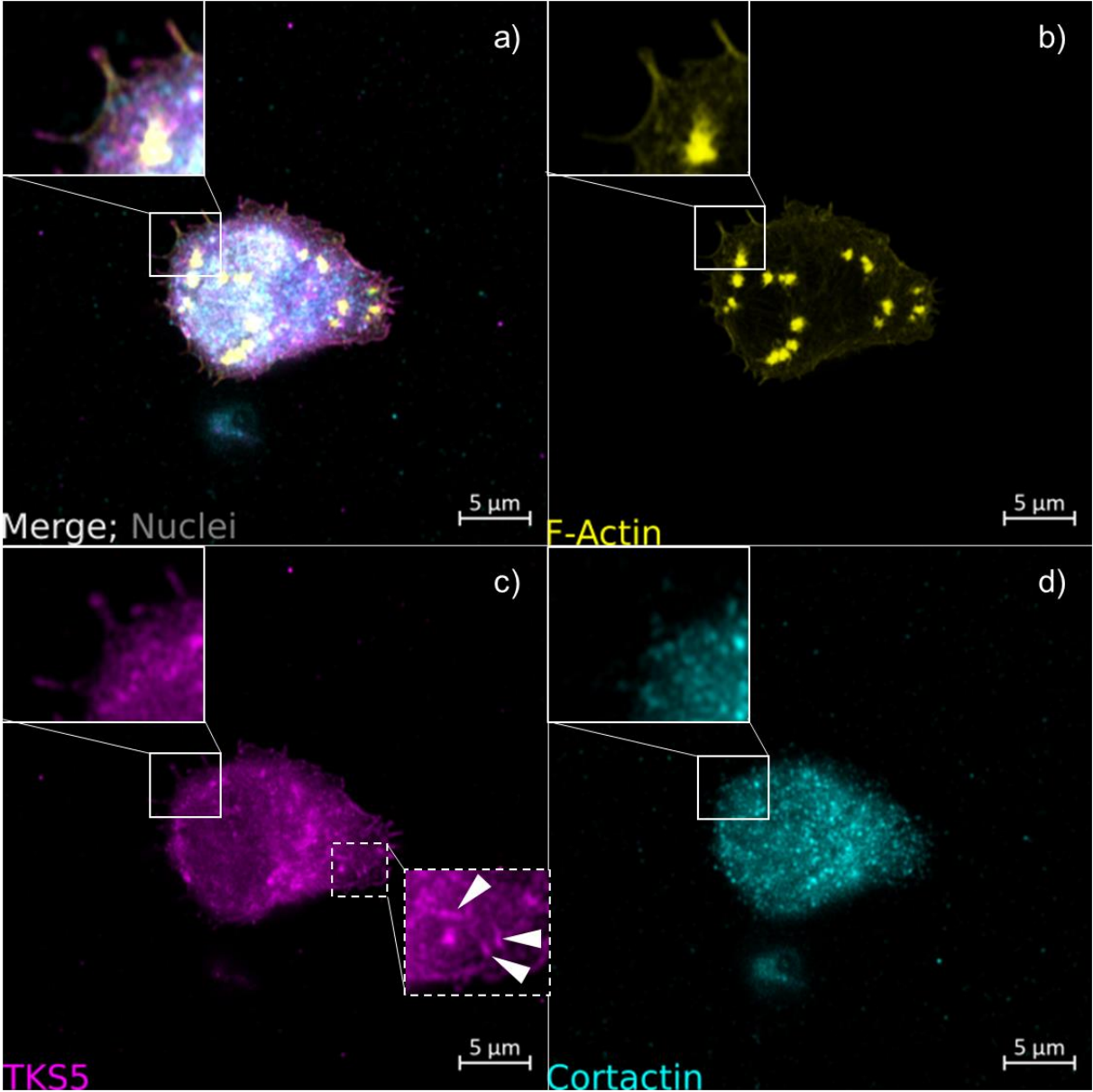
Figure 4.10 Invadopodia marker in adherent HSPC with PLS *Close-ups with solid border label small F-actin protrusions beyond the cell edge colocalized with TKS5; arrowheads in close-up with dotted border indicate small TKS5 fibers. Depicted are images of the ventral cell side of a FN adherent HSPC of **a)** the merged channel images, including the nuclei/DNA (grey); **b)** F-actin (yellow) **c)** TKS5 (magenta) **d)** cortactin (turquoise); representative for n=122 HSPC labelled for TKS5 and cortactin from N=5 independent cord blood donors.*

Lastly, in cells with the arch morphology, TKS5 assembles into large, circular structures in the ventral cell site. Interestingly, even in some small cells, structures that resemble these rings can be observed, although in a less pronounced manner (see Figure 4.11).
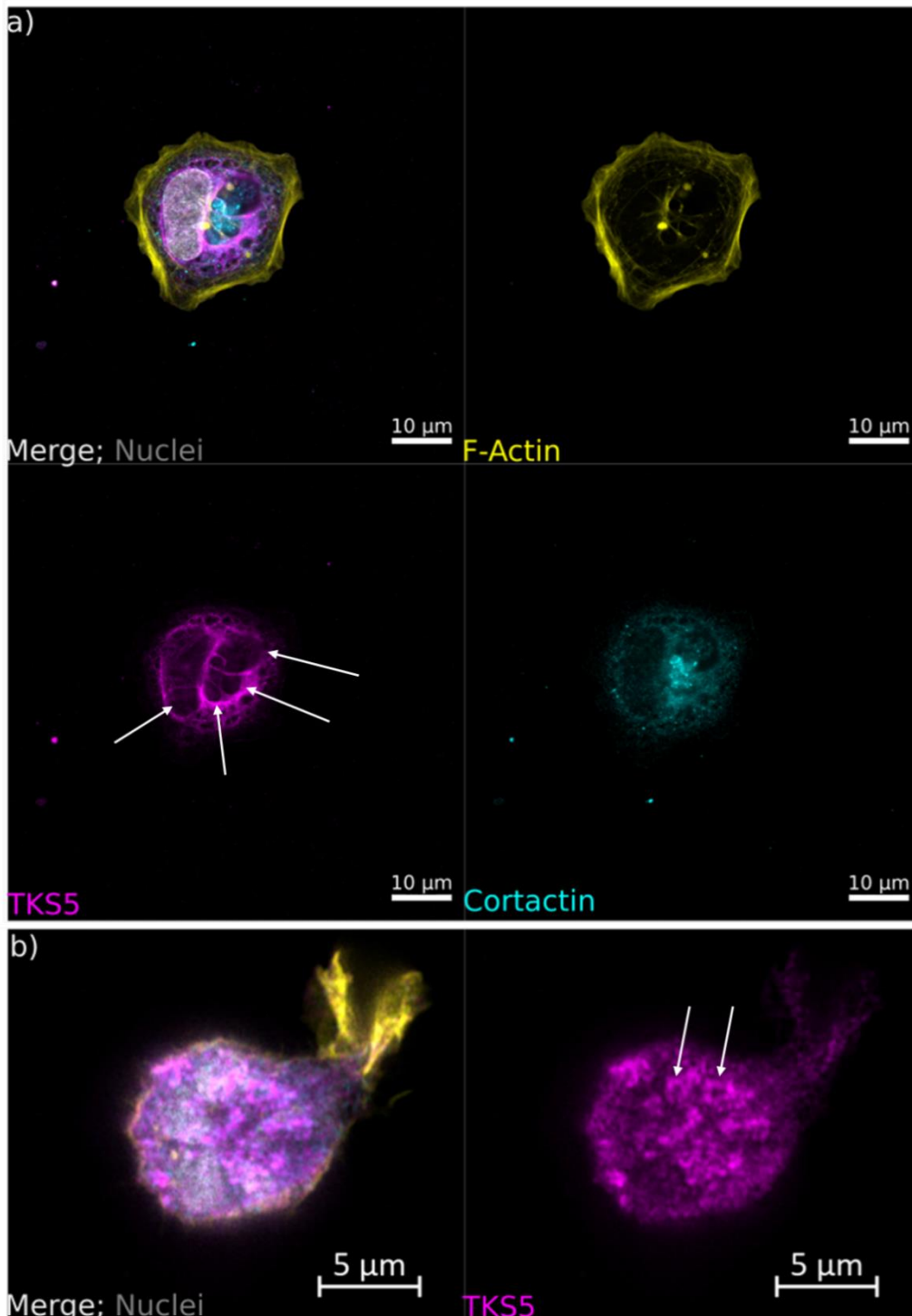
Figure 4.11 Invadopodia marker in adherent HSPC displaying TKS5 rings *Arrows label TKS5 rings. Image **a)** shows a HSPC displaying the arch morphology (representative n=3 cells with arch morphology in N=3 cord blood donors), **b)** depicts a smaller cell (representative for n=122 HSPC labelled for TKS5 and cortactin from N=5 independent cord blood donors). Depicted are images on an FN-adherent HSPC of the merged channel images, including the nuclei/DNA (grey), F-actin (yellow), TKS5 (magenta), cortactin (turquoise).*

### 4.2.3. Mature and native podosome marker in HSPC

The native podosome marker phosphorylated PYK2 (pPYK2) presented itself in a very distinct manner in adherent HSPC displaying the podosome phenotype. It is observed being colocalized to prominent F-actin puncta. Moreover, in some cases pPYK2 is present in ring-like structures in association with actin spots (see Figure 4.12). These structures are predominantly found in the ventral cell side (see Figure 4.14b), arrows).

In cells with the arch morphology or a generally larger cell area, pPYK2 is observed in different, distinct structures. Here, pPYK2 is located at the tips of F-actin fibers, right at the cell edge. Especially in HSPC with arch morphology, that display many long F-actin fibers, pPYK2 is accumulated alongside the cell edge (see Figure 4.13).

The mature podosome marker MMP9 is ubiquitously produced in adherent HSPC. This CAAM is marginally localized at higher levels in dorsal regions, where it has a raw fluorescence intensity value of 311 ± 45[2], compared to ventral regions (raw fluorescence intensity of 226 ± 131[2]) (see Figure 4.14).

---

[2] Mean, raw fluorescence intensity and standard deviation of n=5 cells depicted in Figure 4.14.
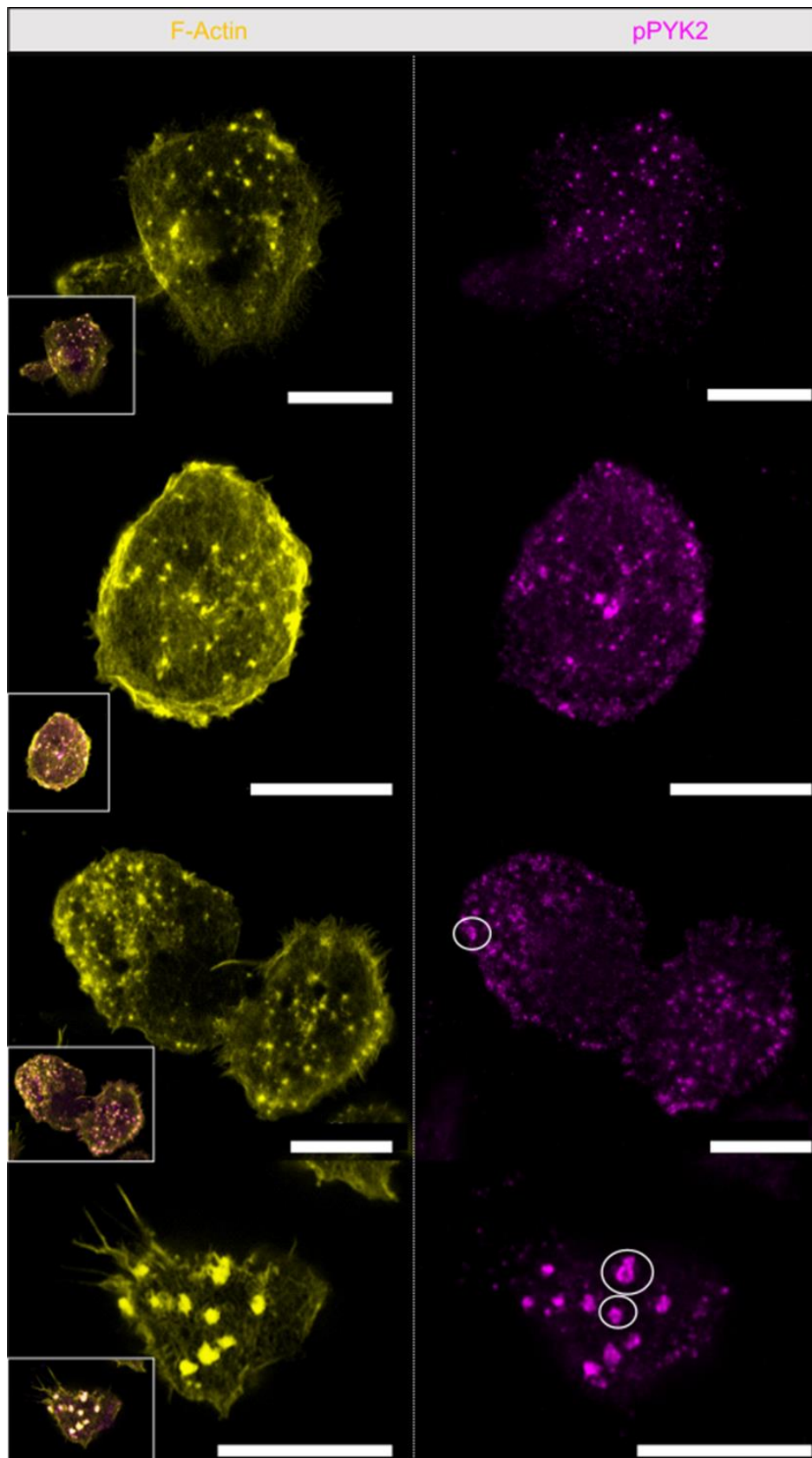
Figure 4.12 pPYK2 in adherent HSPC with podosome morphology. *FN-adherent HSPC with podosome morphology show strong colocalization at PLS with pPYK2. Circles mark ring-like pPYK2 structures. Depicted are images of cells presenting F-actin (yellow, left column) puncta colocalized with pPYK2 (magenta, right column) and merge of these two channels (white frame). Four individual images with the same pPYK2 presentation from top to bottom, representative of n=163 cells with podosome morphology labelled for pPYK2 from N=4 independent cord blood donors. Scale bar = 10 µm.*
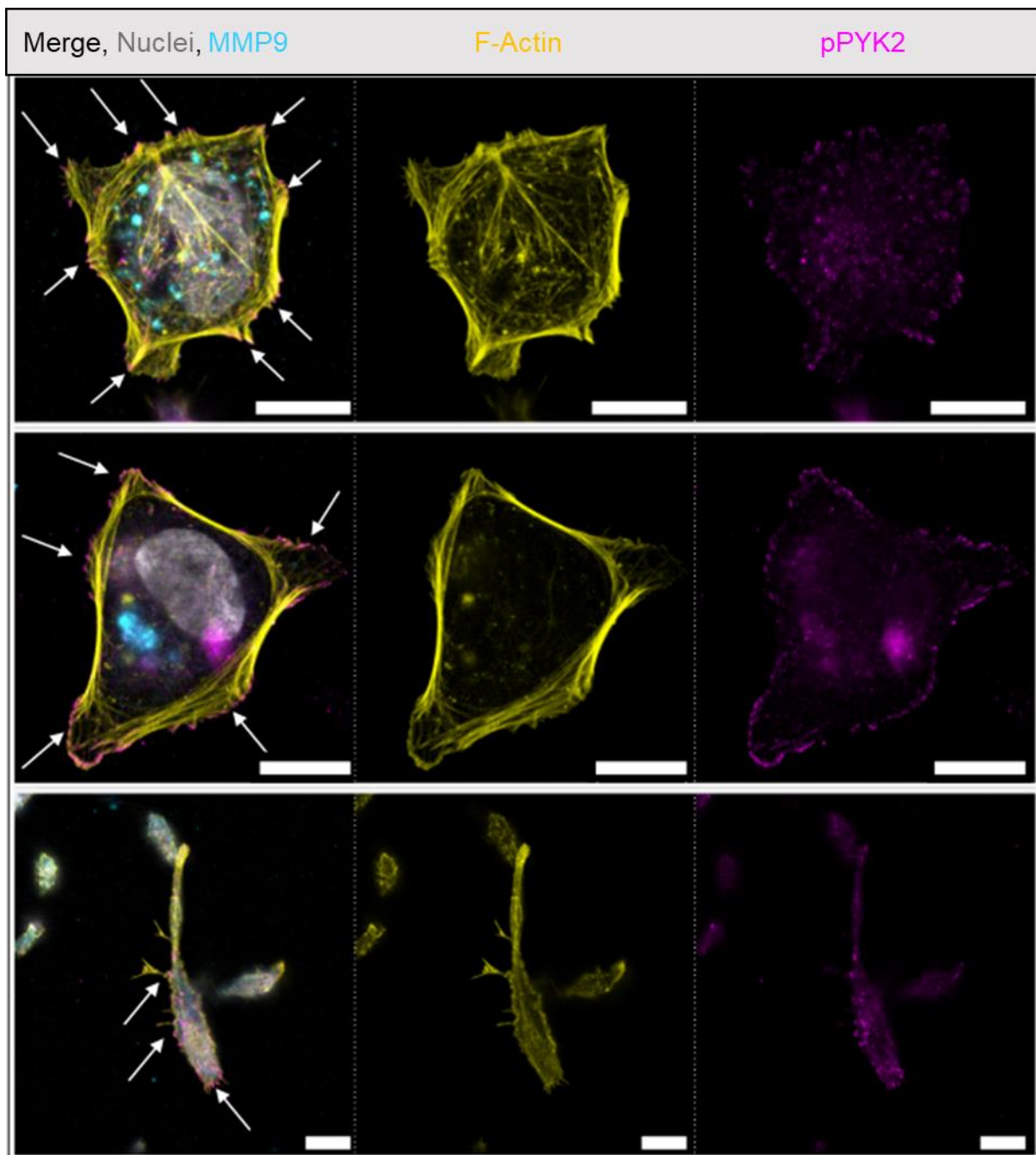
Figure 4.13 Podosome markers in adherent HSPC of arch morphology or larger cell area *Arrows label pPYK2 presence in F-actin fiber tips. Depicted are images of large cells labelled for nuclei/DNA (grey), F-actin (yellow), pPYK2 (magenta), MMP9 (turquoise) and merged channels. Cells in the top and middle row display the arch morphology, while the cell in the bottom row displays a polarized morphology with large cell area. Cells are representative for FN-adherent HSPC displaying a certain morphology of n=196 cells labelled for pPYK2 from N=4 independent cord blood donors. Scale bar = 10 µm.*
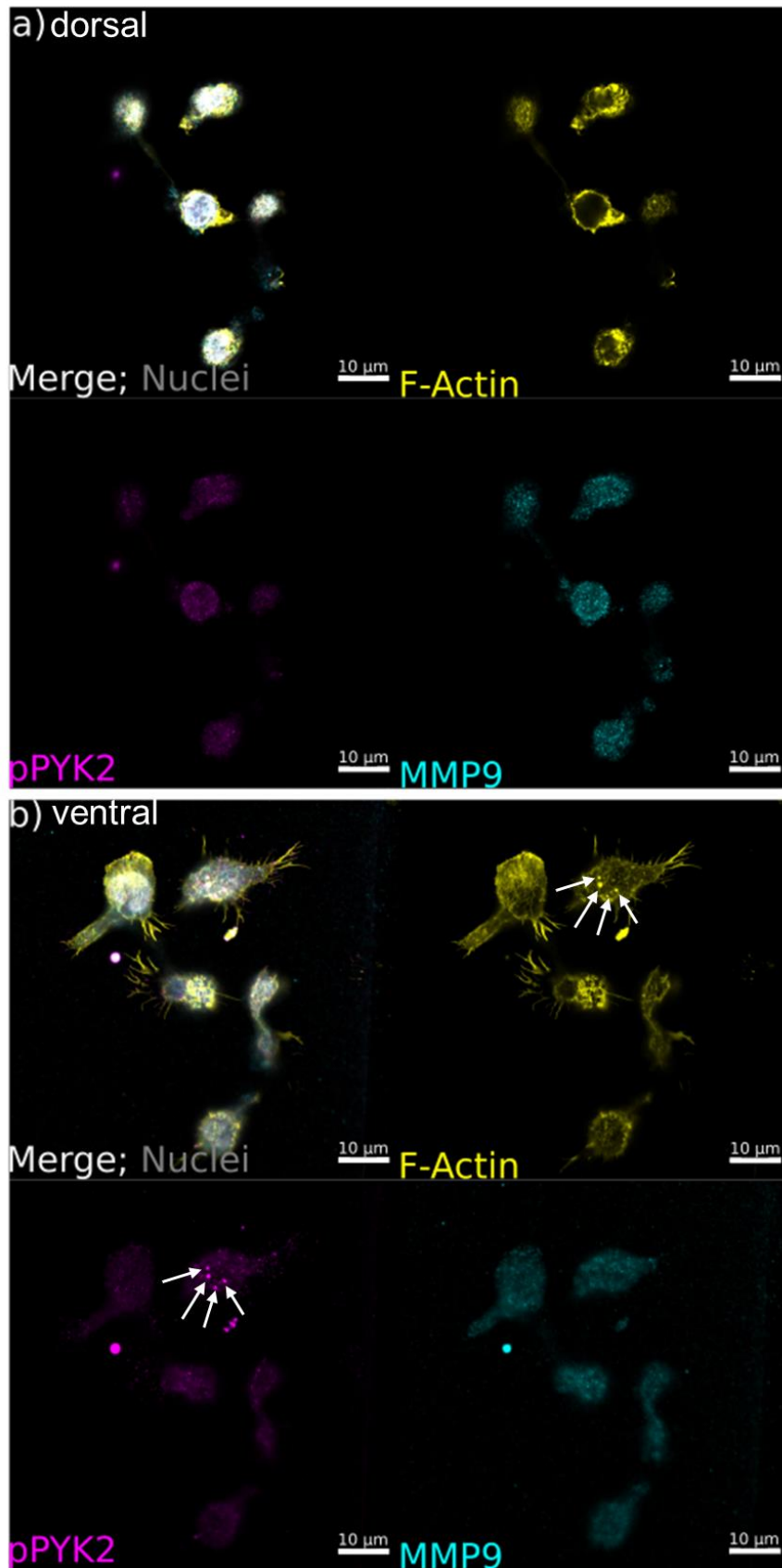
Figure 4.14 Distribution of podosome markers at dorsal and ventral cell side of adherent HSPC
a) Image of dorsal cell regions. *b)* Image of ventral cell regions; arrows label F-actin puncta colocalized with pPYK2. Depicted are images of cells labelled for nuclei/DNA (grey), F-actin (yellow), pPYK2 (magenta), MMP9 (turquoise) and merged channels (representative for n=39 images of cells assessed in *z* and labelled for pPYK2 and MMP9 from N=3 independent cord blood donors.

4.3. Validation of pPYK2 production in HSPC by immunohistochemical blot

Since pPYK2 shows a characteristic appearance in adherent HSPC and is a protein variant produced only in cells of hematopoietic lineage and cells of the nervous system (see 1.2.2), its presence was validated by immunohistochemical blot. Production of pPYK2 was tested in adherent and non-adherent HSPC on FN and BSA. Detections of total PYK2 (tPYK2) and GAPDH were performed to control for correct loading of lysate.
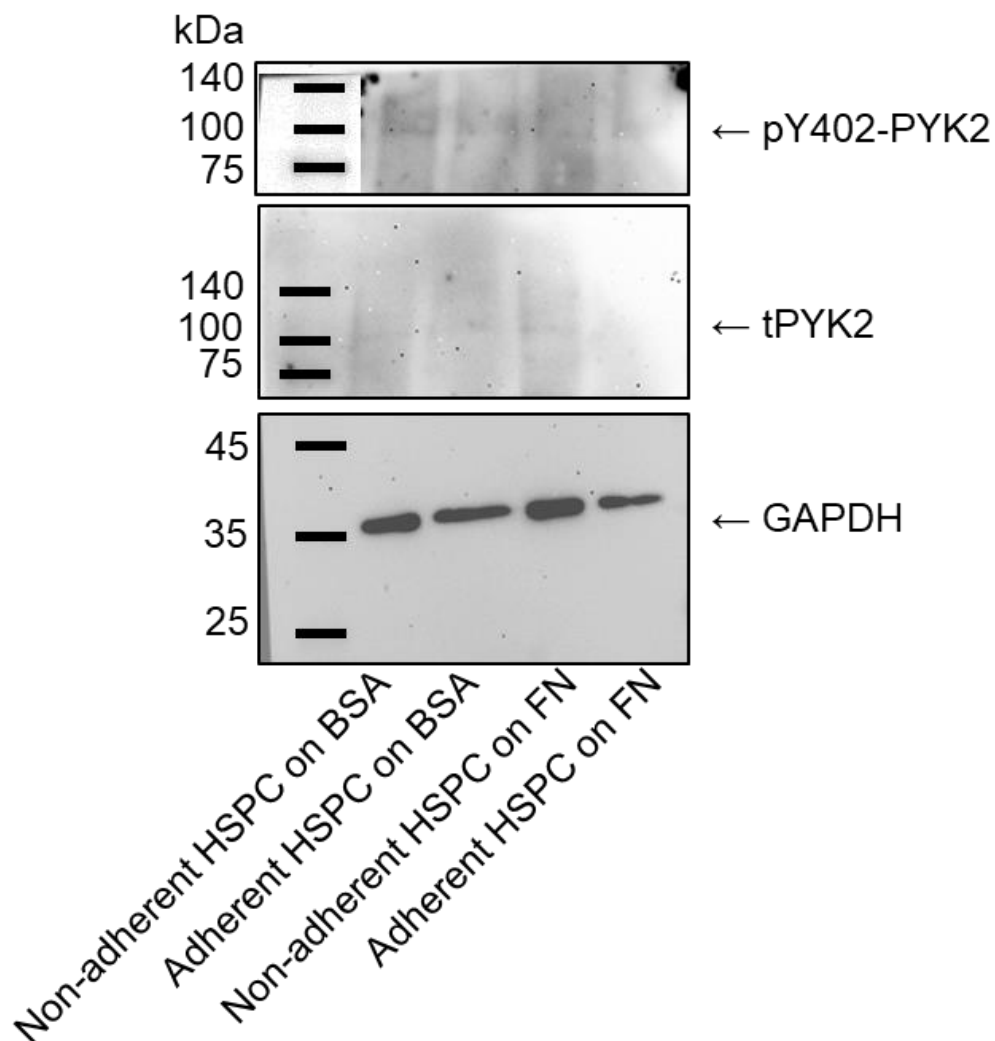
Figure 4.15 Immunoblot detection of pPYK2, tPYK2 and GAPDH in adherent and non-adherent HSPC Cells were left to adhere to BSA or fibronectin for 1 h before collection and lysis. Lysate containing 5 µg protein was separated using a 10 % Bis-Tris-gel and blotted onto a nitrocellulose membrane. Detections of pY402-PYK2 (top), tPYK2 (middle) and GAPDH (bottom) were performed using respective, specific antibodies. Proteins of interest run at 116 kDa (pPYK2 and tPYK2) and 35 kDa (GAPDH). In the top picture protein marker was imaged separately and is presented with +40 % brightness and -40 % contrast, due to a membrane damage in this area. Full, unaltered images in Appendix Figure A.2.

Figure 4.15 shows faint signals for pPYK2 and tPYK2 slightly above the 100 kDa band. These signals are observed for all samples, except the signal of tPYK2 in adherent HSPC on FN that is not visible. Apart from this sample, there is no visible difference between the signals present. It has to be noted that background signal for these two detections is rather high and uneven, making quantitative read out inaccessible. GAPDH signals are detected with comparable intensity between all samples around 35 kDa.

4.4. Spatial distribution of molecules in PLS established by HSPC

A prominent population of adherent HSPC displays a morphology containing PLS (see 4.1.1.5). Additionally the native podosome marker pPYK2 showed a very distinct pattern in adherent HSPC (for reference see 4.2.3). For this reason it is further investigated how pPYK2, and other molecules involved in podosomes (vinculin and paxillin), assemble in these structures of HSPC. Radial intensity profiles of PLS are acquired (see 3.3.4; exemplary images including controls in Appendix Figure A.4, Figure A.5). These show how fluorescence intensity profiles change respectively to the normalized intensity of F-actin puncta.

4.4.1. Radial intensity profiles of individual PLS in adherent HSPC

Analysis of radial intensity profiles of individual PLS established by HSPC shows a variance on single structure level. The individual structures found in even a single cell show different organizational states as depicted in Figure 4.16. However, all identified F-actin puncta display a colocalization with pPYK2. The intensity of pPYK2 reaches a maximum at the same spatial position as F-actin in all profiles shown. In cases, where pPYK2 is observed in a ring-like manner in the immunofluorescence image, its intensity profile displays a double peak around the F-actin maximum (see Figure 4.16 profiles 2 and 6). This is also observed in a less pronounced manner in some profiles, where a ring-like formation cannot be observed in the IF image of pPYK2 (see Figure 4.16 profile 7 and 9). In some pPYK2 radial intensity profiles, shoulders are formed (see Figure 4.16 profile 3 and 5). Spatial features of radial intensity profiles occur independent of pPYK2 fluorescence intensity. In roughly half of the profiles presented

in Figure 4.16 pPYK2 does not reach the same maximum intensity as F-actin while some still display the double peaks (profiles 2, 6, 8 and 9). These PLS also neighbor one another.
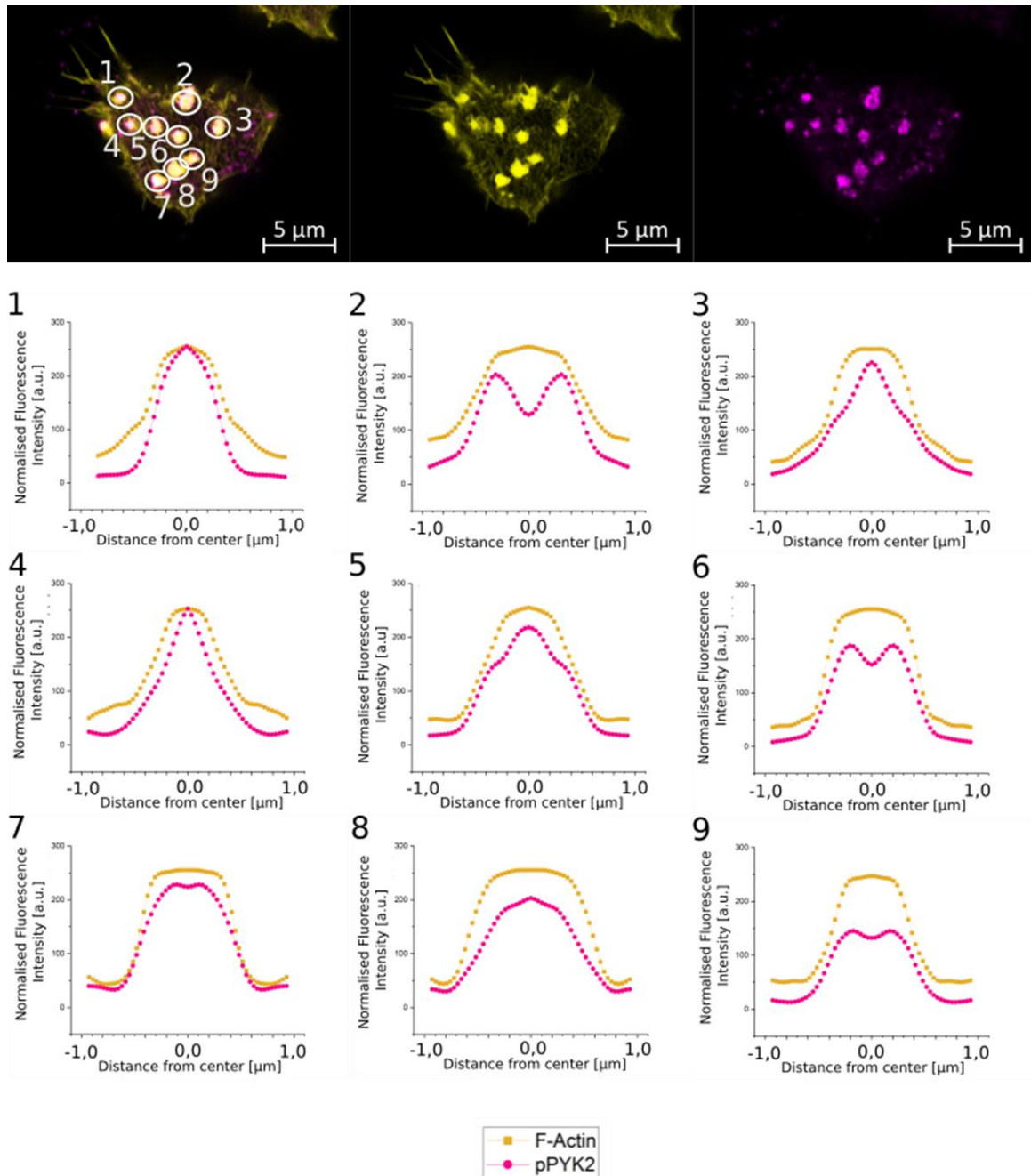
Figure 4.16 Radial intensity profiles of individual PLS in a representative, adherent HSPC
Individual PLS of a single, FN-adherent HSPC show different organizational state regarding pPYK2. F-actin (yellow) and pPYK2 (magenta) were labelled and are depicted alongside the merged image. Immunofluorescence image was submitted to ImageJ macro "Poji" to acquire radial intensity profiles. Profiles of the respective structures in the merged image are labelled with numbers. x-axis shows the distance from the PLS center, which corresponds to the radius of the circle around the PLS. y-axis shows the normalized fluorescence intensity in arbitrary units (a.u.) according to maximum bit range in the F-actin channel.

4.4.2. Radial intensity PLS profiles of individual adherent HSPC of different phenotypes

The entirety of PLS found in one adherent HSPC can be described together in a radial intensity profile describing all PLS of the cell. Immunofluorescent images of HSPC, in which pPYK2 and vinculin/paxillin are visualized, are submitted to the phenotyping process described in 4.1.1. Exemplary profiles for adherent HSPC of different phenotypes are depicted for paxillin and vinculin in Figure 4.17 and Figure 4.18. These show, that variance in spatial distribution occur between cells of different phenotypes but also within phenotype groups.

The spatial distribution of pPYK2 and paxillin on a single cell level shows variances between cells. All of the cells depicted in Figure 4.17 show a clear colocalization of both pPYK2 and paxillin with F-actin puncta. In two of the presented cells, representing the podosome and polarized-filopodia mix phenotypes, both pPYK2 and paxillin profiles form shoulders in intensity roughly 500 nm away from the F-actin core (see Figure 4.17 a) and b)). This is not observed in the other two cells, one of which has the filopodia-podosome mix phenotype and the other of the polarized-filopodia mix phenotype (see Figure 4.17 c)-d)). Comparison of Figure 4.17 b) and d) shows that averaged PLS intensity profiles can differ from cell to cell with the same phenotype.
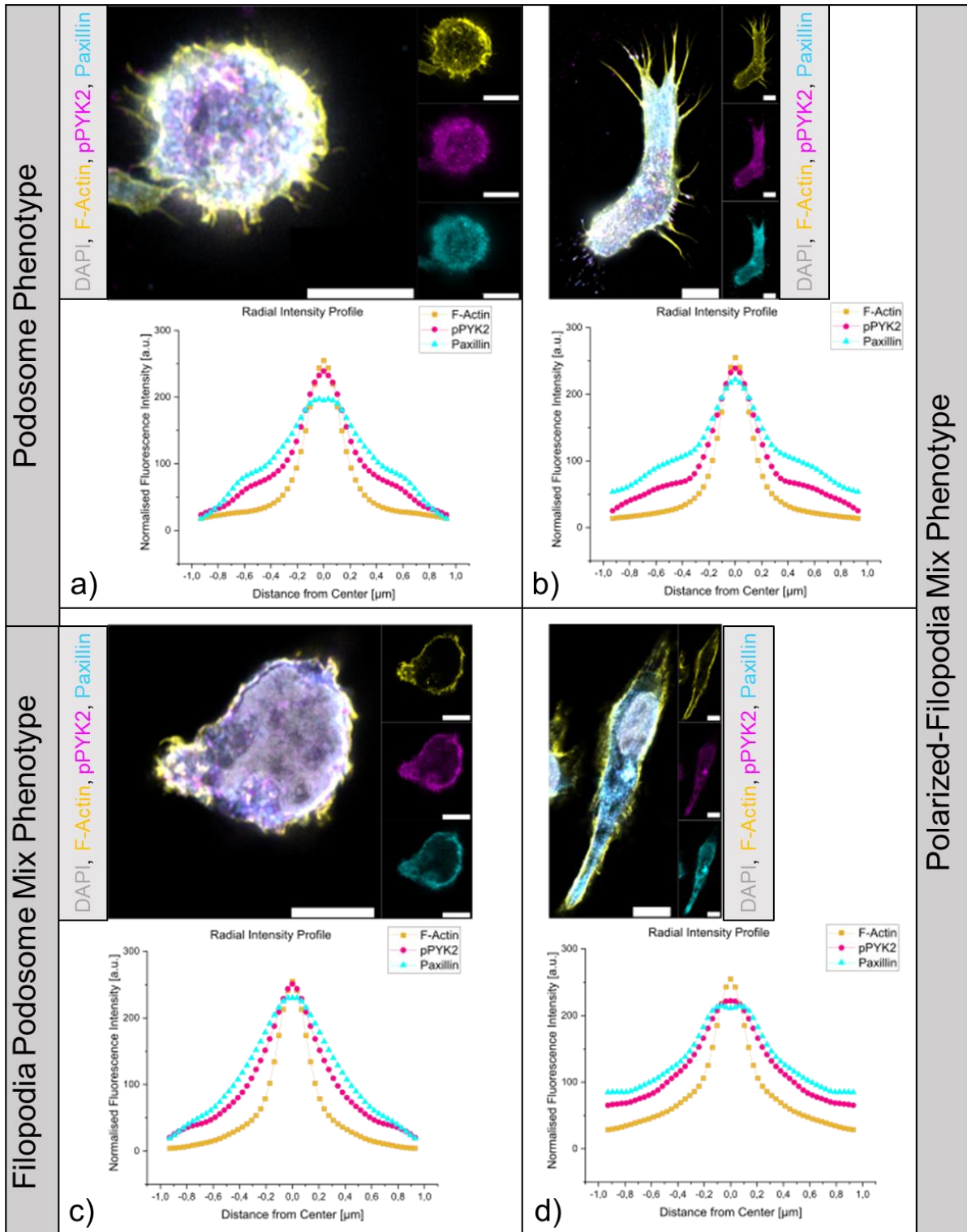
Figure 4.17 Radial intensity profiles of adherent HSPC labelled for pPYK2 and paxillin *Mean radial intensity profile of individual FN-adherent HSPC can vary independent of phenotype. Immunofluorescence images depict F-Actin (yellow), pPYK2 (magenta), paxillin (turquoise) and merge of all channels plus nuclei (grey). Depicted are immunofluorescence images and respective PLS radial intensity profiles of HSPC with a) podosome phenotype, b) polarized-filopodia mix phenotype, c) filopodia-podosome mix phenotype, d) another cell with polarized-filopodia mix phenotype (representative for n=90 images of HSPC from N=3 independent cord blood donors). Scale bar = 5 µm.*

Variance in single cell radial intensity profiles of PLS can be observed also for the spatial distribution of pPYK2 and vinculin. In Figure 4.18 a) and b) two cells with the podosome phenotype are depicted alongside the respective radial intensity profiles. Both profiles show an almost exact colocalization of pPYK2 with the F-actin puncta. However, for the cell displayed in subimage a) the radial intensity profile for vinculin has a sharp double peak with the maxima being around 400 nm away from the center and a minimum right at the center of the F-actin core. Another cell with podosome phenotype depicted in subimage b) just shows a colocalization of vinculin with the F-actin spot. The cell with round phenotype presented in subimage c) shows a radial intensity profile for its PLS that has distinct features regarding both pPYK2 and vinculin. While pPYK2 shows a cojoined peak with the center of the F-actin puncta, it also displays local maxima around 500 nm away from the center. In this cell vinculin is present with a double peak in the profile, both maxima at around 400 nm away from the center. Lastly a cell with filopodia-podosome mix phenotype is depicted, whose radial intensity profile shows an almost exact colocalization of all visualized CAAM at the F-actin spot center (see subimage d)). Beyond this center region, vinculin shows a shoulder in its profile, while the pPYK2 profile stays close to the profile of F-actin.
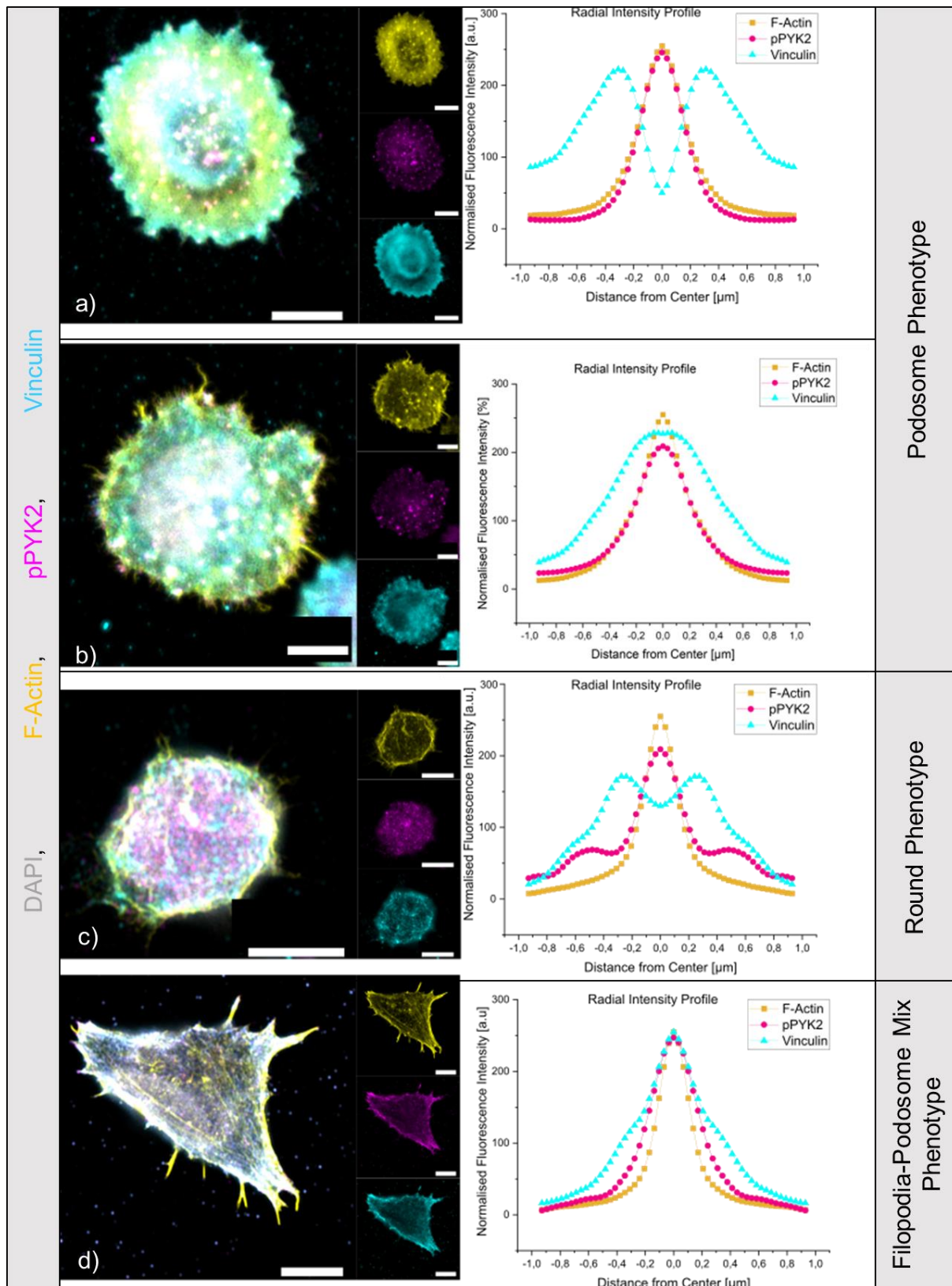
Figure 4.18 Radial Intensity Profiles of adherent HSPC labelled for pPYK2 and vinculin *Mean radial intensity profile of individual FN-adherent HSPC can vary independent of phenotype. Immunofluorescence images depict F-Actin (yellow), pPYK2 (magenta), vinculin (turquoise) and merge of all channels plus nuclei (grey). Depicted are immunofluorescence image and respective PLS radial intensity profiles of HSPC with* ***a)*** *podosome phenotype,* ***b)*** *another cell with podosome phenotype,* ***c)*** *round phenotype,* ***d)*** *filopodia-podosome mix phenotype (representative of n=90 images of HSPC from N=3 independent cord blood donors). Scale bar = 5 µm.*

4.4.3. Radial intensity profiles of HSPC averaged over entire cell populations with different phenotypes

To analyze whether PLS established by HSPC populations of different phenotype have altered spatial distribution of the molecules involved, radial intensity profiles for PLS of the respective cells are acquired. Depicted are the averaged radial intensity profiles of all HSPC, which are assigned the same phenotype according to the accredited shape, filopodia and/or podosome descriptors, as described in 4.1.1. As the impact of individual cells to averaged profiles can be quite high, the mean profiles for each cord blood donor assessed for this analysis can be found in Digital Appendix, to display the individual steps taken to acquire the data that result in the depicted profiles as detailed as possible.

pPYK2, paxillin and vinculin show a colocalization with F-actin in all phenotypes. F-actin spots do not show much variance in size between phenotypes, as peak width does not change. Variance between the assessed CAAM spatial distribution varies only slightly between phenotypes. pPYK2 is more broadly distributed around the F-actin spots. In phenotypes that do not contain the filopodia morphology (round, podosome, polarized, polarized-podosome phenotypes) this phenomenon seems to be even more pronounced (see Figure 4.19, Figure 4.20). Paxillin seems to follow this trend while generally being even more broadly distributed around the F-actin puncta than pPYK2 (see Figure 4.19). Vinculin spans beyond the F-Actin spot and pPYK2 in width in all phenotypes, yet this CAAM does not seem to follow a certain trend between phenotypes, regarding its width around the F-actin spot (see Figure 4.20). For cells of the round phenotype and cells containing the podosome morphology (podosome, polarized-podosome and filopodia-podosome) standard deviations of the pPYK2 profile are larger, especially in the center of the F-actin spot (see Figure 4.19, Figure 4.20, Figure 4.21). Standard deviation was taken into consideration as a result of the high variance between profiles of individual structures of cells as shown in 4.4.1, 4.4.2. It has to be mentioned that this observation was not reproduced in the polarized-podosome phenotype for the data set containing vinculin (see Figure 4.20 f), Figure 4.21 c)). Vinculin itself has a similar display of high standard deviation at the spot center in almost all analyzed phenotypes, with the exception of the polarized-filopodia and polarized-podosome phenotypes (see Figure 4.20, Figure 4.21). Taken together a

trend is visible, in which PLS of round and podosome containing phenotypes seem to have a broader distribution of pPYK2 and vinculin around the F-actin spot.

Some distinct profile features can be observed in cells with lower phenotype population size. For the polarized phenotype the pPYK2 radial PLS profile shows a plateau, with the highest standard deviation around the F-actin spot center detected, resulting in a "valley-like" display of standard deviation (see Figure 4.19 d)), indicating a ring formation of pPYK2 in some of the few cells found with this phenotype. In the second data set, where pPYK2 was visualized together with vinculin, more cells (n=12) with this phenotype were found, and standard deviation is lower (see Figure 4.20 d)). In data sets, where <12 cells were detected for a phenotype, pPYK2 radial PLS profiles have shoulders located 400-800 nm from the F-actin spot center (see Figure 4.19, Figure 4.20).

In summary, the spatial distribution of pPYK2, paxillin and vinculin around F-actin spot PLS as assessed per radial intensity profiles, displays variety on all magnitudes analyzed. Starting at individual structure level (see 4.4.1) pPYK2 displays varying organization around the F-actin spot, ranging from simple colocalization to full ring formation as indicated by double peaks in the radial intensity profile. This is enhanced in the PLS radial intensity profiles of individual HSPC, in which the spatial distribution of pPYK2 and vinculin varies greatly between cells. The varying display does not correlate to cell phenotype, as cells of the same phenotype display radial intensity profiles contrasting each other, e.g. for vinculin (see Figure 4.18), neither does it correlate to distinct spatial distribution of CAAM in cells with the podosome morphology (see Figure 4.17, Figure 4.18). This cumulates into the display of average radial intensity profiles for HSPC of different phenotype populations, were averaging over large populations mitigates the observations made for individual structures, resulting in similar radial intensity profiles for cells of all phenotypes. Small differences can only be found in standard deviation and the width of the radial intensity profile peaks.
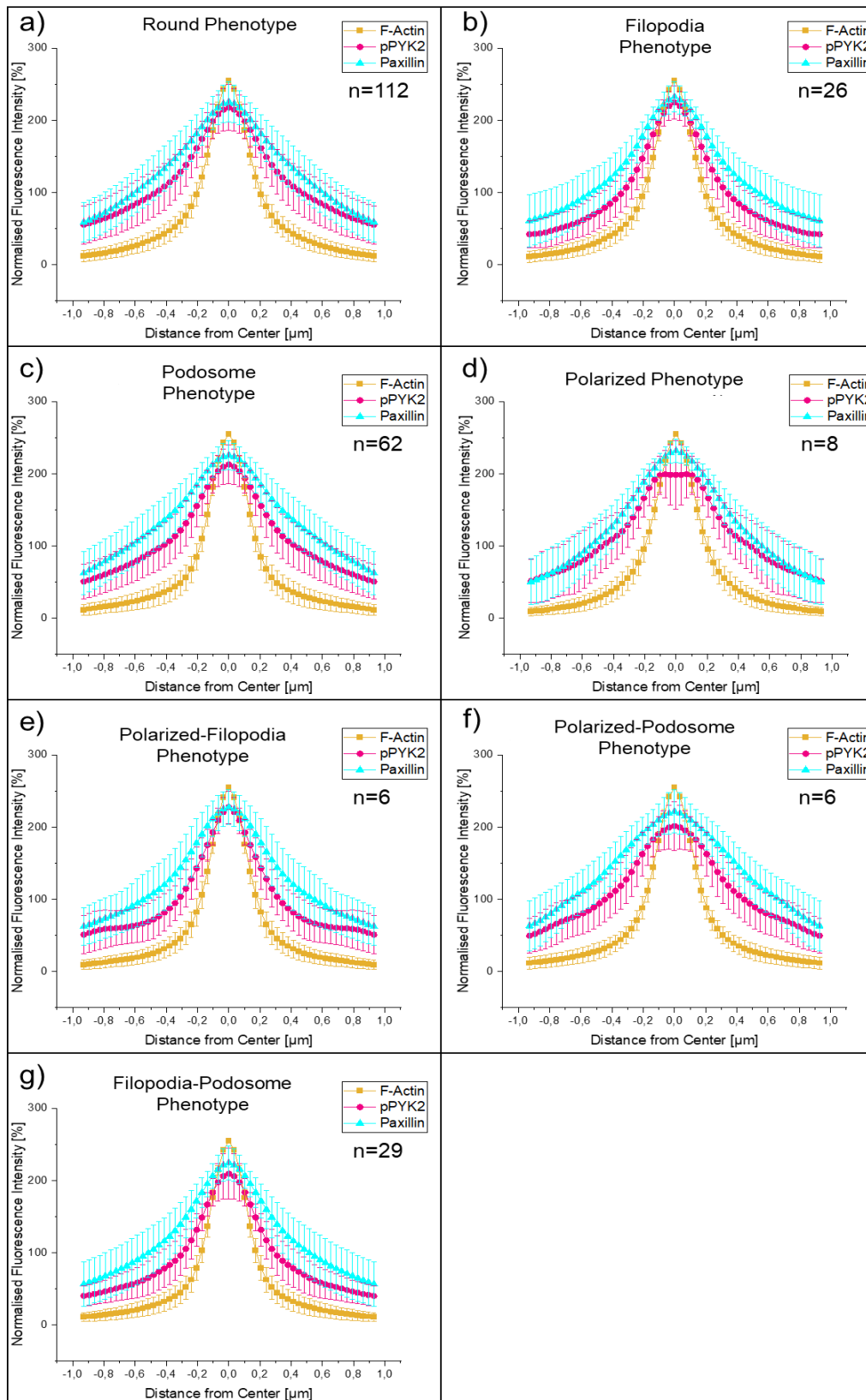
***Figure 4.19 Averaged Radial Intensity Profiles of F-Actin, pPYK2 and paxillin from PLS in
adherent HSPC with different phenotypes.*** *Shown are the mean radial intensity profiles ± SD of **a)**
n=112 cells with round phenotype, **b)** n=26 cells with filopodia phenotype, **c)** n=62 cells with podosome
phenotype, **d)** n=8 cells with polarized phenotype, **e)** n=6 cells with polarized-filopodia phenotype, **f)**
n=6 cells with polarized-podosome phenotype, **g)** n=29 cells with filopodia-podosome phenotype; all
from N=3 independent cord blood donors (#117, #143, #153).*
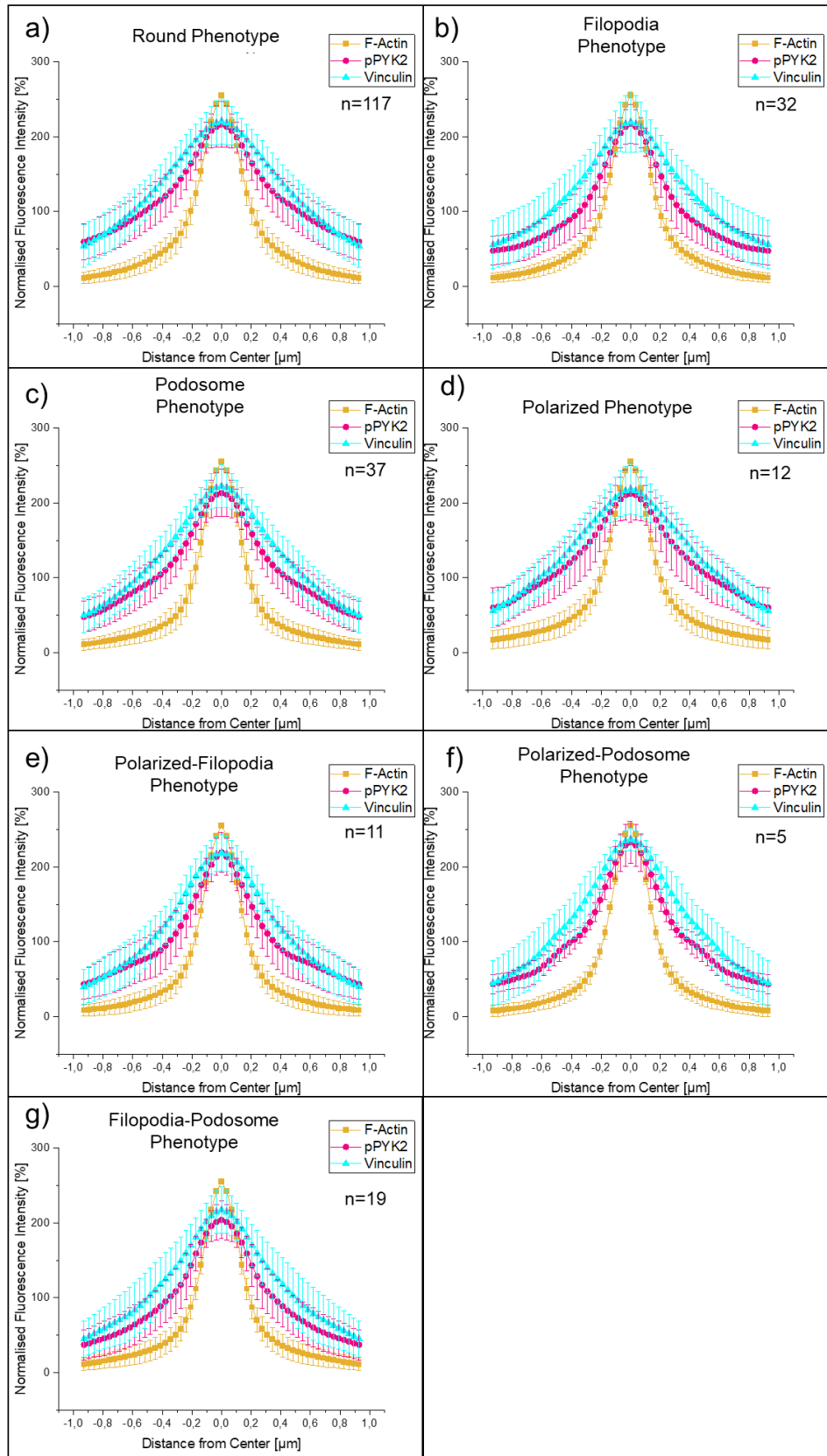
Figure 4.20 Averaged Radial Intensity Profiles of F-Actin, pPYK2 and vinculin from PLS in adherent HSPC with different phenotypes. *Shown are the mean radial intensity profiles ± SD of **a)** n=117 cells with round phenotype, **b)** n=32 cells with filopodia phenotype, **c)** n=37 cells with podosome phenotype, **d)** n=12 cells with polarized phenotype, **e)** n=11 cells with polarized-filopodia phenotype, **f)** n=5 cells with polarized-podosome phenotype, **g)** n=19 cells with filopodia-podosome phenotype; all from N=3 independent cord blood donors (#117, #143, #153).*
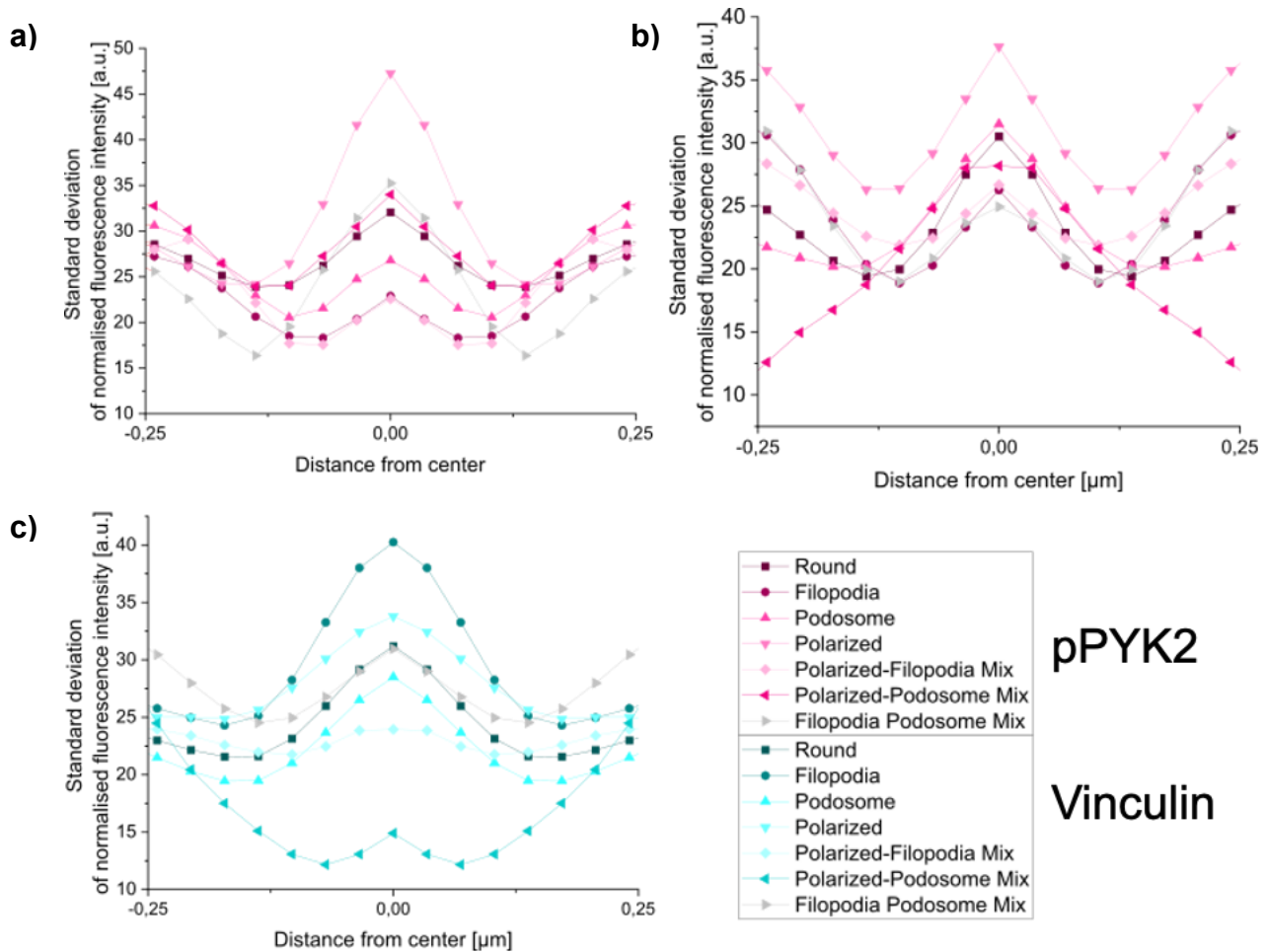
Figure 4.21 Standard deviation of normalized fluorescence intensity in radial intensity profiles of pPYK2 and vinculin according to phenotype *The standard deviation in plotted against the distance from PLS center according to the respective radial intensity profiles. Depicted is the distance between 250 nm from the center in each direction.* ***a)*** *Standard deviation of pPYK2 from data set of colabelling with paxillin;* ***b)*** *Standard deviation of pPYK2 from data set of colabelling with vinculin;* ***c)*** *Standard deviation of vinculin.*

4.4.3.1.   Comparing spatial distribution of podosome-CAAM in PLS of HSPC with different phenotypes utilizing FWHM

In order to compare the distribution of pPYK2, paxillin and vinculin around F-actin puncta statistically between phenotypes, the radial intensity profiles of adherent HSPC are submitted to Gauss fitting. The FWHM is used to compare the spatial distribution of the molecules of interest as depicted in Figure 4.22 and Figure 4.23. Statistical significance is then tested via One-Way Anova with Tukey test.
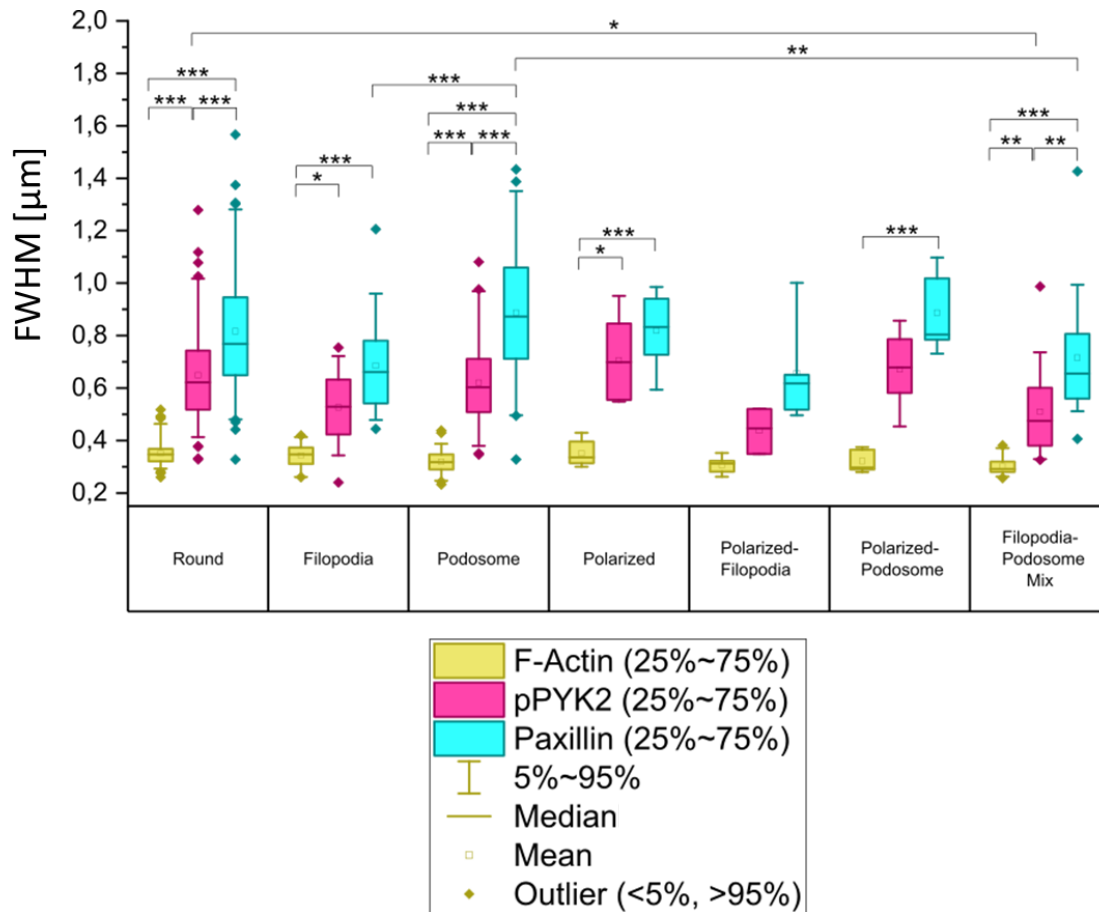
Figure 4.22 FWHM of F-Actin, pPYK2 and paxillin radial intensity profile per HSPC phenotype
Depicted are boxplots of the FWHM data of each radial intensity profile of individual cells. Data is grouped into the respective phenotype of each cell. Boxes mark the 25-75 percentile range of data sets for F-actin (yellow), pPYK2 (magenta) and paxillin (turquoise). Whiskers label the 5-95 percentile range of data sets. Lines mark the median of data sets, squares label the mean and diamonds show outlying data points of the 5-95 percentile range. Statistical analysis with One-Way Anova with Tukey test. Conditions are marked with asterisks to indicate significant differences in same groups or between identical molecules between groups (*: p≤0,05; **: p≤0,01; ***: p≤0,001; full statistical analysis in Digital Appendix). Data corresponds to Figure 4.17; n=249 HSPC from N=3 independent cord blood donors (#117, #143, #153).
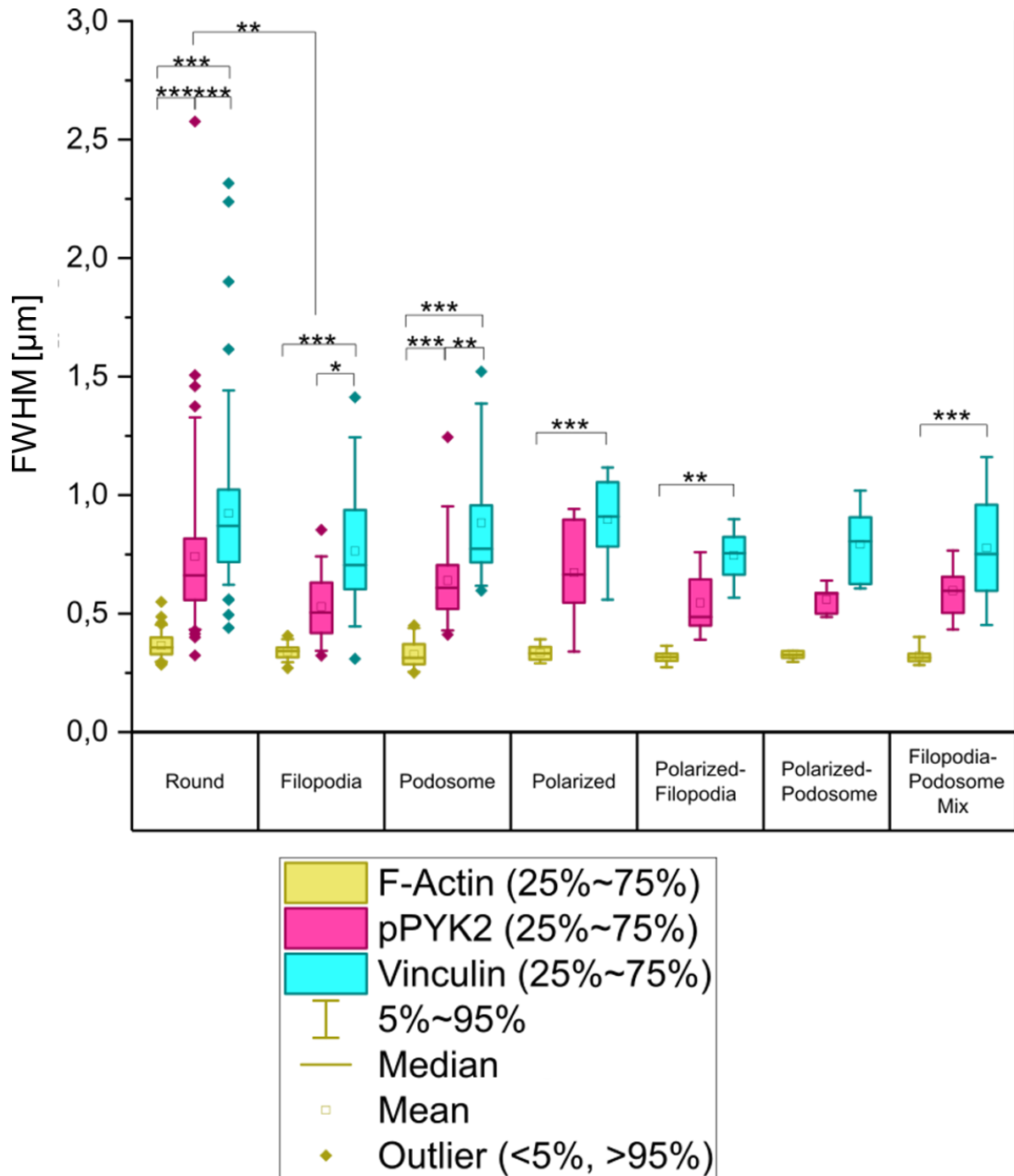
Figure 4.23 FWHM of F-Actin, pPYK2 and vinculin radial intensity profile per HSPC phenotype
Depicted are boxplots of the FWHM data of each radial intensity profile of individual cells. Data is grouped into the respective phenotype of each cell. Boxes mark the 25-75 percentile range of data sets for F-actin (yellow), pPYK2 (magenta) and paxillin (turquoise). Whiskers label the 5-95 percentile range of data sets. Lines mark the median of data sets, squares label the mean and diamonds show outlying data points of the 5-95 percentile range. Statistical analysis with One-Way Anova with Tukey test. Conditions are marked with asterisks to indicate significant differences in same groups or between identical molecules between groups (*: p≤0,05; **: p≤0,01; ***: p≤0,001; full statistical analysis in Digital Appendix). Data corresponds to Figure 4.18, n=233 HSPC from N=3 independent donors (#117, #143, #153).

Analysis of FWHM data reveals that all identified F-actin puncta display approximately the same size. FWHM of all F-actin data points are roughly 330 nm and no significant variance of this value between phenotypes is observed. Additionally, all FWHM of pPYK2, paxillin and vinculin are higher in comparison to the respective values of F-actin for all phenotypes (see Figure 4.22, Figure 4.23).

pPYK2 displays FWHM in its radial intensity profile that is generally lower in phenotype groups where cells present filopodia. The pPYK2 FWHM is significantly higher than F-actin FWHM in cells with round and podosome phenotypes in both datasets displayed (see Figure 4.22, Figure 4.23). In one of the presented datasets concerning pPYK2 (see Figure 4.22) there are also significantly higher FWHM values of pPYK2 compared to F-actin in groups with the filopodia, polarized and filopodia-podosome mix phenotypes. The p-value of these significant findings in the last three groups, however, is higher than in groups with round and podosome phenotypes. In each of the two presented datasets, the spatial distribution of pPYK2 around F-actin puncta is significantly higher in round phenotype HSPC than in filopodia phenotypes according to FWHM values (see Figure 4.23) and filopodia-podosome mix phenotypes respectively (see Figure 4.22). The p-value of these statistical findings is higher in phenotypes containing polarized morphology cells (filopodia-podosome mix phenotype).

FWHM of paxillin appears to be generally lower in groups of cells displaying filopodia morphology, as is the case for pPYK2 as well. Paxillin FWHM are significantly higher than the F-actin FWHM in all presented phenotype groups, except for the polarized-filopodia mix phenotyped cells, where no statistical significance can be detected (see Figure 4.22). Spatial distribution of paxillin around the PLS is significantly higher than that of pPYK2 in round, podosome and filopodia-podosome mix phenotypes. The p-value of this significant finding is higher concerning filopodia-podosome mix phenotypes. In cells of the podosome phenotype paxillin has a significantly higher FWHM than it does for cells of filopodia and filopodia-podosome mix groups. Again, the p-value of these findings is higher for cells with filopodia-podosome mix phenotype.

The FWHM values of the radial intensity profiles of vinculin are marginally lower for groups of cells with filopodia morphology. FWHM values of vinculin is significantly higher compared to F-actin in all phenotype groups, except for the polarized-podosome mix phenotype. p-value of this significance is higher for the polarized-filopodia

phenotype. FWHM values of vinculin are significantly higher than for pPYK2 in groups where cells display round morphology (round, filopodia, podosome phenotypes). The p-value of these findings are the lowest for the round phenotype group, higher in the podosome phenotype group and the highest in the filopodia phenotype group.

Analysis of the FWHM values shows in summary, that pPYK2 is distributed more broadly around F-actin spots of PLS, with paxillin and vinculin spanning even more broadly beyond pPYK2. This distribution is shown to be highly significant for the round and podosome phenotype groups.

## 4.5. Differentiation status of adherent HSPC

As the CD34$^+$ cell population isolated from UCB is still heterogeneous regarding the differentiation status of cells, immunofluorescent visualization of the progenitor markers CD38, CD33 and CD45RA is performed, with the aim of assessing which progenitor population the different, adherent cells belong to. This is based on the fact that certain surface markers start to emerge as the stem cell commits to certain lineages in hematopoiesis (see 1.1.1). This means that CD38$^-$CD45RA$^-$/CD33$^-$ cells are expected to be the early HSC and MPP. CD38$^+$CD45RA$^-$/CD33$^+$ are labelling myeloid lineage, while CD38$^-$CD45RA$^+$ are indicating commitment to lymphoid lineage. Lastly CD38$^+$CD45RA$^+$ cells are expected to belong to the GMP population (see Figure 4.24). It is then assessed whether cell populations of a certain differentiation state also display different morphologies. Exemplary images, including controls, of these stainings are depicted in the Appendix (Figure A.7, Figure A.8).

4.5.1. Assigning progenitor marker descriptors to adherent HSPC

Immediately after cord blood isolation of CD34$^+$ cells, the distribution of the analyzed progenitor markers is assessed via flow cytometry (see 3.1.3.1, 3.1.4). As depicted in Figure 4.24 for a representative UCB donor, over 90 % of the isolated HSPC are positive for the respective markers (full marker distribution for all donors can be found in Figure A.6). However, the observed markers are produced in varying levels across the total cell population. Especially in case of CD45RA two populations of positive cells are observed (see Figure 4.24).

For this reason, after letting HSPC adhere to FN, submitting them to IF staining of progenitor markers and assigning morphology descriptors (see 4.1.1) the cells are also assigned a progenitor marker descriptor to reflect how strongly a marker is produced by each single cell. For this, the CTCF is determined for IF staining of CD38, CD33 and CD45RA respectively (see 3.3.5). By referencing back to the distribution of markers according to flow cytometry (Figure 4.25, Table 4.4 and Figure A.6) CTCF values defining marker production strength are assigned. The median of the CTCF for each marker in each donor was determined. As the median marks the 50 percentile of the population, the CTCF value marking the percentile range of negative cells is then determined from the median by rule of three (for reference of negative populations size see Figure A.6). The positive cells are then split into two groups for CD33 and CD45RA according to the size of positive populations observed in flow cytometry (see Table 4.4 and Figure A.6). Since CD38 production strength seems to be spread homogenously between the cells, four equally large populations are separated. The CTCF boundary values for all these positive groups is also determined by using the median and the rule of three (see Table 4.5). Lastly, since cut off values all fall in roughly the same range for each progenitor marker respectively, the mean is taken from cut off values of each cord blood donor and rounded, to make results comparable. The only exception is CD33, where the CTCF value determining CD33$^-$ cells is defined by the value for donor #117 alone to account for the large number of negative cells in this donor. The boundary CTCF values are listed in Table 4.5 and a schematic depiction of the assignment process can be found in Figure 4.25.
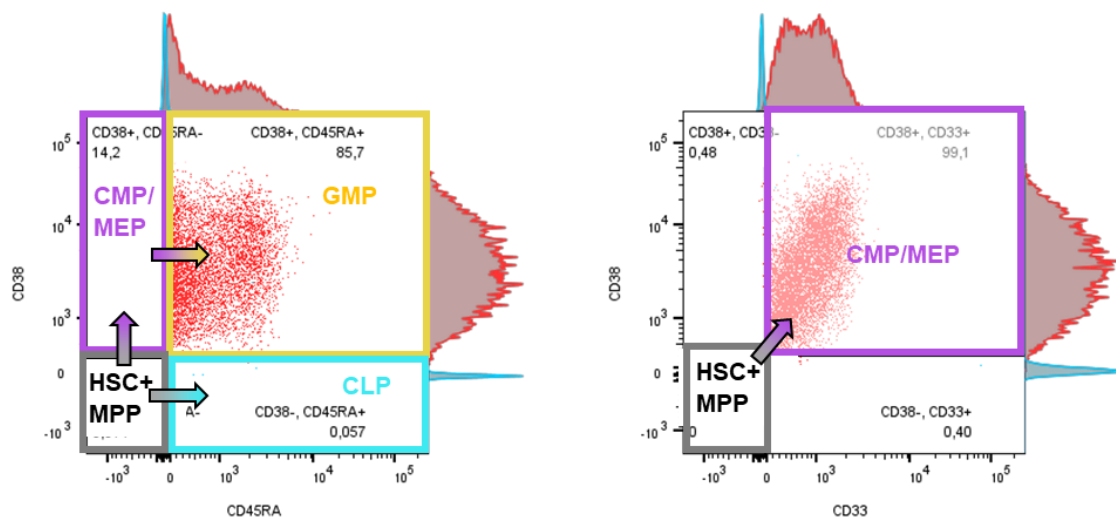
Figure 4.24 Distribution of progenitor marker presence on CD34⁺ HSPC isolated from UCB and schematic depiction of according lineage population assignment. *Shown are dot blots of single events in flow cytometry. Events are distributed according to strength of CD38 production (y-axis) and CD45RA/CD33 production (x-axis). Respective histograms of the single markers are shown above and on the right side of the diagram in red. Blue populations are the isotype controls. Negative and positive populations of analyzed markers are separated according to isotype-control carried out in flow cytometry. This splits the entirety of measured events into quadrants representing the following subpopulations: CD38⁻CD45RA⁻/CD33⁻ = HSC and MPP (grey), CD38⁺CD45RA⁻/CD33⁺ = CMP/MEP (violet), CD38⁻CD45RA⁺ = CLP (turquoise), CD38⁺CD45RA⁺ = GMP (yellow). Differentiation occurs gradually (represented by arrows). The population size in percentage is indicated within the quadrants. Marker distribution is representative of all cells of donors analyzed in this way (cells of n=3 independent cord blood donors (#117, #143, #153)).*
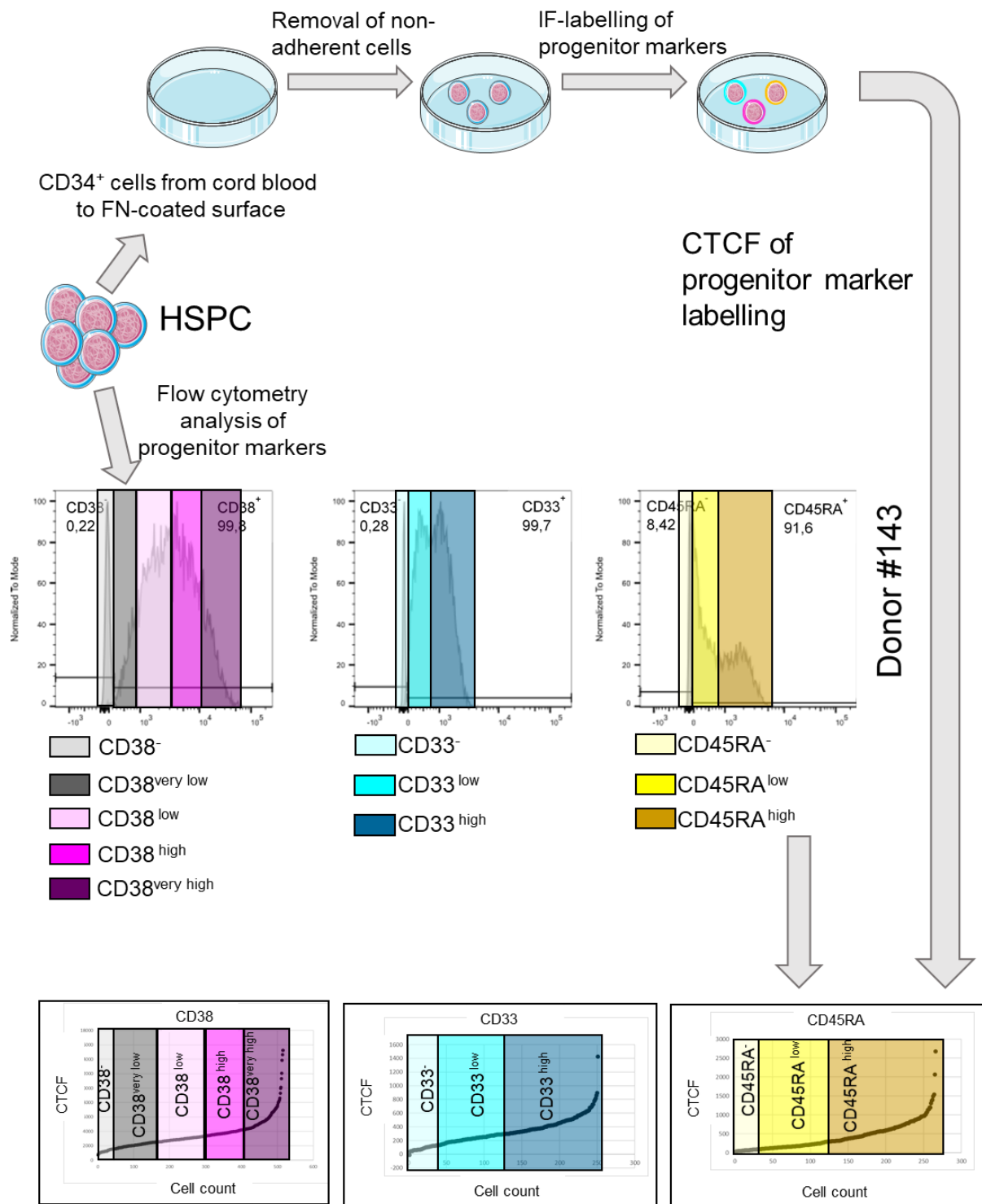
Figure 4.25 Schematic depiction of the assignment process of progenitor marker descriptors.
CD34⁺ cells from UCB are submitted to a FN-coated surface, followed by IF labelling of progenitor marker after adhesion. The marker presence is also assessed via flow cytometry. Flow cytometry data is used to assess population size of cells negative for markers, or with low/high marker levels. CTCF values are gathered from individual cells after IF labelling. The population size resulting from flow cytometry analysis is carried over to CTCF values utilizing the median of CTCF and rule of three.

Table 4.4 Percentile range of HSPC populations with varying progenitor marker levels Population sizes are assessed via flow cytometry for each donor respectively. Populations of positive cells were split into sub-populations of low and high levels of progenitor markers, according to the distribution observed in flow cytometry.

| Marker Descriptor	Corresponding percentile range of total population		
	Donor #117	Donor #143	Donor #153
CD38^{-}	0-1,48 %	0-0,22 %	0-1,66 %
CD38[very low]	1,48-24,69 %	0,22-24,95 %	1,66-24,59 %
CD38^{low}	24,69-49,26 %	24,95-49,89 %	24,59-49,17 %
CD38^{high}	49,26-73,89 %	49,89-74,84 %	49,17-73,76 %
CD38[very high]	73,89-100 %	74,84-100 %	73,76-100 %
CD33^{-}	0-34,7 %	0-0,28 %	0-5,24 %
CD33^{low}	34,7-65,4 %	0,28-43,5 %	5,24-81,9 %
CD33^{high}	65,4-100 %	43,5-100 %	81,9-100 %
CD45RA^{-}	0-3,22 %	0-8,35 %	0-6,36 %
CD45RA^{low}	3,22-41,7 %	8,35-63,2 %	6,36-55,5 %
CD45RA^{high}	41,7-100 %	63,2-100 %	55,5-100 %

Table 4.5 CTCF cut-off values for assignment of progenitor marker descriptors Listed are the CTCF values determined for each individual cord blood donor with respect to the percentile range of total population. Cut-off values were assigned by determining the CTCF value marking the respective percentile utilizing median and rule of three. The cut-off values that are applied for the final assignment are listed in the last column.

Marker Descriptor	CTCF Cut-off values			
	Donor #117	Donor #143	Donor #153	**All**
CD38^{-}	<90	<17	<94	**<65**
CD38[very low]	<1495	<1966	<1399	**<1620**
CD38^{low}	<2991	<3932	<2798	**<3240**
CD38^{high}	<4486	<5898	<4197	**<4860**
CD38[very high]	>4486	>5898	>4197	**>4860**
CD33^{-}	<151	<3	<31	**<150**
CD33^{low}	<284	<397	<484	**<440**
CD33^{high}	>284	>397	>484	**>440**
CD45RA^{-}	<23	<44	<38	**<35**
CD45RA^{low}	<297	<335	<329	**<320**
CD45RA^{high}	>297	>335	>329	**>320**

4.5.2. Distribution of progenitor marker populations in adherent HSPC

Since CD38 is immunofluorescently visualized alongside CD33 and CD45RA respectively, statements of the co-production of these markers and their respective levels according to progenitor marker descriptors can be made (see Figure 4.26, Figure 4.27). The largest cell populations are CD38^{low}CD33^{low} and CD38^{low}CD45RA^{low}, with 38.6 % and 27.1 % respectively. Additionally, the production of CD33 seems to rise with the production of CD38. This is indicated by 0 % of CD33^{high} cells being present in the CD38[very low] population. Then the percentage of CD33^{high} cells grows from 8 % of

CD38^{low} cells to 41.5 % of CD38^{high} cells to 76 % of CD38$^{very\ high}$ cell populations. Similar observations can be made for CD45RA. Here the percentage of CD45RA^{high} cells grows from 32 % to 34 %, 59 % and 67 % of the populations of CD38$^{very\ low}$, CD38^{low}, CD38^{high} and CD38$^{very\ high}$ respectively.
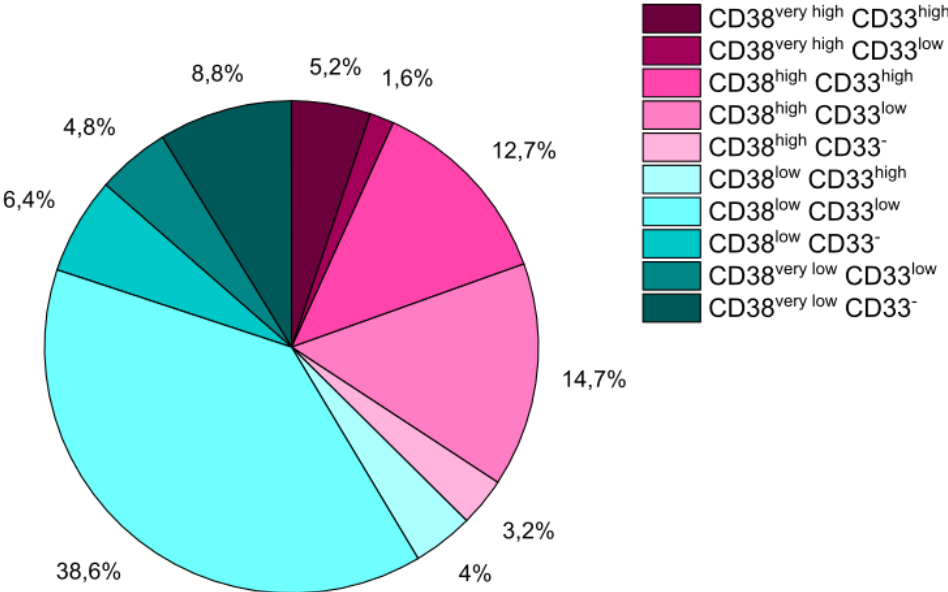
Figure 4.26 Distribution of cell populations with CD38CD33 marker at different levels in adherent HSPC *Shown is a pie-chart of the distribution of cell populations with different CD38-CD33 marker levels according to the assigned marker progenitor markers descriptors. Cells are left to adhere to FN for 1 h before being submitted to immunofluorescence staining. Differentiation marker descriptors for CD38 and CD33 are assigned to each cell according to CTCF in the respective channels. Data gathered from n=249 HSPC from N=3 independent donors (#117, #143, #153).*
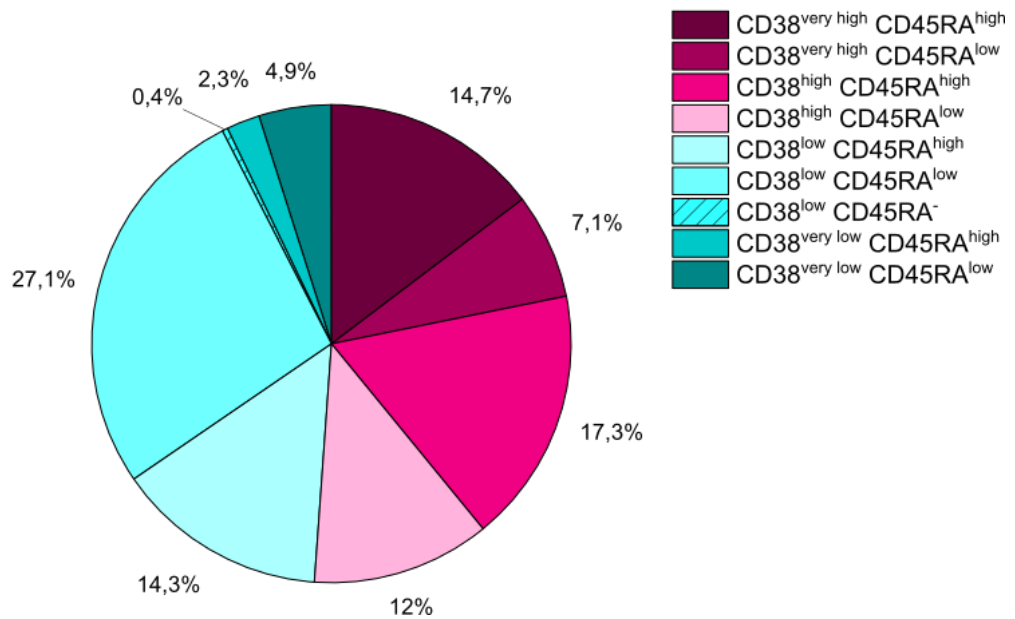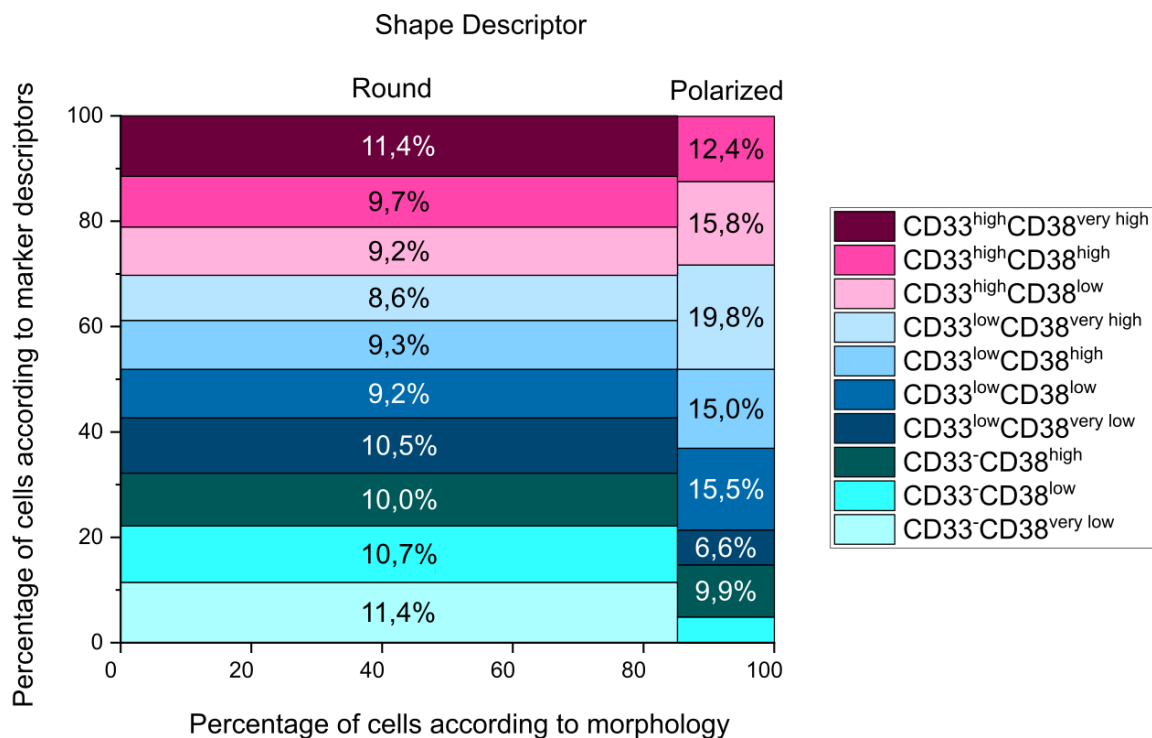
Figure 4.27 Distribution of cell populations with CD38CD45RA marker at different levels in adherent HSPC *Shown is a pie-chart of the distribution of cell populations with different CD38-CD45RA marker levels according to the assigned marker progenitor markers descriptors Cells are left to adhere to FN for 1 h before being submitted to immunofluorescence staining. Differentiation marker descriptors for CD38 and CD45RA are assigned to each cell according to CTCF in the respective channels. Data gathered from n=265 HSPC from N=3 independent donors (#117, #143, #153).*

4.5.3. Distribution of differentiation marker in adherent HSPC according to morphology

To determine whether a relation between HSPC differentiation status and cell morphology exists, progenitor marker populations per morphology are assessed. To analyze whether observations are significant across the entire analyzed cell population the C-M-H-Test is performed (see 3.4). Since some of the phenotype populations consists of only a few cells, it could lead to a miss of correlation that could otherwise be found, if statistics were performed between phenotypes. Therefore, the C-M-H-statistic was performed to find associations between morphology descriptors (as assigned in 4.1.1.1, 4.1.1.2, 4.1.1.3) and marker descriptors (as assigned in 4.1.1 and 4.5.1). Full overview of the C-M-H-statistic can be found in the Digital Appendix.

4.5.3.1. Relation between differentiation marker classes and shape descriptors

Looking at the distribution of CD38CD33 marker populations and CD38CD45RA marker populations in round HSPC all marker classes are rather equally distributed in this large group (see Figure 4.28, Figure 4.29). The overall size of the CD33$^-$ cell population is lower in polarized cells making up 14.9 % compared to 32.1 % in round cells. A decrease is also observed for the CD33^{high} populations, to a lesser extend though, as CD33^{high} population is 30.2 % in round cells and 28.2 % in polarized cells. The CD33^{low} population however increases in polarized cells by 19.3 % when compared to the round morphology group. When observing CD33 and CD38 co-production, CD38$^{very\ low}$ cell populations are smaller in polarized cells than in round cells. The percentage of CD38^{high} and CD38$^{very\ high}$ populations together are slightly larger (8.1 %) in polarized cells than in round cells. Other than that, when observed together with CD33, the CD38 marker populations do not seem to follow a specific trend (see Figure 4.28). The C-M-H-Test finds a weak significant association (p=0.024) between cell shape and CD33 marker proportions.

Figure 4.28 Mosaic Plot of CD38 and CD33 marker population distribution according to shape descriptor population. *Mosaic plot shows that polarized cells are made of a large population of cell producing low levels of CD33. Mosaic plot shows the percentage of marker populations in the total population of the specific shape descriptor in a stack diagram, non-labelled populations are <5 %. Bar width corresponds to population size of shape descriptor (n=212 round morphology cells and n=37 polarized morphology cells of N=3 independent cord blood donors (#117, #143, #153)).*

When assessing co-production of CD45RA with CD38, the CD38^{high} and CD38$^{very\ high}$ populations are more frequent in polarized HSPC than in cells with round morphology (magenta populations in Figure 4.29). CD38$^{very\ low}$ populations are absent in polarized cells as are CD45RA^{-} cells. CD38^{high} populations increase from 20.87 % in round cells to 32.55 % in polarized cells while CD38$^{very\ high}$ populations increase over two fold (19.51 % in round cells and 42.87 % in polarized cells). The CD38^{high} and CD38$^{very\ high}$ marker populations that also produce CD45RA^{low} slightly increase in polarized cells. CD38^{high} and CD38$^{very\ high}$ populations that also produce CD45RA^{low} do not increase as much in polarized cells in comparison to the respective CD45RA^{low} populations. The C-M-H-Test does not find any significant associations of CD38, CD45RA or their combinations and cell shape.
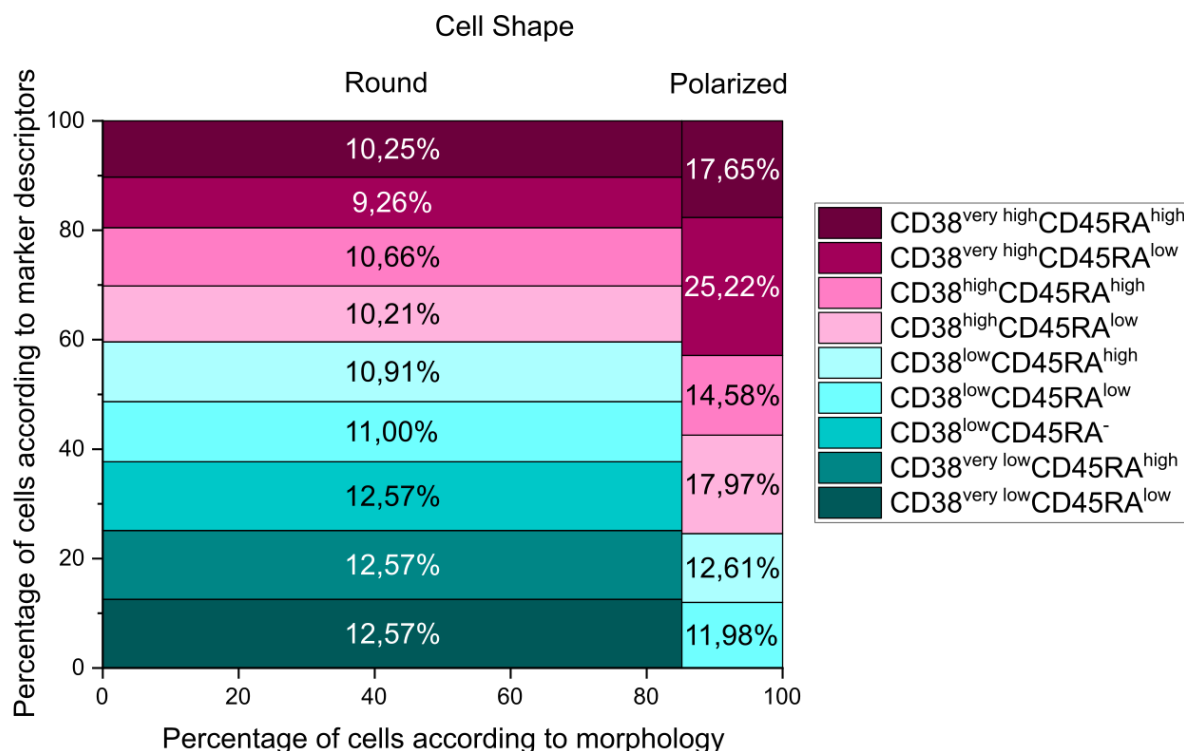
Figure 4.29 Mosaic Plot of CD38 and CD45RA marker population distribution according to shape descriptor population. *Polarized morphology cells are made from populations producing high levels of CD38. Mosaic plot shows the percentage of marker populations in the total population of the specific shape descriptor in a stack diagram, non-labelled populations are <5 %. Bar width corresponds to population size of shape descriptor (n=226 round morphology cells and n=39 polarized morphology cells from N=3 independent cord blood donors (#117, #143, #153)).*

Overall, regarding cell shape, cells that produce low levels of CD33 more often take on a polarized cell shape. Moreover, a weak significance between CD33 marker descriptor and cell shape is found. While there is no significant correlation between CD38 and CD45RA level and cell shape, cells with high levels of these markers display polarized cell morphology in higher numbers compared to cells of round shape.

4.5.3.2. Relation between differentiation marker classes and filopodia presence

The distribution of CD38, CD33 and CD45RA populations and their combinations are observed relatively evenly in HSPC without filopodia. The cell populations with the CD38high marker descriptor more than double in size in cells with filopodia morphology compared to cells not displaying filopodia morphology (see Figure 4.30 a)). Additionally, the CD33low populations grow from 37.2 % in cells without filopodia to 49.1 % in cells with filopodia and thus represent almost half of the cells in this group

(see Figure 4.30 b), blue populations). Conforming to these observations, the CD38^{high}CD33^{low} population makes up the largest in cells with filopodia. Also, in the CD38^{low} and CD38$^{very\ low}$ populations CD33$^-$ cells decrease by more than 2-fold when filopodia are observed, while the CD38^{high}CD33$^-$ population doubles in size as mentioned above. C-M-H-Test finds a highly significant association between presence/absence of filopodia and CD33/CD38 marker classes plus their combinations. Specifically, the p value for association between filopodia and CD38 marker classes is 0.0001072; CD33 marker classes association yield a p value of 0,002354 and their combinations 0.002268.

In HSPC with filopodia morphology CD45RA$^-$ cells are not present at all compared to cells without filopodia morphology where they make up 14.1 %. This is the same for the CD45RA^{low}CD38$^{very\ low}$ population. On the contrary, the populations of CD45RA^{low}CD38$^{high/very\ high}$ and CD45RA^{high}CD38$^{very\ high}$ cells all more than double in size when cells display filopodia morphology (see all Figure 4.31). However, C-M-H-Test results only show a very weak association between CD45RA marker classes and filopodia presence/absence, with p=0.04955.

To summarize, a large population in cells with filopodia morphology produce either low levels of CD45RA and CD38 or the highest levels of these two markers found in adherent cells. Cells that do not produce CD45RA do not seem to form filopodia. Only a weak significant association between CD45RA and filopodia morphology is found. Additionally, the cell populations that show filopodia morphology are in large parts producing CD38 in high levels while not producing CD33. A highly significant correlation is found between the filopodia morphology and the production of these two markers
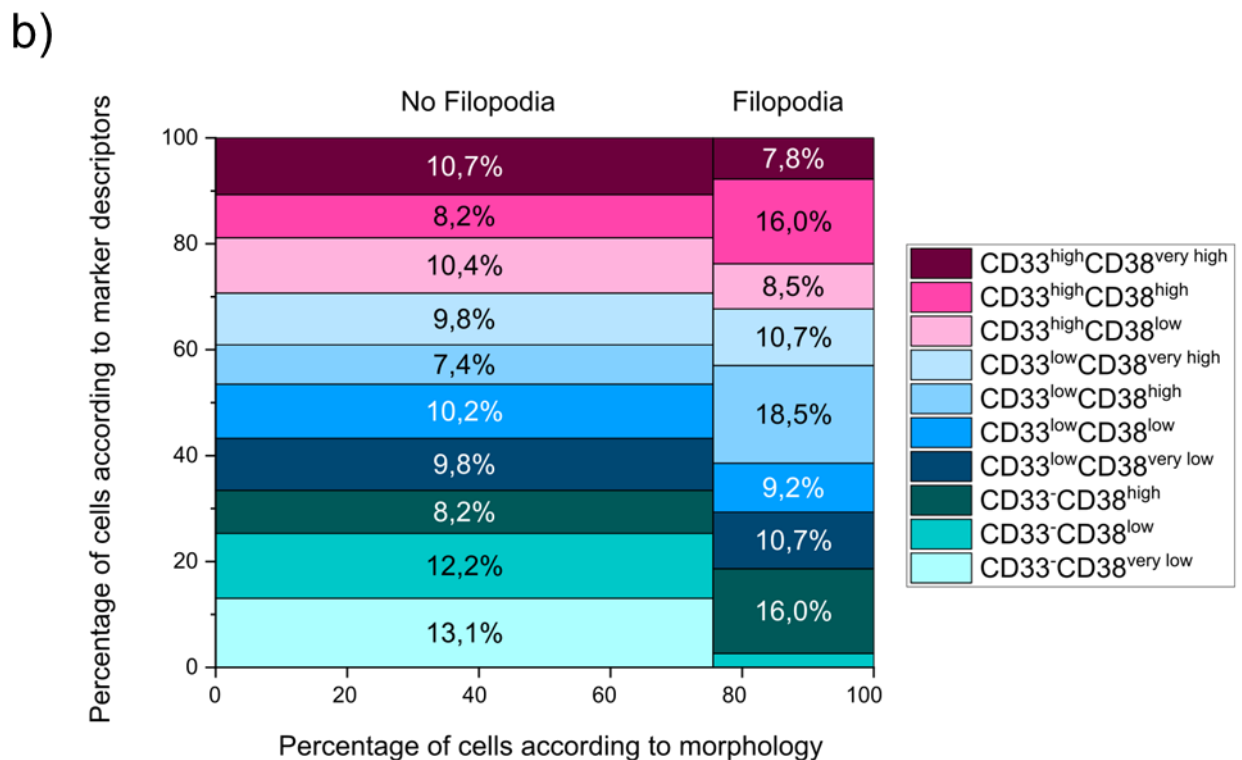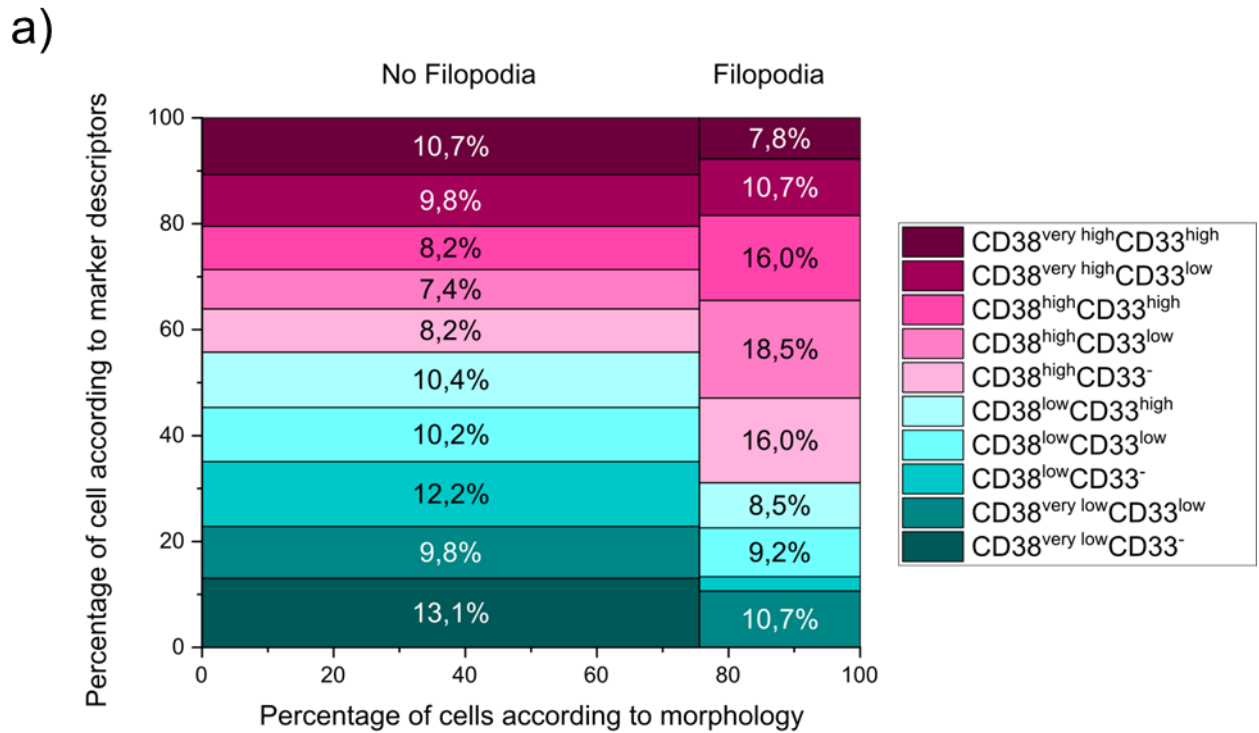
Figure 4.30 Mosaic Plot of CD38 and CD33 marker population distribution according to filopodia descriptor population. *Cells with filopodia morphology produce higher levels of CD38 and CD33 compared to cells without filopodia morphology. Mosaic plot shows the percentage of marker class populations in total population with and without filopodia, non-labelled populations are <5 %. Bar width corresponds to population size with and without filopodia (n=188 cells without filopodia morphology and n=61 cell with filopodia morphology from N=3 independent cord blood donors (#117, #143, #153)).* ***a)*** *and* ***b)*** *depict the same data sets but sorted and colored with emphasis on the two markers CD38 and CD33 respectively for clarity and readers convenience.*
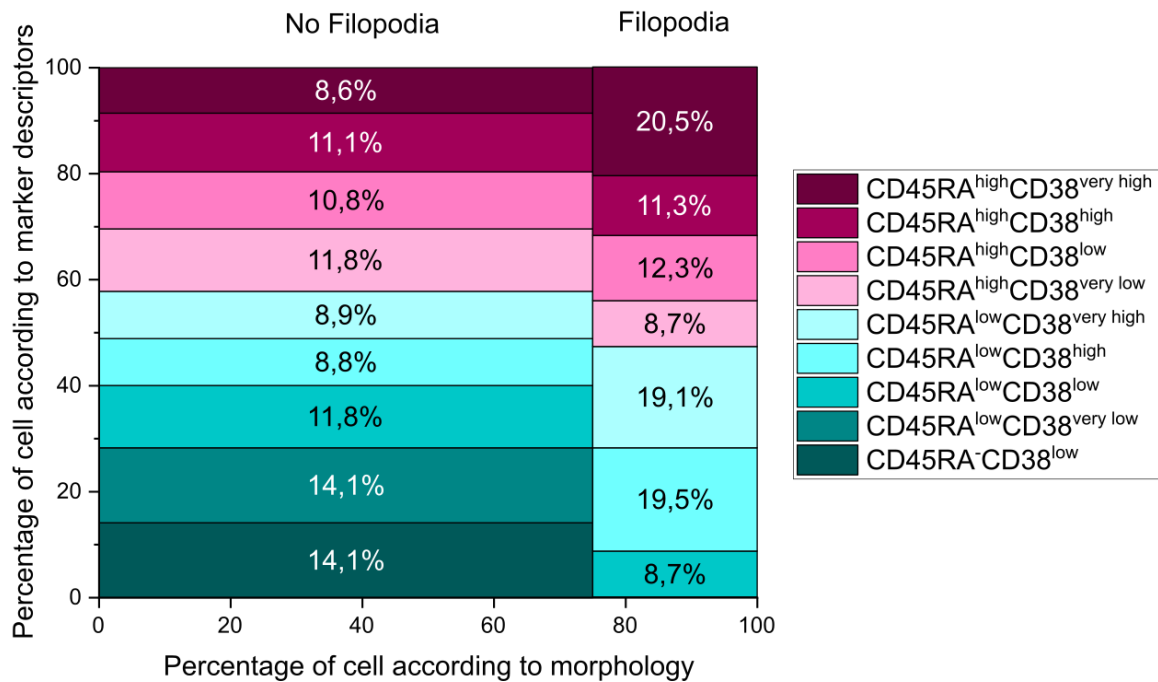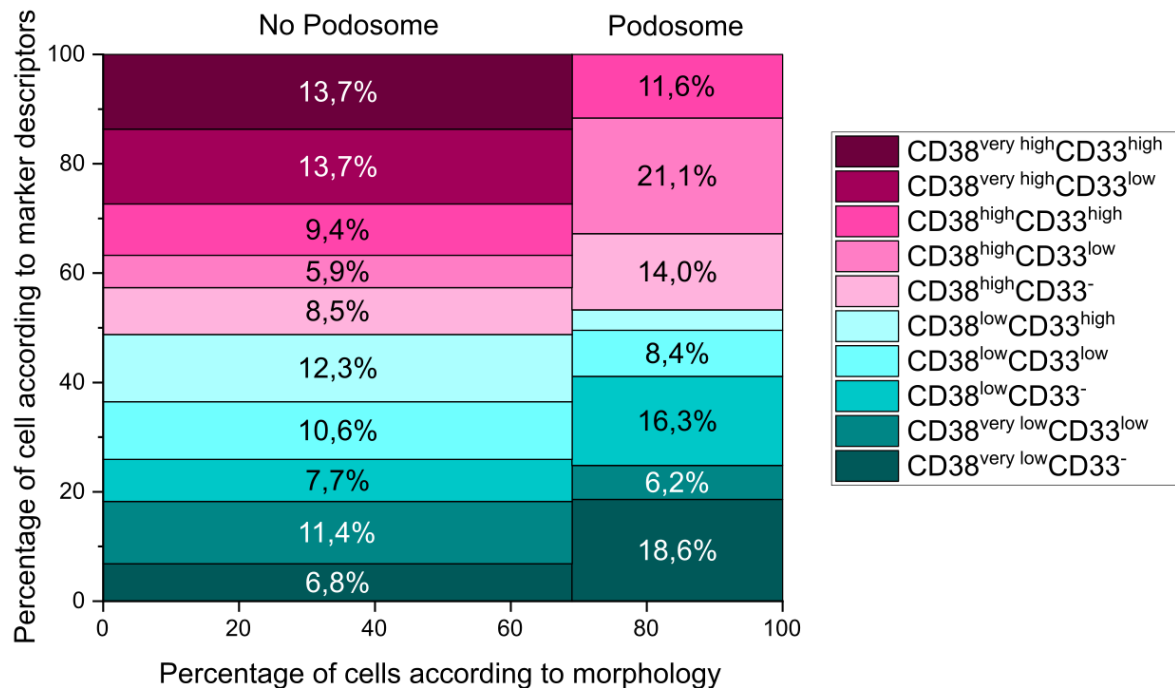
Figure 4.31 Mosaic Plot of CD38 and CD45RA marker population distribution according to filopodia descriptor population. *Cells producing higher levels of CD45RA more often take in the filopodia morphology. Mosaic plot shows the percentage of marker class populations in total population with and without filopodia, non-labelled populations are <5 %. Bar width corresponds to population size with and without filopodia (n=199 cells without filopodia morphology and n=66 cell with filopodia morphology from N=3 independent cord blood donors (#117, #143, #153)).*

4.5.3.3. Relation between differentiation marker classes and podosome presence

Analyzing the association between differentiation marker descriptor and podosome presence/absence it has to be mentioned, that there is a variance between the population size of HSPC with podosome morphology in the two IF staining sets carried across each donor (note bar sizes in Figure 4.32 and Figure 4.33). In cells with podosome morphology the populations of CD38$^{very\ high}$CD33$^{low/high}$ are not present (Figure 4.32, dark magenta groups), though they are the biggest populations in cells without podosome morphology. This is contrasted to the CD38$^{very\ high}$ populations displayed in Figure 4.33 that are not influenced by podosome presence/absence. On the contrary, the smallest population in cells without podosome morphology, the CD33^{-} cell population in total, is the largest population in cells with podosome morphology. Additionally, CD38^{high} populations are larger in cells with podosome morphology compared to cells without. However, overall the total percentage of CD38$^{low/very\ low}$ populations are larger in podosome morphology HSPC (all see Figure 4.32). C-M-H-

Test finds significant correlation between and CD38 and CD38CD33 combination markers and podosome presence/absence (p=0.005446 and p=0.03747 respectively).

***Figure 4.32 Mosaic Plot of CD38 and CD33 marker population distribution according to podosome descriptor population.** Mosaic plot shows that cells with podosome morphology are producing less CD38 and CD33 than cells without podosome morphology. Mosaic plot shows the percentage of marker class populations in total population with and without podosomes, non-labelled populations are <5 %. Bar width corresponds to population size with and without podosomes (n=172 cells without podosome morphology and n=77 cells with podosome morphology from N=3 independent cord blood donors (#117, #143, #153)).*

The CD45RA$^-$ population is the largest in cells without podosome morphology, but is absent in HSPC with podosome morphology. On the contrary, the smallest population in cells without podosomes morphology, the CD38$^{very\ low}$ cells, become the largest in cells with podosome morphology, almost increasing threefold. The residual populations do not vary upon podosome presence/absence. The C-M-H-Test does not find an association between CD38, CD45RA or their combinations in this data set (Figure 4.33).

On the basis of these results, the cells that display podosome morphology are, in large part, not producing CD33 and produce CD38 at lower levels compared to cells not assembling PLS. All cells with this morphology seem to produce CD45RA in varying levels.
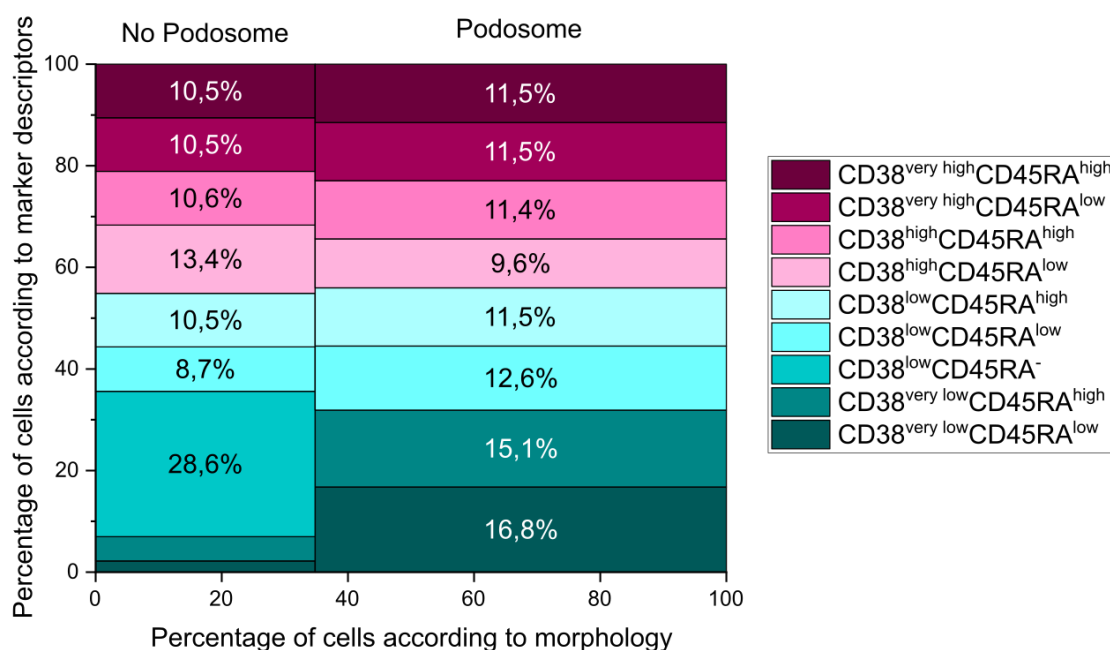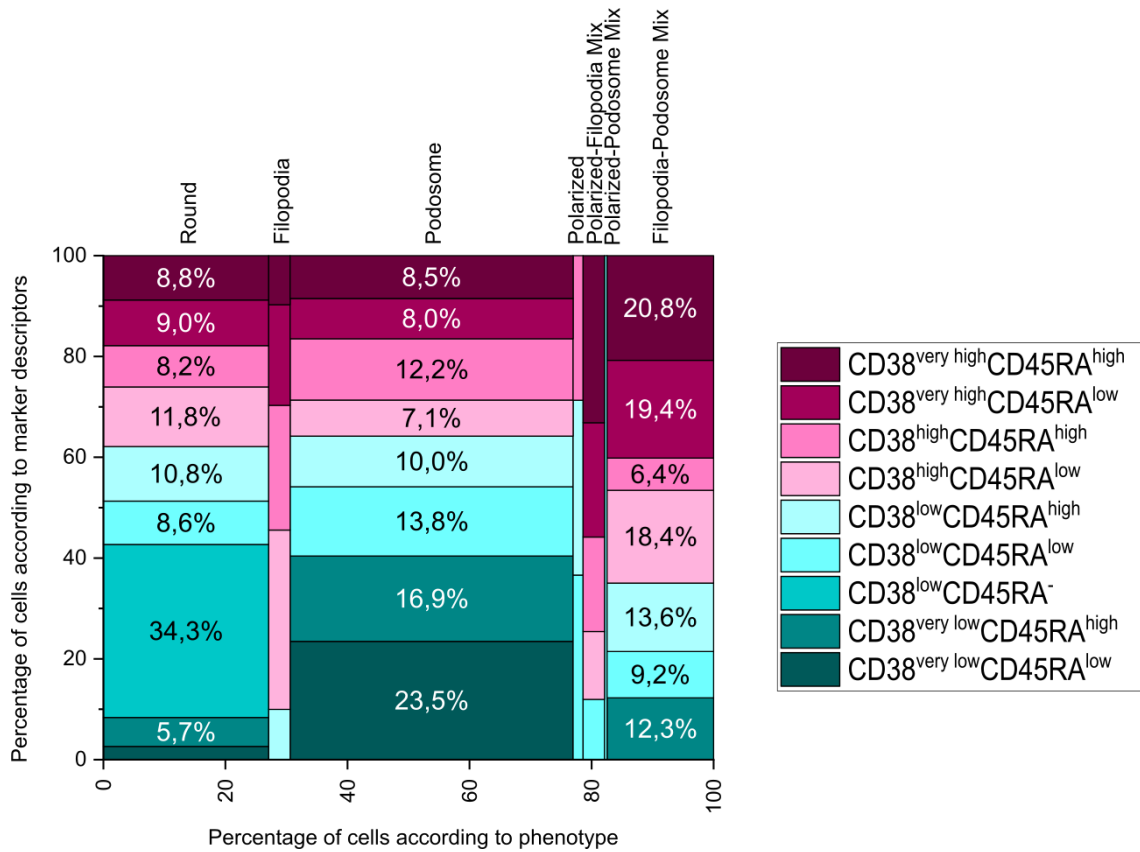
Figure 4.33 Mosaic Plot of CD38 and CD45RA marker population distribution according to podosome descriptor population. *Mosaic plot shows a large population of CD45RA⁻ cells in cells without podosome morphology. Mosaic plot shows the percentage of marker class populations in total population with and without podosomes, non-labelled populations are <5 %. Bar width corresponds to population size with and without podosomes (n=92 cells without podosome morphology and n=173 cells with podosome morphology from N=3 independent cord blood donors (#117, #143, #153)).*

4.5.3.4.   Distribution of differentiation marker populations across adherent HSPC phenotypes

Comparing the distribution of CD38, CD33 and CD45RA marker populations across phenotypes (as assigned in 4.1.1) three major observations can be made. First, in adherent HSPC with the filopodia morphology, the CD38$^{high/very\ high}$ populations are making up over the half of the total cell number (see both Figure 4.34 and Figure 4.35). Second, the CD33 populations differ greatly between HSPC with and without podosome morphology. In cells with podosome morphology the CD33⁻CD38$^{low/very\ low}$ populations are larger compared to phenotypes without podosome morphology. This observation can also be made for the CD33^{low}CD38^{high} population in the podosome phenotype, though this population is even larger in HSPC with the filopodia-podosome phenotype (Figure 4.34). Lastly, regarding CD45RA populations, it stands out, that CD45RA⁻ cells are only present in round phenotype cells. Also CD38$^{very\ low}$CD45RA$^{low/high}$ populations make up 40.4 % of total cells in HSPC with the podosome phenotype (Figure 4.35).
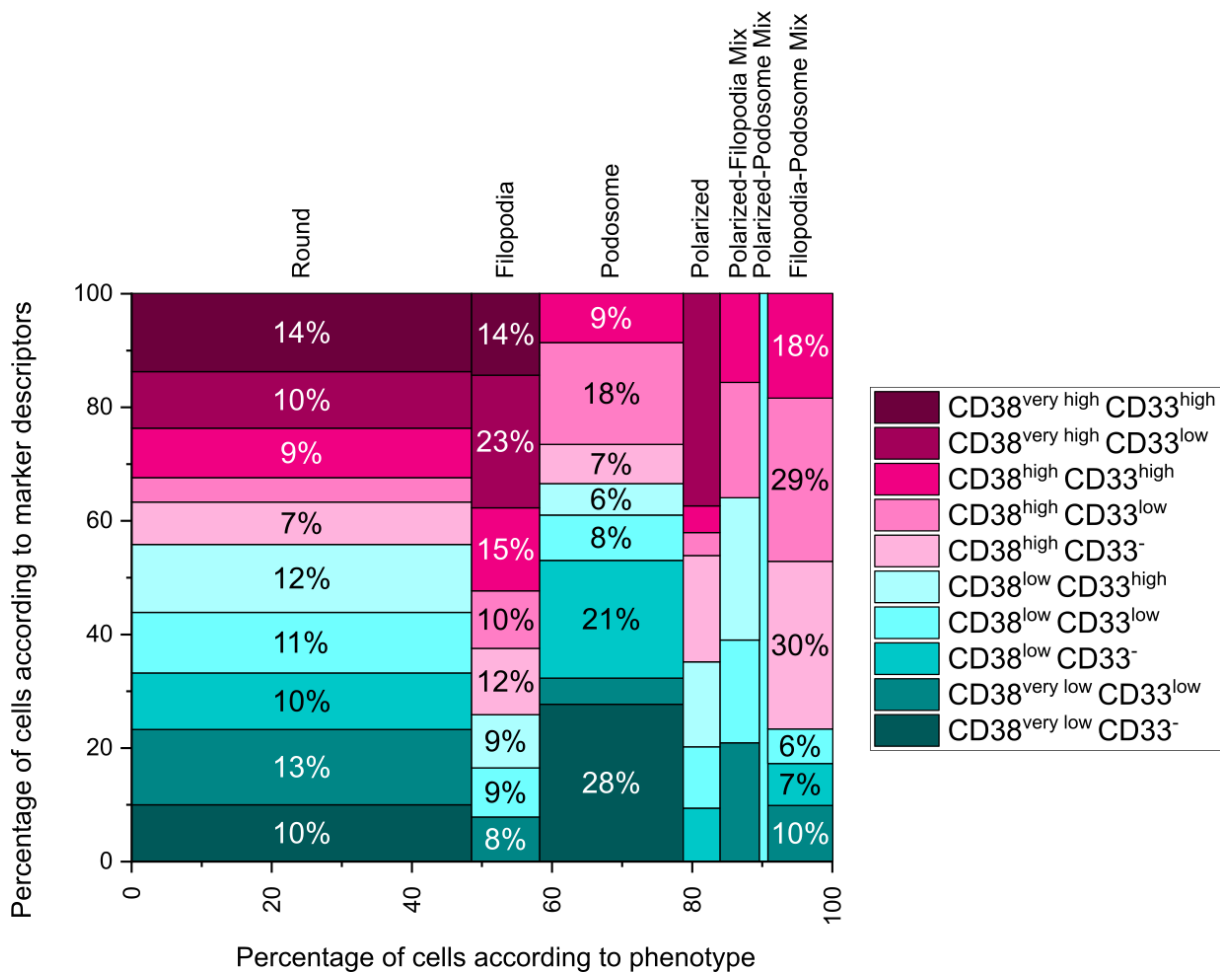
Figure 4.34 Mosaic Plot of CD38 and CD33 marker population distribution according to phenotype. *Mosaic plot shows large populations of CD38$^{high/very\ high}$ cells in phenotypes with filopodia morphology, while CD33$^-$ cells increase in the podosome phenotype cells. Mosaic plot shows the percentage of marker class populations in total population per phenotype, non-labelled populations are <5 %. Bar width corresponds to population size of phenotypes (n=121 cells with round phenotype, n=62 cells with filopodia phenotype, n=78 cells with podosome phenotype, n=30 cell with polarized phenotype, n=14 cells with polarized-filopodia phenotype, n=3 cells with polarized-podosome mix phenotype and n=22 filopodia-podosome mix phenotype from N=3 independent cord blood donors (#117, #143, #153)).*

***Figure 4.35 Mosaic Plot of CD38 and CD45RA marker population distribution according to
phenotype.*** *Mosaic plot shows large populations of CD38^high/very high^ cells in phenotypes with filopodia
morphology, while CD45RA^-^ cells are only present in the round phenotype cells. Mosaic plot shows
the percentage of marker class populations in total population per phenotype, non-labelled populations
are <5 %. Bar width corresponds to population size of phenotypes (n=70 cells with round phenotype,
n=63 cells with filopodia phenotype, n=174 cells with podosome phenotype, n=21 cells with polarized
phenotype, n=9 cells with polarized-filopodia mix phenotype, n=8 cells with polarized-podosome mix
phenotype and n=25 filopodia-podosome mix phenotype from N=3 indepenedent cord blood donors
(#117, #143, #153)).*

5. Discussion

The aim of the here presented work was to analyze the cell-matrix adhesion structures established by HSPC by obtaining high resolution images of said structures. For this purpose, FN was chosen as an adhesion substrate. FN is a prominent ECM molecule that is often used to study the adhesion behavior of HSPC (see 1.1.2.3). First, the overall adhesion behavior and morphology of adherent HSPC and presentation of CAAM were described and discussed. This leads to the analysis of PLS in these cells and their presentation compared to similar reported structures. Lastly, it was assessed whether cells of certain morphology or the assembly of certain structures correlates with a specific lineage determination in HSPC differentiation.

5.1. HSPC show dynamic adhesion behavior

Submitting HSPC to FN resulted in a dynamic behavior of the cells, in which some cells showed fast migration, while others retained in the same place. In agreement with these observations, IF staining of adherent HSPC made it clear, that adherent cells show a variety of different states regarding morphology and adhesion structure assembly. Varying display of migratory behavior and morphologies of HSPC have been shown before, however mostly in context of HSC-MSC contacts or under applied CXCL12 gradients (Bessy et al., 2021; Giebel, 2007; Reichert et al., 2015). In the work presented here, cells were allowed to adhere to FN. FN has been shown to play a significant role in HSPC homing, retention and proliferation (see 1.1.2.3). The ECM molecule is ubiquitously produced by the majority of BM niche cells. The response of HSPC to FN is receptor specific (Wirth et al., 2020). This is likely to modulate the observed heterogeneity of adherent HSPC. Moreover, the attachment behavior of HSPC and similar cells is often described as "semi-adherent", meaning that cells attach in culture but are not dependent on adhesion for maintenance (Daniel et al., 2016; Hümmer et al., 2019; Netsrithong et al., 2020; Oostendorp and Dörmer, 1997). Additionally, HSPC display lower adhesion forces than cells that are dependent on adhesion, as e.g. fibroblasts. Moreover, the adhesion strength of HSPC can vary according to the provided surroundings (Bushell et al., 1999; Reichert et al., 2015). As HSPC have to react to a variety of signaling cues from the niche *in vivo* to induce mobilization for differentiation while also maintaining secure anchorage in their niche,

this "semi-adherent" behavior seems to be by design (Mayani, 2019). This is further supported by the fact that anchoring and mobilization processes are tightly controlled *in vivo*, which is exploited in the context of transplantation (Fonseca et al., 2010). On top of these diverse influences on HSPC adhesion behavior, the CD34+ cell population isolated from cord blood is known to be quite heterogeneous, consisting of the very early LT/ST-HSC, MPP and lineage determined progenitors and also some cells of non-hematopoietic lineage (Brown et al., 1991; Fina et al., 1990; Sidney et al., 2014; Traycoff et al., 1994). This might further influence the heterogeneous display of adhesion behavior and morphology, that has been shown to be present under diverse conditions, as well as in the here presented work.

This circumstance makes it challenging to analyze the adhesion structures formed by HSPC, as the cells are present in an ensemble of morphologically states. Additionally, the structures possibly have a highly dynamic turnover, as some cells show the capacity to rapid migration. Thus, observed, adherent HSPC were grouped according to their morphology with the goal to characterize different states within this ensemble.

5.1.1. Adherent HSPC present different morphologies

The immunofluorescence images of cells were submitted to a phenotyping process to group them, according to their morphology and presence of filopodia and/or PLS (see 4.1.1). This method enabled to differentiate the cells in relation to each other, by referring to the most distinct representatives of certain morphologies. It must be noted that this method can be used to group the cells of the here presented populations but cannot, without alterations and adjustments, be used for cells and samples in different contexts.

By applying the knowledge of adhesion processes to the morphology observed within the HSPC in this work, the appointed phenotypes can be assumed to correspond to adhesion strength. Polarized cells, for a start, are likely to be more firmly attached to the matrix than round cells, since a polarized morphology usually correlates with cell migration (Ridley et al., 2003). Cell migration is facilitated by intracellularly generated forces that work against the matrix to keep the cell from detaching, thus forming a secure attachment (Fournier et al., 2010 and described under 1.2.1). Even stronger adhesion is likely present in cells with the arch morphology. In cells that classically

exhibit this morphology, like epithelial cells, the F-actin arches are part of an intricate contractile adhesion system, effectively generating force in the lamella of the cell and facilitating stretching, cell flattening and migration (Burnette et al., 2014). Cells that establish podosomes or FA also transmit force through these structures (Wang et al., 1993). However, while FA need the transmitted force for maturation and are transiently stable after formation (Hoffman, 2014), podosomes can form without force transmission and usually only have a half-life of 2-4 min (Pal et al., 2022). The attachment formed via FA can therefore be described as more sustainable.

While adhesion strength was not directly assessed within the here presented work, applying the known association between morphology and adhesion strength, the phenotypes can be organized in order of rising attachment strength as follows: round, podosome, filopodia, polarized, polarized-podosome, polarized-filopodia, podosome-filopodia, arch, arch-podosome, arch-podosome-filopodia. This order of phenotypes, containing mix-phenotypes to display transitionary stated, is assumed to represent the continuum of the dynamic adhesion behavior exhibited by HSPC.

Similarities in the distribution of phenotypes can be found across donors. The most striking similarity is the dominance of low-attachment phenotypes – such as round, podosome and filopodia phenotype cells – with filopodia type cells always representing the smallest fraction of these groups in adherent HSPC. Polarized morphology containing phenotypes only occurred in around 10 % of observed cells across donors and filopodia presence was more prevalent in these cells. The high presence of the podosome phenotype across the adherent HSPC is interesting since the ability to assemble PLS has only recently been reported upon stimulation of these cells with PMA by Rademakers et al. (2018). The same study suggested, that HSPC form PLS to cross the BM endothelium transcellularly in the homing process after transplantation, which would go in line with the matrix degrading properties of podosomes (Linder, 2007). However, the formation of PLS in HSPC that are in contact with endothelial cells has not been described. A variety of research has shown that majority of HSPC exhibit a polarized morphology upon contact with stromal cells or osteoblasts (Bessy et al., 2021; Fonseca et al., 2010) or under the influence of growth factors (Giebel et al., 2004), contrary to what is observed within the here presented work. The very same studies also display, that the fraction of polarized HSPC can vary greatly, upon the alteration of culture condition (supplements, supply-cell type, etc.). Additionally,

methods of assessment of polarized cells vary from observing accumulated proteins of interest in one cell side to localizing the centrosome in relation to the cell body. In the here presented work, cells were let to adhere to FN, in serum free conditions under the addition of divalent cations and polarization was determined by AR assessed via F-actin staining. Another source of variance between the observed cell phenotype fractions across donors is the variance between the cord blood donors themselves, that is also apparent in the here presented work. This is expected due to the heterogeneous nature of HSPC isolated from UCB, where a high donor variance is known (Belderbos et al., 2020). This heterogeneity might even be amplified here by the fact, that only a fraction of adherent cells was imaged and underwent the phenotyping process.

The high prevalence of low-attachment phenotypes is in line with the "semi-adherent" attachment behavior of HSPC since these adhesions are strong enough to withstand the shear forces generated by the washing step prior to cell fixation, while still being the phenotypes of lowest adhesion strength within the observed groups. The majority of round, PLS containing cells observed here promised to be an interesting subject in assessing how HSPC interact with their environment in order to maintain their stemness as per niche definition (Mayani, 2019).

5.1.2. Adherent HSPC present cell adhesion associated molecules with variance depending on morphology

During observation of cell morphology of adherent HSPC, PLS already emerged as adhesion sites of interest. Nevertheless, marker of other adhesion structures, like FA and invadopodia, were also analyzed to gather information on other potential adhesion structures in HSPC. Additionally, the CAAM chosen as markers for native and mature adhesion structures (see Table 4.3) mostly also play a role in overall adhesion (Albiges-Rizo et al., 2009; Eleniste and Bruzzaniti, 2012a; Hoshino et al., 2013). Experimental planning considered that the localization and spatial distribution of the markers was indicative of certain adhesion structures, not just presence alone. Another factor considered, is how the CAAM present in the context of other IF labelled proteins, especially F-actin. This also meant that additional information on the assembled structures could be gathered, as marker for specific adhesion structures could also be observed in context of F-actin structures with a differing architecture. The following

paragraphs describe and discuss the presentation of potential FA and invadopodia in the analyzed cells.

5.1.2.1.   Focal adhesion markers and HSPC

Common FA proteins, like vinculin and talin, have been shown to be important to HSC retention and repopulation (Ohmori et al., 2010). Yet, the establishment of FA in HSPC could not be observed until now. In order to analyze if HSPC form structures resembling FA, Arp3 and ASAP3 were visualized in the cells to label native and mature FA structures, respectively. Arp3 is a subunit of the Arp2/3 complex that plays an important role in actin branching and reassembly (Goley and Welch, 2006; Schafer et al., 1998). The Arp2/3 complex facilitates branching in early protrusions in the cell periphery but is not found in fully matured FA (DeMali et al., 2002a; Serrels et al., 2007). Overall, the presentation of Arp2/3 in adherent HSPC does not indicate formation of nascent FA, as it does not present in a way that would be expected for such structures. Arp3 staining is observed as faint spots across the ventral cell side. Occasionally, very strong Arp3 signals can be observed. The Arp3 signals do not accumulate along the cell periphery, as would be expected if FA were established. Especially in cells were filopodia can be observed, Arp3 is not found in the cell periphery. Interestingly, and against expectations, Arp3 signals do not colocalize with prominent F-actin structures, like spots or fibers. However the presence throughout the ventral cell side could stem from interaction with F-actin at points of branching as it resembles what was shown for this process in single molecule imaging of tobacco BY-2 cells (Fišerová et al., 2006; Smith et al., 2013, see Figure A.9).

The spatial distribution of Arp3 in z-direction of the adherent HSPC showed that protein levels were higher in dorsal cell regions. The reason for this could lie within the many cellular processes where Arp2/3 mediated actin branching is involved. These include – in addition to adhesion and formation of the structures involved therein - phagocytosis, endocytosis, exocytosis, organelle motility and intracellular trafficking (Goley and Welch, 2006).

The Arp2/3 complex is also enriched in the core of podosomes or invadopodia and crucial for their formation (Gimona et al., 2008; Hurst et al., 2004). In the here presented work, Arp3 was only faintly colocalized to F-actin spots, barely exceeding

the baseline signal (see Appendix Figure A.10). Arp3 is classically described as a podosome core-protein (van den Dries et al., 2019b). The presentation of Arp3 in the observed adherent HSPC PLS could indicate a reduced amount of branched F-actin in these structures. This could also be a first marker of the high dynamics of these structures, as will be discussed later, since Arp2/3-mediated branch-formation inhibits the polymerization and depolymerization of actin fiber-networks, thus lower amount of the Arp2/3 complex could enable expansion and reorganization of F-actin structures and networks (Liman et al., 2020). Another explanation for this unexpected presentation of Arp3 at PLS might lie in the strong presence of pPYK2 in these structures. Serrels et al. (2007) showed that the autophosphorylation of FAK is mutually exclusive to the binding of Arp3 with FAK. The process of autophosphorylation of FAK and release of Arp3 plays a role in the formation and maturing of adhesion structures at the nascent lamellipodium. Despite the homology found between the responsible FAK FERM-domain and the PYK2 FERM-domain, it is unclear if similar mechanisms regulate PYK2 function (Ceccarelli et al., 2006; Riggs et al., 2011). The Arp2/3 complex has a well described role in invadosomes (Albiges-Rizo et al., 2009; Goley and Welch, 2006). Given the identification of other CAAM in PLS within this work, that are in agreement with what is expected for podosome formation, these findings regarding Arp2/3 require further attention.

ASAP3 was used to test for the assembly of mature FA, as it colocalizes to paxillin and vinculin within these structures, but is not present in invadosomes (Albiges-Rizo et al., 2009). Within adherent HSPC, ASAP3 is ubiquitously present, but not found at the tip of filopodia, protrusions or F-actin fibers. This leads to the conclusion, that fully matured FA are not assembled by HSPC, which complements the previously made observations of few filopodia being present in adherent cells and the "semi-adherent" adhesion behavior. Fully formed FA usually facilitate strong and sustainable adhesions in the cells that assemble them (Albiges-Rizo et al., 2009; Petit and Thiery, 2000). In cells with the arch phenotype, ASAP3 displays ring-like formations, which are occasionally lined with F-actin. This strongly resembles the presentation of ASAP3 in circular dorsal ruffles during cellular movement, that were described ever since the first discovery of the protein in fibroblasts by Ha et al. in 2008. Thus, although ASAP3 is present in adherent HSPC, it shows no formation indicative of the assembly of fully matured FA.

Surprisingly the presentation of pPYK2, especially in HSPC with larger cell area or arch phenotype and strong F-actin stress fibers is very distinct. It shows a similar distribution to its close relative FAK in FA, right at the tip of F-actin fibers, lining the outer cell edge (Wei et al., 2008). This is of special interest as PYK2 levels in hematopoietic cells are increased (Avraham et al., 2000). Additionally, it was shown by Du et al. in 2001 that overexpression of PYK2 in 3T3 fibroblastic cells led to localization of PYK2 to FA, autophosphorylation and reorganization of the cytoskeleton into "'podosome-like' FA". This further highlights the special role of PYK2 in adhesion of HSPC, that is described within the here presented work.

To summarize the observations being made regarding FA, the establishment of these structures by HSPC is unlikely, as none of the marker used to assess FA formation are observed as expected for such structures.

5.1.2.2.   Invadopodia marker and HSPC

Invadopodia and podosomes share several similarities, ranging from overall structure to the CAAM involved (see 1.2.3). The biggest difference is found within the half-life of these two structures. While podosomes undergo dynamic reassembly within 2-4 min, invadopodia can be maintained up to several hours (Albiges-Rizo et al., 2009; Eleniste and Bruzzaniti, 2012a). Since invadopodia are classically labelled as invasive structures established by cancer cells, they are usually found near the nucleus and can form larger elongated structures, which follow the presented substrate and diverge from the usual dot-like presentation of invadosomes (Cambi and Chavrier, 2021).

The scaffolding protein cortactin, that plays a role in F-actin assembly and branching by binding to the Arp2/3 complex was chosen as a marker for native invadopodia formation (Alblazi and Siar, 2015). Due to the fact, that this molecule is specifically required for invadopodia formation and that cortactin is present even prior to F-actin nucleation, it is a promising candidate for being a marker of native invadopodia (Ayala et al., 2008; Eleniste and Bruzzaniti, 2012a; Jeannot and Besson, 2020). Within the work presented here, cortactin was observed to be ubiquitously present throughout the ventral cell side, not exclusively in contact with F-actin, indicating a highly dynamic turnover of structures in this area.

TKS5 was chosen as a marker for mature invadopodia, since it is a prominent molecule in these structures (Saini and Courtneidge, 2018). While in the work presented here this marker was not found to be noticeably pronounced in F-actin puncta, it did, however, present other distinct formations in adherent HSPC. These are shorter and longer fiber-like formations, depending on cell size, that could follow the presentation of FN-fibers as substrate. The absence from F-actin puncta, contrary to expectations, could be explained by Iizuka et al. (2020). They showed, that TKS5 is enriched at the base of invadopodia, not directly colocalizing with F-actin and can also be present in concert with microtubules outside of invadopodia. The elongated fiber like TKS5-structures have recently been described as a possible determining criteria of invadopodia-formation by Cambi and Chavrier (2021). In cells with the arch phenotype large ring structures formed by TKS5 could be observed. These resemble invadopodia in, for example, MDA-MB-231 cells (Ferrari et al., 2019).

Taken together, the observation of the chosen invadopodia marker indicate the presence of invadosome-related structures in adherent HSPC. The low colocalization of these structures with F-actin puncta (see Appendix Figure A.9) and the dynamic behavior of the observed structures, that will be discussed below, give the indication that these structures are more podosomes-like than invadopodia-like.

5.2. Adherent HSPC establish podosome-like structures in a dynamic manner

The high prevalence of the podosome phenotype in adherent HSPC, the absence of focal adhesion structures and the indication of invadosome structures being present according to the invadopodia marker labelling, prompted a more detailed investigation of PLS in HSPC. For this reason, the presentation of the chosen markers for native and mature podosomes will be discussed separately and with a special focus on pPYK2. Additionally, the spatial distribution of CAAM within the PLS was assessed and will also be discussed in the following segment.

5.2.1. The presentation of podosome markers in adherent HSPC

As markers for native and mature podosome structures pPYK2 and MMP9 were chosen, respectively. PYK2 is a molecule that is described to be present in the adhesive ring around the podosome core. It undergoes autophosphorylation upon integrin engagement, which is one of the initial signaling events in adhesion (Duong and Rodan, 2000). MMP9 is a metalloprotease that is present in podosomes, but not known to be involved in invadopodia formation and function, and plays a role in the downstream matrix degradation facilitated by these structures (Buccione et al., 2009; Varon et al., 2006).

MMP9 was found ubiquitously in adherent HSPC with slight enrichment in dorsal cell regions. This is in line with observations made by Varon et al. (2006) for podosome induction in endothelial cells, where MMP9 was present not only at podosome sites but also throughout the cell body. This, and the enrichment of MMP9 in dorsal regions, can be explained by the fact that MMP9 is not membrane bound, but recruited to podosomes before being secreted into the extracellular space, where it is activated (Yabluchanskiy et al., 2013).

The presentation of pPYK2 in adherent HSPC was the most distinct among all analyzed CAAM. It clearly colocalized to prominent F-actin spots present in attached HSPC. It even displayed a ring-like formation in some cases. These observations are in accordance with the expectation of pPYK2 and F-actin in PLS (Duong and Rodan, 2000).

Since PYK2 is a FAK variant whose production is heightened only in certain cell types, like cells of the nervous system, cells of hematopoietic lineage and OB, the levels of pPYK2 and tPYK2 were assessed using immunoblotting (Gelman, 2003). Both pPYK2 and tPYK2 production in HSPC were validated using this method, however, overall levels of both proteins were too low, to make a reliable distinction between adherent and non-adherent cells regarding phosphorylation. Similar tests performed by Salesse et al. in 2004 showed comparable levels of PYK2 in HSPC as observed here. Improvement of the method, and/or employment of complementary methods, will give more information on whether PYK2 is phosphorylated only upon cell attachment. However, the presence of pPYK2 in PLS of adherent HSPC can be considered a specific feature of these adhesion structures.

The presentation of vinculin and paxillin, other typical proteins of the podosome ring, was assessed in the observed structures (Albiges-Rizo et al., 2009). Paxillin clearly colocalized with pPYK2, while vinculin showed a varying localization in adherent HSPC. In some cases, it showed colocalization to pPYK2 while in others it was found to be located more towards the periphery of pPYK2 signal. These results partly conform to the known position of pPYK2, vinculin and paxillin within podosome structures. Usually, they are found in close proximity to one another, as it was observed in HSPC in the present work. However, as they are described to be molecules of the podosome adhesive ring, they are expected to be located in the F-actin spot periphery (van den Dries et al., 2019, 2013). The observation made for adherent HSPC in the current work is less pronounced than what is expected and also varied between cells.

5.2.2. The spatial organization of PLS in adherent HSPC is dynamic

The spatial organization of PLS discussed must be put into the context of the dynamic behavior of these structures, which affects the presented results as magnitudes change from single PLS to entire phenotype populations.

Starting by analyzing single PLS of single cells (see 4.4.1) the radial intensity profiles of F-actin and pPYK2 show that the latter presents rather heterogeneously. This spans from simple colocalization of pPYK2 with the F-actin peak, to slight shoulders in the profile to full double peaks being present, which translate to a ring formation around F-actin as is confirmed in the IF images. A ring formation of pPYK2 around the F-actin core is considered to be displayed by fully matured podosomes (Joosten et al., 2018; Pfaff and Jurdic, 2001; van den Dries et al., 2019b). The presence of various intermediate states indicates a dynamic behavior of PLS assembly and disassembly in HSPC. Interestingly, another phenomenon that has been described in podosomes is also indicated here. Podosomes are protruding structures, and it has been shown that protrusion of podosomes oscillates together with F-actin accumulation and the podosome-ring. This oscillation is also visible in fluorescence intensity of F-actin (Labernadie et al., 2014; van den Dries et al., 2013). Furthermore is has been shown that podosome oscillation of neighboring podosomes exhibits correlation (Proag et al., 2015). In the work presented here the radial intensity profiles display values normalized to the maximum fluorescence intensity of F-actin. Still maximum fluorescence intensity of pPYK2 varies between single PLS radial profiles and neighboring PLS seem to align

regarding this value. This indicates that podosome oscillation is a phenomenon that also appears to play a role in HSPC PLS.

The heterogeneous presentation of single PLS has an effect on the averaged radial intensity profiles of the cell. This is visible in the radial intensity profiles presented under 4.4.2. It would be expected, that cells of the same phenotype show similar radial intensity profiles for their PLS. Additionally, if cells display the podosome morphology, radial intensity profiles of the assessed CAAM are expected to display shoulders or double peaks, indicating the assembly of mature PLS. However, there did not seem to be a correlation of the spatial distribution as depicted in the radial intensity profiles and cell phenotype. Some cells of the same phenotype show different spatial distribution of CAAM around F-actin spots, and some cells displaying podosome morphology show radial intensity profiles without shoulders or double peaks. A variance in the assembly state of podosomes has been shown before, even in cells that establish fully mature podosomes like dendritic cells or osteoclasts (Pfaff and Jurdic, 2001; van den Dries et al., 2013). However, even in these studies, the averaged radial intensity profiles of multiple podosomes from multiple cells, resulted in a homogenous display of ring versus core proteins with double peaks of the former (van den Dries et al., 2013). The heterogeneous display between cells observed in the present work, even of the same phenotype, is likely the result of two circumstances. First, the dynamic display of the PLS as described above that introduces a base level of variance into the analysis. Second, the number of PLS per cell can vary greatly, even between cells of the same phenotype, due to the chosen determining values. Averaging radial intensity profiles for a single cell can therefore lead to smoothing of the profiles and loss of distinct features such as shoulders or double peaks if many PLS are present, which are in a different state of assembly. *Vice versa,* the display of shoulders or double peaks in averaged profiles of lower numbers of PLS could result from few PLS with an advanced maturity state that might not be representative. These factors have an overall impact on how the averaged radial intensity profiles presented and have to be considered in discussing them.

To account for the variability of radial intensity profiles within individual cells and consequently entire cell populations, it was decided to analyze radial intensity profiles by taking the standard deviation into consideration, as it gives more information on the distribution within phenotype groups.

In the polarized phenotype cells the radial intensity profile of pPYK2 shows the highest standard deviation in the center of the PLS amongst all phenotypes, resembling double peaks in the radial intensity profile. In radial intensity profiles of fully matured podosomes double peaks represent a ring formation around the F-actin core (van den Dries et al., 2019b). For the here presented work this would translate into the most matured PLS being assembled by polarized phenotype cells compared with all other phenotypes. However, it is unclear, if this distinct presentation of the CAAM is a specific feature of the PLS in this more adhesive phenotype, associated with migration (see 5.1.1), or simply the result of a phenotype with few cells and few PLS per cell, where single distinct structures have a large impact on the entire profile. In the other phenotypes, where cells do not display the podosome morphology, thus having only few PLS (filopodia and polarized-filopodia phenotypes) no distinct features of pPYK2, paxillin or vinculin can be observed, and the spatial distribution of these CAAM around F-actin spots is more narrow than in other phenotypes. Therefore, it can be assumed, that the presentation of pPYK2 in cells of polarized phenotype is the result of few non-representative PLS having a large impact on a phenotype with few cells when averaging the radial intensity profiles. Therefore, the PLS established by these cells seem to be less mature, compared to cells of round phenotypes and phenotypes containing the podosome descriptor.

It is notable, that the distribution variance of pPYK2 and vinculin, according to the standard deviation, is higher around the center of the structures in cells with phenotypes of lower adhesion strength and/or podosome morphology. The high standard deviation at the PLS center might be indicative of some PLS with double peaks being present within these populations, while other just show a single peak. A double peak in the radial intensity profile reflects a fully formed ring around a podosome core (van den Dries et al., 2019b). Assuming that the high standard deviation displayed by pPYK2 and vinculin in the aforementioned phenotypes stems from double peak formation in some of the PLS, this would mean the PLS formed by cells with this phenotype tend to be in a more mature state. Furthermore, in the radial intensity profiles of pPYK2 across phenotype groups another feature stands out. In cells that are not assigned the filopodia descriptor (phenotypes round, podosome, polarized and polarized-podosome) pPYK2 spans the F-actin peak more broadly. Additionally, Paxillin follows the same trend. Both pPYK2 and paxillin are CAAM associated with the podosome ring (Albiges-Rizo et al., 2009; Pfaff and Jurdic, 2001). Their distribution

towards the F-actin spot periphery in round and podosome morphology cells indicated further, that these cells form more mature PLS than other observed phenotypes. However, comparing these results to radial intensity profiles of ring molecules in fully matured podosomes, a clear difference can be observed (van den Dries et al., 2019b). Therefore the PLS observed within HSPC, as part of the here presented work, appear to still represent less pronounced or immature forms of podosomes.

Obtaining the FWHM value for every single radial intensity profile of every cell provided not only easier access to the spatial distribution of CAAM in the different phenotype populations, but also enabled statistical analysis. The FWHM of F-actin radial profiles are distinctly smaller in adherent HSPC than what is usually reported for podosomes. The F-actin spots here are around 330 nm in diameter, while the radius reported for fully matured podosomes is generally around 0,5-1 µm (Buccione et al., 2004). FWHM of pPYK2, vinculin and paxillin are exceeding the F-actin profile. The usual display of the podosome ring, is that of a double peak and displayed via the diameter of the gauss fit, the FWHM of core proteins has been described as lower than the value of F-actin (van den Dries et al., 2019b). The FWMH higher than that of the F-actin profile points towards a distribution of the CAAM towards the F-actin periphery and is another indication of structures resembling podosomes without showing the formation described for fully matured podosomes. Additionally, while the FWHM of vinculin and paxillin was significantly higher than that of F-actin in almost all analyzed phenotypes, the FWHM of pPYK2 was significantly higher than F-actin values in round and podosome phenotypes, even more so than in other observed phenotypes. As already described above, this finding further solidifies, that the PLS established by cells of this phenotype resemble classic podosomes the most across the observed populations.

These observations point to an architecture of HSPC PLS that is marked by smaller F-actin spots than what is usually reported for podosomes, and that are colocalized with pPYK2, paxillin and vinculin, which are distributed towards the structure's periphery. Paxillin and vinculin can be found in the outermost parts of the structure, while pPYK2 distributes from the center to a place between F-actin and vinculin/paxillin. A colocalization of paxillin, vinculin and pPYK2 in the podosome ring in close proximity to the plasma membrane has been reported by multiple studies (Joosten et al., 2018; Linder et al., 2023; Pfaff and Jurdic, 2001). The offset between PYK2 and paxillin/vinculin localization was not observed in these studies. However, Pfaff and

Jurdic (2001) reported that both paxillin and PYK2 bind to the same integrin in podosomes assembled by monocytic cells undergoing osteoclastic differentiation. The authors suggested that the recruitment of paxillin and PYK2 to the $\alpha V\beta 3$ integrin might serve a specific function within the differentiation process. It stands to question what integrins are involved in the formation of the PLS in HSPC in the work presented here and if a recruitment of different integrins could explain the alternate localization of pPYK2. In fully matured podosomes PYK2, paxillin and vinculin usually form a clearly defined ring around the F-actin puncta (Bruzzaniti et al., 2009; Duong and Rodan, 2000; Pfaff and Jurdic, 2001). The absence of this clear distribution in adherent HSPC indicates the presence of immature PLS and/or is a sign of the high turnover of these structures. However, it appears that in the large majority of cells with round and podosome phenotype, the observed structures move towards a more mature state.

5.3. The morphology of adherent HSPC is associated with lineage determination

Adherent HSPC display a variety of dynamic phenotypes that in turn establish PLS with distinct spatial characteristics. In order to determine, whether the presence of specific morphologies is limited to a distinct progeny of HSPC, the cells were assessed for the presence of progenitor markers in concert with morphology. As described in 1.1.1, the process of hematopoietic differentiation is continuous, but can be followed and marked by immunophenotyping using the presence of CD-molecules on the cell surface. The markers used to identify early HSC and MPP, as well as cells committed to myeloid and lymphoid lineage within the CD34$^+$ cells were CD38, CD33 and CD45RA. Cells lacking all of these three markers are considered early progenitors, not committed to lineage - the HSC and MPP. Cells are expected to start to produce CD45RA when they commit to lymphoid lineage, thus marking the cells from CLP onwards (Rieger and Schroeder, 2012; Sumide et al., 2018). From the CMP onwards cells are considered to produce CD38 and CD33 (Kim et al., 2018; Laszlo et al., 2014). Lastly, the GMP are indicated by production of CD45RA and CD38 but the absence of CD33 (Sumide et al., 2018; Zhang et al., 2018).

Analysis of the production of differentiation markers revealed that the majority of CD34$^+$ cord blood cells were also positive for CD38, CD45RA and CD33. This highlighted an issue with this categorization process quite clearly – the graduality of differentiation.

The understanding that hematopoiesis is a continuous process has emerged and been widely accepted within the last couple of years of hematopoietic research (Buenrostro et al., 2018; Karamitros et al., 2018; Macaulay et al., 2016; Velten et al., 2017; Zhang et al., 2018). By co-labelling CD38 with CD45RA and CD33 respectively, information of the same subpopulation (CMP) is gathered. However, the population of CMP/MEP were not equally large in the two respective samples, even though the cells originate from the same UCB isolation. The reason for this could be found within the gradual production of differentiation markers during hematopoiesis, which conditions the fact, that CD45RA and CD33 production are not entirely mutually exclusive (Chen et al., 2023; Sommarin et al., 2021). This is supported by the presence of two distinct sub-populations of CD45RA$^+$ cells, producing the molecule in higher and lower amounts. The population size of CD45RA^{low} cells is closer to what is observed for CD33$^+$ cells, suggesting that these cells are in a fluent state of differentiating from CMP to GMP. For these reasons and to get a better understanding of the differentiation state of adherent HSPC the differentiation marker descriptors were assigned as explained in 4.5.1.

The distribution of marker production in adherent HSPC (4.5.2) shows that not just a single subpopulation is presenting adhesive properties, but almost all levels of markers in combination with one another are present among the adherent cells. The gradual production of all assessed differentiation markers along the hematopoiesis process is also reflected in the distribution of the marker descriptors combinations. The proportional amount of high CD33 or CD45RA production rises with higher CD38 production, as would be expected along the fraction of the path of hematopoietic differentiation, that was assessed within the here presented work. Interestingly, the largest subpopulations of adherent HSPC are CD45RA^{low}CD38^{low}CD33^{low} cells. As outlined above, these are likely the cells representing cells of myeloid lineage determination. Assuming that the production of the progenitor markers rises gradually with differentiation, it can be argued, that these cells are still in early stages of differentiation. That myeloid lineages are enriched in HSPC sourced from UCB has been reported before by Hess et al. (2020). Additionally, FN has been shown to lead HSPC into myelopoiesis, which could also influence the prevalence of CMP observed here (Wirth et al., 2020).

Looking at associations between cell shape and marker production (see 4.5.3.1), the C-M-H-test detected a weak significant correlation between cell shape and CD33 presence. Looking at the distribution of CD33 marker classes between cells of round and polarized morphology it is striking, that the CD33$^-$ cell fraction is smaller in polarized cells while the proportion of CD33^{low} cells is larger compared to round cells. This indicates that cells of (early) myeloid progeny tend to take on elongated cell shapes upon contact with the ECM. Even though C-M-H-statistics do not report associations between cell shape and CD38 or CD45RA production, the distributions of these markers correspond well with this implication, as CD38$^{high/very\ high}$ cell populations are larger in cells with polarized morphology as well as the CD45RA$^+$ sub-groups. The presence of CD38$^+$CD45RA$^+$ would indicate the presence of GMP cells as described above. However, since CD45RA^{low} fractions are more prevalent and C-M-H-test gives significant correlations regarding CD33, the classification of these cells as CMP is reasonable. It has been shown before, that myeloid lineage cells can respond quickly to extracellular signals by taking on a polarized cell shape (Toyama-Sorimachi et al., 2004).

Testing for association between filopodia presence/absence and differentiation marker classes, C-M-H-statistics result in a highly significant correlation between filopodia morphology and CD38 as well as CD33 and their combined production. A weak significant correlation was detected between filopodia morphology and CD45RA production. In cells with filopodia the populations of CD38^{high}, CD33^{low} and CD45RA^{high} populations are larger than in cells without filopodia. Taken together, the distribution of marker classes within cells establishing filopodia structures indicate that these cells likely also belong to the myeloid lineage group. Given the large numbers of CD45RA^{high} cells it is reasonable to assume that cells assembling filopodia are slightly more differentiated, transforming into the GMP population. That cells of myeloid lineage start forming filopodia in response to e.g. inflammation or other processes if the immune system, has been shown before (Thomas et al., 2008; Toyama-Sorimachi et al., 2004).

Overall, it could be observed that a low fraction of further differentiated cells, marked by the high production of CD38, also tends to take on a polarized cell morphology and the establishment of filopodia. As described in 5.1.1, the mobilization and migration of HSPC is correlated with differentiation and cell polarization (Mayani, 2019).

C-M-H-statistic finds a significant association between PLS presence/absence and the CD38 and CD33 marker classes. However, when looking at the distribution of these subpopulations the trend shifts in favor of more undifferentiated cells compared to what was observed in polarized cells or cells with filopodia. In cells with podosome morphology, CD38$^{very\ low/low}$ fractions are larger than in cells without podosome morphology. The same can be observed for CD33$^{-/low}$ populations. This indicates that cells establishing PLS are less mature than cells that lack these structures. No significant association is registered in C-M-H-statistics between CD45RA and podosome morphology. However, assessing the distribution of CD45RA in cells with podosome morphology the absence of CD45RA$^-$ cells can be observed, while CD45RA$^+$-CD38$^{very\ low}$ fractions are larger than in cells without podosome morphology. This indicates that HSPC establishing PLS are primed towards the lymphoid lineage as CD45RA production is stronger in these cells, while CD38 and CD33 production is low compared to cells not establishing PLS. This is interesting as lymphocytes are known to use podosomes for transcellular crossing of the endothelial barrier, similar to what Rademakers et al. (2018) speculated for HSPC (Carman et al., 2007).

The observations made for marker distribution across the assigned phenotypes are in agreement with the data made for single morphologies. Adherent HSPC that establish filopodia are further differentiated as indicated by high CD38 production. A large party of the podosome phenotype population, however, is defined by lower CD38 production, and higher proportions of CD33$^-$ cells, indicating less differentiated cells leaning towards lymphoid lineage.

5.4. Summary, closing remarks and outlook

By analyzing the adhesion behavior of HSPC, three major observations were made:

1) A large fraction of adherent HSPC display a round cell morphology. In these round cells a large population also displays notable amounts of PLS.
2) The assembled PLS contain pPYK2, vinculin and paxillin. Within cells of round and podosome phenotypes, the spatial distribution of these molecules resemble fully matured podosomes the most among all observed phenotypes.
3) HSPC with round morphology and/or notable amounts of PLS are less differentiated than cells with other morphologies.

Additionally, it was apparent that in each of the analyzed factors, HSPC displayed a highly dynamic turnover – on the continuum of adherent phenotypes and of the PLS assembled by the cells. The role of these highly dynamic PLS in HSPC adherence requires further investigation. As stated before, PLS are discussed to play a role in transcellular endothelial barrier crossing during engraftment of transplanted cells (Rademakers et al., 2018). Yet, there might be a role of these structures in retention of LT-HSC *in vivo*, where the cells reside near the endosteum. In this area, near the bone, the concentration of extracellular calcium ions is exceptionally high. HSC sense these conditions via the calcium-sensing receptor, which plays a role in in HSC retention (Adams et al., 2006). It stands to reason, that the high Ca^{2+} levels also have an effect on integrin engagement (Zhang and Chen, 2012). Interestingly, recent publications reported that under hypoxia conditions, as present at the endosteum, a subpopulation of HSC is present, that is defined by a high Ca^{2+}-influx and a high intracellular Ca^{2+}-level, and displays enhanced stem cell maintenance (Chow et al., 2001; Dausinas Ni et al., 2023). Given the prominent role of pPYK2 in the adhesion structures described in the here presented work, these observations should be taken into account in future research as autophosphorylation of PYK2 is influenced by calcium ion influx (Momin et al., 2022). If the highly dynamic turnover of the analyzed PLS is part of a positive feedback-loop, in which PLS degrade the matrix and thereby release calcium ions and other signaling factors, to maintain HSC stemness, needs to be further investigated. Investigation of the involved adhesion receptors would be crucial for this task. Integrin α4β1 is known to have a positive influence on HSC retention and stem cell maintenance (Grassinger et al., 2009; Scott et al., 2003; Wirth et al., 2020), therefore its role in the formation of HSPC PLS is worth further investigation. The influence of other ECM substrates, like collagen – which is often used as a cell substrate in podosome research – and calcium concentration are also promising targets to further investigate how these adhesion sites are assembled and regulated (Schachtner et al., 2013). To conclude, the adhesion sites of HSPC described within this work pose an interesting subject for further investigation on the mechanisms facilitating interaction of the HSC and the hematopoietic niche. Understanding these interactions is a fundamental step in the building of artificial platforms to maintain HSC *ex vivo*, keeping them readily available for research and medical purposes.

A. Appendix

Verifying continous flow of cells

Determining limits for cell population
Excluding cell debris

Excluding cell dublettes

Comparison of single HSPC to total
cell count

Limiting positive and negative signal
according to fluorescence intensity
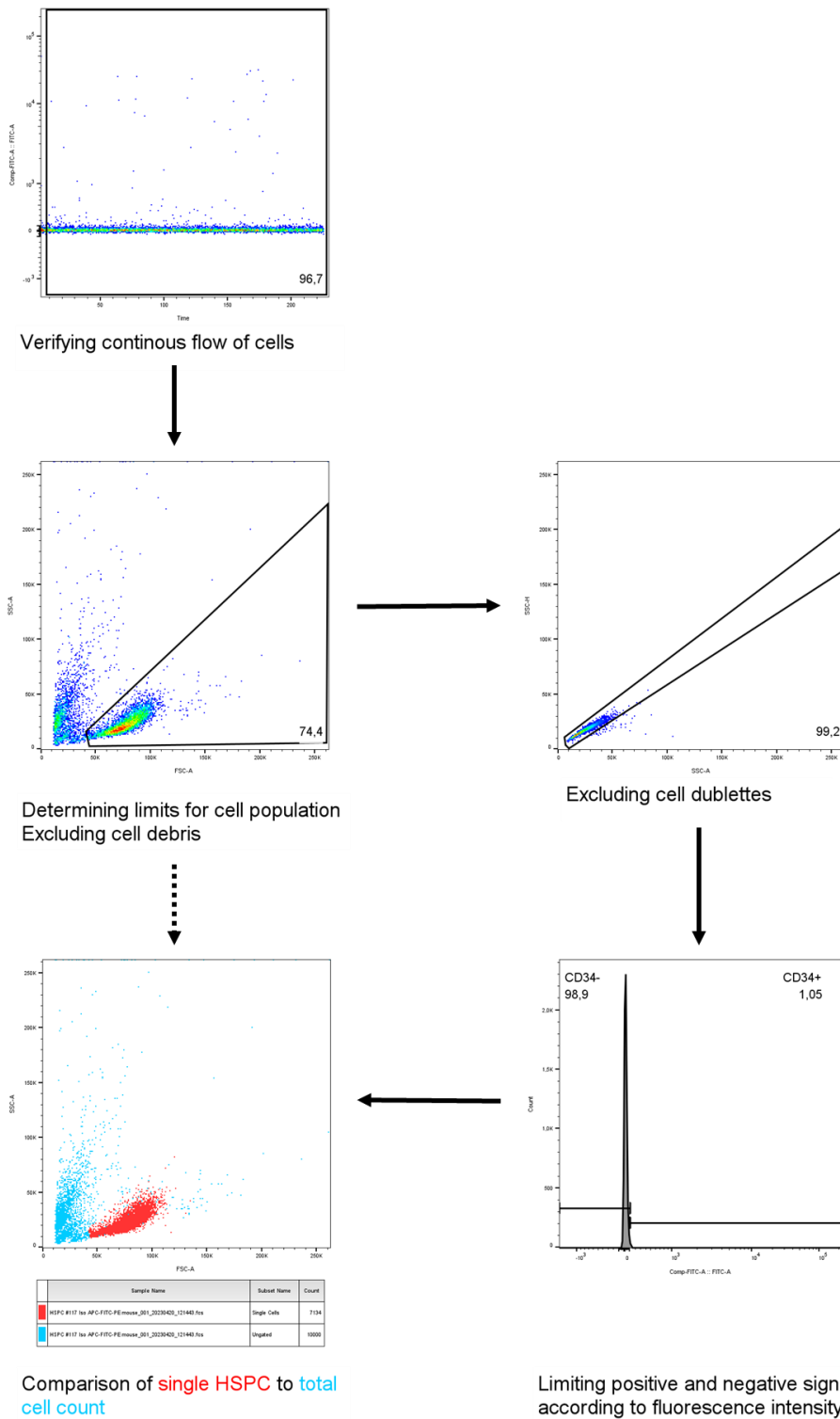
Figure A.1 Flow Cytometry Results Gating Workflow for CD34+ cells *Events were firstly confined by time, by excluding the first seconds of measurement, to avoid carry over between samples and also check for air bubbles in canal. Next the desired cells population is selected by sorting events by forward scatter area (FSC-A) to sideward scatter area (SSC-A). This determines the limits for cell population and excludes cell debris. Next doublets (cell clumps) are excluded by marking the respective population on the SSC-A and sideward scatter height (SSC-H) view. Finally, false negative signals are effectively limited to 1 % by looking and the histogram of the isotype control in the respective fluophore channel. The diagram in the bottom right corner shows the final cell population (red) compared to the total cell population (blue).*
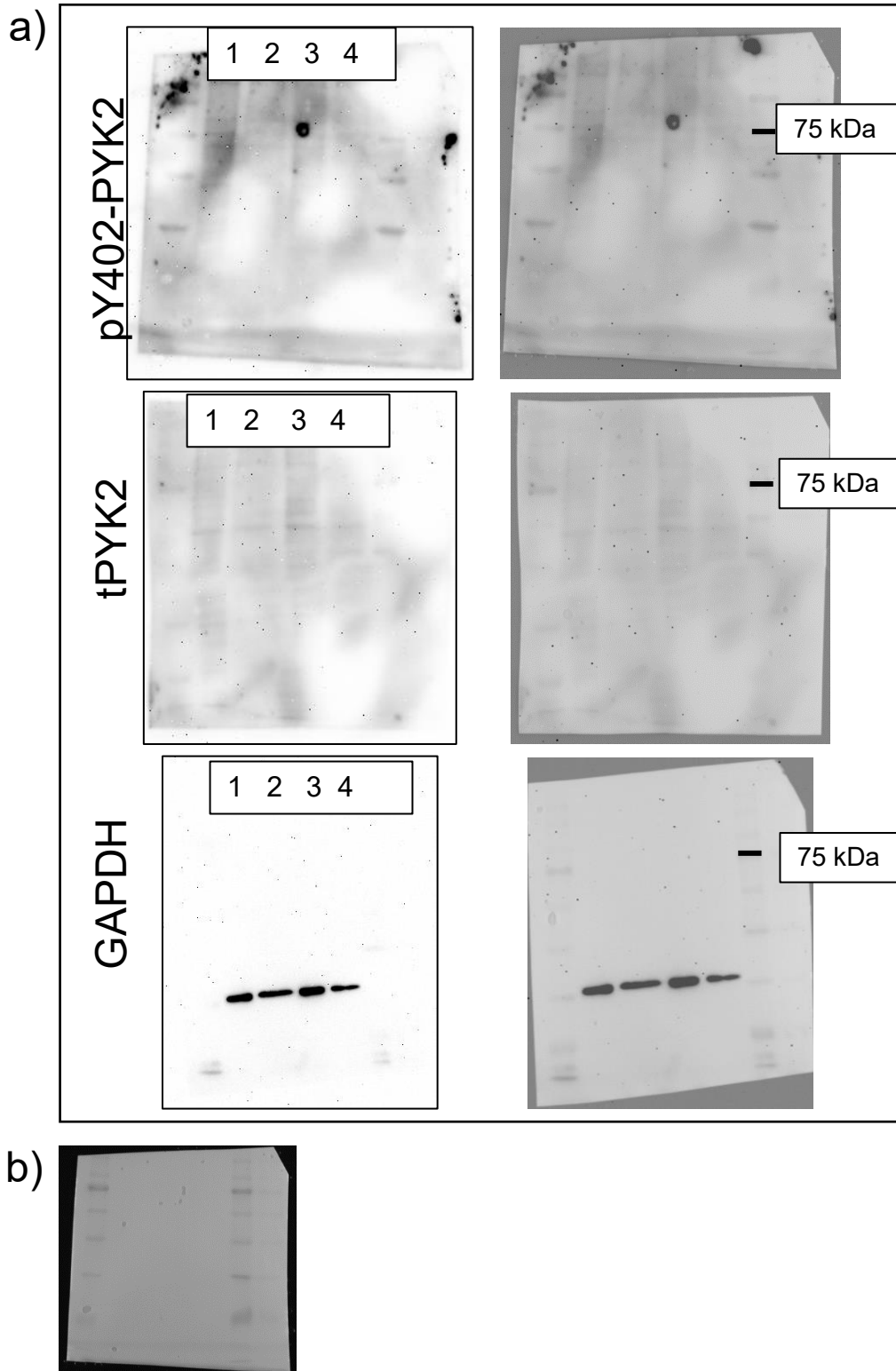
Figure A.2 Immunoblot detection of pPYK2, tPYK2 and GAPDH in adherent and non-adherent HSPC – Full images *Cells were left to adhere to BSA or fibronectin for 1 h before collecting and lysis. 5 µg protein lysate were separated using a 10 % Bis-Tris-gel and blotted onto a nitrocellulose membrane. **a)** Detections of pY402-PYK2 (top), tPYK2 (middle) and GAPDH (bottom) were performed using respective, specific antibodies. Proteins of interest run at 116 kDa (pPYK2 and tPYK2) and 35 kDa (GAPDH) – 75 kDa band is marked. Sample 1: Non-adherent HSPC on BSA, Sample 2: Adherent HSPC on BSA, Sample 3: Non-adherent HSPC on FN, Sample 4: Adherent HSPC on FN; Left column: Raw chemiluminescent signal image of immunoblots after 60 min illumination (PYK2 blots) and 5 min (GAPDH blot); Right column: Merged images of respective chemiluminescent signals and protein marker bands. **b)** Raw image of protein marker on immunoblot respective to p402-PYK2 detection.*
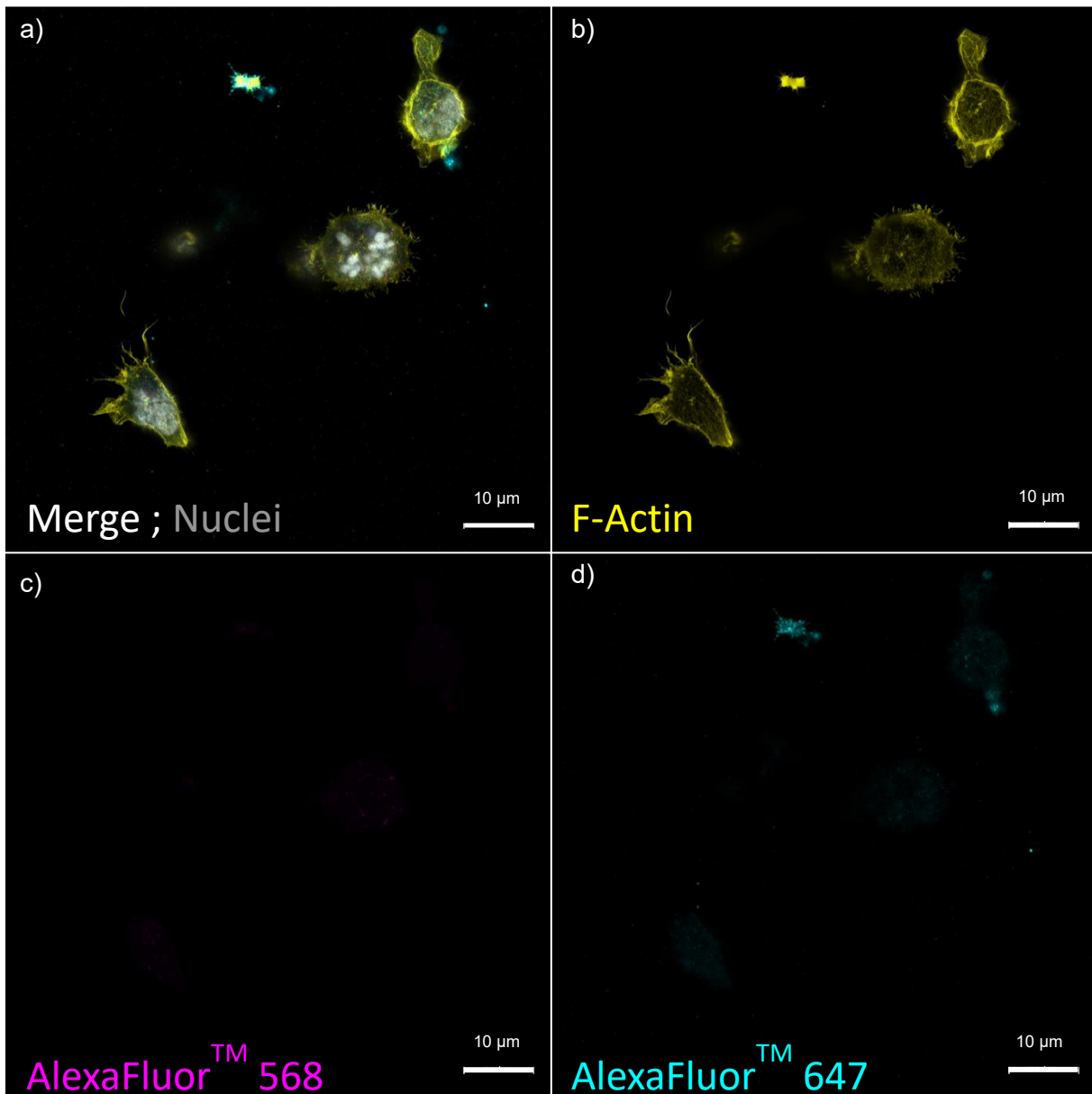
Figure A.3 Immunofluorescence staining control for images depicted in 4.2 *HSPC were left to adhere to fibronectin for 1 h before being submitted to immunofluorescence staining. To control for unspecific binding of secondary antibody, the controls depicted here were prepared, by omitting primary antibody. Shown are images from **a)** merged channels including nuclei/DNA labelled with DAPI (grey), **b)** F-actin labelled with AlexaFluor^{TM} 488 coupled phalloidin (yellow), **c)** channel showing the background intensity for AlexaFluor^{TM} 568 coupled secondary antibody (magenta) and **d)** channel showing the background intensity for AlexaFluor^{TM} 647 coupled secondary antibody (turquoise)*
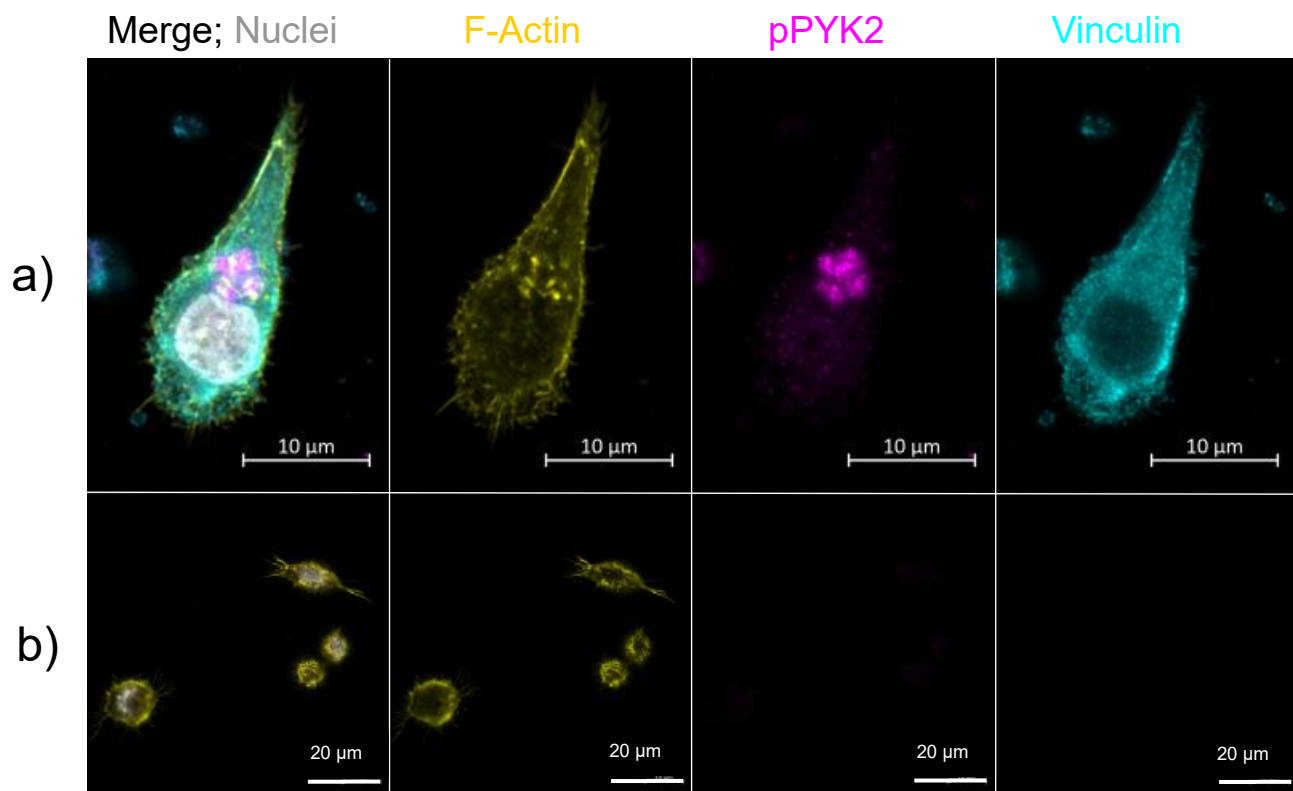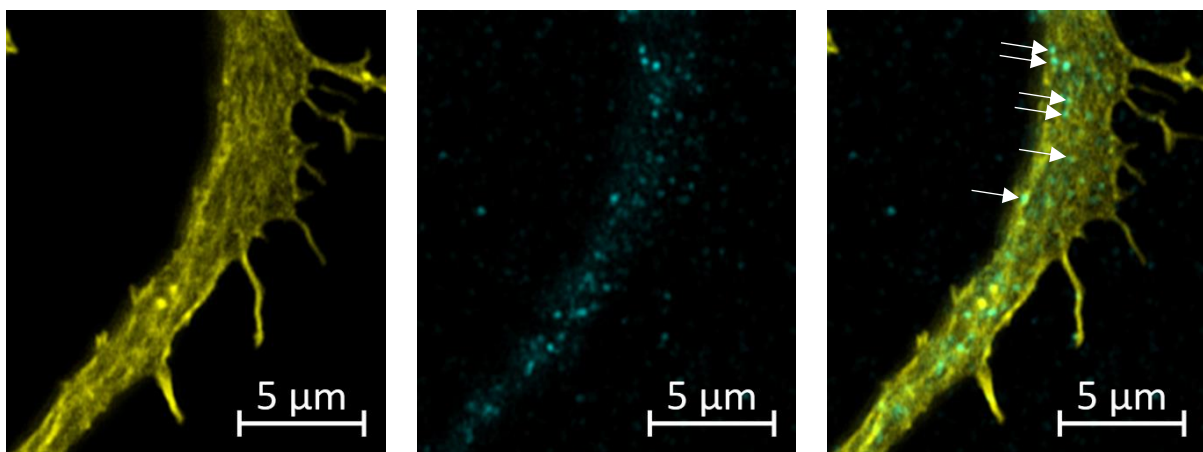
Figure A.4 Exemplary image of immunofluorescent staining of vinculin in HSPC *Cells were left to adhere for 1 h on fibronectin before being submitted to immunofluorescence staining. Depicted are images of the merged channel images, including the nuclei/DNA (grey); F-actin (yellow); pPYK2 (magenta) and vinculin (turquoise).* **a)** *Shows a full stain of the molecules, while* **b)** *depicts the immunofluorescence staining control (omitted primary antibody).*
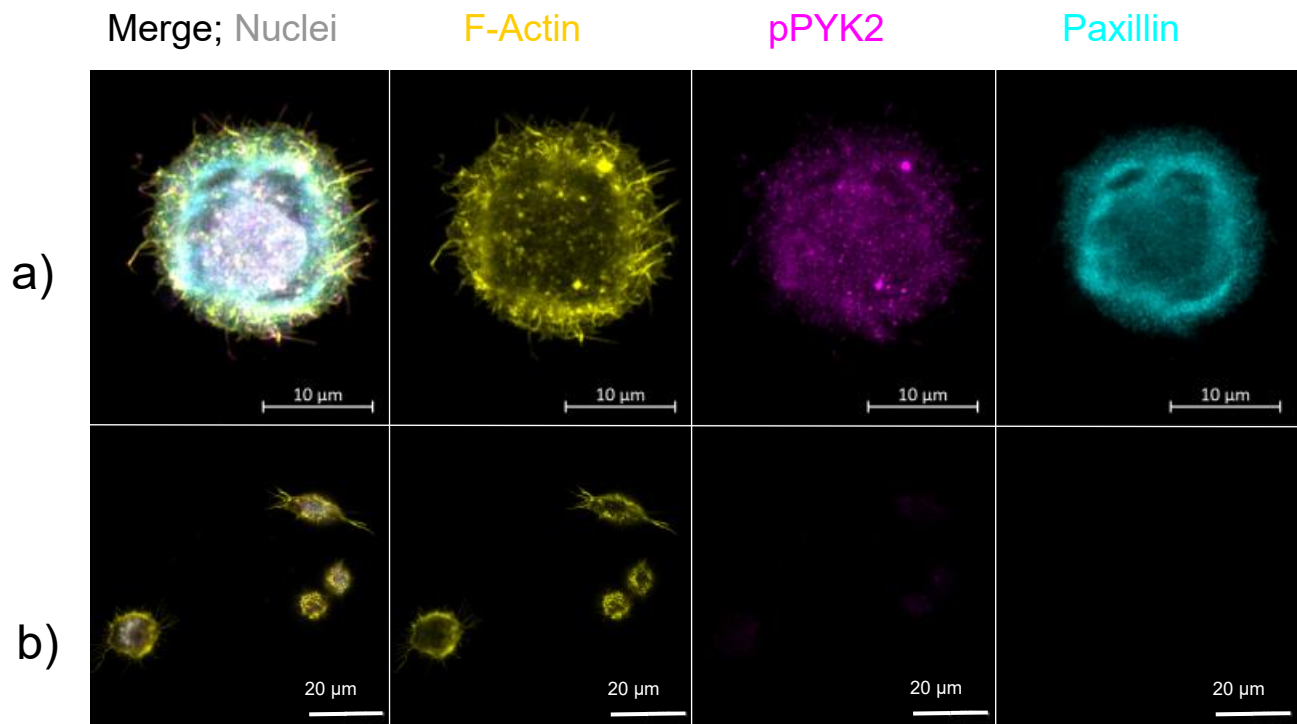
Figure A.5 Exemplary image of immunofluorescent staining of paxillin in HSPC *Cells were left to adhere for 1 h on fibronectin before being submitted to immunofluorescence staining. Depicted are images of the merged channel images, including the nuclei/DNA (grey); F-actin (yellow); pPYK2 (magenta) and paxillin (turquoise).* ***a)*** *Shows a full stain of the molecules, while* ***b)*** *depicts the immunofluorescence staining control (omitted primary antibody).*
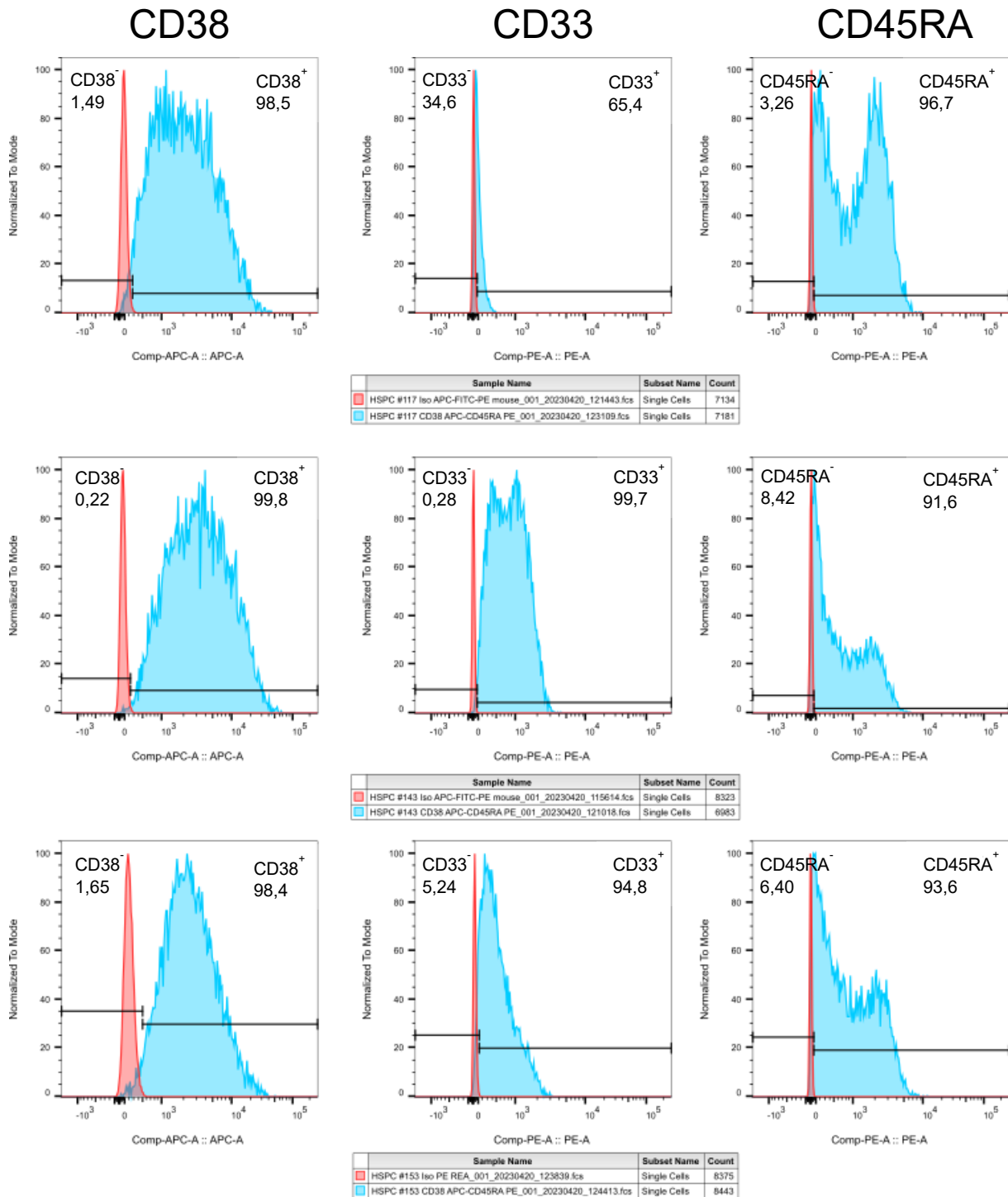
Figure A.6 Percentage of CD38-, CD33- and CD45RA-positive and negative cells per UCB donor
Cells were submitted to Flow Cytometry after isolating CD34+ cells from cord blood and labelling them for CD38, CD33 and CD45RA. Depicted are histograms of CD38 (left column), CD33 (middle column) and CD45RA (left column) labelled cells for three independent cord blood donors (top to bottom rows: #117, #143, #153). Isotype stainings of the cells are depicted in red and determine the boundary settings of positive cells. The populations of CD38/CD33/CD45RA positive and negative cells are labelled accordingly with numbers indicating population size in percent.
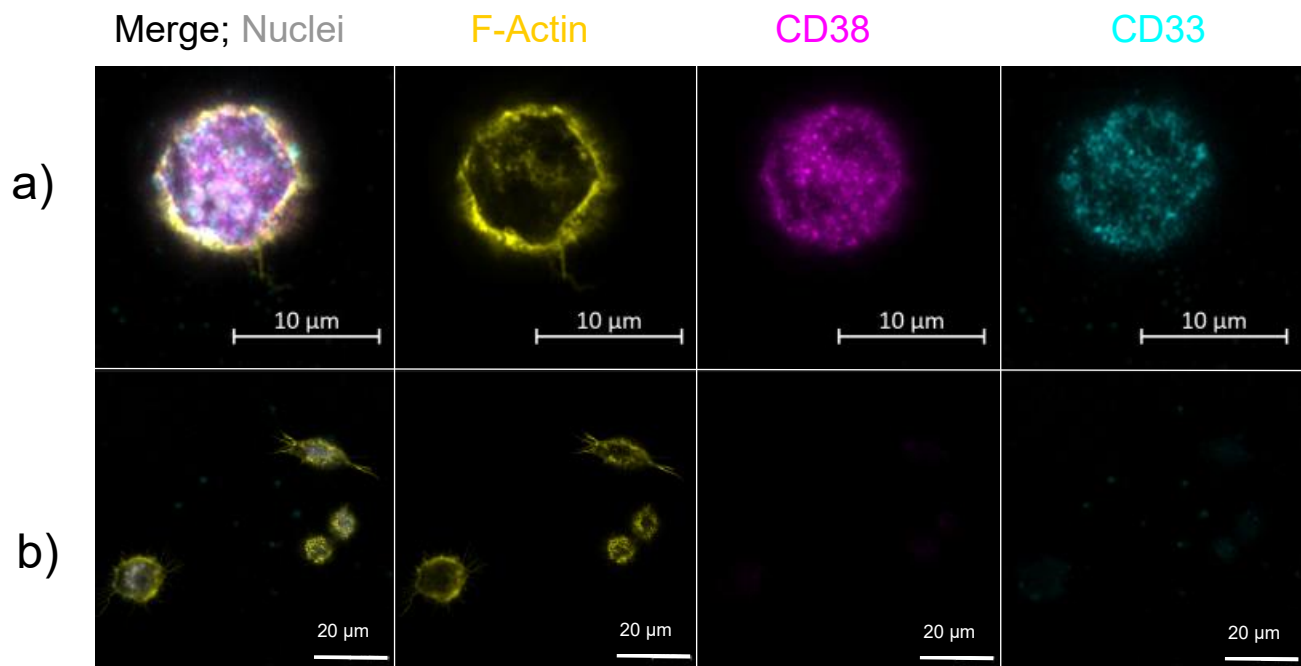
Figure A.7 Exemplary image of immunofluorescent staining of CD33 in HSPC Cells were left to adhere for 1 h on fibronectin before being submitted to immunofluorescence staining. Depicted are images of the merged channel images, including the nuclei/DNA (grey); F-actin (yellow); CD38 (magenta) and CD33 (turquoise). *a)* Shows a full stain of the molecules, while *b)* depicts the immunofluorescence staining control (omitted primary antibody).

| Merge; Nuclei | F-Actin | CD38 | CD45RA |

a)

10 μm   10 μm   10 μm   10 μm

b)

20 μm   20 μm   20 μm   20 μm
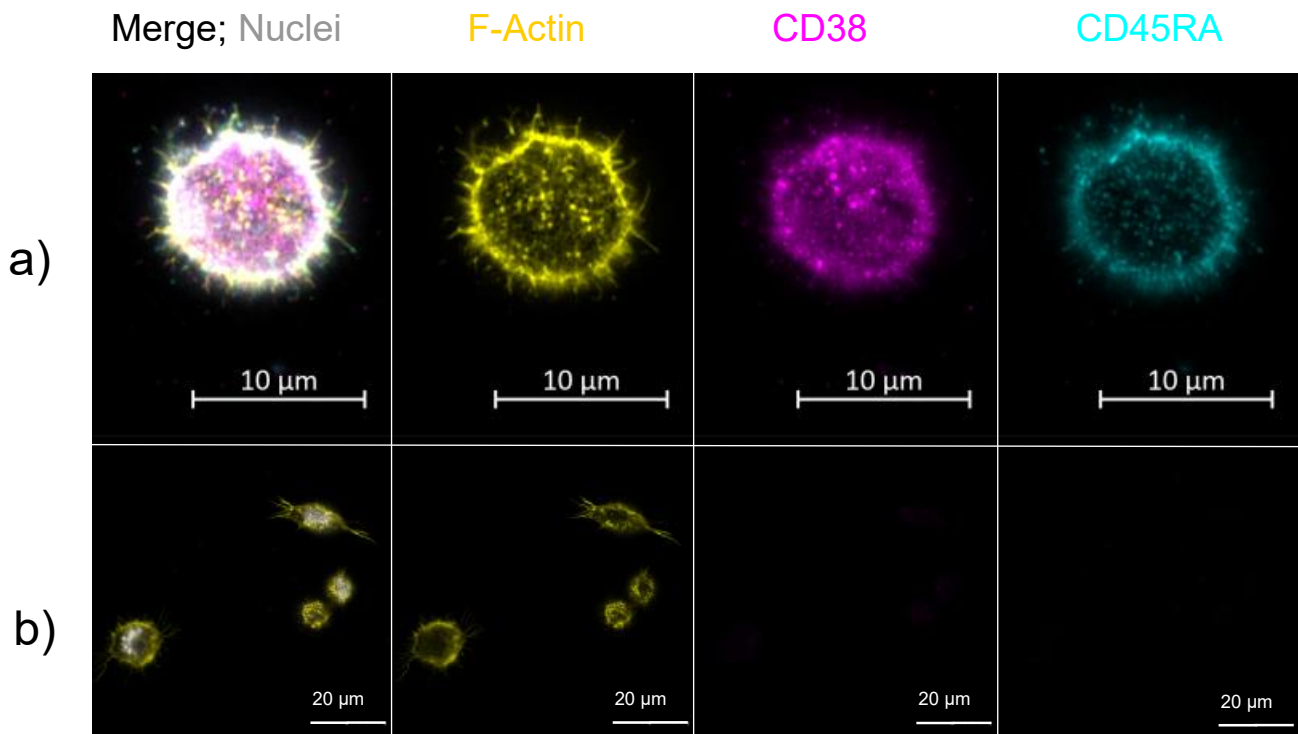
Figure A.8 Exemplary image of immunofluorescent staining of CD45RA in HSPC *Cells were left to adhere for 1 h on fibronectin before being submitted to immunofluorescence staining. Depicted are images of the merged channel images, including the nuclei/DNA (grey); F-actin (yellow); CD38 (magenta) and CD45RA (turquoise).* ***a)*** *Shows a full stain of the molecules, while* ***b)*** *depicts the immunofluorescence staining control (omitted primary antibody).*

5 μm   5 μm   5 μm

Figure A.9 Arp3 is found adjacent to F-actin fibers throughout the ventral cell side *Cells were left to adhere for 1 h on fibronectin before being submitted to immunofluorescence staining. Depicted are images of F-actin (yellow, left); Arp3 (turquoise, middle; and the merged image (right), arrows indicate Arp3 signal adjacent to F-actin fibers.*
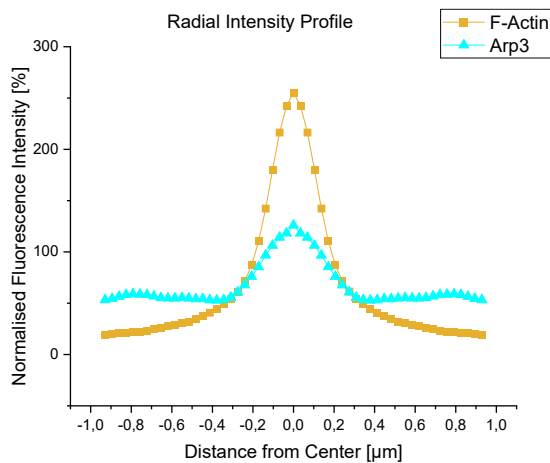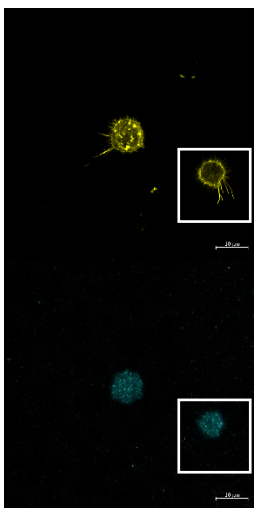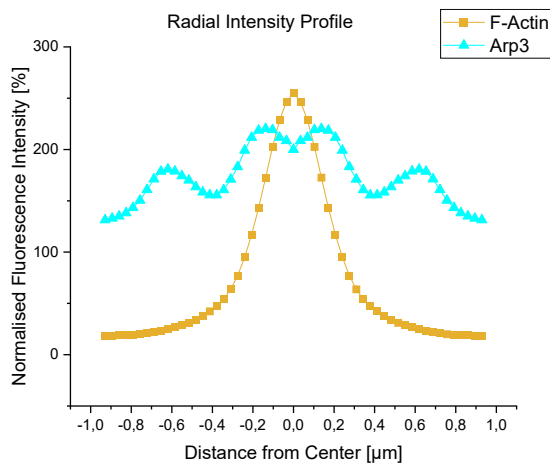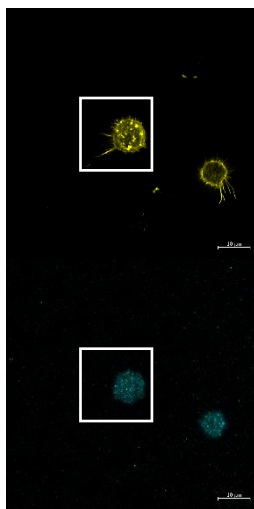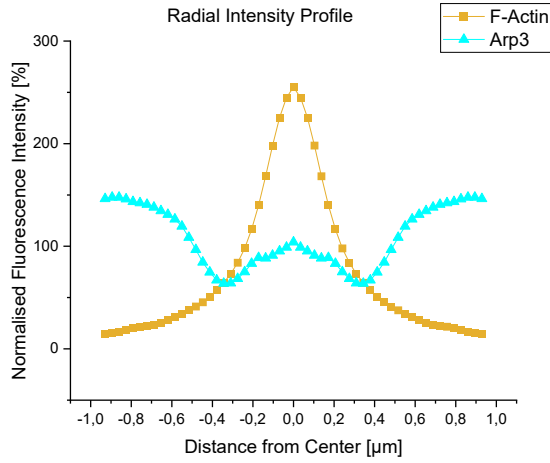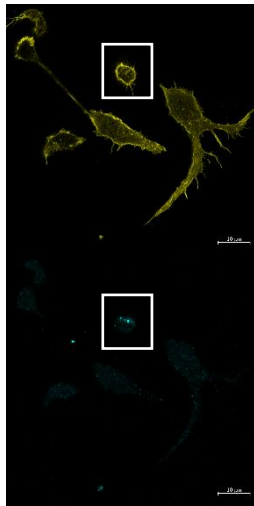
Figure A.10 Radial Intensity Profiles of F-Actin and Arp3 from PLS in HSPC with respective IF images *Cells were left to adhere to fibronectin for 1 h before being submitted to immunofluorescence staining. Shown are three Profiles alongside the respective IF image of the adherent HSPC.*
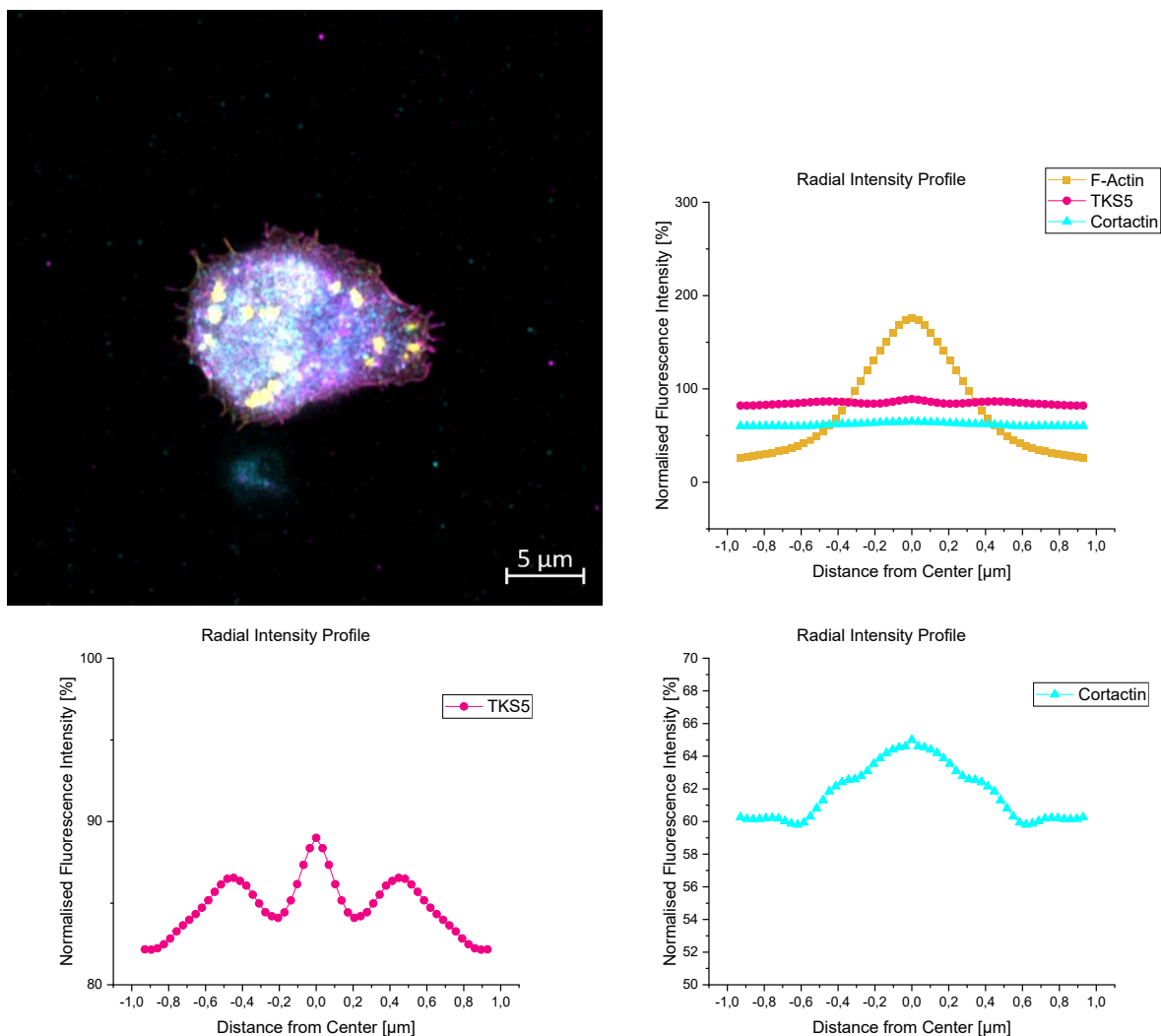
Figure A.11 Radial Intensity Profiles of F-Actin, TKS5 and cortactin from PLS in HSPC with respective IF image *Cells were left to adhere to fibronectin for 1 h before being submitted to immunofluorescence staining. Shown are three Profiles alongside the respective IF image of the adherent HSPC. Note how y-axis of TKS5 and cortactin single profiles have been altered for better visibility of profile, while x-axis was left untouched for comparability with F-actin.*

A.1   Digital Appendix

The digital appendix alongside a digital version of this thesis can be found on the disk secured to the inner back of the cover.

References

Adams, G.B., Chabner, K.T., Alley, I.R., Olson, D.P., Szczepiorkowski, Z.M., Poznansky, M.C., Kos, C.H., Pollak, M.R., Brown, E.M., Scadden, D.T., 2006. Stem cell engraftment at the endosteal niche is specified by the calcium-sensing receptor. Nature 439, 599–603. https://doi.org/10.1038/nature04247

Adams, G.B., Scadden, D.T., 2006. The hematopoietic stem cell in its place. Nat. Immunol. 7, 333–337. https://doi.org/10.1038/ni1331

Akashi, K., Traver, D., Miyamoto, T., Weissman, I.L., 2000. A clonogenic common myeloid progenitor that gives rise to all myeloid lineages. Nature 404, 193–197. https://doi.org/10.1038/35004599

Albiges-Rizo, C., Destaing, O., Fourcade, B., Planus, E., Block, M.R., 2009. Actin machinery and mechanosensitivity in invadopodia, podosomes and focal adhesions. J. Cell Sci. 122, 3037–3049. https://doi.org/10.1242/jcs.052704

Alblazi, K.M.O., Siar, C.H., 2015. Cellular Protrusions - Lamellipodia, Filopodia, Invadopodia and Podosomes - and their Roles in Progression of Orofacial Tumours: Current Understanding. Asian Pac. J. Cancer Prev. 16, 2187–2191. https://doi.org/10.7314/APJCP.2015.16.6.2187

Anthis, N.J., Campbell, I.D., 2011. The tail of integrin activation. Trends Biochem. Sci. 36, 191–198. https://doi.org/10.1016/j.tibs.2010.11.002

Arnaout, M. a., Mahalingam, B., Xiong, J.-P., 2005. Integrin structure, allostery, and bidirectional signaling. Annu. Rev. Cell Dev. Biol. 21, 381–410. https://doi.org/10.1146/annurev.cellbio.21.090704.151217

Artym, V.V., Zhang, Y., Seillier-Moiseiwitsch, F., Yamada, K.M., Mueller, S.C., 2006. Dynamic Interactions of Cortactin and Membrane Type 1 Matrix Metalloproteinase at Invadopodia: Defining the Stages of Invadopodia Formation and Function. Cancer Res. 66, 3034–3043. https://doi.org/10.1158/0008-5472.CAN-05-2177

Audet, J., Miller, C.L., Eaves, C.J., Piret, J.M., 2002. Common and distinct features of cytokine effects on hematopoietic stem and progenitor cells revealed by dose-response surface analysis. Biotechnol. Bioeng. 80, 393–404. https://doi.org/10.1002/bit.10399

Avraham, H., Park, S.Y., Schinkmann, K., Avraham, S., 2000. RAFTK/Pyk2-mediated cellular signalling. Cell. Signal. 12, 123–133. https://doi.org/10.1016/s0898-6568(99)00076-5

Ayala, I., Baldassarre, M., Giacchetti, G., Caldieri, G., Tetè, S., Luini, A., Buccione, R., 2008. Multiple regulatory inputs converge on cortactin to control invadopodia biogenesis and extracellular matrix degradation. J. Cell Sci. 121, 369–378. https://doi.org/10.1242/jcs.008037

Bartelmez, S.H., 2016. Functional Resolution of Long-Term-and Short-Term- Hematopoietic Stem Cells. J. Stem Cell Res. Ther. 1. https://doi.org/10.15406/jsrt.2016.01.00044

Baumheter, S., Singer, M.S., Henzel, W., Hemmerich, S., Renz, M., Rosen, S.D., Lasky, L.A., 1993. Binding of L-selectin to the vascular sialomucin CD34. Science 262, 436–438. https://doi.org/10.1126/science.7692600

Belderbos, M.E., Jacobs, S., Koster, T.K., Ausema, A., Weersing, E., Zwart, E., de Haan, G., Bystrykh, L.V., 2020. Donor-to-Donor Heterogeneity in the Clonal Dynamics of Transplanted Human Cord Blood Stem Cells in Murine Xenografts. Biol. Blood Marrow Transplant. 26, 16–25. https://doi.org/10.1016/j.bbmt.2019.08.026

Berardi, A.C., Wang, A., Levine, J.D., Lopez, P., Scadden, D.T., 1995. Functional isolation and characterization of human hematopoietic stem cells. Science 267, 104–108. https://doi.org/10.1126/science.7528940

Berenson, R.J., Bensinger, W.I., Hill, R.S., Andrews, R.G., Garcia-Lopez, J., Kalamasz, D.F., Still, B.J., Spitzer, G., Buckner, C.D., Bernstein, I.D., 1991. Engraftment after infusion of CD34+ marrow cells in patients with breast cancer or neuroblastoma. Blood 77, 1717–1722.

Bessy, T., Candelas, A., Souquet, B., Saadallah, K., Schaeffer, A., Vianay, B., Cuvelier, D., Gobaa, S., Nakid-Cordero, C., Lion, J., Bories, J.-C., Mooney, N., Jaffredo, T., Larghero, J., Blanchoin, L., Faivre, L., Brunet, S., Théry, M., 2021. Hematopoietic progenitors polarize in contact with bone marrow stromal cells in response to SDF1. J. Cell Biol. 220, e202005085. https://doi.org/10.1083/jcb.202005085

Bhatia, M., Bonnet, D., Kapp, U., Wang, J.C., Murdoch, B., Dick, J.E., 1997. Quantitative analysis reveals expansion of human hematopoietic repopulating cells after short-term ex vivo culture. J. Exp. Med. 186. https://doi.org/10.1084/jem.186.4.619

Bishop, M.R., 2009. Hematopoietic Stem Cell Transplantation. Springer Science & Business Media.

Boulais, P.E., Frenette, P.S., 2015. Making sense of hematopoietic stem cell niches. Blood 125, 2621–9. https://doi.org/10.1182/blood-2014-09-570192

Brown, J., Greaves, M.F., Molgaard, H.V., 1991. The gene encoding the stem cell antigen, CD34, is conserved in mouse and expressed in haemopoietic progenitor cell lines, brain, and embryonic fibroblasts. Int. Immunol. 3, 175–184. https://doi.org/10.1093/intimm/3.2.175

Bruzzaniti, A., Neff, L., Sandoval, A., Du, L., Horne, W.C., Baron, R., 2009. Dynamin Reduces Pyk2 Y402 Phosphorylation and Src Binding in Osteoclasts. Mol. Cell. Biol. 29, 3644–3656. https://doi.org/10.1128/MCB.00851-08

Buccione, R., Caldieri, G., Ayala, I., 2009. Invadopodia: specialized tumor cell structures for the focal degradation of the extracellular matrix. Cancer Metastasis Rev. 28, 137–149. https://doi.org/10.1007/s10555-008-9176-1

Buccione, R., Orth, J.D., McNiven, M.A., 2004. Foot and mouth: podosomes, invadopodia and circular dorsal ruffles. Nat. Rev. Mol. Cell Biol. 5, 647–657. https://doi.org/10.1038/nrm1436

Buenrostro, J.D., Corces, M.R., Lareau, C.A., Wu, B., Schep, A.N., Aryee, M.J., Majeti, R., Chang, H.Y., Greenleaf, W.J., 2018. Integrated Single-Cell Analysis Maps the Continuous Regulatory Landscape of Human Hematopoietic Differentiation. Cell 173, 1535-1548.e16. https://doi.org/10.1016/j.cell.2018.03.074

Burnette, D.T., Shao, L., Ott, C., Pasapera, A.M., Fischer, R.S., Baird, M.A., Der Loughian, C., Delanoe-Ayari, H., Paszek, M.J., Davidson, M.W., Betzig, E., Lippincott-Schwartz, J., 2014. A contractile and counterbalancing adhesion system controls the 3D shape of crawling cells. J. Cell Biol. 205, 83–96. https://doi.org/10.1083/jcb.201311104

Bushell, G.R., Cahill, C., Clarke, F.M., Gibson, C.T., Myhra, S., Watson, G.S., 1999. Imaging and force-distance analysis of human fibroblasts in vitro by atomic force microscopy. Cytometry 36, 254–264. https://doi.org/10.1002/(SICI)1097-0320(19990701)36:3<254::AID-CYTO16>3.0.CO;2-4

Butler, J.M., Nolan, D.J., Vertes, E.L., Varnum-Finney, B., Kobayashi, H., Hooper, A.T., Seandel, M., Shido, K., White, I.A., Kobayashi, M., Witte, L., May, C., Shawber, C., Kimura, Y., Kitajewski, J., Rosenwaks, Z., Bernstein, I.D., Rafii, S., 2010. Endothelial cells are essential for the self-renewal and repopulation of Notch-dependent hematopoietic stem cells. Cell Stem Cell 6, 251–264. https://doi.org/10.1016/j.stem.2010.02.001

Cai, Y., Sheetz, M.P., 2009. Force propagation across cells: mechanical coherence of dynamic cytoskeletons. Curr. Opin. Cell Biol., Cell structure and dynamics 21, 47–50. https://doi.org/10.1016/j.ceb.2009.01.020

Calderwood, D.A., Campbell, I.D., Critchley, D.R., 2013. Talins and kindlins: partners in integrin-mediated adhesion. Nat. Rev. Mol. Cell Biol. 14, 503–517. https://doi.org/10.1038/nrm3624

Calvi, L.M., Adams, G.B., Weibrecht, K.W., Weber, J.M., Olson, D.P., Knight, M.C., Martin, R.P., Schipani, E., Divieti, P., Bringhurst, F.R., Milner, L.A., Kronenberg, H.M., Scadden, D.T., 2003. Osteoblastic cells regulate the haematopoietic stem cell niche. Nature 425, 841–6. https://doi.org/10.1038/nature02040

Cambi, A., Chavrier, P., 2021. Tissue remodeling by invadosomes. Fac. Rev. 10, 39. https://doi.org/10.12703/r/10-39

Cancelas, J.A., 2011. Adhesion, Migration, and Homing of Murine Hematopoietic Stem Cells and Progenitors. Methods Mol. Biol. Clifton NJ 750, 187–196. https://doi.org/10.1007/978-1-61779-145-1_13

Cao, H., Heazlewood, S.Y., Williams, B., Cardozo, D., Nigro, J., Oteiza, A., Nilsson, S.K., 2016. The role of CD44 in fetal and adult hematopoietic stem cell regulation. Haematologica 101, 26–37. https://doi.org/10.3324/haematol.2015.135921

Carman, C.V., Sage, P.T., Sciuto, T.E., de la Fuente, M.A., Geha, R.S., Ochs, H.D., Dvorak, H.F., Dvorak, A.M., Springer, T.A., 2007. Transcellular Diapedesis Is Initiated by Invasive Podosomes. Immunity 26, 784–797. https://doi.org/10.1016/j.immuni.2007.04.015

Carow, C.E., Levenstein, M., Kaufmann, S.H., Chen, J., Amin, S., Rockwell, P., Witte, L., Borowitz, M.J., Civin, C.I., Small, D., 1996. Expression of the hematopoietic growth factor receptor FLT3 (STK-1/Flk2) in human leukemias. Blood 87, 1089–1096.

Case, L.B., Baird, M.A., Shtengel, G., Campbell, S.L., Hess, H.F., Davidson, M.W., Waterman, C.M., 2015. Molecular mechanism of vinculin activation and nanoscale spatial organization in focal adhesions. Nat. Cell Biol. 17, 880–892. https://doi.org/10.1038/ncb3180

Ceccarelli, D.F.J., Song, H.K., Poy, F., Schaller, M.D., Eck, M.J., 2006. Crystal Structure of the FERM Domain of Focal Adhesion Kinase *. J. Biol. Chem. 281, 252–259. https://doi.org/10.1074/jbc.M509188200

Chatterjee, C., Schertl, P., Frommer, M., Ludwig-Husemann, A., Mohra, A., Dilger, N., Naolou, T., Meermeyer, S., Bergmann, T.C., Alonso Calleja, A., Lee-Thedieck, C., 2021. Rebuilding the hematopoietic stem cell niche: Recent developments and future prospects. Acta Biomater., Biomaterials for Personalized Disease Models 132, 129–148. https://doi.org/10.1016/j.actbio.2021.03.061

Chen, Y., Möbius, S., Riege, K., Hoffmann, S., Hochhaus, A., Ernst, T., Rudolph, K.L., 2023. Genetic separation of chronic myeloid leukemia stem cells from normal hematopoietic stem cells at single-cell resolution. Leukemia 37, 1561–1566. https://doi.org/10.1038/s41375-023-01929-6

Chen, Z., Guo, Q., Song, G., Hou, Y., 2022. Molecular regulation of hematopoietic stem cell quiescence. Cell. Mol. Life Sci. 79, 218. https://doi.org/10.1007/s00018-022-04200-w

Chow, D.C., Wenning, L.A., Miller, W.M., Papoutsakis, E.T., 2001. Modeling pO(2) distributions in the bone marrow hematopoietic compartment. II. Modified Kroghian models. Biophys. J. 81, 685–696. https://doi.org/10.1016/S0006-3495(01)75733-5

Chramiec, A., Vunjak-Novakovic, G., 2019. Tissue engineered models of healthy and malignant human bone marrow. Adv. Drug Deliv. Rev. 140, 78–92. https://doi.org/10.1016/j.addr.2019.04.003

Christen, P., Jaussi, R., Benoit, R., 2016. Biochemie und Molekularbiologie: Eine Einführung in 40 Lerneinheiten. Springer, Berlin, Heidelberg. https://doi.org/10.1007/978-3-662-46430-4

Cirulli, V., Yebra, M., 2007. Netrins: beyond the brain. Nat. Rev. Mol. Cell Biol. 8, 296–306. https://doi.org/10.1038/nrm2142

Civin, C.I., Strauss, L.C., Brovall, C., Fackler, M.J., Schwartz, J.F., Shaper, J.H., 1984. Antigenic analysis of hematopoiesis. III. A hematopoietic progenitor cell surface antigen defined by a monoclonal antibody raised against KG-1a cells. J. Immunol. 133, 157–165. https://doi.org/10.4049/jimmunol.133.1.157

Colognato, H., Yurchenco, P.D., 2000. Form and function: the laminin family of heterotrimers. Dev. Dyn. Off. Publ. Am. Assoc. Anat. 218, 213–234. https://doi.org/10.1002/(SICI)1097-0177(200006)218:2<213::AID-DVDY1>3.0.CO;2-R

Conneally, E., Cashman, J., Petzer, A., Eaves, C., 1997. Expansion in vitro of transplantable human cord blood stem cells demonstrated using a quantitative assay of their lympho-myeloid repopulating activity in nonobese diabetic–scid/scid mice. Proc. Natl. Acad. Sci. 94, 9836–9841. https://doi.org/10.1073/pnas.94.18.9836

Daniel, M.G., Lemischka, I.R., Moore, K., 2016. Converting cell fates: generating hematopoietic stem cells de novo via transcription factor reprogramming. Ann. N. Y. Acad. Sci. 1370, 24–35. https://doi.org/10.1111/nyas.12989

Dausinas Ni, P., Hartman, M., Slack, J., Basile, C., Liu, S., Wan, J., O'Leary, H.A., 2023. Novel differential calcium regulation of hematopoietic stem and progenitor cells under physiological low oxygen conditions. J. Cell. Physiol. 238, 1492–1506. https://doi.org/10.1002/jcp.30942

de Pereda, J.M., Wiche, G., Liddington, R.C., 1999. Crystal structure of a tandem pair of fibronectin type III domains from the cytoplasmic tail of integrin alpha6beta4. EMBO J. 18, 4087–4095. https://doi.org/10.1093/emboj/18.15.4087

Delaissé, J.M., Engsig, M.T., Everts, V., del Carmen Ovejero, M., Ferreras, M., Lund, L., Vu, T.H., Werb, Z., Winding, B., Lochter, A., Karsdal, M.A., Troen, T., Kirkegaard, T., Lenhard, T., Heegaard, A.M., Neff, L., Baron, R., Foged, N.T., 2000. Proteinases in bone resorption: obvious and less obvious roles. Clin. Chim. Acta Int. J. Clin. Chem. 291, 223–234. https://doi.org/10.1016/s0009-8981(99)00230-2

DeMali, K.A., Barlow, C.A., Burridge, K., 2002a. Recruitment of the Arp2/3 complex to vinculin: coupling membrane protrusion to matrix adhesion. J. Cell Biol. 159, 881–891. https://doi.org/10.1083/jcb.200206043

Dikic, I., Dikic, I., Schlessinger, J., 1998. Identification of a new Pyk2 isoform implicated in chemokine and antigen receptor signaling. J. Biol. Chem. 273, 14301–14308. https://doi.org/10.1074/jbc.273.23.14301

Ding, L., Morrison, S.J., 2013. Haematopoietic stem cells and early lymphoid progenitors occupy distinct bone marrow niches. Nature 495, 231–235. https://doi.org/10.1038/nature11885

Ding, L., Saunders, T.L., Enikolopov, G., Morrison, S.J., 2012. Endothelial and perivascular cells maintain haematopoietic stem cells. Nature 481, 457–62. https://doi.org/10.1038/nature10783

Doulatov, S., Notta, F., Laurenti, E., Dick, J.E., 2012. Hematopoiesis: A Human Perspective. Cell Stem Cell 10, 120–136. https://doi.org/10.1016/j.stem.2012.01.006

Drexler, H.G., MacLeod, R.A.F., Nagel, S., Dirks, W.G., Uphoff, C.C., Steube, K.G., Quentmeier, H., 2005. Guide to Leukemia-Lymphoma Cell Lines on CD. Blood 106, 4340–4340. https://doi.org/10.1182/blood.V106.11.4340.4340

Du, Q.-S., Ren, X.-R., Xie, Y., Wang, Q., Mei, L., Xiong, W.-C., 2001. Inhibition of PYK2-induced actin cytoskeleton reorganization, PYK2 autophosphorylation and focal adhesion targeting by FAK. J. Cell Sci. 114, 2977–2987. https://doi.org/10.1242/jcs.114.16.2977

Duong, L.T., Rodan, G.A., 2000. PYK2 is an adhesion kinase in macrophages, localized in podosomes and activated by beta(2)-integrin ligation. Cell Motil. Cytoskeleton 47, 174–188. https://doi.org/10.1002/1097-0169(200011)47:3<174::AID-CM2>3.0.CO;2-N

Dylla, S.J., Deyle, D.R., Theunissen, K., Padurean, A.M., Verfaillie, C.M., 2004. Integrin engagement-induced inhibition of human myelopoiesis is mediated by proline-rich tyrosine kinase 2 gene products. Exp. Hematol. 32, 365–374. https://doi.org/10.1016/j.exphem.2004.01.001

Eleniste, P.P., Bruzzaniti, A., 2012a. Focal Adhesion Kinases in Adhesion Structures and Disease. J. Signal Transduct. 2012, 296450. https://doi.org/10.1155/2012/296450

Felschow, D.M., McVeigh, M.L., Hoehn, G.T., Civin, C.I., Fackler, M.J., 2001. The adapter protein CrkL associates with CD34. Blood 97, 3768–3775. https://doi.org/10.1182/blood.v97.12.3768

Ferrari, R., Martin, G., Tagit, O., Guichard, A., Cambi, A., Voituriez, R., Vassilopoulos, S., Chavrier, P., 2019. MT1-MMP directs force-producing proteolytic contacts that drive tumor cell invasion. Nat. Commun. 10, 1–15. https://doi.org/10.1038/s41467-019-12930-y

Ferreira, T., Rasband, W., n.d. ImageJ User Guide - IJ 1.46r [WWW Document]. ImageJ User Guide. URL https://imagej.nih.gov/ij/docs/guide/146.html (accessed 8.9.23).

Fina, L., Molgaard, H.V., Robertson, D., Bradley, N.J., Monaghan, P., Delia, D., Sutherland, D.R., Baker, M.A., Greaves, M.F., 1990. Expression of the CD34 gene in vascular endothelial cells. Blood 75, 2417–2426.

Fišerová, J., Schwarzerová, K., Petrášek, J., Opatrný, Z., 2006. ARP2 and ARP3 are localized to sites of actin filament nucleation in tobacco BY-2 cells. Protoplasma 227, 119–128. https://doi.org/10.1007/s00709-006-0146-6

Fonseca, A.-V., Freund, D., Bornhäuser, M., Corbeil, D., 2010. Polarization and Migration of Hematopoietic Stem and Progenitor Cells Rely on the RhoA/ROCK I Pathway and an Active Reorganization of the Microtubule Network. J. Biol. Chem. 285, 31661–31671. https://doi.org/10.1074/jbc.M110.145037

Fournier, M.F., Sauser, R., Ambrosi, D., Meister, J.-J., Verkhovsky, A.B., 2010. Force transmission in migrating cells. J. Cell Biol. 188, 287–297. https://doi.org/10.1083/jcb.200906139

Gekas, C., Graf, T., 2013. CD41 expression marks myeloid-biased adult hematopoietic stem cells and increases with age. Blood 121, 4463–4472. https://doi.org/10.1182/blood-2012-09-457929

Gelman, I., 2003. Pyk 2 FAKs, any two FAKs. Cell Biol. Int. 27, 507–510. https://doi.org/10.1016/S1065-6995(03)00078-7

Giebel, B., 2007. Cell Polarity and Asymmetric Cell Division within Human Hematopoietic Stem and Progenitor Cells. Cells Tissues Organs 188, 116–126. https://doi.org/10.1159/000112842

Giebel, B., Corbeil, D., Beckmann, J., Höhn, J., Freund, D., Giesen, K., Fischer, J., Kögler, G., Wernet, P., 2004. Segregation of lipid raft markers including CD133 in polarized human hematopoietic stem and progenitor cells. Blood 104, 2332–8. https://doi.org/10.1182/blood-2004-02-0511

Gimona, M., Buccione, R., Courtneidge, S.A., Linder, S., 2008. Assembly and biological role of podosomes and invadopodia. Curr. Opin. Cell Biol., Cell regulation 20, 235–241. https://doi.org/10.1016/j.ceb.2008.01.005

Goley, E.D., Welch, M.D., 2006. The ARP2/3 complex: an actin nucleator comes of age. Nat. Rev. Mol. Cell Biol. 7, 713–26. https://doi.org/10.1038/nrm2026

Grassinger, J., Haylock, D.N., Storan, M.J., Haines, G.O., Williams, B., Whitty, G.A., Vinson, A.R., Be, C.L., Li, S., Sørensen, E.S., Tam, P.P.L., Denhardt, D.T., Sheppard, D., Choong, P.F., Nilsson, S.K., 2009. Thrombin-cleaved osteopontin regulates hemopoietic stem and progenitor cell functions through interactions with alpha9beta1 and alpha4beta1 integrins. Blood 114, 49–59. https://doi.org/10.1182/blood-2009-01-197988

Gu, Y.-C., Kortesmaa, J., Tryggvason, K., Persson, J., Ekblom, P., Jacobsen, S.-E., Ekblom, M., 2003. Laminin isoform–specific promotion of adhesion and migration of human bone marrow progenitor cells. Blood 101, 877–885. https://doi.org/10.1182/blood-2002-03-0796

Ha, V.L., Bharti, S., Inoue, H., Vass, W.C., Campa, F., Nie, Z., Gramont, A., Ward, Y., Randazzo, P.A., 2008. ASAP3 Is a Focal Adhesion-associated Arf GAP That Functions in Cell Migration and Invasion*S. J. Biol. Chem. 283, 14915–26. https://doi.org/10.1074/jbc.M709717200

Hannum, C., Culpepper, J., Campbell, D., McClanahan, T., Zurawski, S., Kastelein, R., Bazan, J.F., Hudak, S., Wagner, J., Mattson, J., Luh, J., Duda, G., Martina, N., Peterson, D., Menon, S., Shanafelt, A., Muench, M., Kelner, G., Namikawa, R., Rennick, D., Roncarolo, M.-G., Zlotnik, A., Rosnet, O., Dubreuil, P., Birnbaum, D., Lee, F., 1994. Ligand for FLT3/FLK2 receptor tyrosine kinase regulates growth of haematopoietic stem cells and is encoded by variant RNAs. Nature 368, 643–648. https://doi.org/10.1038/368643a0

Haylock, D.N., Nilsson, S.K., 2006. Osteopontin: a bridge between bone and blood. Br. J. Haematol. 134, 467–474. https://doi.org/10.1111/j.1365-2141.2006.06218.x

Herzog, R., van, den D.K., Cervero, P., Linder, S., 2020. Poji: a Fiji-based tool for analysis of podosomes and associated proteins. J. Cell Sci. 133. https://doi.org/10.1242/jcs.238964

Hess, N.J., Lindner, P.N., Vazquez, J., Grindel, S., Hudson, A.W., Stanic, A.K., Ikeda, A., Hematti, P., Gumperz, J.E., 2020. Different Human Immune Lineage Compositions

Are Generated in Non-Conditioned NBSGW Mice Depending on HSPC Source. Front. Immunol. 11, 573406. https://doi.org/10.3389/fimmu.2020.573406

Hines, M., Nielsen, L., Cooper-White, J., 2008. The hematopoietic stem cell niche: what are we trying to replicate? J. Chem. Technol. Biotechnol. 83, 421–443. https://doi.org/10.1002/jctb.1856

Hitchcock, I.S., Kaushansky, K., 2014. Thrombopoietin from beginning to end. Br. J. Haematol. 165, 259–68. https://doi.org/10.1111/bjh.12772

Hoffman, B.D., 2014. Chapter One - The Detection and Role of Molecular Tension in Focal Adhesion Dynamics, in: Engler, A.J., Kumar, S. (Eds.), Progress in Molecular Biology and Translational Science, Mechanotransduction. Academic Press, pp. 3–24. https://doi.org/10.1016/B978-0-12-394624-9.00001-4

Holst, J., Watson, S., Lord, M.S., Eamegdool, S.S., Bax, D.V., Nivison-Smith, L.B., Kondyurin, A., Ma, L., Oberhauser, A.F., Weiss, A.S., Rasko, J.E.J., 2010. Substrate elasticity provides mechanical signals for the expansion of hemopoietic stem and progenitor cells. Nat. Biotechnol. 28, 1123–8. https://doi.org/10.1038/nbt.1687

Hoshino, D., Branch, K.M., Weaver, A.M., 2013. Signaling inputs to invadopodia and podosomes. J. Cell Sci. 126, 2979–89. https://doi.org/10.1242/jcs.079475

Hümmer, J., Koc, J., Rosenhahn, A., Lee-Thedieck, C., 2019. Microfluidic Shear Force Assay to Determine Cell Adhesion Forces, in: Klein, G., Wuchter, P. (Eds.), Stem Cell Mobilization: Methods and Protocols, Methods in Molecular Biology. Springer, New York, NY, pp. 71–84. https://doi.org/10.1007/978-1-4939-9574-5_6

Hurst, I.R., Zuo, J., Jiang, J., Holliday, L.S., 2004. Actin-related protein 2/3 complex is required for actin ring formation. J. Bone Miner. Res. Off. J. Am. Soc. Bone Miner. Res. 19, 499–506. https://doi.org/10.1359/JBMR.0301238

Huss, R., 2000. Isolation of primary and immortalized CD34-hematopoietic and mesenchymal stem cells from various sources. Stem Cells Dayt. Ohio 18, 1–9. https://doi.org/10.1634/stemcells.18-1-1

Hynes, R.O., 1990. Fibronectins, Springer Series in Molecular Biology. Springer, New York, NY. https://doi.org/10.1007/978-1-4612-3264-3

Iizuka, S., Leon, R.P., Gribbin, K.P., Zhang, Y., Navarro, J., Smith, R., Devlin, K., Wang, L.G., Gibbs, S.L., Korkola, J., Nan, X., Courtneidge, S.A., 2020. Crosstalk between invadopodia and the extracellular matrix. https://doi.org/10.1101/2020.02.26.966762

Inlay, M.A., Bhattacharya, D., Sahoo, D., Serwold, T., Seita, J., Karsunky, H., Plevritis, S.K., Dill, D.L., Weissman, I.L., 2009. Ly6d marks the earliest stage of B-cell specification and identifies the branchpoint between B-cell and T-cell development. Genes Dev. 23, 2376–2381. https://doi.org/10.1101/gad.1836009

Jacquemet, G., Paatero, I., Carisey, A.F., Padzik, A., Orange, J.S., Hamidi, H., Ivaska, J., 2017. FiloQuant reveals increased filopodia density during breast cancer progression. J. Cell Biol. 216, 3387–3403. https://doi.org/10.1083/jcb.201704045

Jeannot, P., Besson, A., 2020. Cortactin function in invadopodia. Small GTPases 11, 256–270. https://doi.org/10.1080/21541248.2017.1405773

Joosten, B., Willemse, M., Fransen, J., Cambi, A., van den Dries, K., 2018. Super-Resolution Correlative Light and Electron Microscopy (SR-CLEM) Reveals Novel Ultrastructural Insights Into Dendritic Cell Podosomes. Front. Immunol. 9, 1908. https://doi.org/10.3389/fimmu.2018.01908

Juin, A., Billottet, C., Moreau, V., Destaing, O., Albiges-Rizo, C., Rosenbaum, J., Génot, E., Saltel, F., 2012. Physiological type I collagen organization induces the formation of a novel class of linear invadosomes. Mol. Biol. Cell 23, 297–309. https://doi.org/10.1091/mbc.E11-07-0594

Karamitros, D., Stoilova, B., Aboukhalil, Z., Hamey, F., Reinisch, A., Samitsch, M., Quek, L., Otto, G., Repapi, E., Doondeea, J., Usukhbayar, B., Calvo, J., Taylor, S., Goardon, N., Six, E., Pflumio, F., Porcher, C., Majeti, R., Göttgens, B., Vyas, P., 2018. Single-cell analysis reveals the continuum of human lympho-myeloid progenitor cells. Nat. Immunol. 19, 85–97. https://doi.org/10.1038/s41590-017-0001-2

Kent, D., Copley, M., Benz, C., Dykstra, B., Bowie, M., Eaves, C., 2008. Regulation of hematopoietic stem cells by the steel factor/KIT signaling pathway. Clin. Cancer Res.

Off. J. Am. Assoc. Cancer Res. 14, 1926–30. https://doi.org/10.1158/1078-0432.CCR-07-5134

Khurana, S., Schouteden, S., Manesia, J.K., Santamaria-Martínez, A., Huelsken, J., Lacy-Hulbert, A., Verfaillie, C.M., 2016. Outside-in integrin signalling regulates haematopoietic stem cell function via Periostin-Itgav axis. Nat. Commun. 7, 13500. https://doi.org/10.1038/ncomms13500

Kiel, M.J., Yilmaz, Omer H., Iwashita, T., Yilmaz, Osman H., Terhorst, C., Morrison, S.J., 2005. SLAM family receptors distinguish hematopoietic stem and progenitor cells and reveal endothelial niches for stem cells. Cell 121, 1109–1121. https://doi.org/10.1016/j.cell.2005.05.026

Kikushige, Y., Yoshimoto, G., Miyamoto, T., Iino, T., Mori, Y., Iwasaki, H., Niiro, H., Takenaka, K., Nagafuji, K., Harada, M., Ishikawa, F., Akashi, K., 2008. Human Flt3 is expressed at the hematopoietic stem cell and the granulocyte/macrophage progenitor stages to maintain cell survival. J. Immunol. Baltim. Md 1950 180, 7358–67. https://doi.org/10.4049/jimmunol.180.11.7358

Kim, M.Y., Yu, K.-R., Kenderian, S.S., Ruella, M., Chen, S., Shin, T.-H., Aljanahi, A.A., Schreeder, D., Klichinsky, M., Shestova, O., Kozlowski, M.S., Cummins, K.D., Shan, X., Shestov, M., Bagg, A., Morrissette, J.J.D., Sekhri, P., Lazzarotto, C.R., Calvo, K.R., Kuhns, D.B., Donahue, R.E., Behbehani, G.K., Tsai, S.Q., Dunbar, C.E., Gill, S., 2018. Genetic Inactivation of CD33 in Hematopoietic Stem Cells to Enable CAR T Cell Immunotherapy for Acute Myeloid Leukemia. Cell 173, 1439-1453.e19. https://doi.org/10.1016/j.cell.2018.05.013

Kim, Y.-J., Broxmeyer, H.E., 2011. Immune regulatory cells in umbilical cord blood and their potential roles in transplantation tolerance. Crit. Rev. Oncol. Hematol. 79, 112–126. https://doi.org/10.1016/j.critrevonc.2010.07.009

Klein, G., 1995. The extracellular matrix of the hematopoietic microenvironment. Experientia 51, 914–926. https://doi.org/10.1007/BF01921741

Klein, G., Beck, S., Müller, C.A., 1993. Tenascin is a cytoadhesive extracellular matrix component of the human hematopoietic microenvironment. J. Cell Biol. 123, 1027–1035. https://doi.org/10.1083/jcb.123.4.1027

Koenigsmann, M., Griffin, J.D., DiCarlo, J., Cannistra, S.A., 1992. Myeloid and erythroid progenitor cells from normal bone marrow adhere to collagen type I. Blood 79, 657–665.

Kondo, M., Weissman, I.L., Akashi, K., 1997. Identification of Clonogenic Common Lymphoid Progenitors in Mouse Bone Marrow. Cell 91, 661–672. https://doi.org/10.1016/S0092-8674(00)80453-5

Kulkarni, R., Kale, V., 2020. Physiological Cues Involved in the Regulation of Adhesion Mechanisms in Hematopoietic Stem Cell Fate Decision. Front. Cell Dev. Biol. 8, 611. https://doi.org/10.3389/fcell.2020.00611

Kunisaki, Y., Bruns, I., Scheiermann, C., Ahmed, J., Pinho, S., Zhang, D., Mizoguchi, T., Wei, Q., Lucas, D., Ito, K., Mar, J.C., Bergman, A., Frenette, P.S., 2013. Arteriolar niches maintain haematopoietic stem cell quiescence. Nature 502, 637–43. https://doi.org/10.1038/nature12612

Kurreck, J., Engels, J.W., Lottspeich, F. (Eds.), 2022. Bioanalytik. Springer Berlin Heidelberg, Berlin, Heidelberg. https://doi.org/10.1007/978-3-662-61707-6

Labernadie, A., Bouissou, A., Delobelle, P., Balor, S., Voituriez, R., Proag, A., Fourquaux, I., Thibault, C., Vieu, C., Poincloux, R., Charrière, G.M., Maridonneau-Parini, I., 2014. Protrusion force microscopy reveals oscillatory force generation and mechanosensing activity of human macrophage podosomes. Nat. Commun. 5, 5343. https://doi.org/10.1038/ncomms6343

Lampreia, F.P., Carmelo, J.G., Anjos-Afonso, F., 2017. Notch Signaling in the Regulation of Hematopoietic Stem Cell. Curr. Stem Cell Rep. 3, 202–209. https://doi.org/10.1007/s40778-017-0090-8

Laszlo, G.S., Estey, E.H., Walter, R.B., 2014. The past and future of CD33 as therapeutic target in acute myeloid leukemia. Blood Rev. 28, 143–153. https://doi.org/10.1016/j.blre.2014.04.001

Lee, D., Kim, D.W., Cho, J.-Y., 2020. Role of growth factors in hematopoietic stem cell niche. Cell Biol. Toxicol. 36, 131–144. https://doi.org/10.1007/s10565-019-09510-7

Lee-Thedieck, C., Rauch, N., Fiammengo, R., Klein, G., Spatz, J.P., 2012. Impact of substrate elasticity on human hematopoietic stem and progenitor cell adhesion and motility. J. Cell Sci. 125, 3765–75. https://doi.org/10.1242/jcs.095596

Lee-Thedieck, C., Schertl, P., Klein, G., 2022. The extracellular matrix of hematopoietic stem cell niches. Adv. Drug Deliv. Rev. 181, 114069. https://doi.org/10.1016/j.addr.2021.114069

Leiss, M., Beckmann, K., Girós, A., Costell, M., Fässler, R., 2008. The role of integrin binding sites in fibronectin matrix assembly in vivo. Curr. Opin. Cell Biol., Cell-to-cell contact and extracellular matrix 20, 502–507. https://doi.org/10.1016/j.ceb.2008.06.001

Levesque, J.-P., Winkler, I.G., 2016. Cell Adhesion Molecules in Normal and Malignant Hematopoiesis: from Bench to Bedside. Curr. Stem Cell Rep. 2, 356–367. https://doi.org/10.1007/s40778-016-0066-0

Liman, J., Bueno, C., Eliaz, Y., Schafer, N.P., Waxham, M.N., Wolynes, P.G., Levine, H., Cheung, M.S., 2020. The role of the Arp2/3 complex in shaping the dynamics and structures of branched actomyosin networks. Proc. Natl. Acad. Sci. U. S. A. 117, 10825–10831. https://doi.org/10.1073/pnas.1922494117

Lin, K., Asaro, R.J., 2022. Nascent Adhesion Clustering: Integrin-Integrin and Integrin-Substrate Interactions. Biophysica 2, 34–58. https://doi.org/10.3390/biophysica2010004

Linder, S., 2007. The matrix corroded: podosomes and invadopodia in extracellular matrix degradation. Trends Cell Biol. 17, 107–117. https://doi.org/10.1016/j.tcb.2007.01.002

Linder, S., Cervero, P., Eddy, R., Condeelis, J., 2023. Mechanisms and roles of podosomes and invadopodia. Nat. Rev. Mol. Cell Biol. 24, 86–106. https://doi.org/10.1038/s41580-022-00530-6

Liu, A., Wang, Y., Ding, Y., Baez, I., Payne, K.J., Borghesi, L., 2015. Hematopoietic stem cell expansion and common lymphoid progenitor depletion requires hematopoietic-derived, cell-autonomous TLR4 in a model of chronic endotoxin. J. Immunol. Baltim. Md 1950 195, 2524–2528. https://doi.org/10.4049/jimmunol.1501231

Long, M., Dixit, V., 1990. Thrombospondin functions as a cytoadhesion molecule for human hematopoietic progenitor cells. Blood 75, 2311–2318. https://doi.org/10.1182/blood.V75.12.2311.2311

Long, M.W., Briddell, R., Walter, A.W., Bruno, E., Hoffman, R., 1992. Human hematopoietic stem cell adherence to cytokines and matrix molecules. J. Clin. Invest. 90, 251–255. https://doi.org/10.1172/JCI115844

Macaulay, I.C., Svensson, V., Labalette, C., Ferreira, L., Hamey, F., Voet, T., Teichmann, S.A., Cvejic, A., 2016. Single-Cell RNA-Sequencing Reveals a Continuous Spectrum of Differentiation in Hematopoietic Cells. Cell Rep. 14, 966–977. https://doi.org/10.1016/j.celrep.2015.12.082

MacMillan, M.L., Weisdorf, D.J., Brunstein, C.G., Cao, Q., DeFor, T.E., Verneris, M.R., Blazar, B.R., Wagner, J.E., 2009. Acute graft-versus-host disease after unrelated donor umbilical cord blood transplantation: analysis of risk factors. Blood 113, 2410–2415. https://doi.org/10.1182/blood-2008-07-163238

Majeti, R., Park, C.Y., Weissman, I.L., 2007. Identification of a Hierarchy of Multipotent Hematopoietic Progenitors in Human Cord Blood. Cell Stem Cell 1, 635–645. https://doi.org/10.1016/j.stem.2007.10.001

Mathé, G., Amiel, J.L., Schwarzenberg, L., Cattan, A., Schneider, M., DE VRIES, M.J., TUBIANA, M., LALANNE, C., BINET, J.L., PAPIERNIK, M., SEMAN, G., MATSUKURA, M., MERY, A.M., SCHWARZMANN, V., FLAISLER, A., 1965. Successful Allogenic Bone Marrow Transplantation in Man: Chimerism, Induced Specific Tolerance and Possible Anti-Leukemic Effects. Blood 25, 179–196. https://doi.org/10.1182/blood.V25.2.179.179

Mayani, H., 2019. Human Hematopoietic Stem Cells: Concepts and Perspectives on the Biology and Use of Fresh Versus In Vitro–Generated Cells for Therapeutic

Applications. Curr. Stem Cell Rep. 5, 115–124. https://doi.org/10.1007/s40778-019-00162-1

McLellan, A.D., Kämpgen, E., 2000. Functions of myeloid and lymphoid dendritic cells. Immunol. Lett. 72, 101–105. https://doi.org/10.1016/s0165-2478(00)00167-x

Mitchison, T., Kirschner, M., 1988. Cytoskeletal dynamics and nerve growth. Neuron 1, 761–772. https://doi.org/10.1016/0896-6273(88)90124-9

Miyamoto, T., 2013. Role of osteoclasts in regulating hematopoietic stem and progenitor cells. World J. Orthop. 4, 198–206. https://doi.org/10.5312/wjo.v4.i4.198

Momin, A.A., Mendes, T., Barthe, P., Faure, C., Hong, S., Yu, P., Kadaré, G., Jaremko, M., Girault, J.-A., Jaremko, Ł., Arold, S.T., 2022. PYK2 senses calcium through a disordered dimerization and calmodulin-binding element. Commun. Biol. 5, 1–15. https://doi.org/10.1038/s42003-022-03760-8

Moore, K.A., Lemischka, I.R., 2006. Stem Cells and Their Niches. Science 311, 1880–1885. https://doi.org/10.1126/science.1110542

Morrison, S.J., Scadden, D.T., 2014. The bone marrow niche for haematopoietic stem cells. Nature 505, 327–334. https://doi.org/10.1038/nature12984

Nagasawa, T., 2014. CXC chemokine ligand 12 (CXCL12) and its receptor CXCR4. J. Mol. Med. Berl. Ger. 92, 433–439. https://doi.org/10.1007/s00109-014-1123-8

Nagasawa, T., 2006. Microenvironmental niches in the bone marrow required for B-cell development. Nat. Rev. Immunol. 6, 107–116. https://doi.org/10.1038/nri1780

Netelenbos, T., van den Born, J., Kessler, F.L., Zweegman, S., Merle, P.A., van Oostveen, J.W., Zwaginga, J.J., Huijgens, P.C., Dräger, A.M., 2003. Proteoglycans on bone marrow endothelial cells bind and present SDF-1 towards hematopoietic progenitor cells. Leukemia 17, 175–184. https://doi.org/10.1038/sj.leu.2402738

Netsrithong, R., Suwanpitak, S., Boonkaew, B., Trakarnsanga, K., Chang, L.-J., Tipgomut, C., Vatanashevanopakorn, C., Pattanapanyasat, K., Wattanapanitch, M., 2020. Multilineage differentiation potential of hematoendothelial progenitors derived from human induced pluripotent stem cells. Stem Cell Res. Ther. 11, 481. https://doi.org/10.1186/s13287-020-01997-w

Nilsson, S.K., Johnston, H.M., Whitty, G.A., Williams, B., Webb, R.J., Denhardt, D.T., Bertoncello, I., Bendall, L.J., Simmons, P.J., Haylock, D.N., 2005. Osteopontin, a key component of the hematopoietic stem cell niche and regulator of primitive hematopoietic progenitor cells. Blood 106, 1232–1239. https://doi.org/10.1182/blood-2004-11-4422

Notta, F., Doulatov, S., Laurenti, E., Poeppl, A., Jurisica, I., Dick, J.E., 2011. Isolation of Single Human Hematopoietic Stem Cells Capable of Long-Term Multilineage Engraftment. Science 333, 218–221. https://doi.org/10.1126/science.1201219

Ohmori, T., Kashiwakura, Y., Ishiwata, A., Madoiwa, S., Mimuro, J., Furukawa, Y., Sakata, Y., 2010. Vinculin is indispensable for repopulation by hematopoietic stem cells, independent of integrin function. J. Biol. Chem. 285, 31763–31773. https://doi.org/10.1074/jbc.M109.099085

Oostendorp, R.A.J., Dörmer, P., 1997. VLA-4-Mediated Interactions Between Normal Human Hematopoietic Progenitors and Stromal Cells. Leuk. Lymphoma. https://doi.org/10.3109/10428199709055581

Osawa, M., Hanada, K., Hamada, H., Nakauchi, H., 1996. Long-term lymphohematopoietic reconstitution by a single CD34-low/negative hematopoietic stem cell. Science 273, 242–245. https://doi.org/10.1126/science.273.5272.242

Page, K.M., Zhang, L., Mendizabal, A., Wease, S., Carter, S., Gentry, T., Balber, A.E., Kurtzberg, J., 2011. Total Colony-Forming Units Are a Strong, Independent Predictor of Neutrophil and Platelet Engraftment after Unrelated Umbilical Cord Blood Transplantation: A Single-Center Analysis of 435 Cord Blood Transplants. Biol. Blood Marrow Transplant. 17, 1362–1374. https://doi.org/10.1016/j.bbmt.2011.01.011

Pal, K., Tu, Y., Wang, X., 2022. Single-Molecule Force Imaging Reveals That Podosome Formation Requires No Extracellular Integrin-Ligand Tensions or Interactions. ACS Nano 16, 2481–2493. https://doi.org/10.1021/acsnano.1c09105

Pankov, R., Yamada, K.M., 2002. Fibronectin at a glance. J. Cell Sci. 115, 3861–3863. https://doi.org/10.1242/jcs.00059

Partridge, M.A., Marcantonio, E.E., 2006. Initiation of Attachment and Generation of Mature Focal Adhesions by Integrin-containing Filopodia in Cell Spreading. Mol. Biol. Cell 17, 4237–4248. https://doi.org/10.1091/mbc.e06-06-0496

Peled, A., Kollet, O., Ponomaryov, T., Petit, I., Franitza, S., Grabovsky, V., Slav, M.M., Nagler, A., Lider, O., Alon, R., Zipori, D., Lapidot, T., 2000. The chemokine SDF-1 activates the integrins LFA-1, VLA-4, and VLA-5 on immature human CD34+ cells: role in transendothelial/stromal migration and engraftment of NOD/SCID mice. Blood 95, 3289–3296. https://doi.org/10.1182/blood.V95.11.3289

Petit, V., Thiery, J.-P., 2000. Focal adhesions: Structure and dynamics. Biol. Cell 92, 477–494. https://doi.org/10.1016/S0248-4900(00)01101-1

Pfaff, M., Jurdic, P., 2001. Podosomes in osteoclast-like cells: structural analysis and cooperative roles of paxillin, proline-rich tyrosine kinase 2 (Pyk2) and integrin αVβ3. J. Cell Sci. 114, 2775–2786. https://doi.org/10.1242/jcs.114.15.2775

Pinho, S., Frenette, P.S., 2019. Haematopoietic stem cell activity and interactions with the niche. Nat. Rev. Mol. Cell Biol. 20, 303–320. https://doi.org/10.1038/s41580-019-0103-9

Porter, K.R., n.d. Determining Fluorescence Intensity and Signal [WWW Document]. URL https://kpif.umbc.edu/image-processing-resources/imagej-fiji/determining-fluorescence-intensity-and-positive-signal/ (accessed 8.9.23).

Potocnik, A.J., Brakebusch, C., Fässler, R., 2000. Fetal and adult hematopoietic stem cells require beta1 integrin function for colonizing fetal liver, spleen, and bone marrow. Immunity 12, 653–663. https://doi.org/10.1016/s1074-7613(00)80216-2

Poulos, M.G., Guo, P., Kofler, N.M., Pinho, S., Gutkin, M.C., Tikhonova, A., Aifantis, I., Frenette, P.S., Kitajewski, J., Rafii, S., Butler, J.M., 2013. Endothelial Jagged-1 is necessary for homeostatic and regenerative hematopoiesis. Cell Rep. 4, 1022–1034. https://doi.org/10.1016/j.celrep.2013.07.048

Proag, A., Bouissou, A., Mangeat, T., Voituriez, R., Delobelle, P., Thibault, C., Vieu, C., Maridonneau-Parini, I., Poincloux, R., 2015. Working Together: Spatial Synchrony in the Force and Actin Dynamics of Podosome First Neighbors. ACS Nano 9, 3800–3813. https://doi.org/10.1021/nn506745r

Puhr, S., Lee, J., Zvezdova, E., Zhou, Y.J., Liu, K., 2015. Dendritic Cell Development – History, Advances, and Open Questions. Semin. Immunol. 27, 388–396. https://doi.org/10.1016/j.smim.2016.03.012

Rademakers, T., Goedhart, M., Hoogenboezem, M., García Ponce, A., van Rijssel, J., Samus, M., Schnoor, M., Butz, S., Huveneers, S., Vestweber, D., Nolte, M.A., Voermans, C., van Buul, J.D., 2018. Hematopoietic Stem and Progenitor Cells Use Podosomes to Transcellularly Home to the Bone Marrow. https://doi.org/10.1101/269704

Reichert, D., Friedrichs, J., Ritter, S., Käubler, T., Werner, C., Bornhäuser, M., Corbeil, D., 2015. Phenotypic, Morphological and Adhesive Differences of Human Hematopoietic Progenitor Cells Cultured on Murine versus Human Mesenchymal Stromal Cells. Sci. Rep. 5, 15680. https://doi.org/10.1038/srep15680

Renders, S., Svendsen, A.F., Panten, J., Rama, N., Maryanovich, M., Sommerkamp, P., Ladel, L., Redavid, A.R., Gibert, B., Lazare, S., Ducarouge, B., Schönberger, K., Narr, A., Tourbez, M., Dethmers-Ausema, B., Zwart, E., Hotz-Wagenblatt, A., Zhang, D., Korn, C., Zeisberger, P., Przybylla, A., Sohn, M., Mendez-Ferrer, S., Heikenwälder, M., Brune, M., Klimmeck, D., Bystrykh, L., Frenette, P.S., Mehlen, P., de Haan, G., Cabezas-Wallscheid, N., Trumpp, A., 2021. Niche derived netrin-1 regulates hematopoietic stem cell dormancy via its receptor neogenin-1. Nat. Commun. 12, 608. https://doi.org/10.1038/s41467-020-20801-0

Reya, T., Morrison, S.J., Clarke, M.F., Weissman, I.L., 2001. Stem cells, cancer, and cancer stem cells. Nature 414, 105–111. https://doi.org/10.1038/35102167

Ridley, A.J., Schwartz, M.A., Burridge, K., Firtel, R.A., Ginsberg, M.H., Borisy, G., Parsons, J.T., Horwitz, A.R., 2003. Cell migration: integrating signals from front to back. Science 302, 1704–1709. https://doi.org/10.1126/science.1092053

Rieger, M.A., Schroeder, T., 2012. Hematopoiesis. Cold Spring Harb. Perspect. Biol. 4, a008250. https://doi.org/10.1101/cshperspect.a008250

Riggs, D., Yang, Z., Kloss, J., Loftus, J.C., 2011. The Pyk2 FERM regulates Pyk2 complex formation and phosphorylation. Cell. Signal. 23, 288–296. https://doi.org/10.1016/j.cellsig.2010.09.015

Rocha, V., Wagner, J.E., Sobocinski, K.A., Klein, J.P., Zhang, M.-J., Horowitz, M.M., Gluckman, E., 2000. Graft-Versus-Host Disease in Children Who Have Received a Cord-Blood or Bone Marrow Transplant from an HLA-Identical Sibling. N. Engl. J. Med. 342, 1846–1854. https://doi.org/10.1056/NEJM200006223422501

Rodgers, K.D., San Antonio, J.D., Jacenko, O., 2008. Heparan sulfate proteoglycans: a GAGgle of skeletal-hematopoietic regulators. Dev. Dyn. Off. Publ. Am. Assoc. Anat. 237, 2622–42. https://doi.org/10.1002/dvdy.21593

Sackstein, R., Merzaban, J.S., Cain, D.W., Dagia, N.M., Spencer, J.A., Lin, C.P., Wohlgemuth, R., 2008. Ex vivo glycan engineering of CD44 programs human multipotent mesenchymal stromal cell trafficking to bone. Nat. Med. 14, 181–187. https://doi.org/10.1038/nm1703

Sagar, B.M.M., Rentala, S., Gopal, P.N.V., Sharma, S., Mukhopadhyay, A., 2006. Fibronectin and laminin enhance engraftibility of cultured hematopoietic stem cells. Biochem. Biophys. Res. Commun. 350, 1000–1005. https://doi.org/10.1016/j.bbrc.2006.09.140

Saini, P., Courtneidge, S.A., 2018. Tks adaptor proteins at a glance. J. Cell Sci. 131, jcs203661. https://doi.org/10.1242/jcs.203661

Salesse, S., Dylla, S.J., Verfaillie, C.M., 2004. p210BCR/ABL-induced alteration of pre-mRNA splicing in primary human CD34+ hematopoietic progenitor cells. Leukemia 18, 727–733. https://doi.org/10.1038/sj.leu.2403310

Scadden, D.T., 2006. The stem-cell niche as an entity of action. Nature 441, 1075–1079. https://doi.org/10.1038/nature04957

Schachtner, H., Calaminus, S.D.J., Thomas, S.G., Machesky, L.M., 2013. Podosomes in adhesion, migration, mechanosensing and matrix remodeling. Cytoskeleton 70, 572–589. https://doi.org/10.1002/cm.21119

Schafer, D.A., Welch, M.D., Machesky, L.M., Bridgman, P.C., Meyer, S.M., Cooper, J.A., 1998. Visualization and Molecular Analysis of Actin Assembly in Living Cells. J. Cell Biol. 143, 1919–1930. https://doi.org/10.1083/jcb.143.7.1919

Schneider, C.A., Rasband, W.S., Eliceiri, K.W., 2012. NIH Image to ImageJ: 25 years of image analysis. Nat. Methods 9, 671–675. https://doi.org/10.1038/nmeth.2089

Schofield, R., 1978. The relationship between the spleen colony-forming cell and the haemopoietic stem cell. Blood Cells 4, 7–25.

Scott, L.M., Priestley, G.V., Papayannopoulou, T., 2003. Deletion of alpha4 integrins from adult hematopoietic cells reveals roles in homeostasis, regeneration, and homing. Mol. Cell. Biol. 23, 9349–9360. https://doi.org/10.1128/MCB.23.24.9349-9360.2003

Sens, C., Huck, K., Pettera, S., Uebel, S., Wabnitz, G., Moser, M., Nakchbandi, I.A., 2017. Fibronectins containing extradomain A or B enhance osteoblast differentiation via distinct integrins. J. Biol. Chem. 292, 7745–7760. https://doi.org/10.1074/jbc.M116.739987

Serrels, B., Serrels, A., Brunton, V.G., Holt, M., McLean, G.W., Gray, C.H., Jones, G.E., Frame, M.C., 2007. Focal adhesion kinase controls actin assembly via a FERM-mediated interaction with the Arp2/3 complex. Nat. Cell Biol. 9, 1046–1056. https://doi.org/10.1038/ncb1626

Servida, F., Soligo, D., Caneva, L., Bertolini, F., de Harven, E., Campiglio, S., Corsini, C., Deliliers, G.L., 1996. Functional and morphological characterization of immunomagnetically selected CD34+ hematopoietic progenitor cells. Stem Cells Dayt. Ohio 14, 430–438. https://doi.org/10.1002/stem.140430

Shattil, S.J., 2005. Integrins and Src: dynamic duo of adhesion signaling. Trends Cell Biol. 15, 399–403. https://doi.org/10.1016/j.tcb.2005.06.005

Sidney, L.E., Branch, M.J., Dunphy, S.E., Dua, H.S., Hopkinson, A., 2014. Concise Review: Evidence for CD34 as a Common Marker for Diverse Progenitors. Stem Cells Dayt. Ohio 32, 1380–1389. https://doi.org/10.1002/stem.1661

Smith, B.A., Daugherty-Clarke, K., Goode, B.L., Gelles, J., 2013. Pathway of actin filament branch formation by Arp2/3 complex revealed by single-molecule imaging. Proc. Natl. Acad. Sci. 110, 1285–1290. https://doi.org/10.1073/pnas.1211164110

Smith, P.K., Krohn, R.I., Hermanson, G.T., Mallia, A.K., Gartner, F.H., Provenzano, M.D., Fujimoto, E.K., Goeke, N.M., Olson, B.J., Klenk, D.C., 1985. Measurement of protein using bicinchoninic acid. Anal. Biochem. 150, 76–85. https://doi.org/10.1016/0003-2697(85)90442-7

Sommarin, M.N.E., Dhapola, P., Safi, F., Warfvinge, R., Ulfsson, L.G., Erlandsson, E., Konturek-Ciesla, A., Thakur, R.K., Böiers, C., Bryder, D., Karlsson, G., 2021. Single-Cell Multiomics Reveals Distinct Cell States at the Top of the Human Hematopoietic Hierarchy. https://doi.org/10.1101/2021.04.01.437998

Springer, T.A., Wang, J.-H., 2004. The three-dimensional structure of integrins and their ligands, and conformational regulation of cell adhesion. Adv. Protein Chem. 68, 29–63. https://doi.org/10.1016/S0065-3233(04)68002-8

Stylli, S.S., Stacey, T.T.I., Verhagen, A.M., Xu, S.S., Pass, I., Courtneidge, S.A., Lock, P., 2009. Nck adaptor proteins link Tks5 to invadopodia actin regulation and ECM degradation. J. Cell Sci. 122, 2727–2740. https://doi.org/10.1242/jcs.046680

Sugiyama, T., Kohara, H., Noda, M., Nagasawa, T., 2006. Maintenance of the Hematopoietic Stem Cell Pool by CXCL12-CXCR4 Chemokine Signaling in Bone Marrow Stromal Cell Niches. Immunity 25, 977–988. https://doi.org/10.1016/j.immuni.2006.10.016

Sumide, K., Matsuoka, Y., Kawamura, H., Nakatsuka, R., Fujioka, T., Asano, H., Takihara, Y., Sonoda, Y., 2018. A revised road map for the commitment of human cord blood CD34-negative hematopoietic stem cells. Nat. Commun. 9, 2202. https://doi.org/10.1038/s41467-018-04441-z

Sun, Z., Guo, S.S., Fässler, R., 2016. Integrin-mediated mechanotransduction. J. Cell Biol. 215, 445–456. https://doi.org/10.1083/jcb.201609037

Susek, K.H., Korpos, E., Huppert, J., Wu, C., Savelyeva, I., Rosenbauer, F., Müller-Tidow, C., Koschmieder, S., Sorokin, L., 2018. Bone marrow laminins influence hematopoietic stem and progenitor cell cycling and homing to the bone marrow. Matrix Biol. 67, 47–62. https://doi.org/10.1016/j.matbio.2018.01.007

Tabansky, I., Stern, J.N.H., 2016. Basics of Stem Cell Biology as Applied to the Brain, in: Pfaff, D., Christen, Y. (Eds.), Stem Cells in Neuroendocrinology. Springer, Cham (CH).

Taichman, R.S., Reilly, M.J., Emerson, S.G., 1996. Human osteoblasts support human hematopoietic progenitor cells in vitro bone marrow cultures. Blood 87, 518–524.

Takada, Y., Ye, X., Simon, S., 2007. The integrins. Genome Biol. 8, 215. https://doi.org/10.1186/gb-2007-8-5-215

Tammi, M.I., Day, A.J., Turley, E.A., 2002. Hyaluronan and homeostasis: a balancing act. J. Biol. Chem. 277, 4581–4584. https://doi.org/10.1074/jbc.R100037200

Thomas, J.W., Cooley, M.A., Broome, J.M., Salgia, R., Griffin, J.D., Lombardo, C.R., Schaller, M.D., 1999. The role of focal adhesion kinase binding in the regulation of tyrosine phosphorylation of paxillin. J. Biol. Chem. 274, 36684–36692. https://doi.org/10.1074/jbc.274.51.36684

Thomas, L.M., Chu, J., Watkins, S.C., Stolz, D., Salter, R.D., 2008. Extracellular ATP induces IL-1beta secretion and formation of filopodia in myeloid lineage cells through distinct P2X7-dependent pathways. FASEB J. 22, 672.21-672.21. https://doi.org/10.1096/fasebj.22.1_supplement.672.21

Toyama-Sorimachi, N., Tsujimura, Y., Maruya, M., Onoda, A., Kubota, T., Koyasu, S., Inaba, K., Karasuyama, H., 2004. Ly49Q, a member of the Ly49 family that is selectively expressed on myeloid lineage cells and involved in regulation of cytoskeletal

architecture. Proc. Natl. Acad. Sci. 101, 1016–1021.
https://doi.org/10.1073/pnas.0305400101

Traycoff, C.M., Abboud, M.R., Laver, J., Brandt, J.E., Hoffman, R., Law, P., Ishizawa, L., Srour, E.F., 1994. Evaluation of the in vitro behavior of phenotypically defined populations of umbilical cord blood hematopoietic progenitor cells. Exp. Hematol. 22, 215–222.

Umemoto, T., Yamato, M., Ishihara, J., Shiratsuchi, Y., Utsumi, M., Morita, Y., Tsukui, H., Terasawa, M., Shibata, T., Nishida, K., Kobayashi, Y., Petrich, B.G., Nakauchi, H., Eto, K., Okano, T., 2012. Integrin-αvβ3 regulates thrombopoietin-mediated maintenance of hematopoietic stem cells. Blood 119, 83–94. https://doi.org/10.1182/blood-2011-02-335430

van den Dries, K., Linder, S., Maridonneau-Parini, I., Poincloux, R., 2019a. Probing the mechanical landscape – new insights into podosome architecture and mechanics. J. Cell Sci. 132, jcs236828. https://doi.org/10.1242/jcs.236828

van den Dries, K., Meddens, M.B.M., de Keijzer, S., Shekhar, S., Subramaniam, V., Figdor, C.G., Cambi, A., 2013. Interplay between myosin IIA-mediated contractility and actin network integrity orchestrates podosome composition and oscillations. Nat. Commun. 4, 1412. https://doi.org/10.1038/ncomms2402

van den Dries, K., Nahidiazar, L., Slotman, J.A., Meddens, M.B.M., Pandzic, E., Joosten, B., Ansems, M., Schouwstra, J., Meijer, A., Steen, R., Wijers, M., Fransen, J., Houtsmuller, A.B., Wiseman, P.W., Jalink, K., Cambi, A., 2019b. Modular actin nano-architecture enables podosome protrusion and mechanosensing. Nat. Commun. 10, 5171. https://doi.org/10.1038/s41467-019-13123-3

van der Loo, J C, Xiao, X., McMillin, D., Hashino, K., Kato, I., Williams, D.A., 1998. VLA-5 is expressed by mouse and human long-term repopulating hematopoietic cells and mediates adhesion to extracellular matrix protein fibronectin. J. Clin. Invest. 102, 1051–61. https://doi.org/10.1172/JCI3687

Van Der Rest, M., Garrone, R., 1991. Collagen family of proteins. FASEB J. 5, 2814–2823. https://doi.org/10.1096/fasebj.5.13.1916105

Varnum-Finney, B., Purton, L.E., Yu, M., Brashem-Stein, C., Flowers, D., Staats, S., Moore, K.A., Le Roux, I., Mann, R., Gray, G., Artavanis-Tsakonas, S., Bernstein, I.D., 1998. The Notch ligand, Jagged-1, influences the development of primitive hematopoietic precursor cells. Blood 91, 4084–4091.

Varon, C., Tatin, F., Moreau, V., Van Obberghen-Schilling, E., Fernandez-Sauze, S., Reuzeau, E., Kramer, I., Génot, E., 2006. Transforming growth factor beta induces rosettes of podosomes in primary aortic endothelial cells. Mol. Cell. Biol. 26, 3582–3594. https://doi.org/10.1128/MCB.26.9.3582-3594.2006

Velten, L., Haas, S.F., Raffel, S., Blaszkiewicz, S., Islam, S., Hennig, B.P., Hirche, C., Lutz, C., Buss, E.C., Nowak, D., Boch, T., Hofmann, W.-K., Ho, A.D., Huber, W., Trumpp, A., Essers, M.A.G., Steinmetz, L.M., 2017. Human haematopoietic stem cell lineage commitment is a continuous process. Nat. Cell Biol. 19, 271–281. https://doi.org/10.1038/ncb3493

Vicente-Manzanares, M., Choi, C.K., Horwitz, A.R., 2009. Integrins in cell migration – the actin connection. J. Cell Sci. 122, 199–206. https://doi.org/10.1242/jcs.018564

von Au, A., Vasel, M., Kraft, S., Sens, C., Hackl, N., Marx, A., Stroebel, P., Hennenlotter, J., Todenhöfer, T., Stenzl, A., Schott, S., Sinn, H.-P., Wetterwald, A., Bermejo, J.L., Cecchini, M.G., Nakchbandi, I.A., 2013. Circulating fibronectin controls tumor growth. Neoplasia N. Y. N 15, 925–938. https://doi.org/10.1593/neo.13762

Wagers, A.J., Allsopp, R.C., Weissman, I.L., 2002. Changes in integrin expression are associated with altered homing properties of Lin−/loThy1.1loSca-1+c-kit+ hematopoietic stem cells following mobilization by cyclophosphamide/granulocyte colony-stimulating factor. Exp. Hematol. 30, 176–185. https://doi.org/10.1016/S0301-472X(01)00777-9

Wagner, J., Rosenthal, J., Sweetman, R., Shu, X., Davies, S., Ramsay, N., McGlave, P., Sender, L., Cairo, M., 1996. Successful transplantation of HLA-matched and HLA-mismatched umbilical cord blood from unrelated donors: analysis of engraftment and

acute graft-versus-host disease. Blood 88, 795–802.
https://doi.org/10.1182/blood.V88.3.795.795

Wagner, J.E., Barker, J.N., DeFor, T.E., Baker, K.S., Blazar, B.R., Eide, C., Goldman, A., Kersey, J., Krivit, W., MacMillan, M.L., Orchard, P.J., Peters, C., Weisdorf, D.J., Ramsay, N.K.C., Davies, S.M., 2002. Transplantation of unrelated donor umbilical cord blood in 102 patients with malignant and nonmalignant diseases: influence of CD34 cell dose and HLA disparity on treatment-related mortality and survival. Blood 100, 1611–1618. https://doi.org/10.1182/blood-2002-01-0294

Walasek, M.A., van Os, R., Haan, G., 2012. Hematopoietic stem cell expansion: challenges and opportunities. Ann. N. Y. Acad. Sci. 1266, 138–50. https://doi.org/10.1111/j.1749-6632.2012.06549.x

Wang, J.F., Park, I.W., Groopman, J.E., 2000. Stromal cell-derived factor-1alpha stimulates tyrosine phosphorylation of multiple focal adhesion proteins and induces migration of hematopoietic progenitor cells: roles of phosphoinositide-3 kinase and protein kinase C. Blood 95, 2505–2513.

Wang, N., Butler, J.P., Ingber, D.E., 1993. Mechanotransduction across the cell surface and through the cytoskeleton. Science 260, 1124–7. https://doi.org/10.1126/science.7684161

Wei, W.-C., Lin, H.-H., Shen, M.-R., Tang, M.-J., 2008. Mechanosensing machinery for cells under low substratum rigidity. Am. J. Physiol. Cell Physiol. 295, C1579-89. https://doi.org/10.1152/ajpcell.00223.2008

Wirth, F., Lubosch, A., Hamelmann, S., Nakchbandi, I.A., 2020. Fibronectin and Its Receptors in Hematopoiesis. Cells 9, 2717. https://doi.org/10.3390/cells9122717

Xiao, H., Bai, X.-H., Kapus, A., Lu, W.-Y., Mak, A.S., Liu, M., 2010. The Protein Kinase C Cascade Regulates Recruitment of Matrix Metalloprotease 9 to Podosomes and Its Release and Activation. Mol. Cell. Biol. 30, 5545–5561. https://doi.org/10.1128/MCB.00382-10

Yabluchanskiy, A., Ma, Y., Iyer, R.P., Hall, M.E., Lindsey, M.L., 2013. Matrix Metalloproteinase-9: Many Shades of Function in Cardiovascular Disease. Physiology 28, 391–403. https://doi.org/10.1152/physiol.00029.2013

Ye, F., Hu, G., Taylor, D., Ratnikov, B., Bobkov, A.A., McLean, M.A., Sligar, S.G., Taylor, K.A., Ginsberg, M.H., 2010. Recreation of the terminal events in physiological integrin activation. J. Cell Biol. 188, 157–173. https://doi.org/10.1083/jcb.200908045

Zhang, J., Niu, C., Ye, L., Huang, H., He, X., Tong, W.-G., Ross, J., Haug, J., Johnson, T., Feng, J.Q., Harris, S., Wiedemann, L.M., Mishina, Y., Li, L., 2003. Identification of the haematopoietic stem cell niche and control of the niche size. Nature 425, 836–841. https://doi.org/10.1038/nature02041

Zhang, K., Chen, J., 2012. The regulation of integrin function by divalent cations. Cell Adhes. Migr. 6, 20–29. https://doi.org/10.4161/cam.18702

Zhang, Y., Gao, S., Xia, J., Liu, F., 2018. Hematopoietic Hierarchy – An Updated Roadmap. Trends Cell Biol. 28, 976–986. https://doi.org/10.1016/j.tcb.2018.06.001

Zhou, B.O., Yu, H., Yue, R., Zhao, Z., Rios, J.J., Naveiras, O., Morrison, S.J., 2017. Bone marrow adipocytes promote the regeneration of stem cells and hematopoiesis by secreting SCF. Nat. Cell Biol. 19, 891–903. https://doi.org/10.1038/ncb3570

Zhu, J., Luo, B.-H., Xiao, T., Zhang, C., Nishida, N., Springer, T.A., 2008. Structure of a complete integrin ectodomain in a physiologic resting state and activation and deactivation by applied forces. Mol. Cell 32, 849–861. https://doi.org/10.1016/j.molcel.2008.11.018

Zou, Y.-R., Kottmann, A.H., Kuroda, M., Taniuchi, I., Littman, D.R., 1998. Function of the chemokine receptor CXCR4 in haematopoiesis and in cerebellar development. Nature 393, 595–599. https://doi.org/10.1038/31269

Zsebo, K.M., Williams, D.A., Geissler, E.N., Broudy, V.C., Martin, F.H., Atkins, H.L., Hsu, R.Y., Birkett, N.C., Okino, K.H., Murdock, D.C., 1990. Stem cell factor is encoded at the Sl locus of the mouse and is the ligand for the c-kit tyrosine kinase receptor. Cell 63, 213–224. https://doi.org/10.1016/0092-8674(90)90302-u

Acknowledgements/Danksagung

Curriculum Vitae and Publications List

PERSONAL INFORMATION

Name   Miriam Frommer

Date of Birth   04.01.1994

Place of Birth   Hannover

EMPLOYMENT

December 2023 - present **June 2019 - June 2023**	Leibniz University Hannover, Institute for Cell Biology and Biophysics
	Employment as scientific assistant
	Research in Cell-matrix interaction in hematopoietic stem cell niche
	Tutoring and Teaching of Basic Cell Biology and biochemical methods to students of Life Science and Biology
May 2018 - September 2018	Internship in department for Technology & IP /Chemical and Biochemical Sensors at Drägerwerk AG & Co. KGaA
	Development of new strategies in ultrafast detection of drugs in saliva using immunochromatographic test strips
	Field study using a DrugCheck3000 based prototype at a music festival
August 2016 - November 2017	Hannover Medical School
	Employment as student assistant for aiding scientific staff in their tasks of research and education
	Tutoring in basic biochemical methods course for students of Biochemistry, Biology and Medicine & Dentistry

EDUCATION

June 2019 - present	Leibniz University Hannover, Institute for Cell Biology and Biophysics
	PhD student
	Research in Cell-matrix interaction in hematopoietic stem cell niche
October 2018 - April 2019	Hannover Medical School, Institute of Pharmacology
	Master thesis (grade: 1,3)
	"Analysis of the function of the histamine H4 receptor in the human colonocyte model HT-29"

April 2017 - April 2019	Hannover Medical School
	M.Sc. Biochemistry (grade: 1,8)
October 2016 - January 2017	Hannover Medical School, Institute of Pharmacology
	Bachelor thesis (grade: 1,3)
	"Analysis of Signaling Events Emerging at the Mouse Histamine-H_2 Receptor Stably Expressed in HEK 293 Cells"
October 2013 - April 2017	Gottfried Wilhelm Leibniz University Hannover
	B.Sc. Biochemistry (grade: 2,0)
2004-2012	Musisches Haus – Gotthold Ephraim Lessing
	Sportgymnasium Neubrandenburg
	Abitur (grade: 1,4)

PUBLICATIONS

Schrammel, J.C., König, M., Frommer, M. et al.
Histamine H1- and H4-receptor expression in human colon-derived cell lines.
Naunyn-Schmiedeberg's Arch Pharmacol (2023).
https://doi.org/10.1007/s00210-023-02565-8

Chandralekha Chatterjee, Peter Schertl, Miriam Frommer, Anita Ludwig-Husemann, Anna Mohra, Nadine Dilger, Toufik Naolou, Sophia Meermeyer, Timna Claire Bergmann, Alejandro Alonso Calleja, Cornelia Lee-Thedieck
Rebuilding the hematopoietic stem cell niche: Recent developments and future prospects
Acta Biomaterialia, Volume 132, 2021, Pages 129-148
ISSN 1742-7061, https://doi.org/10.1016/j.actbio.2021.03.061.